Three Dimensional Nonlinear Soil and Site-City Effects in Urban Regions

Submitted in partial fulfillment of the requirements for

the degree of

Doctor of Philosophy

in

Civil and Environmental Engineering

Ricardo Taborda

B.S., Civil Engineering, EAFIT University
M.S., Civil Engineering, National Autonomous University of Mexico
M.S., Civil Engineering, University of Southern California

Carnegie Mellon University
Pittsburgh, PA

September, 2010

To Maria del Carmen

Acknowledgements

I am deeply thankful to my advisor, Professor Jacobo Bielak, for his vision and guidance. During our work together I was lucky to find in you the particular ability for conducting a student's work towards better research, without ever losing perspective of the humanity in all of us. Jacobo, you reopened the door, allowed me in, and helped me fulfill a dream—and succeed at it—in ways I would have never imagined. For that I will be ever grateful to you. The continued company and support you and Joyce have offered to Maria del Carmen and me during all this time has been but a blessing to us and to Amelia. You are a good advisor, and a good person.

Special acknowledgements to the members of my doctoral committee: Prof. David O'Hallaron, Prof. Amit Acharya, Dr. Julio López, and Dr. Enrique Bazan. In particular, I am in debt with Prof. Acharya for first suggesting to us the use a rate-dependent plasticity approach to modeling nonlinear soil response, and for his careful review of its formulation and implementation; and to Dr. López for his time generosity in evaluating the code and his valuable suggestions for improvements to the modified meshing process for incorporating building models—Julio, thank you, above all, for your friendship.

This individual accomplishment could not have been possible without the inexhaustible support and friendship of many others. Thanks to all my friends at the CEE Department. Special gratitude to Leonardo Ramírez-Guzmán for having helped me see the possibility of coming to Carnegie Mellon, and for his continued partnership; to Saurabh Puri and Mudasar Zahoor for their patience during my first steps into the theory of plasticity; to Shahzeen Attari, Heather Wakeley, Paulina Jaramillo, and Mario Berges, for many moments of fresh air; and to the wonderful CEE Faculty and Staff, with special affection to Maxine Leffard, Cornelia Moore, and Jim Garret. Thank you all for making the load lighter and the road smoother. An ingrately short note of acknowledgement go to my mentors and friends at EAFIT and UNAM; and my pardons to those many others I do not include here explicitly because of limitations of space and memory.

All my gratitude and love to my parents, siblings, and family at large; but above all, to my beautiful wife, Maria del Carmen, who has endured so much, some of it in silence—almost unnoticeably;

and to my beloved daughter, Amelia, who has unknowingly sacrificed many moments and things in her short life. I know it would be foolish of me to promise you any kind of compensation, so I only wish life will offer you the same happiness you two bring to my life every day.

The research work underlying this thesis was supported by National Science Foundation awards: Towards Petascale Simulation of Urban Earthquake Impacts (OCI-0749227); Outward on the Spiral: Petascale Inference in Earthquake System Science, SCEC PetaShake Project (OCI-0905019); A Petascale Cyberfacility for Physics-Based Seismic Hazard Analysis, PetaSHA-2 (EAR-0744493); Enabling Earthquake System Science Through Petascale Calculations, PetaShake (OCI-0749313); A Petascale Cyberfacility for Physics-Based Seismic Hazard Analysis (EAR-0623704); Multiresolution High Fidelity Earthquake Modeling: Dynamic Rupture, Basin Response, Blind Deconvolution Seismic Inversion, and Ultrascale Computing (ITR/NGS EAR-0326449); and The SCEC Community Modeling Environment: An Information Infrastructure for System-Level Earthquake Research (ITR/AP EAR-0122464). Funding was also provided by U.S. Geological Survey award Hybrid Three-Dimensional Modeling of Earthquake Ground Motion in Basins, Including Nonlinear Wave Propagation in Soils (08HQGR0018). SCEC is funded through the NSF Cooperative Agreements EAR-0106924, EAR-0529922; and USGS Cooperative Agreements 02HQAG0008, 07HQAG0008. This research was also possible thanks to an allocation of advanced computing resources supported by the National Science Foundation, and allocations through the TeraGrid Advanced Support Program. The computations were performed on Kraken at the National Institute for Computational Sciences (NICS). Additional support was provided by Mr. and Mrs. Bertucci, and the Carnegie Institute of Technology, through a Bertucci Graduate Fellowship.

Abstract

The main objective of this thesis is to build a framework for performing earthquake simulations capable of including nonlinear soil behavior and the presence of the built environment in highly heterogeneous basins, and to study their influence on the final response of the ground in large urban areas exposed to high seismic hazard. To this end, we use a finite elements approach and extend the capabilities of *Hercules*, the parallel octree-based earthquake simulator developed by the Quake Group at Carnegie Mellon.

Nonlinear soil behavior is incorporated in ground motion simulations employing a rate-dependent plasticity approach to predict the nonlinear state of the material explicitly at every time step. The soil is modeled as a perfectly elastoplastic material. The presence of urban structures is modeled representing buildings as homogeneous blocks made up of the same type of hexahedral elements used in the mesh. These elements are generated automatically through a new set of application programming interfaces, which extend Hercules' meshing capabilities while preserving its core octree-based formulation.

Both implementations are tested under realistic earthquake conditions in heterogeneous geological structures. In the case of nonlinear ground motion modeling, results indicate that soil nonlinearities greatly modify the ground response, confirming previous observations for deamplification effects and spatial variability, and evidencing three-dimensional basin effects not fully observed before. In turn, the presence of building clusters causes multiple soil-structure interaction phenomena that change both the near ground-motion and the individual performance of the buildings themselves. This substantiates the argument that in soft-soil basins may it not be longer valid to ignore the presence of neighboring structures.

These new implementations represent important advances in computational seismology and help make a direct connection to subjects of interest in earthquake engineering. The analysis drawn from the applications presented here confirms aspects known from previous, though limited studies, and broadens our knowledge of the effects of nonlinear soil and the built environment on the ground motion due to earthquakes at a regional level not explored before.

Contents

List of Tables

List of Figures

1

Introduction

Direct observations from past earthquakes, experiments, and modeling, have shown that the ground motion during earthquakes is dominated by a great variety of factors at multiple scales. From source characteristics to specific site conditions, the final response of the ground is affected by path, directivity, and basin effects at the regional scale; and by the soil properties of geotechnical layers and specific site conditions at the local scale. In addition, it has also been observed that structures and foundation systems actively interact with the soil during earthquake induced shaking, sending vibrations back to the ground and creating complex patterns of wave interferences. Moreover, in dense urban areas, the multiple instances of soil-structure interaction systems further change the ground response and the response of the structures themselves. Consideration of these phenomena altogether poses a problem of great complexity and gives rise to numerous questions of high relevance in seismology and earthquake engineering.

The multiscale nature of the problem just described requires advanced, yet pragmatic approaches. For the last two decades the availability of supercomputers for public research, in combination with the power of numerical methods, have made it possible to simulate earthquake related problems at scales never considered before. However, many aspects remain far from being well-understood. Among those of relevance to both seismologists and earthquake engineers are the effects of nonlinear soil behavior and the presence of the built environment on the ground motion, in addition to the effect that the latter may have on the dynamic response of individual structures due to the occurrence of simultaneous multiple soil-structure interaction phenomena. The main objective of this thesis is to provide a framework for performing earthquake simulations capable of including soil nonlinearities and the presence of urban structures in highly heterogeneous basins, and to apply this methodology to a representative set of problems in order to study the influence that these considerations have

on the final response of the ground in highly seismic large urban areas regions. To accomplish this, we use finite-element techniques and extend the simulation capabilities of *Hercules*—the parallel octree-based earthquake simulator developed by the Quake Group at Carnegie Mellon.

Through the necessary implementations and the corresponding analysis of case studies, this research makes contributions that address the following questions:

1. How does the soil nonlinearity affect the ground motion, what is the level of deamplification observed in peak ground response, how does it changes the energy content in frequency, and to what extent does nonlinear behavior reshape the spatial distribution of the ground motion?
2. What are the three-dimensional effects that the presence of structures exert on earthquake ground motion, and how does the response of buildings change due to the multiple interaction phenomena when a realistic cluster of structures is considered in earthquake ground motion simulations?

To answer these questions, nonlinear soil behavior is incorporated into Hercules employing a rate-dependent plasticity approach that predicts the nonlinear state of the material in an explicit way at every time step, without requiring approximations through iterative procedures. Using this methodology, we model the soil as a perfectly elastoplastic Drucker-Prager material as a first approach to understanding nonlinear soil effects in 3D simulations.

We model urban environments by representing individual buildings as prismatic blocks of rectangular cross-section aligned with the mesh coordinate system and filled with homogeneous material, such that their natural periods of vibration match those of their real-world counterparts. Each block representing a building is composed of a subset of hexahedral elements that are part of the entire simulation-domain mesh. These implementations are tested under realistic conditions and pertinent case studies are analyzed.

1.1 Seismic Ground Motion Simulation

Generation of ground-motion synthetics of earthquakes is necessary due to the need to acquire information about the expected response in areas where we do not have or have limited records from past earthquakes. Ideally, one would confront this challenge deterministically using numerical methods like finite difference, finite element or boundary element methods. In practice, doing this for large geographical areas containing the source of excitation, the site conditions, and other characteristics of interest is not trivial. That is why, although some of these numerical methods

had been known for more than half a century, their real application was not possible until relatively recently.

The general public has limited access to large-scale parallel computers and only a small number of scientists in universities and research centers are conducting deterministic simulations of earthquakes at scale. Meanwhile, the preferred ways to obtain synthetics have been the stochastic method and the use of empirical Green's functions (EGF). The latter were first introduced to seismology by Hartzell (1978), followed by Irikura (1984) and Mueller (1985). The main assumption in EGF is that, if the complex fault rupturing process can be broken down into multiple simpler sub-faults, i.e., treated as the sum of small impulsive earthquakes, then the complex propagation of waves from the source to its final destination can be described by a function that encompasses all path and site effects. Such functions, for a single point source, are called Green's functions. Microtremors, small earthquakes and aftershocks, have been used to derive EGF that are later used for source inversions and simulations of larger (scaled) earthquake scenarios. There is an extensive literature on the development of appropriate methodologies (e.g. Hadley and Helmberger, 1980; Irikura, 1986; Wennerberg, 1990) and application of EGF on ground motion simulation (e.g. Munguia and Brune, 1984; Somerville et al., 1991; Irikura and Kamae, 1994; Kamae and Irikura, 1998; Miyake et al., 2003). A detailed review is outside the scope of this thesis. One point that is worth mentioning is that underneath the application of this methodology for the generation of synthetics lays the assumption of a linear system, though linearity, as discussed ahead, does not always hold.

In turn, the stochastic method consists of combining information and parametric descriptions about the path and site characteristics by means of simplified functions and the source spectrum—usually considered to follow the ω-squared model (Aki, 1967)—with the assumption that the phase spectrum of the source may be represented randomly. The method uses this procedure as a tool to generate multiple realizations that, on average, give a sense of what an earthquake may look like at observation points. A detailed review of the most common approach to simulation of ground motions using the stochastic method may be found in Boore (2003b). This reference also includes two tables listing numerous publications with variations and applications of the method. The stochastic method is the most widely used approach to generate earthquake ground motion synthetics (e.g. Boore, 2003a; Silva et al., 2003; Roumelioti et al., 2004; Gorini et al., 2004; Kohrs-Sansorny et al., 2005; Castro and Ruiz-Cruz, 2005; Pousse et al., 2006; Sørensen et al., 2007; Fernández León, 2007). One of the reasons why the stochastic method is particularly attractive, is because it has been shown that (on average) it appropriately simulates the high frequency (> 1 Hz) content of ground motions.

This has made it advantageous to be combined with other methodologies that perform better at or are limited to low frequencies. In particular, the combination of the EGF with deterministic finite-difference simulations for long-period motion and the stochastic method for the complementary short-periods is known as the hybrid Green's function method (Kamae et al., 1998). This method has been successfully applied for obtaining broad-band simulations and study near-fault and attenuation aspects (e.g. Pitarka et al., 2000, 2002; Mena et al., 2006).

On the other hand, deterministic simulations come mainly in three categories: finite differences (FD), finite elements (FE), and high order FE or spectral elements (SE). FE and FD methods were introduced in seismology in the late 1960s, starting with simple structures (e.g. Alterman and Karal, 1968; Boore, 1970, 1972; Lysmer and Drake, 1972; Kelly et al., 1976; Archuleta and Frazier, 1978; Archuleta and Day, 1980). Since then, we have witnessed the rise of numerical solutions, also propelled by the accelerated growth of supercomputers, especially in the last fifteen years. Among the earliest three dimensional (3D) simulations done on a geographical-scale large enough for synthesizing recorded earthquake data, there is the one performed by Frankel and Vidale (1992), who aimed at reproducing the effects of a far-field point source from an aftershock of the 1989 Loma Prieta earthquake in the Santa Clara Valley, California, using a finite differences approach.

After Frankel and Vidale (1992), FD became the standard method for large-scale earthquake simulations (e.g. Frankel, 1993; Olsen et al., 1995a,b; Olsen and Archuleta, 1996; Graves, 1996, 1998; Pitarka et al., 1998; Sato et al., 1999; Furumura and Koketsu, 2000; Frankel and Stephenson, 2000). Others began to implement the solution of the elastodynamic equations for fairly realistic three-dimensional non-planar layered systems using low-order FE (e.g. Bao et al., 1996, 1998; Bielak et al., 1999, 2005), or high-order FE methods with diagonal mass matrix, or SE methods (e.g. Seriani and Priolo, 1994; Faccioli et al., 1997; Seriani, 1998; Komatitsch and Vilotte, 1998; Komatitsch et al., 2004; Käser and Dumbser, 2006; Käser and Gallovic, 2008). Moderate-size problems with relatively simple geometry and geological conditions have been addressed using boundary element, coupled boundary-domain element, and discrete wavenumber methods (e.g. Bouchon and Aki, 1980; Mossessian and Dravinski, 1987; Kawase and Aki, 1990; Bielak et al., 1991; Hisada et al., 1993; Sánchez-Sesma and Luzón, 1995; Bouchon and Barker, 1996; Hisada and Bielak, 2003). A detailed introduction and tutorial, and a more comprehensive review of the FD, FE, and hybrid FD-FE methods may be found in Moczo et al. (2007).

In seismic ground motion simulation, the size of a problem, and thus the expected computational demand, is determined by the scale in both the time domain and the space domain for which the

simulation aims to represent physical phenomena. As a consequence, the size of the simulations is ultimately determined by the combination of two main parameters: the minimum shear wave velocity ($V_{s_{min}}$) and the maximum simulation frequency (f_{max}). Together, they define the mesh resolution (and number of elements), and the time-step size (and number of solving cycles) required for the targeted simulation. For large enough areas, the combination of low shear-wave velocities ($V_{s_{min}} \leq 500$ m/s) and high frequencies ($f_{max} \geq 1$ Hz) may result in billions of elements and hundreds of thousand time-steps, thus the need for supercomputers.

Noted large-scale simulations using FD include those by Olsen et al. (2006, 2008, 2009), who analyzed the ground response in Souther California and, in particular, that of the greater Los Angeles basin for the M_w 7.7 TeraShake and the M_w 7.8 ShakeOut earthquake scenarios. These authors used a staggered FD approach to simulate the wavefield generated by kinematic and dynamic source representations of these two hypothetical earthquakes in the southern portion of the San Andreas fault. In both cases, a simulation domain of 600 km $\times$ 300 km $\times$ 80 km was used to simulate the events for a combination of $V_{s_{min}} = 500$ m/s, $f_{max} = 0.5$ Hz—equivalent to 1.8 billion nodes at a 200 m resolution.

Despite their success and valuable contributions to understanding the importance of basin, directivity, and wave guiding effects—only visible through large scale 3D simulations—standard FD approaches are limited by the use of uniform grids. This constrains the method for modeling non-prismatic domains. Moreover, it imposes a high computational demand for simulations with higher frequencies and lower soil-velocities. Recently, a FD simulation of an M 8 earthquake scenario in a volume domain of 800 km $\times$ 400 km $\times$ 100 km required 32 billion elements and over 600 thousand CPU hours for a 100 m resolution grid (as reported in Potluri et al., 2010), meaning that any small increase in f_{max} or reduction in $V_{s_{min}}$ binds FD codes to use the largest available supercomputing facilities at capability mode—an untenable condition.

By contrast, though not as popular as FD, mainly because of the complexity involved throughout the meshing process, FE techniques offer a more versatile alternative. Introduced in the early 1970s in seismology (Lysmer and Drake, 1972), FE has been successfully and increasingly used in large-scale earthquake simulations and seismic inversion and rupture problems during the last fifteen years (e.g. Bao et al., 1996, 1998; Hisada et al., 1998; Bielak et al., 1999; Kim et al., 2003; Akcelik et al., 2003; Bielak et al., 2005; Askan et al., 2007; Ramírez-Guzmán, 2008). In particular, Hisada et al. (1998) did a 3D simulation for the long-period (> 0.9 s) response of the Kobe region during the mainshock and an aftershock of the 1995 Hyogoken-Nanbu (Kobe) earthquake; and Bielak et al. (1999) studied

the response of a small valley in Kirovakan during the 1988 Armenia earthquake. Both studies stressed the importance of basin effects in 2D and 3D analysis and highlighted the potential of FE simulations on parallel computers. Bielak et al. (2005) implemented an octree-based finite element method for large-scale earthquake ground-motion simulations on realistic basins, exploiting special characteristics of computing data-structures to achieve high parallel performance. This procedure had been earlier used by Kim et al. (2003) to simulate the seismic response of the greater Los Angeles basin for a mainshock of the 1994 Northridge, California earthquake for frequencies up to 1 Hz in a volume domain of 80 km × 80 km × 30 km. These works later culminated with the development of *Hercules* by Tu et al. (2006).

Hercules is an octree-based finite-element parallel software for performing highly efficient end-to-end earthquake simulations. Within the framework of scientific collaborations at the Southern California Earthquake Center, we used Hercules to simulate and verify the TeraShake and ShakeOut scenario earthquakes described above (Taborda et al., 2006b, 2007b; Bielak et al., 2010). Hercules has allowed us to further push simulation boundaries, i.e., to lower $V_{s_{min}}$ and raise f_{max}, at a much lower computational cost than FD-based simulators (Taborda et al., 2006a, 2009). Using Hercules, Taborda et al. (2009) reproduced the ground motion of the greater Los Angeles basin during 100 s of the M_w 5.4 2008 Chino Hills earthquake in a volume domain of 180 km × 135 km × 62 km for $V_{s_{min}} = 200$ m/s and $f_{max} = 2$ Hz. For this simulation Hercules generated an unstructured mesh with 708 million elements (the smallest element being of ~10 m size) and consumed only 72 thousand CPU hours. Using FD, a simulation of this size and equivalent resolution requires a grid with more than 180 billion nodes, and it would demand over 25 million CPU hours, i.e., more than 4 days of continued computing at the largest supercomputer available for public research today, using 220K core processors.

This thesis further advances Hercules simulation capabilities with application to problems of high relevance in seismology and earthquake engineering.

1.2 Nonlinear Soil in Seismology and Engineering

The potential influence of nonlinear soil behavior on the ground motion during earthquakes has been known to engineers since the late 1960s (Seed and Idriss, 1969). Early in the 1970s, Hardin and Drnevich (1972) showed through laboratory tests that with increasing strain amplitude, the shear modulus of soils decreases and the damping ratio increases. Evidence of such phenomena during

earthquakes was disputed by seismologists for some time. It appeared to seismologists that the soil responses being observed during earthquakes were satisfactorily explained by other considerations. Pondering soil nonlinearity at sites, other than those involving liquefaction, was for some time regarded as a dubious proposition. It might actually be possible that during a considerable period of time, and mainly due to the absence of sufficient and reliable data, the presence of nonlinearities was overlooked (Beresnev and Wen, 1996). As recognized by Aki (2003), this situation changed with the growing number of available accelerograms and better characterization of sites, particularly after observations from the 1989 Loma Prieta and 1994 Northridge earthquakes.

Based on observations, one of the first cases to provide reliable records of events for the study of nonlinear site effects were the downhole accelerograph arrays of Taiwan, SMART1 and SMART2 (Abrahamson et al., 1987). The analysis of their recordings revealed significant nonlinear soil response, manifested in deamplification of the motion and reduction of shear wave velocities for peak ground accelerations larger than 0.15 g (e.g. Chang et al., 1989; Wen, 1994; Beresnev et al., 1995; Beresnev, 1995; Elgamal et al., 1995; Zeghal et al., 1995). Using surface-to-downhole spectral ratios, Chang et al. (1989) observed reductions in shear moduli of up to 80 percent for peak ground accelerations greater than 0.21 g, and Wen (1994) reported reductions in shear-wave velocities of up to 50 percent for accelerations over 0.26 g. In turn, Beresnev et al. (1995) observed reductions ranging between 0.4 and 2.9 in amplification of soil-to-rock spectral ratios in strong ground motion relative to the weak events for a frequency range between approximately 1 and 9 Hz, and also reported reductions of up to 50 percent in shear-wave velocities for the strongest of the events considered. Using calibrated models for vertical propagation of waves, Elgamal et al. (1995) and Zeghal et al. (1995), associated the reductions in shear-wave velocities to the rise in pore pressure.

The 1989 Loma Prieta earthquake in California clearly exposed the effects of nonlinear soil behavior for the first time during a strong seismic event (e.g. Chin and Aki, 1991; Darragh and Shakal, 1991; Bardet and Kapuskar, 1993; Beresnev, 2002; Rubinstein and Beroza, 2004a,b; Schaff and Beroza, 2004). Chin and Aki (1991) studied nonlinear effects at sediment sites in the epicentral region and, after eliminating the influences of radiation pattern and topography, concluded that nonlinear effects occurred at levels above 0.1–0.3 g. Using soil-to-rock spectral ratios for the main event and three aftershocks, Darragh and Shakal (1991) observed important deamplification effects in soft-soil deposits for frequencies raging between 0.5 and 2 Hz that were not present at stiff-soil sites. Beresnev (2002) compared linear simulations to recorded data and found differences attributable to soil nonlinearities in the range of 1–3 Hz. Rubinstein and Beroza (2004a) used recordings from

repeating sequences south from the rupture zone and consistently observed late-arriving S-phases strongly correlated to shaking magnitudes exceeding the strength of rocks, thus evidencing nonlinear behavior of the crust near the surface. Similar results were obtained by Schaff and Beroza (2004).

Following the 1994 Northridge earthquake, more plausible evidence of nonlinear effects was brought to the attention of the engineering and seismological community (e.g. Davis and Bardet, 1996; Bardet and Davis, 1996a,b; Trifunac and Todorovska, 1996; Field et al., 1997; Cultrera et al., 1999). Bardet and Davis (1996a) and their two companion studies noted that the absence or filtering of high frequencies in recordings at the van Norman complex in San Fernando valley were due to the nonlinear behavior, lateral spreading, and liquefaction of underlying soil layers. Further analysis of the van Norman complex by Cultrera et al. (1999) reaffirmed a substantial nonlinear response of the soils in the area. Trifunac and Todorovska (1996) analyzed the strong motion amplitudes in the San Fernando valley and found that a noticeable reduction in recorded horizontal peak accelerations occurred when the strains exceeded 10^{-3}, at sites with shear wave velocities less than 360 m/s and at distances of less than 15–20 km from the fault. Field et al. (1997) compared the main shock to the aftershocks and reported sediment deamplification up to a factor of 2, implying significant nonlinearities. Moreover, Field et al. argued that the confirmation of nonlinearities questioned the use of empirical Green's functions to study or predict strong ground motions—an issue that remains unresolved as they are still in use, although mainly for low frequencies, where the influence of nonlinear soil may not be as prominent.

Similar studies have been conducted in other regions prone to earthquakes such as Seattle, Washington (Frankel et al., 2002), and Japan (Satoh et al., 1995; Sato et al., 1996; Aguirre and Irikura, 1997; Tsuda et al., 2006; Rubinstein et al., 2007). In Seattle, Frankel et al. (2002) computed soil-to-rock spectral ratios for 35 locations using recordings of the M 6.8 2001 Nisqually earthquake and its M_{L} 3.4 aftershock to study site response and basin effects in the region. They found that site amplification was correlated to surficial geology and the nonlinearity of soft soils, even for the modest accelerations of the Nisqually main shock. In Japan, Satoh et al. (1995) reported changes in the S-wave velocities and damping factors obtained for the stronger (M_{J} 5.1) of four events near the Ashigara valley, using surface-to-borehole spectral ratios. Sato et al. (1996) and Aguirre and Irikura (1997) also used spectral ratios to study recordings from the 1995 Hyogoken-Nambu earthquake in Port Island. They observed large variations in the surface-to-borehole ratios between the main shock and the aftershocks, with reductions in the upper layers' velocity of up to 20 percent during the main shock. In turn, Tsuda et al. (2006) used a spectral inversion method to compare estimates of

ground response for the main and aftershock events of the M_w 2003 Miyagi-Oki earthquake. Their comparison of the site amplification from aftershocks with the main event indicated that nonlinear soil behavior occurred at the stations with a softer near-surface velocity structure. More recently, Rubinstein et al. (2007) identified delays in arrival times associated with reductions in seismic velocities using repeating earthquake sequences near Hokkaido, caused by the 2003 Tokachi-Oki earthquake. These various evidences of changes in amplification factors, dominant frequencies, and wave velocities revealed strong nonlinear effects and a correlation between low near-surface material velocity and the degree of nonlinearity.

In terms of modeling and simulations, the first studies in geotechnical engineering also date back to the late 1960s and 1970s (e.g. Idriss and Seed, 1968a,b, 1970; Schnabel et al., 1972a; Streeter et al., 1974; Joyner, 1975; Joyner and Chen, 1975; Finn et al., 1978). Most of these studies were done for horizontally layered half-spaces under vertically incident waves, or analogous models. Some of them proposed and applied linear equivalent methodologies to represent the change in soil properties due to expected nonlinear behavior (e.g. Idriss and Seed, 1968a, 1970; Schnabel et al., 1972a). Streeter et al. (1974) and Finn et al. (1978) later showed that the use of equivalent linear approaches is undesirable because they overestimate the seismic response of soils due to pseudo-resonance at periods corresponding to the strain-compatible stiffness used in the final elastic iteration analysis. Moreover, since the material remains elastic with the equivalent linear approach, it cannot produce permanent deformations such as those expected from strong seismic loading. Such deformations, however, are of high importance for assessing damage in (long) structures susceptible to the effect of differential ground motion, such as bridges. By contrast, direct nonlinear methods naturally reproduce these characteristics given that the shear modulus, and thus the stresses, are modified and computed at every time step according to the current state of strains and the history of stresses. Therefore, whatever the constitutive law is, the nonlinear stress-strain relationship is closely followed.

Several rules have been used to model the yielding conditions and cyclic behavior of soils, or backbone curves, for representing the stress-strain relationship evolution over time. They include, linear (Idriss and Seed, 1968b), multilinear (Joyner, 1975; Yu et al., 1993), and a wide variety of models following the classical theory of plasticity with different yield criteria, and flow and hardening rules, which have been adapted for reproducing the behavior of both cohesive and cohesionless soils, with and without pore-pressure considerations. Most of these more complex models are based on the developments by Mróz (1967) and Iwan (1967), and subsequent improvements by Prevost (1977,

1978, 1985), Mróz (1980), Dafalias and Popov (1975, 1977) and Dafalias (1986), and have been enlarged and adapted by many others (see Prevost and Popescu, 1996).

Notwithstanding the many available models, linear equivalent methods are still the prevalent approach in engineering practice—through computer programs such as SHAKE-91 (Schnabel et al., 1972b; Idriss and Sun, 1993). More elaborate studies predominantly incorporate nonlinearity performing a one-dimensional (1D) analysis on a soil column subjected to a vertically incident wave for each location of interest. In such cases, the incident motion at the interface between the softer sediments and the harder substrata is previously obtained from the deconvolution of the surface synthetics of a 3D analysis, or from recordings on a rock site (e.g. Archuleta et al., 2003; Assimaki et al., 2008). Although these hybrid techniques yield reasonable estimates under vertically incident seismic excitation, they cannot represent surface waves and basin effects in conjunction with the influence of nonlinearities. The few 2D and $2\frac{1}{2}$D studies of nonlinear soil amplification (e.g. Joyner and Chen, 1975; Joyner, 1975; Elgamal, 1991; Marsh et al., 1995; Zhang and Papageorgiou, 1996), though they have confirmed the importance of nonlinearity on site response, cannot ensure that they are a valid substitute for 3D modeling, which would add much more information and would require better interpretation of results. In particular, a $2\frac{1}{2}$D study of the Marina District in San Francisco during the 1989 Loma Prieta earthquake found that the focusing and lateral interferences often observed in studies based on linear soil behavior are still present for strong excitation (Zhang and Papageorgiou, 1996). However, the authors used a linear equivalent approach—thus no permanent deformations were reproduced.

Three-dimensional simulations of nonlinear effects have been very limited. Mainly because of complexity, their use is almost reserved for special structures such as bridges, dams, or nuclear power plants; and the modeling scale is constrained by the computational cost of the simulations and available resources. One of the few exceptions is the research done on the seismic response of the Humboldt Bay Middle Channel Bridge (Zhang et al., 2003; Yang et al., 2003; Zhang et al., 2004; Yan, 2006; Zhang et al., 2008; Elgamal et al., 2008), where 2D and 3D models were used to study the seismic reliability of the structure-foundation-ground system, considering nonlinear soil. However, this kind of simulations are of a local scale (< 1 km).

To our knowledge, the only full 3D simulation aimed at addressing the problem at a larger scale has been the work of Xu (1998) and Xu et al. (2003). Xu et al. used a finite element methodology to study the response of an idealized basin (4 km $\times$ 4 km $\times$ 1 km) under vertically incident SH-waves, considering the soil within the basin as a Drucker-Prager elastoplastic material (after Drucker

and Prager, 1952). Their results showed that whereas the ground motion decreases due to soil nonlinearity, the spatial variation of the surface motion followed that of the linear model, having clear basin effects. They also observed permanent deformations and reductions in peak ground accelerations by about a factor of 2 in the deepest regions of the basin, where the shear strains were the largest.

This thesis seeks to extend 3D ground motion simulation in inelastic media to even larger, regional scales (10–100 km), in highly heterogeneous media, and under arbitrary and realistic seismic excitation, while maintaining a balance with respect to the computational cost of modeling, thus advancing the state of the art in ground motion simulations.

1.3 Site-City Effects and Urban Seismology

The term *site-city interaction* was first coined by Guéguen et al. (2000b) who aimed at modeling the effect of an arbitrary collection of buildings on the close free-field when the system is subjected to a realistic seismic input motion. In a more regional perspective, following Meremonte et al., 1996, Fernández-Ares (2003) described the effects of the built environment on the ground motion as a subject of *urban seismology*. Boutin and Roussillon (2004) referred to a similar problem as the *urbanization effect* due to *soil-city interaction* phenomena. Regardless of the differences in terminology, which underline some level of distinction with respect to the scale of each case, they all address a common question, that is, what is the effect that the multiplicity of soil-structure systems has on the near- and mid-range ground motion and in the response of individual structures as each one is affected by the presence of neighboring ones and vice versa. The answer to this is, in part, the subject of this thesis.

Studies of classical soil-structure interaction (SSI) effects represent the natural precursor of site-city interaction problems in urban seismology. The study of SSI problems goes back to the 1950s. Merritt and Housner (1954) studied the interaction effects on the maximum base shear force and change in the fundamental period of vibration of typical tall buildings subjected to ground accelerations of actual earthquakes. They found that the period of flexible-base systems could increase up to 10 percent with respect to that of a fixed-base assumption if the foundation compliance was high enough (i.e., a stiff structure resting on soft soil). This study only considered the interaction due to rocking of the foundation and the structures were modeled as lumped-mass 2D systems. Based on observations of recordings from two buildings during the 1952 Arvin-Tehachapi earthquake, Hous-

ner (1957) noted that stiff structures resting in soft soils with large enough foundation dimensions will reduce the amplitude of incoming seismic waves. Housner also predicted that, if the horizontal coupling between the structure and the soil were to be strong enough, the oscillation of the building in its fundamental mode would impart a periodic motion to the base that would be recordable on the ground nearby. Using recordings from vibration tests on the Millikan Library at the California Institute of Technology, Jennings (1970) found that the motion induced into the ground by the vibration of the structure could be registered in the horizontal motion of the surface at 4.8 km in the area of Pasadena, and up to 10.7 km away from the testing site, at Mt. Wilson. Since the excitation was induced from the building to the ground, Jennings called it *structure-soil interaction*.

This structure-soil coupling phenomenon was later suggested by Bard et al. (1996) as a possible contribution to the characteristics observed in some ground motion records in Mexico City during 1985, Michoacán earthquake. Similar results for the case of structure-soil interaction were more recently found by Guéguen et al. (2000a) through both full-scale experiments and analytical models. Guéguen et al. compared the recordings of a set of pull-out tests on a scaled structure with those of a 3 degree-of-freedom (DOF) system (after Jennings and Bielak, 1973), and found that at twice and ten times the building base, the ground motion was about 25 and 5 percent that of the base motion, respectively. 10 and 3 percent were the corresponding values computed by Bard et al. (1996) for their 3D model. Guéguen et al. concluded that the maximum spectral-amplitude spatial-decay lies in the range between $1/r$ and $1/\sqrt{r}$. Jennings (1970) reported this rate to be between $1/r$ and $1/r^{3/2}$.

The first works on multiple SSI systems date back to the mid 1970s. Luco and Contesse (1973) studied the structure-soil-structure interaction effects of two parallel infinitely long shear-walls with rigid semi-circular foundations perfectly bonded to the soil on a half-space under vertically incident harmonic SH waves. They observed coupling effects that mainly changed the response of the smaller of the two shear-walls, and concluded that more realistic 3D models would produce coupling between the horizontal, rocking, torsional and vertical motion of the foundations. Wong and Trifunac (1975) extended the same problem to multiple (≥ 2) shear walls under plane SH-waves with variable angle of incidence. They considered the cases of two, three, and five buildings with different heights, separations, and stiffness properties; and concluded that structure-soil-structure interaction is especially prominent when the structure of interest is smaller and lighter than its neighbors, and that the scattering of waves in the vicinity of the foundations could also alter the free-field motion appreciably.

Two decades later, Bard et al. (1996) and Wirgin and Bard (1996) revived the interest on the subject after their suggesting that the long duration and monochromatic characteristics of some of the lake-zone recordings in Mexico City during the 1985, Michoacán earthquake was partially attributable to the influence of (high-rise) buildings. Bard et al. (1996) used a wavenumber technique to analyze the wavefield radiated by a single degree-of-freedom on a flexible mat foundation resting at the surface of a horizontally stratified half-space. The results confirmed the possibility of significant modifications on the free-field motion up to a distance of a few hundred meters for large buildings resting on very soft soils ($V_s < 100$ m/s). The level of perturbation for embedded foundations was of 31, 23, 12, 6 and 3 percent of the free-field peak acceleration, for distances of 50, 100, 200, 500 and 1000 m, respectively. Wirgin and Bard (1996) used a 2D set of buildings resting on a layered half-space subjected to vertically incident SH waves in antiplane motion. The buildings were modeled as parallel periodic blocks with rectangular shapes, filled with isotropic elastic material, and in full (welded) contact with the ground. Their results indicated that the effects of multiple soil-structure interaction are significant up to distances of 1 km, consisting of larger intensities and longer durations. They also found that the density and damping characteristics of the building blocks, other than their presence, did not particularly influence the free-field perturbation, but had only an effect on their own response. In their discussion of results, Wirgin and Bard acknowledged that their model omitted important aspects such as lateral variations in the geological structure and inplane motions, i.e., tridimensionality—a consideration which this thesis overcomes.

After Guéguen et al. (2000b), there came a series of works dedicated to the broader picture of multiple structures in interaction with specific site conditions, resulting in what we now define as site-city interaction effects and problems of urban seismology (e.g., Clouteau and Aubry, 2001; Chávez-García and Cárdenas-Soto, 2002; Guéguen et al., 2002; Semblat et al., 2002; Tsogka and Wirgin, 2003b; Fernández-Ares, 2003; Boutin and Roussillon, 2004; Semblat et al., 2004; Kham et al., 2006; Fernández-Ares and Bielak, 2006).

Clouteau and Aubry (2001) presented a numerical method to account for a 3D spatial distribution of buildings with surface-rigid foundations resting on a layered elastic-half-space under vertically incident plane waves. After analyzing the response of regular and random city sets, Clouteau and Aubry concluded that, although there were important interactions for the random city case, the influence on the response of the buildings themselves was not as important. This is contrary to previous results and has been attributed to limitations in their model (that excluded kinematic interaction).

Chávez-García and Cárdenas-Soto (2002) investigated changes on the 'free-field' motion using data from microtremors recorded on soft soils in Mexico City using spectral ratios, and observed SSI effects at distances about five times the buildings base, but they were not able to identify wave trains emitted by specific buildings. Guéguen et al. (2002) used an analytical model to account for the individual effects of 180 buildings in the Roma district in Mexico City and, although they found the effects of the buildings to be considerable, their calculations neglected the effect of kinematic interactions and simultaneous structure-to-structure interactions.

In turn, Semblat et al. (2002) used the boundary element method in a 2D model resembling the alluvial valley of Nice, France, that included a set of buildings modeled as homogeneous blocks in full contact with the ground, concluding that if the building periods matched that of the soil stratum, it was possible to observe amplifications of up to 50 percent in the ground motion. Tsogka and Wirgin (2003b) solved a similar problem for a 2D layered halfspace with embedded homogeneous blocks representing the buildings under a vertically incident SH Ricker pulse, and found that, despite the short and transient nature of the excitation, the response of the system with structures was considerably longer than that without them.

Kham et al. (2006) also used a 2D boundary element method to study two simplified site-city configurations with different setups in terms of homogeneity of structures and periodicity of space between them, for a constant depth (trapezoidal) basin excited with a Ricker pulse. Apart from reaffirming previous observations, Kham et al. showed that the irregularity of the city (i.e., different building types in a non-periodical arrangement) influences the group effect because it reduces the coherency of the buildings response, which may result in constructive interferences between perturbations of up to 30 percent of the free-field.

More recently, Laurenzano et al. (2010) studied the interaction between two buildings on soft soil, one of which suffered significant damage during the 2002 Molise, Italy seismic sequence. Using a 2D Chebyshev spectral element method, the authors concluded that there was spectral amplification effect due to the presence of the buildings and to their interaction during the seismic excitation.

Most of the studies mentioned thus far were done using 2D approaches under vertically incident wavefields of excitation at local scales. By contrast, Fernández-Ares (2003) studied the problem from a broader—urban seismology—point of view, using full 3D models. In his thesis work and later publications (Fernández-Ares and Bielak, 2004, 2006), Fernández-Ares aimed at analyzing the dynamic response of dense urban areas on soft-soil basins. To that end, he used the Domain Reduction Method (Bielak et al., 2003) to extract a subdomain of 6 km $\times$ 3 km $\times$ 1.2 km and model

the response of an idealized set of structures (with fundamental frequencies equal to 1 and 2 Hz, and three different types of foundations) near the edge of a shallow lens-like basin of circular cross-section in a layered halfspace resembling the conditions of Mexico City. Fernández-Ares concluded that SSI effects for a particular structure within a city are incomplete if the effect of surrounding buildings is not accounted for, and suggested that further research was required to understand the different aspects involved and assess the impact that these phenomena have in urban regions located in high earthquake-hazard areas.

Other somewhat relevant studies worth mentioning in passing are those by Kanamori et al. (1991), Erlingsson and Bodare (1996), Erlingsson (1999), Kim et al. (2001), Cornou et al. (2004), and Guéguen and Bard (2005). These are not necessarily dedicated to the subject of multiple SSI in the sense of site-city effects or urban seismology, but adequately exemplify the presence of structure-soil or structure-soil-structure interactions and their importance.

This thesis aims at contributing towards the goal of understanding the effect that the built environment has on the ground motion. It corroborates previous observations and addresses questions raised by valuable but limited previous studies, and extends the simulation capabilities necessary to represent complex large-scale 3D site-city interaction problems in urban regions prone to earthquakes. In so doing, it paves the road for future micro-zonation studies involving multiple SSI effects, which would ultimately help to the improvement of building codes.

2

Earthquake Simulations Framework

2.1 Wave Propagation in Elastic Media

2.1.1 Governing Equations

Deterministic earthquake ground motion simulation entails obtaining the solution of the linear momentum equation, or equation of motion for a continuum, as shown in (2.1) for Cartesian coordinates in indicial notation. Here, σ_{ij} represents the Cauchy stress tensor, ρ is the mass density, and f_i and u_i are the body forces and displacements in the i direction. Dots stand for time derivatives and subscripts following a comma mean partial derivatives in space with respect to the x_j coordinate. Repeated subscripts imply summation.

$$\sigma_{ij,j} + f_i = \rho \ddot{u}_i \tag{2.1}$$

$$\sigma_{ij} = \lambda \epsilon_{kk} \delta_{ij} + 2\mu \epsilon_{ij} \tag{2.2}$$

For the special case of elastic isotropic solids, stresses relate to strains following Hooke's law of elasticity as seen in (2.2), where δ_{ij} is the Kronecker's delta, and μ and λ are the Lamé parameters that determine the stiffness properties of the material. Using the strain-displacement relationships given in (2.3), the Cauchy stress tensor may be expressed in terms of displacements as shown in (2.4). Substituting (2.4) into (2.1) allows to fully express the linear momentum equation in terms of displacements, as in (2.5).

$$\epsilon_{ij} = \frac{1}{2} \left(u_{i,j} + u_{j,i} \right) \tag{2.3}$$

$$\sigma_{ij} = \lambda u_{k,k}\delta_{ij} + \mu\left(u_{i,j} + u_{j,i}\right) \tag{2.4}$$

$$\lambda u_{k,ki} + \mu\left(u_{i,jj} + u_{j,ij}\right) + f_i = \rho\ddot{u}_i \tag{2.5}$$

This equation is known as Navier's equation of elasticity for an isotropic, heterogeneous body. Applying Helmholtz's decomposition, it is possible to show that the displacement field, u, may be represented as the combination of two terms, each corresponding to waves traveling at different speeds. These are the primary, V_p, and shear, V_s, wave velocities, which relate to the Lamé constants according to (2.6).

$$V_\mathrm{p} = \sqrt{\frac{\lambda + 2\mu}{\rho}} \qquad\qquad V_\mathrm{s} = \sqrt{\frac{\mu}{\rho}} \tag{2.6}$$

$$V_\mathrm{p}^2 u_{j,ji} + V_\mathrm{s}^2\left(u_{i,jj} - u_{j,ji}\right) + \frac{f_i}{\rho} = \ddot{u}_i \tag{2.7}$$

V_p and V_s are common parameters in seismology and engineering for referring to material properties in wave propagation problems. It is therefore sometimes convenient to express Navier's equation in terms of seismic velocities as done in (2.7) after substituting (2.6) into (2.5). Nonetheless, for the numerical discretization process described ahead, we will use it in its original form in terms of displacements, i.e., as in (2.5).

2.1.2 Numerical Discretization

Applying finite elements in space to the linear momentum equation using the standard Galerkin method, the weak form of Navier's equation becomes (2.8). $\mathbf{M}$ and $\mathbf{K}$ are the system's mass and stiffness matrices given by (2.9) and (2.10), respectively. $\mathbf{f}$ is the assembled vector of body forces given by (2.11), which, for the seismic problem, represents the earthquake source. $\mathbf{u}$ is the vector of nodal displacements, ϕ_i is the finite element global basis function associated with the i-th node, and Ω is the volume domain. For convenience, we have omitted terms associated with boundary conditions.

$$\mathbf{M}\ddot{\mathbf{u}} + \mathbf{K}\mathbf{u} = \mathbf{f} \tag{2.8}$$

$$\mathbf{M}_{ij} = \int_\Omega \rho\phi_i\phi_j d\Omega \tag{2.9}$$

$$\mathbf{K}_{ij} = \int_\Omega \left(\mu + \lambda\right)\nabla\phi_i\nabla\phi_j^T d\Omega + \int_\Omega \mu\nabla\phi_i^T\nabla\phi_j\mathbf{I}d\Omega \tag{2.10}$$

$$\mathbf{f}_i = \int_\Omega \phi_i f d\Omega \tag{2.11}$$

Viscous damping may be added to (2.8) in different forms. A common practice in engineering is to use an attenuation approximation known as Rayleigh damping by introducing a damping matrix, $\mathbf{C}$ that can be expressed as a linear combination of the mass and stiffness matrices. The new system of equations considering attenuation becomes (2.12), where $\mathbf{C}$ is determined by (2.13). The superscript $\mathbf{e}$ indicates that we are working at the element level. α and β are the corresponding mass and stiffness factors of proportionality, which are set to minimize the target fraction of critical damping.

$$\mathbf{M}\ddot{\mathbf{u}} + \mathbf{C}\dot{\mathbf{u}} + \mathbf{K}\mathbf{u} = \mathbf{f} \tag{2.12}$$

$$\mathbf{C}^\mathbf{e} = \alpha\mathbf{M}^\mathbf{e} + \beta\mathbf{K}^\mathbf{e} \tag{2.13}$$

Using central differences to express the first and second derivatives of displacement, (2.12) is reduced to a system of difference equations (2.14), where Δt represents the time step and the subscript n represents a given step at time $t = n\Delta t$. Note that we have used a backward first order approximation for the first derivative of displacements to avoid a second appearance of $\mathbf{u}_{n+1}$. Furthermore, using a diagonally lumped mass matrix, the system decouples with respect to $\mathbf{M}$ and the forward solution of displacements for any given node i in the mesh, is given by (2.15).

$$\mathbf{M}\left(\frac{\mathbf{u}_{n-1} - 2\mathbf{u}_n + \mathbf{u}_{n+1}}{\Delta t^2}\right) + \mathbf{C}\left(\frac{\mathbf{u}_n - \mathbf{u}_{i-n}}{\Delta t}\right) + \mathbf{K}\mathbf{u}_n = \mathbf{f}_n \tag{2.14}$$

$$u^i_{n+1} = \frac{\Delta t^2}{m^i} f^i_n - \left(u^i_{n-1} - 2u^i_n\right) - \frac{\Delta t^2}{m^i}\left(\sum_\mathbf{e} \mathbf{K}^\mathbf{e}\mathbf{u}^\mathbf{e}_n\right)_i - \frac{\Delta t}{m^i}\left(\sum_\mathbf{e} \mathbf{C}^\mathbf{e}\left(\mathbf{u}^\mathbf{e}_n - \mathbf{u}^\mathbf{e}_{n-1}\right)\right)_i \tag{2.15}$$

$$\begin{aligned} u^i_{n+1} \quad = \quad & \frac{\Delta t^2}{m^i} f^i_n + \left(2u^i_n - u^i_{n-1}\right) - \alpha\Delta t\left(u^i_n - u^i_{n-1}\right) \\ & -\frac{\Delta t}{m^i}\beta\left(\sum_\mathbf{e} \mathbf{K}^\mathbf{e}\left(\mathbf{u}^\mathbf{e}_n - \mathbf{u}^\mathbf{e}_{n-1}\right)\right)_i - \frac{\Delta t^2}{m^i}\left(\sum_\mathbf{e} \mathbf{K}^\mathbf{e}\mathbf{u}^\mathbf{e}_n\right)_i \end{aligned} \tag{2.16}$$

Here, m^i and f^i are the mass and body force associated with the i-th node of interest, and $\mathbf{K}^\mathbf{e}$ and $\mathbf{u}^\mathbf{e}$ are the local stiffness matrix and corresponding vector of displacements of all elements associated with node i. Substituting (2.13) into (2.15), the forward solution of displacements becomes (2.16).

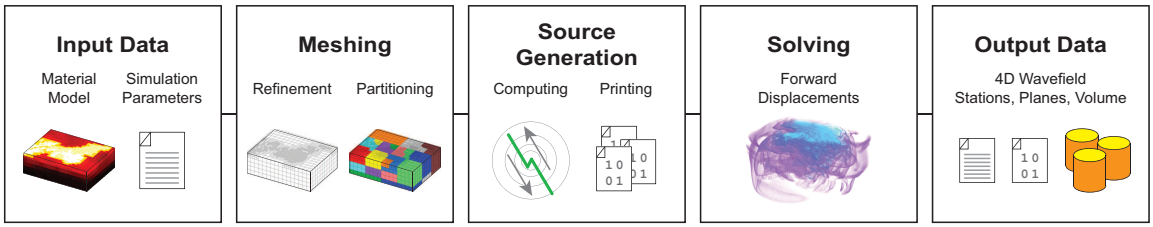

Figure 2.1: Schematic representation of the simulation process using Hercules.

This expression is the analytical kernel used in Hercules for the solution of the wave propagation in a linear-elastic heterogeneous medium.

2.2 Hercules

Hercules is the finite-element parallel software for earthquake simulations developed by the Quake Group at Carnegie Mellon. First introduced in Tu et al. (2006), Hercules has been in continued development for the last five years. It relies on an octree-based mesher and solves the elastic wave equation (2.1) by approximating the spatial variability of the displacements and the time evolution with finite elements and central differences, respectively. The resulting scheme has a quadratic convergence rate for displacements, in both time and space. Since the traction-free boundary conditions at the free-surface are natural in the FE, no special treatment is required at the surface (e.g. Bao et al., 1998). For the absorbing boundary conditions, Hercules uses a plane wave approximation (Lysmer and Kuhlemeyer, 1969). Attenuation in the bulk is introduced by means of a Rayleigh proportional damping mechanism (Bielak et al., 1999). At the moment, this scheme does not distinguish between P- and S-waves attenuation, but uses instead a single overall target quality factor Q, which is set to $Q = kV_s$, where k is a dimensionless scalar and V_s is given in kilometers per second (Graves and Pitarka, 2004; Graves, 2008). Excluding the special case related to absorbing boundary conditions, the forward solution for the displacements at the mesh nodes as implemented in Hercules is given by (2.16) in the previous section.

A particular feature of Hercules is that it implements an end-to-end approach to large-scale simulations unlike many other simulation codes (Tu et al., 2006). It combines the processing of input data necessary for the generation of earthquake-source forces, the mesh generation and partitioning, a forward explicit finite element solver, and application interfaces for I/O operations, all in the same code. This gives Hercules versatility and portability. Figure 2.1 shows a schematic representation of

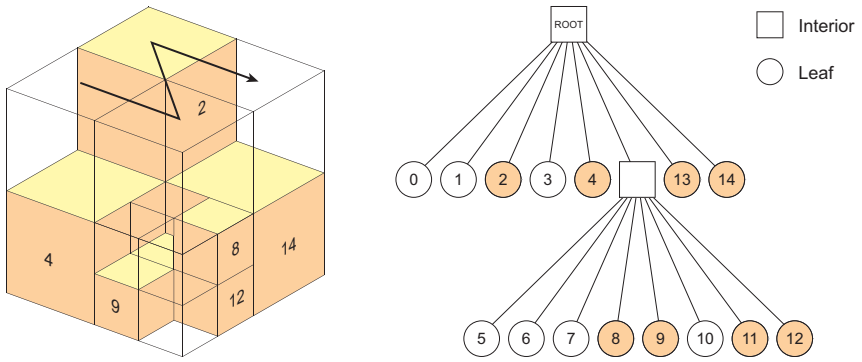

(a) Domain representation **(b)** Tree representation

Figure 2.2: Octree data structure used in the meshing process. Colors are used to relate the two representations, i.e., filled octants on the left correspond to the filled leaves on the right following the numbering in z-order.

the simulation process using Hercules. The following sections discuss in greater detail some relevant aspects of the code.

2.2.1 Meshing Process

Careful understanding of the meshing process is necessary for incorporating building models to the mesh in order to simulate site-city interaction effects, which is later described in Chapter 4. In principle, the meshing process in Hercules consists in partitioning the domain by recursively subdividing it into eight cubes or hexahedra, here called *octants*, depending on the targeted S-wavelengths. This process consists of five major procedures: (1) creation and distribution, (2) refinement, (3) balancing, (4) partitioning, and (5) extraction. Each of these steps is executed through methods contained in Hercules' *octor* library. This library helps manipulate the *octree* data structures at the core of the meshing process. An octree is a tree-like abstraction extensively used in computer science to manipulate massive volumetric data using pointers to interior and leaf nodes with a particular payload. Figure 2.2 shows the equivalent representation of an octree.

$$e \leq \left(\frac{V_s}{f_{max}}\right) \Big/ p \tag{2.17}$$

The creation and distribution step is performed by the `octor_newtree` method. In this method each processor creates a very coarse mesh of the full domain with enough elements to be distributed among all processors. Then, each processor is assigned an equal number of elements in consecutive z-order (Orenstein and Merrett, 1984; Orenstein, 1986). In the refinement step, done by the

`octor_refinetree` method, each processor produces a local sub-mesh through recursive subdivision of its elements until all of them satisfy the size-rule in (2.17), where e is the edge-size of a given octant, V_s is the shear wave velocity associated to the element according to the material model and p is the number of points per wavelength set for the simulation. Next, the `octor_balancetree` method performs the balancing step, which enforces a continuity condition requiring that no two octants sharing a face or an edge differ in size by more than a factor of two. This 2-to-1 constraint is imposed to guarantee the (linear) continuity of the displacement field between the hanging and anchored (independent) nodes. Hanging nodes are those nodes in an element that are at the middle of and edge or face of an adjacent bigger element. Then, `octor_partitiontree` exchanges elements among processors so that each local mesh gets the same number of elements (± 1), while preserving their consecutive z-order in memory. Finally, the `octor_extractmesh` transforms the octree into the final mesh structure with a set of tables for the elements and the nodes (dangling and anchored). Figure 2.3 shows a schematic representation of the meshing process for a coarse mesh of a particular simulation domain. A more detailed explanation of the use of octrees for mesh generation purposes can be found in Tu and O'Hallaron (2004a,b,c) and Tu et al. (2005).

2.2.2 Stiffness Contribution Computation

After applying FE and the principle of virtual work to the linear momentum equation, it can be shown that the system's stiffness matrix in (2.10) may be expressed as in (2.18), where the summation means assembling of all the element's individual stiffness matrices, $\mathbf{K^e}$. $\mathbf{E}$ is the tensor of material stiffness which, for an elastic isotropic material, can be expanded in terms of the Lamé parameters μ and λ; Ω_e is the volume of the element; and ψ' is the matrix of first spatial derivatives of the element's shape functions. The shape functions are expressed in terms of the local coordinates of the element, i.e. $\psi = \psi(\xi_{j=1,2,3})$.

$$\mathbf{K} = \sum_{\mathbf{e}} \left(\int_{\Omega_e} \psi' \mathbf{E} \, (\psi')^T d\Omega_e \right) = \sum_{\mathbf{e}} (\mathbf{K^e}) \tag{2.18}$$

Using (2.18), any product of the type $c\,\mathbf{K^e x_m^e}$ in (2.16), can be written as in (2.19), where c is a scaling factor, and $\mathbf{x_m^e}$ is any given local vector of displacement at step m. This is the *conventional method* to compute the stiffness contributions to the forward solution of displacements. Notice that after replacing (2.10) in (2.16), four $c\,\mathbf{K^e x_m^e}$ products must be computed for each element in the

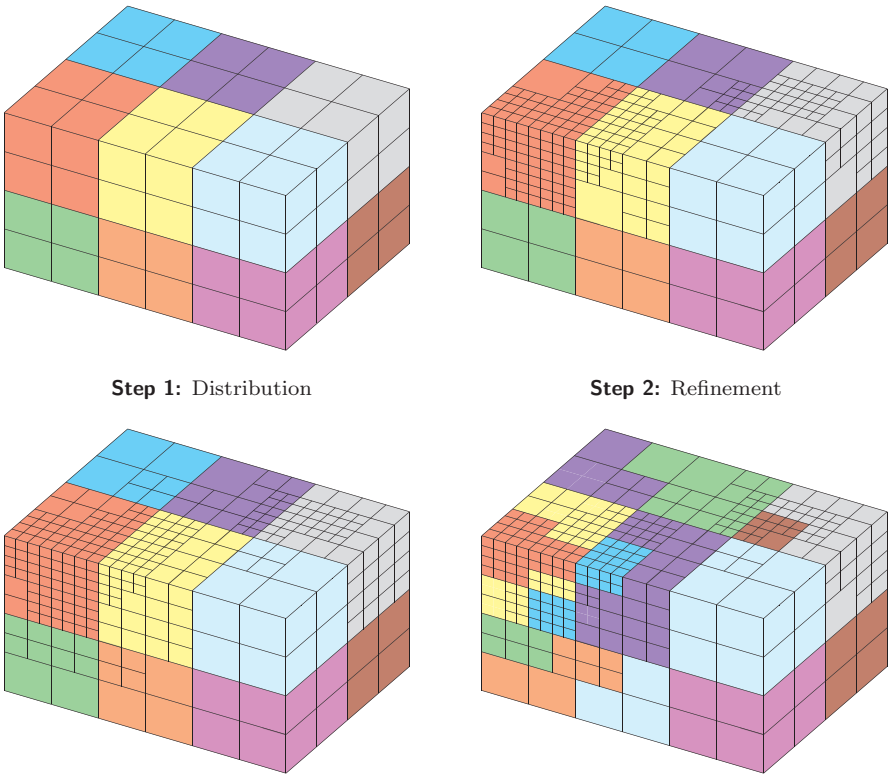

Step 1: Distribution

Step 2: Refinement

Step 3: Balancing

Step 4: Mesh partition

Figure 2.3: Steps followed in the mesh generation process. At each step colors indicate different processors. Note the change in the mesh from the second to the third step, where the continuity 2-to-1 constraint is enforced. Also notice the redistribution of elements at the fourth step to ensure that all processors have the same number of elements. The fifth and final step, extraction (not shown here) consists in writing the element and node tables to the local mesh structure at each processor.

mesh at every time-step. This is by far the most expensive computation per cycle. It may account for up to 95 percent the total solving time in a given simulation.

$$c\,\mathbf{K^e x^e} = c\int_{\Omega_e} \psi' \mathbf{E}\,(\psi')^T\,d\Omega_e\,\mathbf{x^e} \tag{2.19}$$

Hercules implements a change of variables in the element shape functions to compute in a more efficient manner the stiffness contributions to the solution. This *efficient method*, adopted from Balazovjech and Halada (2007) and Moczo et al. (2007), consists of expressing ψ as the product of a vector ϕ and an auxiliary matrix $\mathbf{A}$ as shown in (2.20). $\mathbf{A}$ is a matrix of constants, $\mathbf{a_{ij}} \in \Re$, and ϕ a matrix composed of terms of the form ξ_j^m, where ξ_j are the local coordinate variables of the master element in the shape functions and $m = 0, 1, ..., k$. After substituting (2.20) into (2.19) the latter becomes (2.21).

$$\psi = \mathbf{A}^T \phi \tag{2.20}$$

$$c\,\mathbf{K^e x}^e = c\,\mathbf{A}^T \int_{\Omega_e} \phi' \mathbf{E}\,(\phi')^T\; d\Omega_e\; \mathbf{A x}^e = c\left(\mathbf{A}^T \mathbf{H A}\right)\mathbf{x} \tag{2.21}$$

At first, it may appear that the change of variables introduced in (2.20) results in a larger number of operations in (2.21), because we now need to compute three matrix-vector multiplications instead of one. However, $\mathbf{H}$ is a sparse matrix, i.e., most of the elements in $\mathbf{H} = [\mathbf{h}_{ij}]$ are zero. In addition, all the elements in $\mathbf{A} = [\mathbf{a}_{ij}]$ are either 1 or -1. Thus, the product $\left(\mathbf{A}^T \mathbf{H A}\right)\mathbf{x}$ can be easily written in expanded form, without ever performing a matrix-vector multiplication, following the steps in (2.22). This results in considerably fewer total number of operations and in an overall reduction in total solving time of up to a factor of 3.2X.

$$\begin{array}{lrcll}
1. & \alpha_i & = & \sum \mathbf{a}_{ij}\mathbf{x}_j & \\
2. & \beta_i & = & \sum \mathbf{h}_{ij}\alpha_j & \text{only if} \quad \mathbf{h}_{ij} \neq 0 \\
3. & \gamma_i & = & \sum \mathbf{a}_{ji}\beta_j & \\
4. & c\,(\mathbf{K^e x^e})_i & = & c\,\gamma_i &
\end{array} \tag{2.22}$$

A step by step comparison between the conventional and efficient methods for a longitudinal wave propagation problem modeled with a 1D second-order element is included in the Appendix B.

2.2.3 Performance and Scalability

An important aspect of large-scale simulations using parallel supercomputers is its performance and scalability. It is out of the scope of this thesis to do a thorough review of Hercules' computational performance. Partial analysis of some of the aspects involved in this subject have been addressed elsewhere (e.g. Tu et al., 2006). However, new and larger supercomputers have become available since the numerical experiments reported by Tu et al., making them somewhat outdated. Moreover, Hercules has evolved considerably in the last couple of years—the transition from the conventional to the efficient method just described above, being the most recent and relevant change. It is therefore worth reporting the latest results about scalability and performance.

Figure 2.4 shows strong and weak scaling curves for a set of experiments ran in Kraken at the National Institute or Computational Sciences (NICS). In the set of experiments for evaluating strong scalability, the problem size was fixed for a varying number of processors. In the weak or

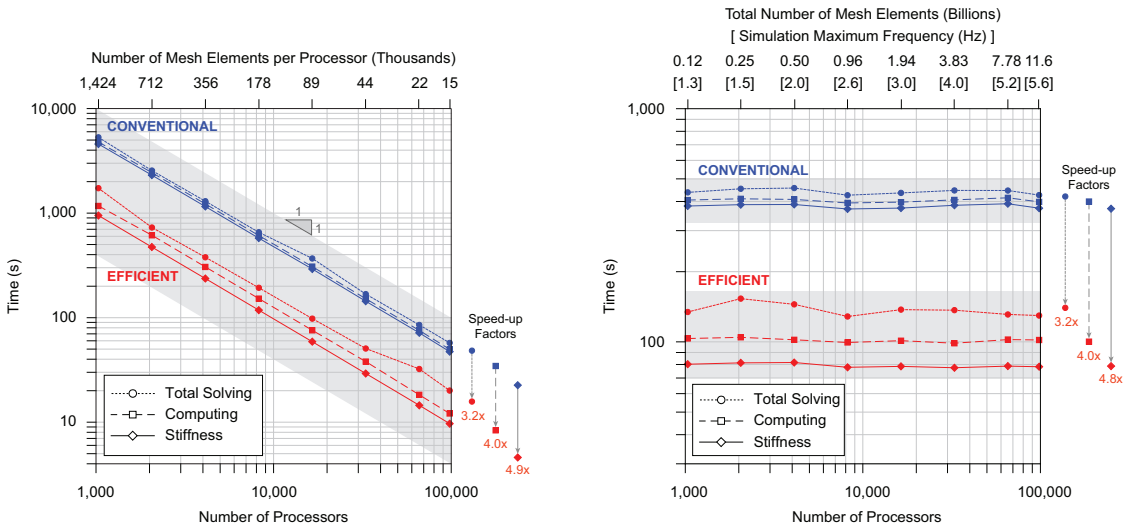

(a) Strong scaling **(b)** Weak scaling

Figure 2.4: Hercules scalability for a set of experiments ran in Kraken at the National Institute or Computational Sciences (NICS) using both the conventional and efficient methods for simulations in a volume domain of 180 km × 135 km × 62 km.

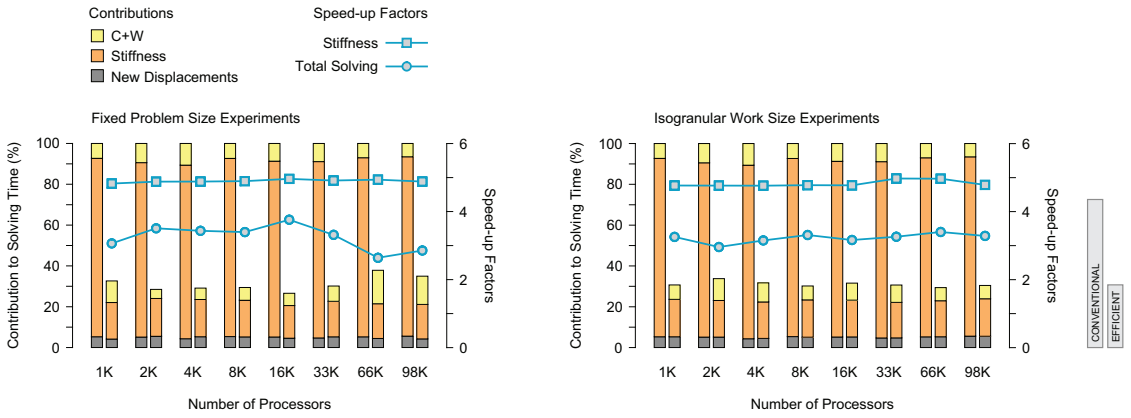

(a) Strong scaling **(b)** Weak scaling

Figure 2.5: Contribution of each module to the total solving time of both methods, using as reference the results for the conventional method. Speed-up factors for the total solving and stiffness computation are superimposed.

isogranular scalability, the amount of work per processor was maintained approximately constant across simulations and the size of the problem or total amount of work grows as the number of processors increases. In both cases we varied the number of processors from 1,032 to 98,040. The physical problem corresponded to a volume domain of 180 km × 135 km × 62 km. In all cases the minimum shear wave velocity was set as $V_{s_{min}} = 500$ m/s. Light gray strips in the figures indicate the expected (perfect) scalability trends. Hercules shows excellent performance in both cases, with only minor oscillations due to communication and waiting time, not shown in the figures.

This particular set of experiments were run with the objective of measuring the benefit of the optimization introduced by the efficient method explained in the previous section with respect to the conventional approach. The figures show two sets of three different lines with solid circles, squares, and diamonds for the total solving time, the time expended solely in computing, and that spent in calculating the contribution of stiffness, respectively, for the conventional (blue) and efficient (red) methods. We found that the use of the efficient methodology improved Hercules performance by an average factor of 4.9X in matrix-vector multiplications and an average factor of 3.2X in the total solving time. This is contrasted with the contribution of the different modules to the total running time in Fig. 2.5. A more detailed description and analysis of Hercules' performance and scalability is presented in Taborda et al. (2010).

2.3 Verification and Validation

One last subject of importance in earthquake simulations is the matter of verification and validation. The concepts of veracity and validity have profound implications for modelers aiming to represent and reproduce physical phenomena and systems, especially in complex open systems like earthquakes. There are different ways to address these and other concepts like confirmation and correctness (e.g. Kleindorfer and Ganeshan, 1993; Oreskes et al., 1994). Here, we adopt the terminology proposed by Schlesinger et al. (1979), where model verification refers to evaluating the correctness of the implementation of a computer model when compared to the theoretical concepts on which it is based, and model validation refers to how well the simulation results compare to actual data from the real system or problem entity being modeled. These concepts have been widely used in software engineering and other computational fields and have been carefully studied elsewhere (e.g. Adrion et al., 1982; Balci, 1994; Sargent, 2005). The next two sections summarize our efforts in this area.

2.3.1 ShakeOut Verification

The Great California ShakeOut scenario was a hypothetical seismic event prepared by the U.S. Geological Survey (USGS) in coordination with the Southern California Earthquake Center (SCEC), the California Geological Survey, and nearly 200 other partners from government, industry, academia, and emergency response agencies with the objective of identifying the physical, social and economic consequences of a major earthquake in southern California (Jones et al., 2008).

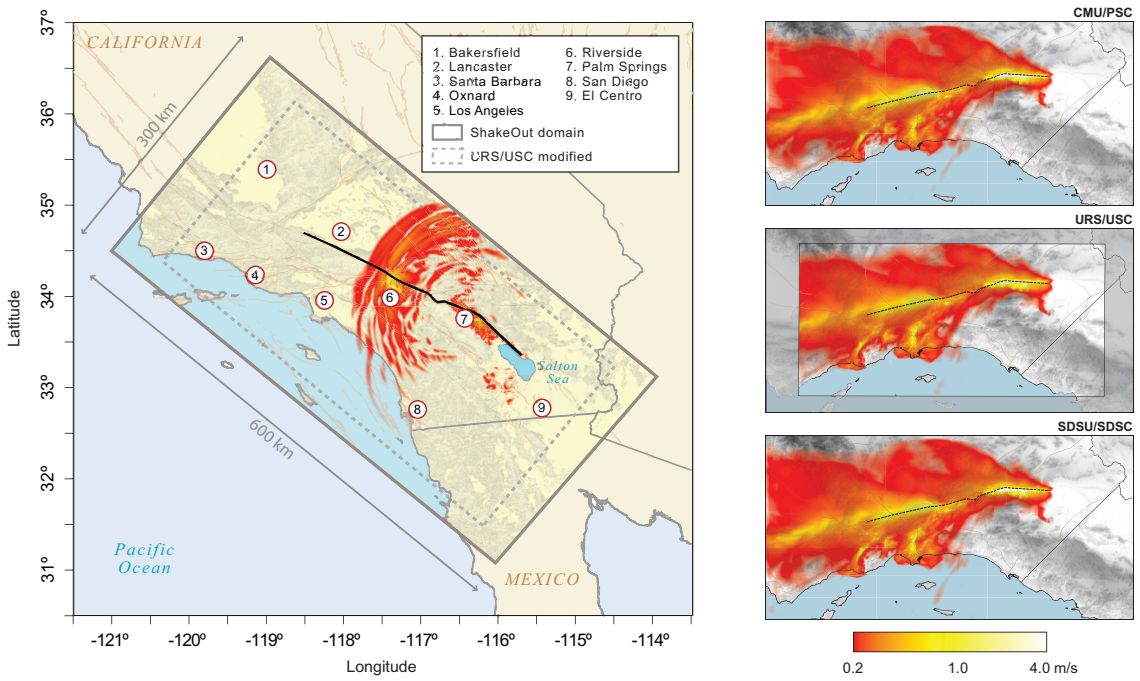

(a) ShakeOut region and simulation domain

(b) Horizontal peak ground velocity

Figure 2.6: The ShakeOut scenario and verification of three simulation sets.

For the scientific component of the ShakeOut, researchers from USGS and SCEC designed an earthquake of magnitude M_{w} 7.8 rupturing North-West along 300 km of the San Andreas fault (Fig. 2.6a). Using a kinematic description of the fault rupture, three research groups conducted simulations of this earthquake scenario in a volume domain of 600 km × 300 km × 80 km including all major populated areas in southern California. CMU's Quake Group was one of them, the other two were from San Diego State University and URS Corporation. Both SDSU and URS simulations were performed using a staggered FD code. All three groups used the same input data, i.e., source description (Jones et al., 2008), material model (Taborda et al., 2007a), and simulation parameters $V_{\mathrm{s}_{\mathrm{min}}} = 200$ m/s and $f_{\mathrm{max}} = 0.5$ Hz. These simulations provided a unique opportunity to conduct *computerized model verification* by means of comparisons between the three models sharing the same basic assumptions.

Figure 2.6b shows the results of the comparison for the cummulative peak ground velocity at the surface for the three simulation sets, and Fig. 2.7 shows the particle velocities at four selected locations in each direction of motion. Considering the size and complexity of the problem, the few minor differences visible from these comparisons are negligible. The more complete verification study that we conducted can be found in Bielak et al. (2010), where qualitative and quantitative

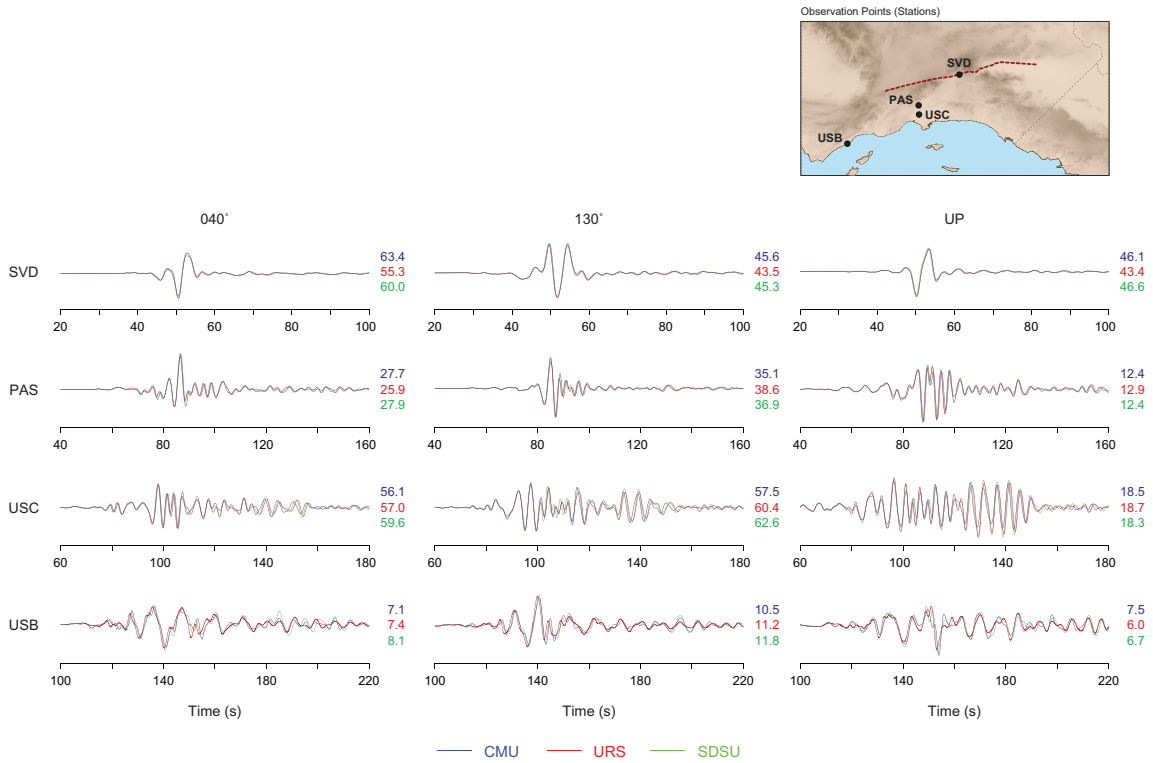

Figure 2.7: Comparison of velocity time histories for the verification of the ShakeOut scenario. Peak values in cm/s are shown on the right-hand side of each signal for the three simulation sets. Total durations were chosen for each station to include only the intense phase of motion.

verification of the three simulation sets were performed using different goodness-of-fit (Anderson, 2004) and misfit (Kristekova et al., 2006) criteria. In light of the intrinsic differences between the methods (FE vs. FD, meshes vs. grids) and their implementations (Hercules vs. AWP FD-codes) with respect to aspects such as source representation, attenuation, and boundary conditions, we found that the results were in very close agreement. Thus the codes, including Hercules, are sufficiently robust and reliable to conduct independent or complementary studies of ground motion modelling in large regions.

Additional results from the ShakeOut project with emphasis in seismic hazard, broadband simulations, and spontaneous rupture propagation can be found in Jones et al. (2008), Graves et al. (2008), and Olsen et al. (2009), respectively.

2.3.2 Chino Hills Validation

The ultimate goal of any simulation process is to be able to reproduce, up to an acceptable level of accuracy, the observations from the real world, i.e., to validate both the conceptual and sim-

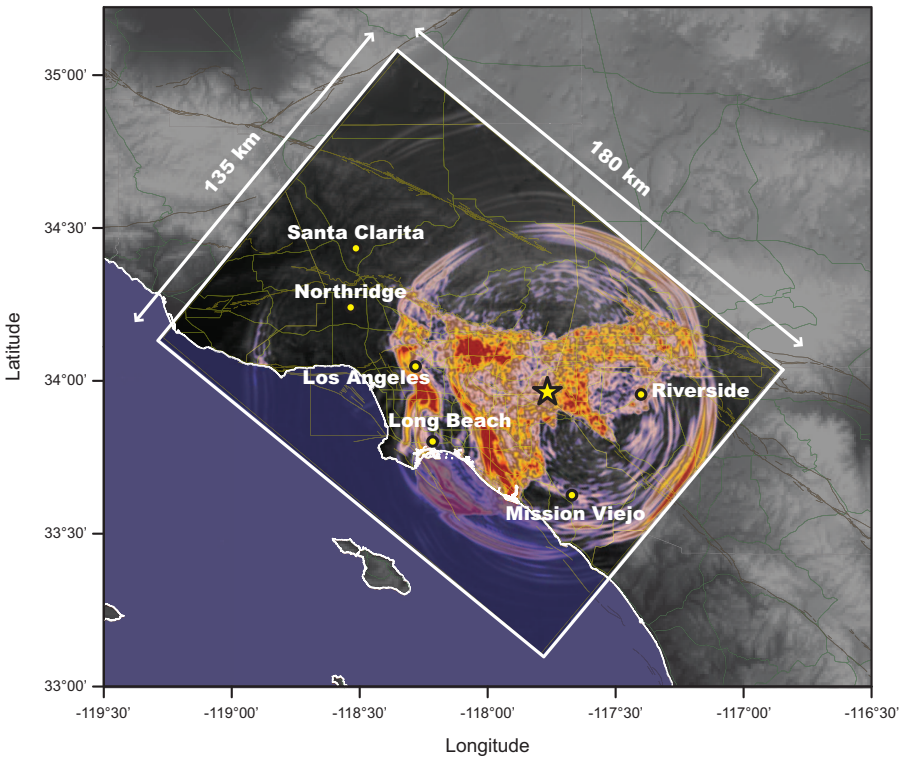

Figure 2.8: Chino Hills region and simulation domain.

ulation models by successfully reproducing experimental data or natural phenomena. There have been plausible attempts to validate both stochastic and deterministic ground motion simulations by comparisons with earthquake data in the literature (e.g. Beresnev and Atkinson, 1998; Hartzell et al., 1999; Graves and Wald, 2004; Komatitsch et al., 2004; Hartzell et al., 2006; Aagaard et al., 2008; Mavroeidis et al., 2008; Kim et al., 2010). However, with the exception of stochastic simulations, where the objective is limited to reproducing peak and amplitude response (on average and regardless of phase), most of the validations done with deterministic simulations have been restricted to very low ($f_{\max} \leq 0.1$ Hz) or low frequencies ($f_{\max} \leq 0.5$ Hz), with only a few exceptions at $f_{\max} = 1$ Hz (Hartzell et al., 1999, 2006). To contribute to this matter, to evaluate the validity of results in simulations using Hercules, and to present evidence in support of deterministic earthquake modeling for frequencies above 1 Hz, we recently conducted a validation study on the 2008 Chino Hills earthquake for a simulation with $f_{\max} = 2$ Hz and $V_{s_{\min}} = 200$ m/s, in a volume domain of 180 km $\times$ 135 km $\times$ 62 km.

The M_w 5.4 Chino Hills earthquake of July 29, 2008 was the strongest earthquake in the greater Los Angeles metropolitan area since Northridge in 1994 (Fig. 2.8). The ground motion originated by the rupture between the Whittier and Chino faults, west of Los Angeles, was recorded by all

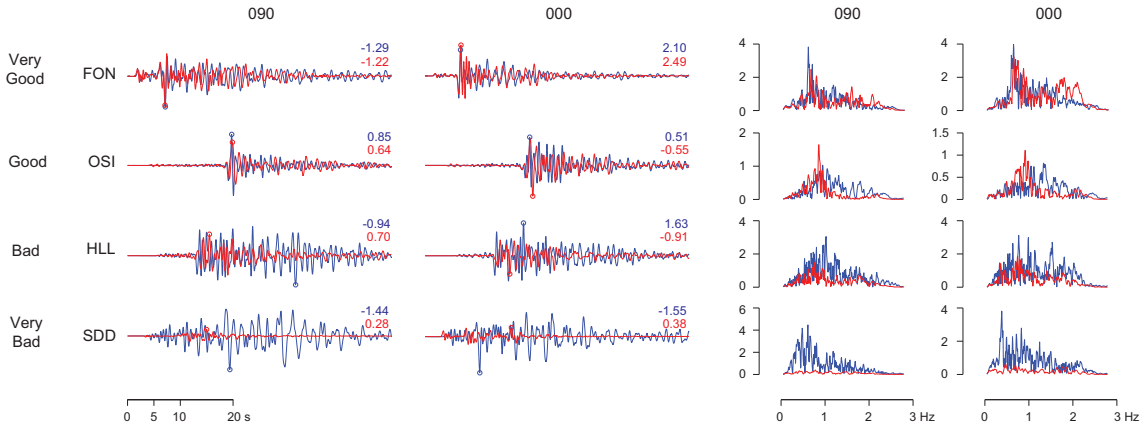

Figure 2.9: Comparison between synthetics (red) and data (blue) for the surface velocity (left) and the corresponding Fourier transform (right) at four stations. Peak velocity values are shown to the right of each trace set. The results are qualified from very good to very bad depending on their similarity.

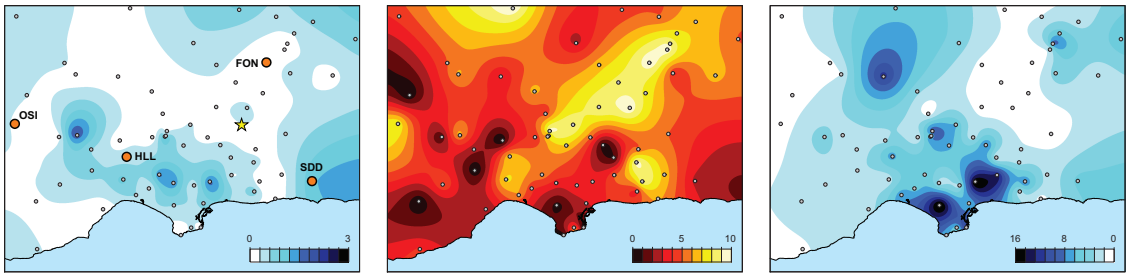

Figure 2.10: Metrics of the comparison between synthetics and data for the 2008 Chino Hills earthquake using 65 stations. **(a)** Absolute difference in seconds for the first arrival of P-waves; **(b)** Goodness-of-fit for the peak ground velocities (parameter C6 in Anderson, 2004); and **(c)** absolute difference in seconds at which the peak velocities occurred. In all three contour maps, lighter colors indicate a better match, white being perfect.

major strong ground motion networks in the metropolitan area. Due to the availability of data and because it could still be considered a relatively minor earthquake, its occurrence constituted an excellent opportunity to validate (linear) earthquake simulations. Figure 2.9 shows the comparison of synthetics with data at four stations scattered throughout the region, near and far from the epicenter (see Fig. 2.10a for reference) for the two horizontal components of motion, in both the time and the frequency domains. We found that at certain stations the fidelity with respect to data was very good, whereas in other places it was the opposite. In total, we compared ground motion histories at 65 stations and performed different quantitative comparisons between records and synthetics. Figure 2.10 shows contour maps built with the results from weighting the comparisons for all stations using three measuring parameters: the absolute difference in the first P-wave arrival in seconds

(Fig. 2.10a); the goodness-of-fit for peak ground velocities (Fig. 2.10b, after Anderson, 2004); and the absolute difference in seconds for the times at which such peaks occurred (Fig. 2.10c).

These comparisons, and others presented in greater detail in Taborda et al. (2009), led us to conclude that, despite the differences observed at some particular locations (SDD in Fig. 2.9), the overall validation balance is positive and, based in the very good results (FON in Fig. 2.9), it seems that while simulation frameworks such as Hercules are attuned for (linear) earthquake ground motion modeling, there is still much work to do in improving material models and source descriptions. At the same time, it is also necessary to move further towards a more complex and complete description of the earthquake phenomena and its impact in urban areas. This thesis addresses that objective in the following chapters through the incorporation of nonlinear soil behavior and the introduction of urban structures in large-scale earthquake ground motion modeling.

3

Nonlinear Ground Motion Modeling

3.1 Theory of Plasticity

3.1.1 Rate-Independent Plasticity

Elastic Limit and Yield Function

Materials typically exhibit an *elastic range* within which their behavior can be characterized by linear conditions. This region is bounded by an *elastic limit*. When the stresses reach the elastic limit, the material is said to *yield*. Beyond this *yielding point*, the material suffers permanent deformations characterized by *plastic strain*, ϵ^p. Figure 3.1a shows the stress-strain relationship under uniaxial loading conditions for a material with elastic limit at point A, which corresponds to the *yielding stress*, σ_{Y}. Some materials are capable of withstanding greater stress beyond the elastic limit. The rise of the stress-strain relationship (from A to B) is known as *strain hardening* or *work hardening*. At B, the material may fail or exhibit a reduction in strength. If the material continues to deform plastically beyond B, it is said to exhibit *strain softening*. After unloading and reloading (Fig. 3.1b), or during reverse or cyclic loading (Fig. 3.1c), the material returns to the elastic range and then reaches back a *subsequent yield stress*, σ_{SY} that defines a new point of transition to inelasticity. The difference between σ_{Y} and σ_{SY} is defined by the *hardening condition*.

The concept of an elastic limit is relatively easy to characterize under conditions of pure stress, i.e., under pure shear or uniaxial tension and compression, as described for the examples in Fig. 3.1. In general, however, the elastic limit or yielding stress is a function of the complete tensor of stresses, σ_{ij}. Therefore, it is necessary to express it in the form of a *yield function* as in (3.1), where k_1, $k_2, \ldots$

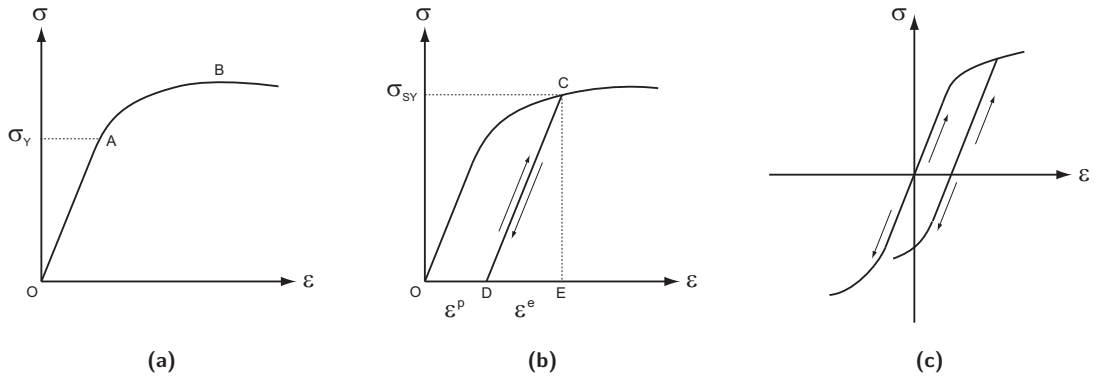

Figure 3.1: Stress-strain uniaxial diagrams for different loading conditions: **(a)** uniaxial monotonic loading; **(b)** loading, unloading and reloading; and **(c)** reverse or cyclic loading.

are material constants that define the elastic limit and hardening conditions of the material. These constants are determined experimentally.

In practice, it is desirable to express the stresses acting on an arbitrary plane defined by a unit vector $\mathbf{n}$ as the combination of two projected stresses, one parallel to $\mathbf{n}$ called the normal stress, σ_n, and a second one perpendicular to $\mathbf{n}$ called the shear stress, τ_n. In material modeling, however, it is convenient to express the stress tensor (σ_{ij}) as composed of two parts: the spherical or hydrostatic tensor, whose elements are $p\delta_{ij}$, where $p = \frac{1}{3}\sigma_{kk}$; and the stress deviator tensor, $s_{ij} = \sigma_{ij} - p\delta_{ij}$. The hydrostatic tensor relates to the normal components of stresses through the first invariant of the stress tensor (I_1) as $\sigma_n = \frac{1}{3}I_1$, where $I_1 = \sigma_{kk}$; and the deviatoric stress relates to the shear stress through its second invariant (J_2) as $\tau_n^2 = \frac{1}{3}J_2$, where $J_2 = \frac{1}{2}s_{ij}s_{ji}$. Therefore, it has been found advantageous to express σ_{ij} in (3.1) in terms of the first invariant of the Cauchy stress, I_1, and the second and third invariants of its deviator, J_2 and J_3, as shown in (3.2).

$$f\left(\sigma_{ij},\, k_1,\, k_2, \ldots\right) = 0 \tag{3.1}$$

$$f\left(I_1,\, J_2,\, J_3,\, k_1,\, k_2, \ldots\right) = 0 \tag{3.2}$$

A common configuration of the yield function is shown in (3.3), where $F(\sigma_{ij})$ describes the current state of stresses and $k(\sigma_{ij}, k_n)$ defines the corresponding yield condition based on the history of the stress-strain relationship and the material constants. This implies that at the points at which the combination of stresses reach the elastic limit described by $k(\sigma_{ij}, k_n)$, there exists a yield surface defined by (3.4). Notice that $k(\sigma_{ij}, k_n)$ not only defines the elastic-limit condition and thus the

position of the yield surface, but it also describes the hardening rule that the material follows after yielding. For the special case of elastic-perfectly plastic models, $k(\sigma_{ij}, k_n) = k$ constant.

$$f\left(\sigma_{ij},\, k\right) = F\left(\sigma_{ij}\right) - k\left(\sigma_{ij},\, k_n\right) = 0 \tag{3.3}$$

$$F\left(\sigma_{ij}\right) = k\left(\sigma_{ij}, k_n\right) \tag{3.4}$$

Incremental Stress-Strain Relationships

It can be seen from Fig. 3.1b that the plastic strain $\overline{OD} = \epsilon^p$ is unlimited under plastic deformation or *plastic flow*. Therefore, it becomes necessary to formulate the total strain $\overline{OE} = \epsilon_{ij}$ in terms of infinitesimal changes or increments, $\dot{\epsilon}_{ij}$. Assuming that at any point in time the total strain can be expressed as the sum of its elastic and plastic contributions, that is $\overline{OE} = \overline{DE} + \overline{OD}$, then its increment may also be written as the sum of these parts as seen in (3.5). Furthermore, from Hooke's law of elasticity we know that the elastic strain tensor ϵ^e relates to the stress tensor σ_{ij} according to (3.6), where D_{ijkl} is the compliance tensor, or the inverse of the material elastic constant tensor C_{klmn}. From (3.5) and (3.6) follows that the total strain may be expressed as in (3.7).

$$\dot{\epsilon}_{ij} = \dot{\epsilon}^e_{ij} + \dot{\epsilon}^p_{ij} \tag{3.5}$$

$$\dot{\epsilon}^e_{ij} = D_{ijkl}\dot{\sigma}_{kl} \tag{3.6}$$

$$\dot{\epsilon}_{ij} = D_{ijkl}\dot{\sigma}_{kl} + \dot{\epsilon}^p_{ij} \tag{3.7}$$

Flow Rule, Plastic Potential, and Plastic Multiplier

The existence of a yield function implies that the position of a stress point in plastic deformation or plastic flow is governed by a *flow rule* that provides the information necessary to determine the plastic increment or inelastic change of strains, $\dot{\epsilon}^p_{ij}$ while the material remains in plastic flow. The concept of a flow rule was introduced by von Mises in 1928 and can be written as in (3.8). $\dot{\lambda}$ is a positive scalar factor of proportionality for the plastic strain rate commonly known as the *plastic multiplier*. $g(\sigma_{ij})$ is a scalar function that defines a *plastic potential*.

$$\dot{\epsilon}^p_{ij} = \dot{\lambda}\frac{\partial g}{\partial \sigma_{ij}} \tag{3.8}$$

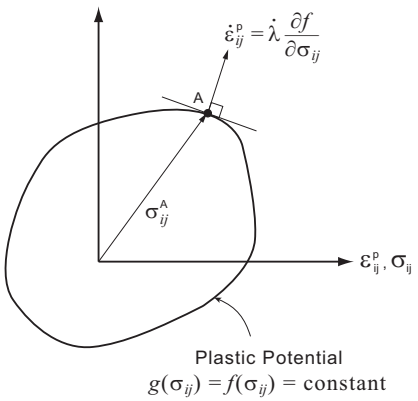

Figure 3.2: Geometric representation of plastic potential and associated flow rule.

$$\dot{\epsilon}^{p}_{ij} = \dot{\lambda}\frac{\partial f}{\partial \sigma_{ij}} \tag{3.9}$$

A special case of flow theory is when the plastic potential coincides with the yield function, i.e., $g(\sigma_{ij}) = f(\sigma_{ij})$. In this case we call the flow rule to be an *associated flow rule*, as in (3.9). The relationship between the plastic strain increment and the plastic potential given by the (associated) flow rule can be illustrated geometrically as in Fig. 3.2. Since plastic flow only occurs when a stress point remains on the yield surface, i.e., when $f(\sigma_{ij}, k) = 0$, then the change in plastic strain is different from zero ($\dot{\epsilon}^{p}_{ij} \neq 0$) only if there is plastic deformation. Therfore, $\dot{\lambda}$ must obey the conditions in (3.10).

$$\dot{\lambda} \quad \begin{cases} = 0 & \text{wherever} \quad f(\sigma_{ij}, k) < 0 \\ \geq 0 & \text{wherever} \quad f(\sigma_{ij}, k) = 0 \end{cases} \tag{3.10}$$

3.1.2 Rate-Dependent Plasticity

Problems related to the temporal growth of plastic deformations or *strain rate* are modeled under the formulations for viscoplasticity. In general, elastic-visco-plastic models are considered to be the most complete (and complex) representation of solid materials because they are dependent on the plastic strain rate and on the plastic strain itself. Materials that adjust to these conditions are called *rate-dependent*. Rate-dependency is particularly important for reproducing the effects of viscosity, especially in metals, and for materials that exhibit a tendency to suffer permanent deformations under the influence of (persistent) stresses, or *creep*. For most geomaterials, with the exception of rocks under high pressure, the effect of viscosity is neglected. Therefore, soils in geotechnical engineering are usually treated as elasto-plastic rate-independent materials. This is a widely accepted

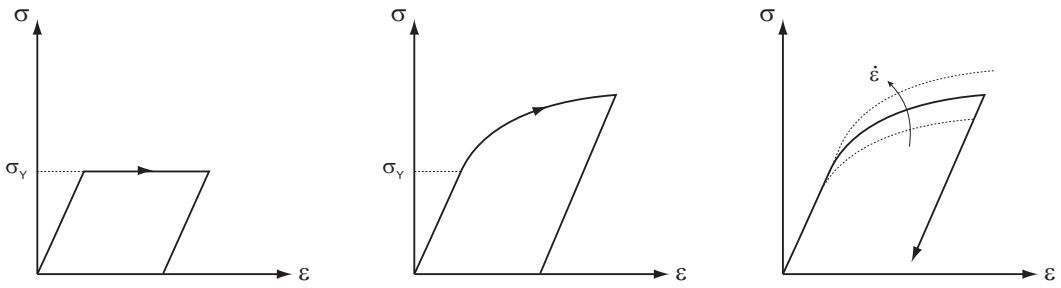

(a) Elastic prefectly-plastic **(b)** Elastoplastic **(c)** Elastic visco-plastic

Figure 3.3: Comparison between three basic material models in (rate-independent) plasticity and (rate-dependent) viscoplasticity.

simplification. Figure 3.3 shows a comparison between the basic elastic perfectly-plastic, elastoplastic, and viscoplastic material models, and a schematic representation of the influence of the strain rate on the behavior of materials.

Provided that the selection of a constitutive model with a particular yield function and flow rule has been made, from expressions (3.3—3.10) it follows that deriving the contribution of plastic deformation to the state of stresses depends on determining the value of the plastic multiplier $\dot{\lambda}$, at any point in time. This is important because the decision of whether to model a material as rate-dependent or rate-independent is central to how one obtains $\dot{\lambda}$, and therefore ϵ_{ij}^{p}.

In rate-independent theory of plasticity, the plastic strain is obtained by solving a succession of elasticity problems for which a formulation or path (in some of the simplest cases, an exact one) is provided. That is, in a rate-independent formulation, the change in the plastic strain is independent of time, and as a consequence, the (plastic) strain at a given time step n, or point of 'departure' (A in Fig. 3.4), is not sufficient to infer the plastic strain (increment) for the next time step $n+1$, or point of 'arrival' (B in Fig. 3.4). Then, the formulation uses the plastic multiplier to approximate the state of stresses at B. This makes it necessary to use an iterative procedure to ensure that the stresses at the point of arrival satisfy the yield function and hardening rule, and thus consistently solve the elastic-plastic boundary value problem (taking into account the history of deformation). There are many alternatives to addressing this iterative process, consisting of different integration algorithms. Figure 3.4 shows a generic representation of the iterations, where points A and B are the departure and arrival states of stresses, respectively.

On the other hand, in rate-dependent viscoplasticity, since the change in the plastic strain is dependent of time, one can directly 'predict' the plastic strain increment, and thus obtain the plastic strain at the next time step, based on the current plastic strain ($\epsilon_{n+1}^{p} = \epsilon_{n}^{p} + \Delta t \dot{\epsilon}^{p}$); and the resultant

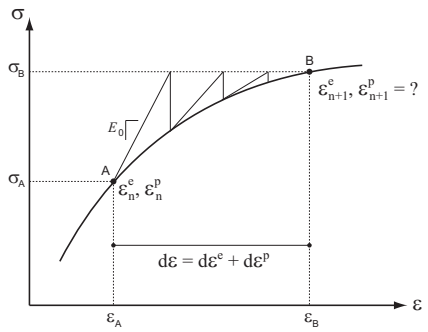

Figure 3.4: Example of a Newton-like iteration process as commonly used in rate-independent plasticity.

state of stresses will be consistent with the constitutive model of the material. In this case, $\dot{\lambda}$ in (3.8) can be defined as in (3.11), after Perzyna (1963, 1966), from where it follows that (3.8) becomes (3.12). Here, $\dot{\lambda_0}$ is the material's strain rate and m is the strain-rate sensitivity factor. The $\langle \cdot \rangle$ operator is such that $\langle \Theta \rangle \neq 0$ only if $\Theta > 0$. A great advantage from using rate-dependent plasticity is the fact that as $m \to 0$, the closer is the solution to that of the rate-independent formulation. In fact, it can be shown that the rate-independent formulation is a special case of the rate-dependent theory (Perzyna, 1966).

$$\dot{\lambda} = \dot{\lambda_0} \left\langle \frac{F(\sigma_{ij})}{k(\sigma_{ij}, k_n)} \right\rangle^{\frac{1}{m}} \tag{3.11}$$

$$\dot{\epsilon}^p_{ij} = \dot{\lambda_0} \left\langle \frac{F(\sigma_{ij})}{k(\sigma_{ij}, k_n)} \right\rangle^{\frac{1}{m}} \frac{\partial g}{\partial \sigma_{ij}} \tag{3.12}$$

This concept has been successfully adapted and implemented for finite-element approaches (e.g. Zienkiewicz and Cormeau, 1974). However, to our knowledge, for reasons that are unclear in the literature, its use in geotechnical engineering has been somewhat limited, with only a few applications in soil mechanics (e.g. Adachi and Oka, 1982; Katona, 1984). A probable reason is that there is little experimental data about the strain rate of soils. Nonetheless, as stated above, if m is small enough, this lack of knowledge is irrelevant as the solution, in the limit, will approach that of rate-independent plasticity; as it has been shown analytically by Perzyna (1966). This result is intuitively apparent from the comparison in Fig. 3.3.

Here we will adopt a rate-dependent formulation. A more detailed discussion of other relevant concepts such as the difference between constant, isotropic, and kinematic hardening, the Bauschinger effect, and other aspects of cyclic loading that are out of the scope of this thesis may be found in Lemaitre and Chaboche (1990) and Lubliner (1990).

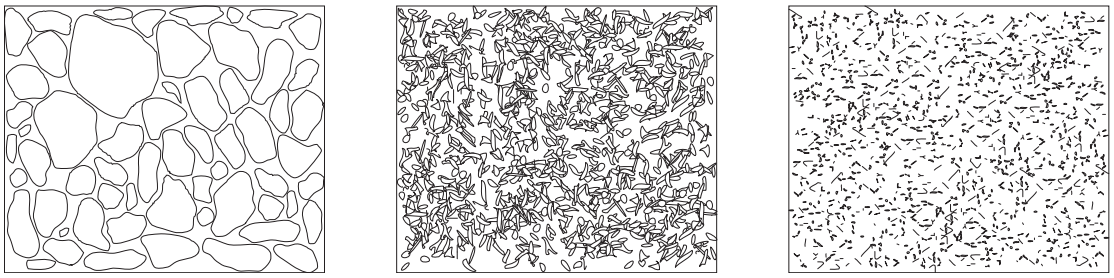

(a) Sand **(b)** Silt **(c)** Clay

Figure 3.5: Typical soil types.

3.2 Material Models

3.2.1 Soils

Soil materials are composed of particles with different sizes and shapes in contact with each other. The interstices between these particles or pores are filled with water and air, or other fluids and gasses (Fig. 3.5). When a soil is considered to be dry, that is, in drained conditions, the soil is generally considered as a material whose condition can be described by its state of stresses and strains. A single phase continuum description is also acceptable when there is no flow in saturated soils, i.e., no drainage is allowed, or when the drainage conditions are such that the steady-state pore-fluid pressures depend only on the hydraulic conditions or are independent of the soil skeleton response to external loads, i.e., when free drainage conditions prevail. However, other cases of saturated soils, and certainly in the case of partially saturated soils, a two-phase or a multiphase formulation describing the *effective stresses* transmitted between the particles and the *pore fluid pressures* carried in the fluid phase is required. Although there is still some level of uncertainty on how to deal with partially saturated soils, there are two-phase continuum formulations available in the literature for incorporating the effects of pore-pressure for elastic and nonlinear inelastic porous media (e.g. Biot, 1956a,b, 1962; Prevost, 1977, 1980). Two- and multi-phase materials are important in earthquake engineering for modeling liquefaction in soils. Soils in undrained conditions are out of the scope of this thesis and shall be a subject of study in future work.

At the microscopic level, the complex behavior of soils is dominated by the interaction between its constituent particles. Sands, for example, aggregate particles of different sizes and forms that transmit tangential and normal forces to one another other at their contact points. Under external loading, considering the particles to be incompressible, any local loss of equilibrium results in a

rearrangement of the granular assembly, conforming a new microstructure. Same occurs with clays, which consist of plate-shaped particles of minerals with gravity and electrostatic forces at their points of contact. These complex changes in the microstructure of the soil skeleton cause the overall material to exhibit permanent deformations, anisotropy, or local instabilities. To follow particle behavior at the microscopic level is impractical; therefore, it has been a common practice to idealize soils at the macroscopic level as continua. At this level, concepts such as elasticity, viscosity, hardening, softening, brittleness and ductility apply all the same as they do for metals, alloys, and other composites like concrete. This allows one to use concepts from continuum mechanics to analyze and model soil behavior.

Although there is no clear understanding on how to characterize three-dimensional stress-strain relations in soils, numerous constitutive models have been developed for a wide variety of soil properties and loading conditions. A historical account and discussion of constitutive theories can be found in Scott (1985). According to the comprehensive review of constitutive relations for soil materials by Prevost and Popescu (1996), a material model idealization should posses three necessary properties: (1) the model has to be complete, i.e., to be able to characterize all possible stress and strain paths; (2) its parameters have to be identifiable through a small number of standard or simple material tests; and (3) it must be founded in a coherent physical interpretation of the conditions the material is under and its expected response. From the first condition, the model should be capable of providing the state of a point in the stress space, and its corresponding strains, at any point in time. The second condition is desirable, yet not strictly necessary, and the third condition states that if, for example, permanent deformations are to be expected, then the model must account properly for them.

It would be desirable to have elaborate models that account for realistic soil behavior and comply with the conditions just stated. In this regard, the promising and accepted ones are those that adjust to elasto-visco-plastic constitutive models of solid mechanics. However, in light of the complexity involved in large-scale earthquake ground motion modeling, we have opted for two of the simplest available models for perfectly elastoplastic materials, the von Mises and Drucker-Prager models. Despite their simplicity, their formulations still comply with the three necessary properties posed by Prevost and Popescu (1996). They completely define the state of stresses and can reproduce permanent deformations. In particular, they are easy to relate with soil properties known from laboratory tests, i.e., cohesion and friction angle. In addition, since we have opted for a rate-dependent formulation, adjustment of the strain-rate and rate-sensitivity parameters allows us to

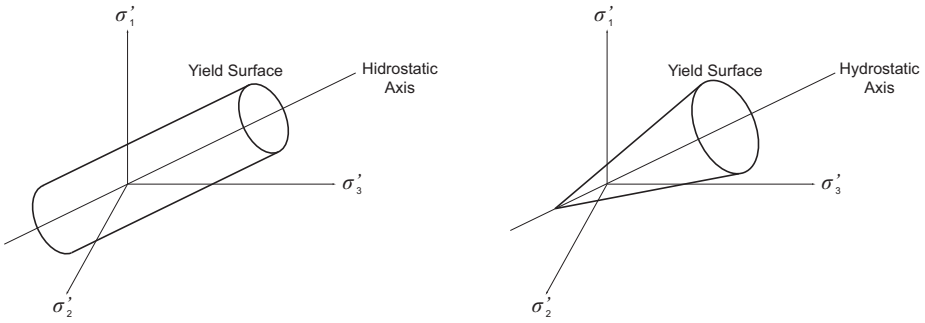

(a) von Mises **(b)** Drucker-Prager

Figure 3.6: Yield surfaces in the principal stresses space for the two material constitutive models considered.

"smooth" the transitions from and into the elastic and plastic ranges, which provides some sense of non-constant hardening (and softening) behavior, as seen in the preceding section (Fig. 3.3c).

3.2.2 von Mises

Formulated in 1913, the von Mises yield criterion is a smooth version of the Tresca yield function that accounts for the influence of intermediate stresses by relating the maximum strength at the point of yield with the octahedral shearing stress, τ_{oct}. It states that the plastic flow occurs when τ_{oct} reaches a certain value k', or elastic limit. Since τ_{oct} is proportional to the second invariant of the deviator tensor, the von Mises yield criterion corresponding to (3.3) is written only in terms of J_2 as done in (3.15). Notice that the von Mises yield criterion is independent of hydrostatic pressure, i.e., it is not a function of I_1. A representation of the yield surface in the principal stresses space can be seen in Fig. 3.6a.

$$\tau_{\text{oct}} = k' \tag{3.13}$$

$$\tau_{\text{oct}} = \sqrt{\frac{2}{3}J_2} \qquad k' = \sqrt{\frac{2}{3}}k \tag{3.14}$$

$$f\left(J_2\right) = J_2 - k^2 = 0 \tag{3.15}$$

3.2.3 Drucker-Prager

The Drucker-Prager yield criterion was introduced in 1952 as an extension of the von Mises model to account for hydrostatic pressure. At the same time, it may be seen as a smooth version of the Mohr-Coulomb failure criterion which is a generalization of the Tresca pressure independent model.

This model incorporates the influence of the normal or hydrostatic stresses into the yield criterion by including an additional term as seen in (3.16), where α and k are material constants related to the cohesion, c, and the internal friction-angle, ϕ, according to (3.17). In the principal stresses space, the Drucker-Prager yield surface represents a cone that circumscribes the hexagonal pyramid of the Mohr-Coulomb yield surface.

$$f\left(I_1, J_2\right) = \alpha I_1 + \sqrt{J_2} - k = 0 \tag{3.16}$$

$$\alpha = \frac{2\sin\phi}{\sqrt{3}\left(3 - \sin\phi\right)} \qquad k = \frac{6c\cos\phi}{\sqrt{3}\left(3 - \sin\phi\right)} \tag{3.17}$$

Notice that when the material is frictionless, i.e., $\phi = 0$, the constant α vanishes and the yield function becomes that of the von Mises criterion. The shape of the Drucker-Prager yield surface is shown in Fig. 3.6b.

3.3 Wave Propagation in Inelastic Media

3.3.1 Inelastic Governing Equations

In order to reproduce inelastic behavior in wave propagation problems, the governing equations discussed in Section 2.1.1 need to be modified accordingly. We start by applying the Galerkin method to (2.1) and obtain the weak form of the linear momentum equation (3.18).

$$\int_\Omega \rho v_i \frac{\partial^2 u_i}{\partial t^2} d\Omega + \int_\Omega \frac{\partial v_i}{\partial x_j}\sigma_{ij} d\Omega = \int_\Omega \partial v_i f_i d\Omega + \int_\Gamma \partial v_i \sigma_{ij} n_j d\Gamma \tag{3.18}$$

Using Hooke's law of elasticity (3.19), and assuming that the total components of the strain tensor can be expressed as the corresponding sum of its elastic and inelastic parts as done for the incremental relationships in Section 3.1.1, and shown here in (3.20); we rewrite these two relations as seen in (3.21) and (3.22), thus obtaining the Cauchy stress tensor, σ_{ij} in terms of the three dimensional elastic constitutive matrix, C_{ijmn}, and the difference between the tensor of total strains, ϵ_{ij}, and its component of plastic deformation, ϵ^p_{ij}.

$$\sigma_{ij} = C_{ijmn}\epsilon^e_{mn} \tag{3.19}$$

$$\epsilon_{ij} = \epsilon^e_{ij} + \epsilon^p_{ij} \tag{3.20}$$

$$\epsilon^e_{ij} = \epsilon_{ij} - \epsilon^p_{ij} \tag{3.21}$$

$$\sigma_{ij} = C_{ijmn}\left(\epsilon_{mn} - \epsilon^p_{mn}\right) \tag{3.22}$$

$$\int_\Omega \rho v_i \frac{\partial^2 u_i}{\partial t^2} d\Omega + \int_\Omega \frac{\partial v_i}{\partial x_j} C_{ijmn}\left(\epsilon_{mn} - \epsilon^p_{mn}\right) d\Omega = \int_\Omega \partial v_i f_i d\Omega \tag{3.23}$$

Substituting (3.22) into (3.18) and dropping the last term in (3.18), which is associated to the boundary conditions, one obtains (3.23). This is the modified weak form of the linear momentum equation for wave propagation in inelastic media. Using strain-displacement relationships, it can be shown that when the plastic strain vanishes ($\epsilon^p_{ij} = 0$), (3.23) is equivalent to (2.5).

3.3.2 Numerical Discretization

Introducing finite elements for spatial discretization of the trial functions v_i and displacements u_i in (3.23), as defined in (3.24), it can be shown that (3.23) becomes (3.25).

$$v^m = \sum_{m=1}^{M} \phi^m v^m_i \qquad u^n = \sum_{n=1}^{N} \phi^n u^n_i \tag{3.24}$$

$$\mathbf{M\ddot{u}} + \sum_e \int_{\Omega_e} \nabla\psi_j C_{ijmn}\left(\epsilon_{mn} - \epsilon^p_{mn}\right) d\Omega_e = \mathbf{f} \tag{3.25}$$

The expansion of $\sigma_{ij} = C_{ijmn}\left(\epsilon_{mn} - \epsilon^p_{mn}\right)$ in (3.23) and (3.25) is exhibited only to illustrate the point at which the plastic strain is involved in the discrete form of the linear momentum equation. For computing purposes we preserve the second integral in (3.25) in terms of stresses as in (3.26), which results from substituting (3.22) back into (3.25). (3.26) can be further synthetized by writing it as in (3.27). The integral in (3.27) represents an internal resistance force, and $\mathbf{B}$ is the strain matrix (see Section 3.4.2).

$$\mathbf{M\ddot{u}} + \sum_e \int_{\Omega_e} \nabla\psi_j\left(\sigma_{ij}\right) d\Omega_e = \mathbf{f} \tag{3.26}$$

$$\mathbf{M\ddot{u}} + \sum_e \int_{\Omega_e} \mathbf{B}^{\mathrm{T}} \sigma_{ij} d\Omega_e = \mathbf{f} \tag{3.27}$$

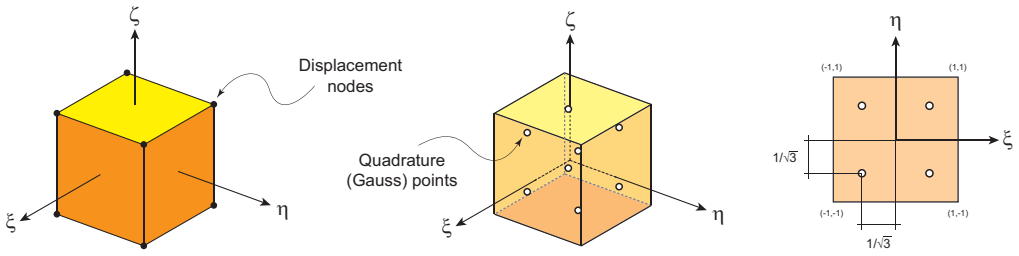

Figure 3.7: Location of the quadrature points used for the hexahedron elements in Hercules.

Proceeding with (3.27) as we did in Section 2.1.2 for (2.8), i.e., including intrinsic attenuation, decoupling the system with respect to the mass matrix, and applying central differences to replace time derivatives, results in (3.28). This is the modified solving kernel for the next-step displacements of inelastic wave propagation problems as implemented in Hercules.

$$\begin{aligned} u^i_{n+1} \quad = \quad & \frac{\Delta t^2}{m^i} f^i_n + \left(2u^i_n - u^i_{n-1}\right) - \alpha\Delta t\left(u^i_n - u^i_{n-1}\right) \\ & -\frac{\Delta t}{m^i}\beta\left(\sum_{\mathbf{e}} \mathbf{K^e}\left(\mathbf{u^e_n} - \mathbf{u^e_{n-1}}\right)\right)_i - \frac{\Delta t^2}{m^i}\left(\sum_e \int_{\Omega_e} \left(\mathbf{B}^{\mathrm{T}}\sigma_{ij}\right)_n d\Omega_e\right)_i \end{aligned} \tag{3.28}$$

3.4 Implementation and Other Considerations

3.4.1 Quadrature Points

The stresses (σ_{ij}) and strains (in the strain matrix $\mathbf{B}$) present in the integral in the last term in (3.28) imply that derivatives of the shape functions and a subsequent integration must be done at the element level in order to compute the internal resistance force due to the stiffness contribution (modified for inelasticity). In most finite element calculations, the numerical evaluation of this integral is done using a Gaussian quadrature rule of the form shown in (3.29) for a master element (in 3D) with local coordinates (ξ, η, ζ) varying from -1 to 1. W_n is the product of the weights from the one-dimensional rule. For the regular master hexahedron element used in Hercules, we employ an eight-point quadrature rule ($N = 2$) with Gauss points located at $1/\sqrt{3}$ from the center as shown in Fig. 3.7. The contribution weight of each quadrature point is $W_n = 1/8$, with $n = 1, \ldots, 8$.

$$\int_{\Omega_e} G(\xi, \eta, \zeta) d\xi d\eta d\zeta = \sum_{n=1}^{N^3} W_n G(\xi, \eta, \zeta) \tag{3.29}$$

3.4.2 Internal Resistance Force

The internal resistance force corresponding to the integral in the parenthesis of the last term in (3.28) for each displacement node i may be expressed as a vector of forces $\mathbf{p}_i$ with components in the three directions (x, y, z). These forces are the result of adding the contribution of each quadrature point in a given element (associated with the node of interest) as expressed in (3.30), where σ is the stress tensor obtained at each of the eight j Gauss points.

The product $\mathbf{B}^{\mathrm{T}}\sigma$ in (3.30) is given in expanded form in (3.31). In turn, the stresses are obtained from applying Hooke's law of elasticity as shown in (3.22), now in expanded form in (3.32); and the total strains ϵ are computed for each quadrature point by adding the contribution of displacement from each node, as shown in (3.33). The current plastic strains ϵ^p should have been updated using the power law (3.12) for plastic increment as seen in Section 3.1.2. Note that, since the stress (σ_{ij}) and strain (ϵ_{ij}) tensors are symmetric, we have opted for writing (3.31–3.33) in vector form (with only six elements as opposed to nine).

$$\mathbf{p}_i = [\ p_{xi} \quad p_{yi} \quad p_{zi}\ ] = \sum_{j=1}^{8} \left(W_j \left(\mathbf{B}^{\mathrm{T}} \sigma \right)_j \right) \tag{3.30}$$

$$\mathbf{B}^{\mathrm{T}}\sigma = \begin{bmatrix} \frac{\partial \psi_i}{\partial x} & 0 & 0 & \frac{\partial \psi_i}{\partial y} & 0 & \frac{\partial \psi_i}{\partial z} \\ 0 & \frac{\partial \psi_i}{\partial y} & 0 & \frac{\partial \psi_i}{\partial x} & \frac{\partial \psi_i}{\partial z} & 0 \\ 0 & 0 & \frac{\partial \psi_i}{\partial z} & 0 & \frac{\partial \psi_i}{\partial y} & \frac{\partial \psi_i}{\partial x} \end{bmatrix} \begin{bmatrix} \sigma_x \\ \sigma_y \\ \sigma_z \\ \sigma_{xy} \\ \sigma_{yz} \\ \sigma_{xz} \end{bmatrix} \tag{3.31}$$

$$\begin{bmatrix} \sigma_x \\ \sigma_y \\ \sigma_z \\ \sigma_{xy} \\ \sigma_{yz} \\ \sigma_{xz} \end{bmatrix} = \begin{bmatrix} \lambda + 2\mu & \mu & \mu & 0 & 0 & 0 \\ \mu & \lambda + 2\mu & \mu & 0 & 0 & 0 \\ \mu & \mu & \lambda + 2\mu & 0 & 0 & 0 \\ 0 & 0 & 0 & 2\mu & 0 & 0 \\ 0 & 0 & 0 & 0 & 2\mu & 0 \\ 0 & 0 & 0 & 0 & 0 & 2\mu \end{bmatrix} \begin{bmatrix} \epsilon_x - \epsilon_x^p \\ \epsilon_y - \epsilon_y^p \\ \epsilon_z - \epsilon_z^p \\ \epsilon_{xy} - \epsilon_{xy}^p \\ \epsilon_{yz} - \epsilon_{yz}^p \\ \epsilon_{xz} - \epsilon_{xz}^p \end{bmatrix} \tag{3.32}$$

$$\begin{bmatrix} \epsilon_x \\ \epsilon_y \\ \epsilon_z \\ \epsilon_{xy} \\ \epsilon_{yz} \\ \epsilon_{xz} \end{bmatrix} = \sum_{i=1}^{8} \left(\begin{bmatrix} \frac{\partial \psi_i}{\partial x} & 0 & 0 \\ 0 & \frac{\partial \psi_i}{\partial y} & 0 \\ 0 & 0 & \frac{\partial \psi_i}{\partial z} \\ \frac{\partial \psi_i}{\partial y} & & \\ \frac{\partial \psi_i}{\partial x} & 0 & \\ & 0 \frac{\partial \psi_i}{\partial z} & \frac{\partial \psi_i}{\partial y} \\ \frac{\partial \psi_i}{\partial z} & 0 & \frac{\partial \psi_i}{\partial x} \end{bmatrix} \begin{bmatrix} u_{xi} \\ u_{yi} \\ u_{zi} \end{bmatrix} \right) \tag{3.33}$$

3.4.3 Solution Algorithm

The formulation described for incorporating nonlinear material behavior in wave propagation is introduced in the solving algorithm of Hercules by adding two loops over the elements that are allowed to deform nonlinearly through the replacement of the (linear) stiffness contribution (described in Section 2.2.2). The pseudocode of these two new modules of computation are described in Fig. 3.8.

3.4.4 Geostatic Loading

An important consideration when modeling nonlinear materials with constitutive laws for pressure dependent materials (e.g., Drucker-Prager) is that the initial conditions of stresses and strains need to be known. In ground motion modeling, in the absence of external loading, the initial state of deformation (and stress) is dominated by the natural consolidation of soils due to gravitational loads. However, gravitational forces cannot be directly applied because the system would become unstable due to the absence of balancing (confinement) forces at the boundaries of the computational domain. This is due to the fact that the absorbing boundary conditions that have been implemented in Hercules to avoid unnatural reflections due to the finiteness nature of simulation domains consist of simple viscous dampers. Additionally, solving the static problem is unpractical. Therefore, a staged procedure is necessary in order to allow the material to gain some initial strength and preserve the functionality of the absorbing boundaries. This procedure consists of the following steps.

1. The start of the simulation is delayed in a certain amount of time T_{g_0} by resetting the start time to $t_0 = -T_{g_0}$. The new number of time steps is $M = N + N_g$, where $N = T/\Delta t$ was the initially required number of steps for the simulation time T and step-size Δt, and $N_g = \Delta t / T_{g_0}$.
2. At $t = -T_{g_0}$, the mesh nodes at the bottom of the domain are fixed in the vertical (z) direction by prescribing $u_z = 0$ at every time step.

foreach *nonlinear element* **do**

Get element nodal displacements $(u_i)_n$

foreach *quadrature point* **do**

Compute current state of stresses σ_n:

$\epsilon_n = \frac{1}{2}\left(\nabla\psi_j \mathrm{u}_n + \nabla\psi_j^T \mathrm{u}_n\right)$ (3.33)

$\epsilon_n^e = \epsilon_n - \epsilon_n^p$

$\sigma_n = C_{ijkl}\epsilon_n^e$ (3.32)

Predict plastic strain for next time step ϵ_{n+1}^p:

$I_1,\ J_2,\ F(\sigma)$

$f(\sigma, k) = F(\sigma) - k$ (3.15) or (3.16)

$\dot{\lambda} = \dot{\lambda}_0 \langle \frac{F}{k} \rangle^{1/m}$ (3.11)

$\dot{\epsilon}^p = \dot{\lambda}\frac{\partial f}{\partial \sigma}$ (3.12)

$\epsilon_{n+1}^p = \epsilon_n^p + \Delta t \dot{\epsilon}^p$

end

end

$\vdots$

foreach *nonlinear element* **do**

Compute Internal resistance force for current step $\mathbf{p}_n$:

foreach *element node* i **do**

$\epsilon_n^e = \epsilon_n - \epsilon_n^p$

$\sigma_n = C_{ijkl}\epsilon_n^e$ (3.32)

$\mathbf{p}_i = \sum_{j=1}^{8}\left(W_j\left(\mathbf{B}^T\sigma\right)\right)$ (3.30) and (3.31)

end

end

Figure 3.8: Pseudocode of the new module for nonlinear ground motion modeling implemented in Hercules. The first block computes the current (step n) state of stresses (σ_n) considering the plastic component of strains obtained at the previous time-step, and uses the power law of rate-dependent plasticity to predict the next step $(n+1)$ plastic strain (ϵ_{n+1}^p) for future use. The second block, computes the internal resistance force ($\mathbf{p}_i$) to be used in the forward solution of displacements. Equation numbers associated with specific operations are shown on the right hand side.

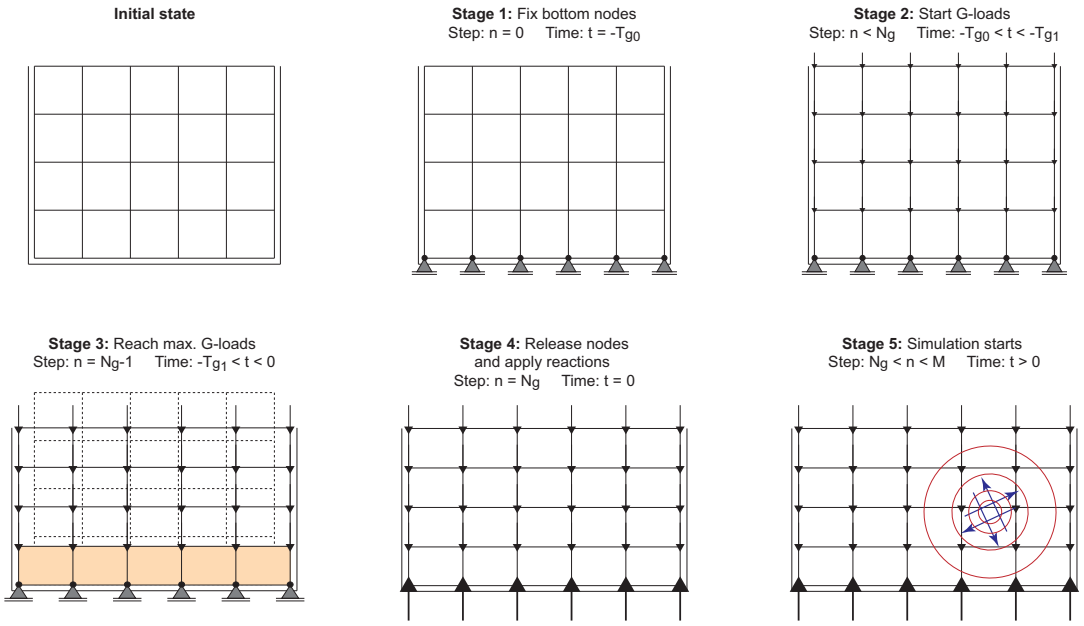

Figure 3.9: Schematic representation of the steps followed to include the effect of gravitational consolidation.

3. Gravitational loads are applied monotonically. The weight of each element is distributed among its nodes. Magnitude of the gravitational force is zero at $t = -T_{g_0}$ and increases as a smooth function of time, reaching its maximum value at time $T_{g_1} < T_g$.
4. The system is left to stabilize during the simulation cycles corresponding to $T_{g_1} < t \leq -\Delta t$. At the end of this stabilization stage, the displacements of the upper nodes of all elements at the bottom of the domain are used to calculate equivalent reactions to the gravitational load.
5. At $t = 0$, the bottom mesh nodes are released and the reactions calculated in the previous step are applied at these same nodes as counteracting forces to the gravitational loading. After this, the original simulation starts. Both the gravity forces in all nodes and the reactions at the bottom ones are left active for the rest of the simulation time.

This procedure is illustrated in Fig. 3.9.

4

Modeling Urban Environments

4.1 Modeling Approach

With the growth of personal computers processing capability, structural engineering analysis and design has reached high levels of complexity and refinement. Although for most small-size structures equivalent static and response spectrum analysis continue to be the standard practice—and minimum requirement enforced by most seismic design codes—linear dynamic analysis has become a common approach in high earthquake hazard regions. Other more elaborate methods such as nonlinear static (pushover) and nonlinear dynamic analysis have also gained acceptance among structural engineers, especially for the case of high-rise buildings, bridges, and other sensitive infrastructure projects such as dams or nuclear power plants. With the exception of the latter two, most of these structures—buildings, in particular—are modeled using beam and column frames in combination with plate and shell elements. In some cases, models also include finite elements for particular delicate sections of structures like shear and retaining walls or for addressing irregular shapes of structural relevance. Foundation systems are, for the most part, considered to be *fixed-base*, that is, in full contact with the ground which is considered to be infinitely rigid—neglecting soil-structure interaction. The cases that do consider flexibility at the base, usually employ an arrangement of springs and dashpots to represent the soil or, in rare occasions, by actually modeling the surrounding soil using finite elements.

Highly elaborate modeling considerations for buildings like the ones just described are not feasible for the objectives of the present work. One reason for that is because beam and column elements would require a much smaller size time-step than that needed for regular wave propagation problems. In addition, these elements have additional degrees of freedom (rotation and torsion) which

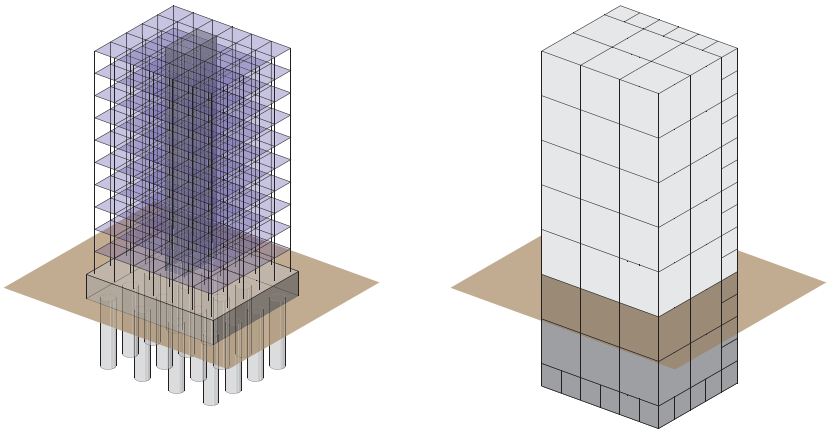

(a) Real structure **(b)** Blocks model

Figure 4.1: Building model using homogeneous blocks. The superstructure and foundation system are replaced by hexahedral elements. Geometric characteristics are adjusted to the mesh. Properties of the superstructure and the foundation elements are independent of each other, and their material properties are chosen so that they reproduce the general dynamic characteristics of the real structure.

would be needed to deal with using special joints at the contact nodes with the ground in order to provide continuity of displacements. There exist alternatives to these and other potential difficulties. However, construction and calibration of such models is time consuming and it would result unpractical to develop detailed models for large building inventories in urban areas. Therefore, to gain some initial physical insight of the effects of buildings on ground motion and of structure to structure interaction effects, it is sufficient to consider only simplified building models that retain the main characteristics of actual buildings. Such models will need to satisfy the following basic requirements.

- Reproduce the general dynamic properties of the buildings.
- Differentiate between the superstructure and foundation system.
- Integrate complete soil-structure interaction effects.
- Easy to assemble with the simulation mesh.
- Easy to model in large numbers.

With these considerations in mind, the most practical approach at the moment was to model the buildings as homogeneous blocks, using hexahedral elements, as done for the crustal mesh. A sample of such a model is shown in Fig. 4.1. This same concept has been used by others for problems of site-city interaction effects in 2D models using analytical (Wirgin and Bard, 1996; Wirgin, 2002), boundary element (Kham et al., 2006; Semblat et al., 2002, 2004), finite element (Tsogka and Wirgin, 2003a,b; Groby et al., 2005; Groby and Wirgin, 2008), and high-order spectral element (Laurenzano

et al., 2010) methods for vertically incident waves. Other alternatives were to use single mass oscillators with rigid foundations attached to the ground using rotational and translational springs (as in Bard et al., 1996; Guéguen et al., 2000b, 2002), or lumped mass models attached to beam-frame foundation systems (as in Fernández-Ares, 2003). However, these alternatives did not offer the same modeling flexibility and posed undesirable restrictions. Lumped mass models, for example, need auxiliary (link) elements to reproduce rocking and torsional motion at the base; and foundations systems modeled with bending beam elements do not satisfy conditions of continuity with soil elements. In addition, either one of these other alternatives required special accommodations in terms of load distribution among processors; otherwise the spatial distribution of buildings would need to be restricted to the physical partition of the model. These issues can be more efficiently addressed with the homogeneous blocks described ahead.

4.1.1 Basic Assumptions

The following are the assumptions made by using the blocks analogy to model buildings in site-city interaction problems with Hercules.

- Real structure dynamic properties can be reproduced on average by an equivalent homogeneous raised-up cantilever beam composed of solid finite elements.
- Real structure dimensions and location adjust to the nearest mesh grid in accordance with the minimum octant size of the mesh as provided by the user.
- The structure foundation and impedance with respect to the surrounding soil can be approximated by a set of homogenous blocks.
- Elements of the foundation systems (piles and/or footings) present a group behavior for which an equivalent embedded foundation can be modeled with the homogeneous blocks analogy.
- The base of the building or its embedded foundation is in full contact with the soil.

4.1.2 Building Properties

Beyond the geometric considerations, the key aspect of the homogeneous blocks analogy for modeling buildings and their foundation systems rests on the selection of the building properties. For the superstructure we follow two classical conceptual approximations in earthquake engineering. The first is that the natural period of a stratum soil-column (T_{S_0}) may be approximated by (4.1), where h is the thickness of the stratum and V_s is its shear wave velocity in m/s. The second one says that

the natural period of a building (T_{B_0}, in seconds) may be approximated as a fraction of the number of stories (N) as in (4.2)—a well-known rule of thumb, first introduced in a report by the U.S. Coast and Geodetic Survey (1936).

$$T_{\mathrm{S}_0} = \frac{4h}{V_{\mathrm{s}}} \tag{4.1}$$

$$T_{\mathrm{B}_0} = \frac{N}{10} \tag{4.2}$$

$$h = 0.7H \tag{4.3}$$

$$N = \frac{H}{h_{\mathrm{s}}} \tag{4.4}$$

Then, assuming that the buildings behave as soil-columns in a stratum, (4.1) equals (4.2). However, h cannot be directly taken as the height of the building but as the effective height associated to the first mode of vibration of the structure as in (4.3), following the recommendations for soil-structure interaction problems by FEMA P-705 (2009). In addition, the total number of stories relates to the total height of the building as in (4.4). h_{s} is the inter-story height. Therefore, combining (4.1) through (4.4) yields (4.5). Hence the shear wave velocity for the hexahedra representing the buildings is defined by (4.6)

$$\frac{0.7H}{V_{\mathrm{s}}} = \frac{H}{10h_{\mathrm{s}}} \tag{4.5}$$

$$V_{\mathrm{s}} = 28h_{\mathrm{s}} \tag{4.6}$$

Inter-story height of typical structures varies between 3.5 and 4.5 m. This yields V_{s} values between 98 and 126 m/s. In this study we use $V_{\mathrm{s}} = 100$ m/s for the superstructures; for the foundation blocks we tried different values between 100 and 400 m/s. The value of the primary waves velocity was set as $V_{\mathrm{p}} = 2.5V_{\mathrm{s}}$, an acceptable simplified approximation from the several correlations suggested in the literature (e.g. Brocher, 2005). Intrinsic attenuation quality factor was set to $Q = 20$. This corresponds to 5 percent of critical damping ratio—a common assumption in structural engineering. The buildings material density was set to 300 kg/m^3. These values are in agreement with others used in similar 2D studies (e.g. Wirgin and Bard, 1996; Tsogka and Wirgin, 2003b; Semblat et al., 2004; Kham et al., 2006; Laurenzano et al., 2010).

4.2 Modified Meshing Procedure

Modeling building sets using hexahedra entailed implementing new meshing provisions to create the vertical 'extrusions' in the mesh for representing the superstructures and to adapt portions of the 'interior' mesh to represent the foundation systems. To this end we developed an entirely new module in Hercules with application interfaces that interact with the main *psolve* module, and with Hercules' meshing *octor* library (described earlier in Section 2.2.1).

Because Hercules' meshing structure was designed to produce unstructured representations of rectangular shape volumes, adding the buildings implied altering the final shape of the mesh to now have elements protruding from the surface. The first alternative considered to confront this challenge was to allocate some dedicated processors to handle an independent mesh for the buildings and to arrange communications between the dedicated and the main solving processors. This implied changing the communication protocols in Hercules for handling continuity of displacements at the nodes of contact between the two parallel meshes. In addition, operations such as printing stations and planes would overlap between the main solving processors and the dedicated ones, posing additional conflicts.

A second alternative was to add the new building hexahedra in the first z-negative octant of the simulation Cartesian domain and to provide the meshing library with information about the location and properties of the buildings. This was not feasible because the octree database structure in the meshing library would have required pervasive modifications in its inner core data-structure, adding unacceptable complexity.

The third alternative was to deceive the program by 'pushing' the surface down by a certain distance in depth (the height of the tallest building) and meshing in the buildings within the rectangular domain filling all other elements around the buildings and above the (pushed) surface as air. In this alternative, the air elements would have a negligible mass and would be counted out of the stiffness contribution computing loop. This alternative entailed the construction of a parallel table of elements to distinguish the air elements from the rest, causing a misuse of memory.

All these alternatives implied an unbalancing of the workload among processors. Therefore, having considered these different options, we identified that the best possible alternative would be one that satisfy the following requirements.

- Maintain Hercules communication scheme.
- Seamlessly integrate with the meshing library.

- Guarantee a balanced workload among all processors.
- Allow buildings to be shared between processors.

To comply with these requirements we came up with a strategy for compiling all the positive aspects of the alternatives discussed above, while at the same time addressing their shortcomings. The main idea of the chosen approach is to build the mesh with air as in the last alternative but to discard the 'air' elements at some point during the meshing procedure so that the final table of elements in each processor does not have useless memory buckets while keeping a balanced distribution as in a regular mesh. The final modified meshing procedure consists of the following steps.

1. Push the surface of the domain down by a depth equal or larger than the height of the tallest building to be considered. Since all depth dimensions continue to be positive quantities, this implies modifying (by the same amount) the z-coordinate of the source, the stations, and the planes. All this is done when parsing the input data.
2. Replace the vacuum created by pushing the surface with elements tagged as 'air' elements for later disposal. Tagging consists of assigning a negative V_{p} value to the element. This does not affect the original meshing procedure that is only dependent on the value of V_{s}. Air elements' V_{s} is set as a function of depth. An element just above the surface has the same V_{s} that its counterpart beneath the surface and the value increases as the elements move farther up from the surface.
3. Proceed with refinement as usual but now check if any element is within a building or crosses a building boundary. If that is the case, subdivide the element so that both the dimensions of the building are met by a minimum grid standard, and the V_{s} assigned to the building superstructure or its foundation satisfies the size-rule (2.17) given in Section 2.2.1. Also, refine the meshing when an element crosses the surface until the surface 'depth' matches with the mesh. See section 4.2.1 for details.
4. Balance elements so that the continuity 2-to-1 condition (see section 2.2.1) is met. This is done for all elements regardless of them being air, buildings, foundations, or crust elements.
5. Discard all 'air' elements by carving the buildings out of the mesh. In this step each processor traverses its local octree mesh structure and checks if an element is tagged (i.e., has a negative V_{p}). If that is the case, it eliminates the element and refurbishes the local mesh. This carving procedure is explained in greater detail in Section 4.2.2.

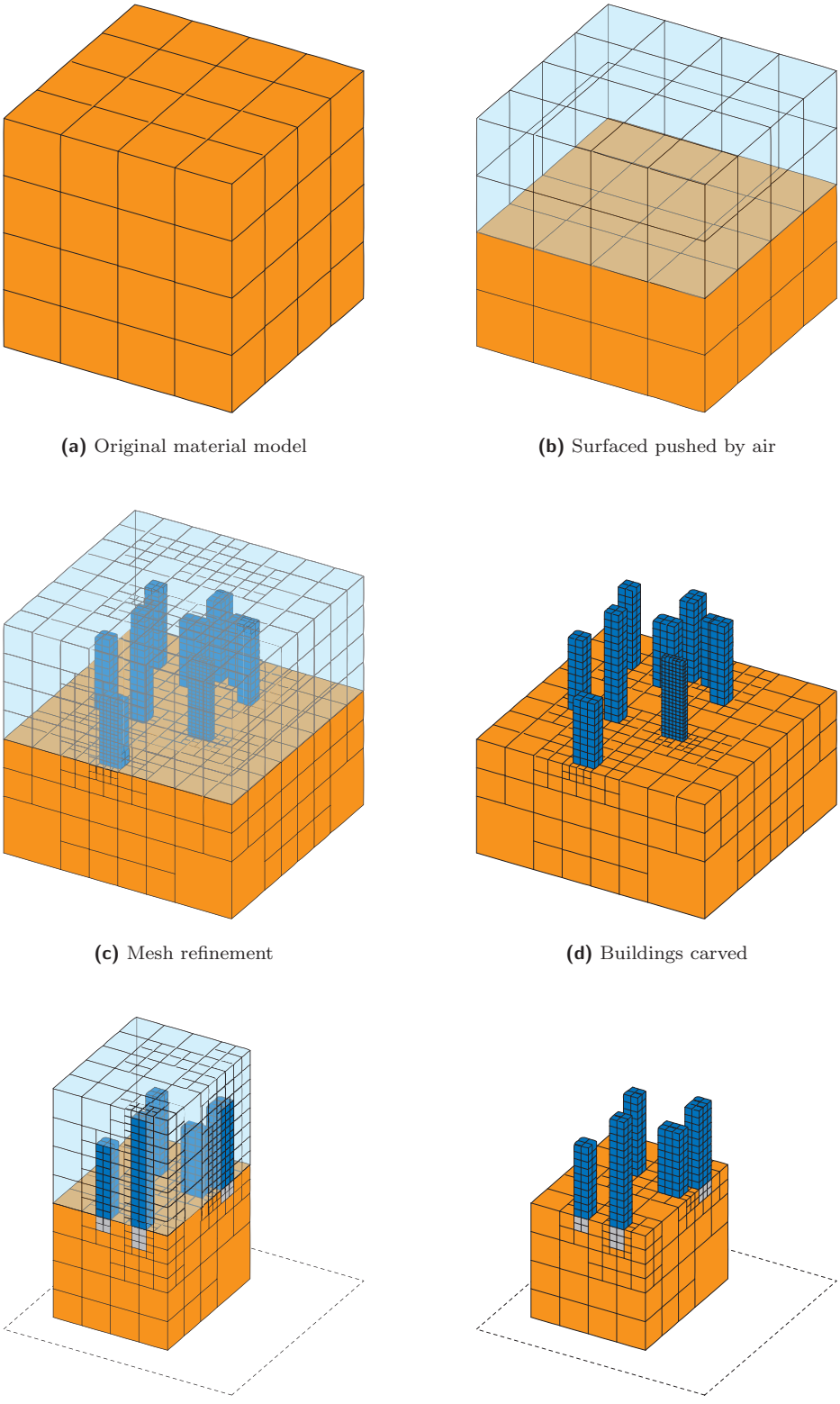

(a) Original material model

(b) Surfaced pushed by air

(c) Mesh refinement

(d) Buildings carved

(e) Refinement—foundations cut

(f) Carving—foundations cut

Figure 4.2: Buildings meshing and carving process.

6. Partition the mesh as usual. Since the 'air' elements have already been eliminated from the local octree meshes, the final result of the partition is a workload balanced mesh across all processors independently of them having building elements or not. By default, it also happens that processors exchange elements from buildings, thus it becomes irrelevant if a building is shared or not among processors—it comes naturally to the mesh.
7. Extract the mesh from the octree structure and write to each processor's memory the element and node tables. This last step is the most complex and delicate one because protruding elements representing the buildings modify the original logic behind mesh extraction in Hercules, affecting the existent correlation between the two tables. The modified extraction procedure is explained in greater detail in Section 4.2.3.

Figure 4.2 displays the main features of the new meshing procedures and the following sections describe in greater detail the core methods comprised in steps 3, 5 and 7 above. The final (modified) meshing algorithm is presented at the end of this chapter in Section 4.2.4.

4.2.1 Modified Mesh Refinement

The first major modification in the meshing procedure comes at the refinement process. However, the `octor_refinetree` method in the octor library remains unchanged. The modification then comes with the plug-ins that Hercules' main program (*psolve*) handles to the mesher. These are the `toexpand` and `setrec` methods. The former defines whether an octant needs to be subdivided in eight new octants or not. The latter provides the properties for any given octant along the refinement process regardless of whether the octant will need to be subdivided or not. Figure 4.3a shows the algorithm of the `toexpand` method highlighting in blue the new additions. A companion method called `toexpand_bldgs` is shown in Fig. 4.3b. In turn, the algorithm of the modified `setrec` and companion `setrec_bldgs` methods are shown in Fig. 4.4. All buildings related or companion methods were bundled in the new `buildings.c,h` module in Hercules.

4.2.2 The Carve-Buildings Method

The second significant modification in the meshing procedure comes with the insertion of the new method `octor_carvebuildings`. This method eliminates the air tagged elements from the local octree mesh in each processor. Figure 4.5 shows the pseudocode of this procedure and that of a

```
Input: Octant with data
Output:
  1: Expand
  0: Do not expand

if data = null then
    return 1
end

if Num. of Bldgs > 0 then
    res = bldgs_toexpand(octant)
    if res ≠ −1 then
        return res;
    end
end

if octant satisfies V_s-rule then
    return 0
else
    return 1
end
```

(a) Plug-in `toexpand`

```
Input: octant with data
Output:
    1: In a building, expand
    0: In a building, do not expand
   −1: Not in a building

foreach building do
    if octant is in building then
        if crosses bldg boundary or
           does not satisfy V_s-rule
        then
            return 1
        else
            return 0
        end
    end
end

if octant crosses the surface then
    return 1
end

return −1
```

(b) Plug-in companion `toexpand_bldgs`

Figure 4.3: Algorithms of the modified `toexpand` and new `toexpand_bldgs` methods as implemented in Hercules for controlling whether an octant needs to be refined into eight new octants or not during the execution of the `octor_refinetree` method in the meshing process.

companion method for ensuring that once an octant is eliminated from the mesh, the octree structure maintains all interior and leaf nodes properly placed.

4.2.3 Modified Mesh Extraction

The last step in the meshing process is the actual extraction of the mesh out of the octree data structure and into the element and node tables of each processor. Extracting the table of elements is rather easy. The count of elements is known, memory is allocated for the table, and then the leaves of the octree are traversed while writing the data for each element in sequential z-order. On the other hand, the extraction of the table of nodes is probably the most complex operation during the entire meshing process. The difficulties lie in that each node is at the same time a vertex shared by several octants, which in turn may or may not be in the same processor. In addition, nodes can be *anchored* or *dangling* depending on the 2-to-1 provision for linear continuity of displacements. For the dangling nodes, it is necessary to find the anchored ones they depend on. Therefore, proper steps are required to characterize the nodes, determine the octants they are associated with, establishing the necessary relations with respect to the element table, and set up the communication controller

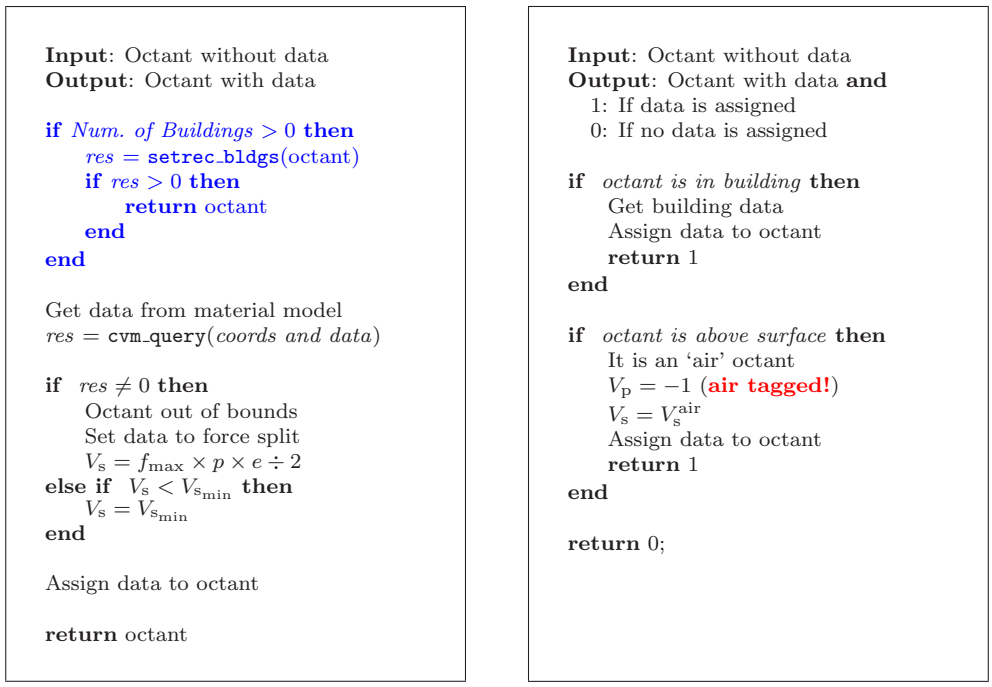

(a) Plug-in `setrec` **(b)** Plug-in companion `setrec_bldgs`

Figure 4.4: Algorithms of the modified `setrec` and new `setrec_bldgs` methods as implemented in Hercules for handling back the data associated to a given octant.

for inter-processor communications during the simulation. This process has been explained in detail by Tu and O'Hallaron (2004b,c) and Tu et al. (2005). In summary, the `octor_extractmesh` performs the following set of operations.

1. Extract mesh nodes from the parallel (balanced) octree and compute their coordinates.
2. Identify and tag the dangling nodes.
3. Assign each element and node to an owner processor.
4. Establish a communication protocol for processors sharing nodes.
5. Assign global IDs to elements and nodes.
6. Assign local IDs to elements and nodes.
7. Correlate local and global node and element ids.
8. Correlate the node and element tables locally (mesh connectivity).
9. Correlate local dangling nodes to local anchored nodes.

The most critical of these operations is identifying the nodes as anchored or dangling. The key piece of information for being able to determine whether a node is dangling or not is the number of

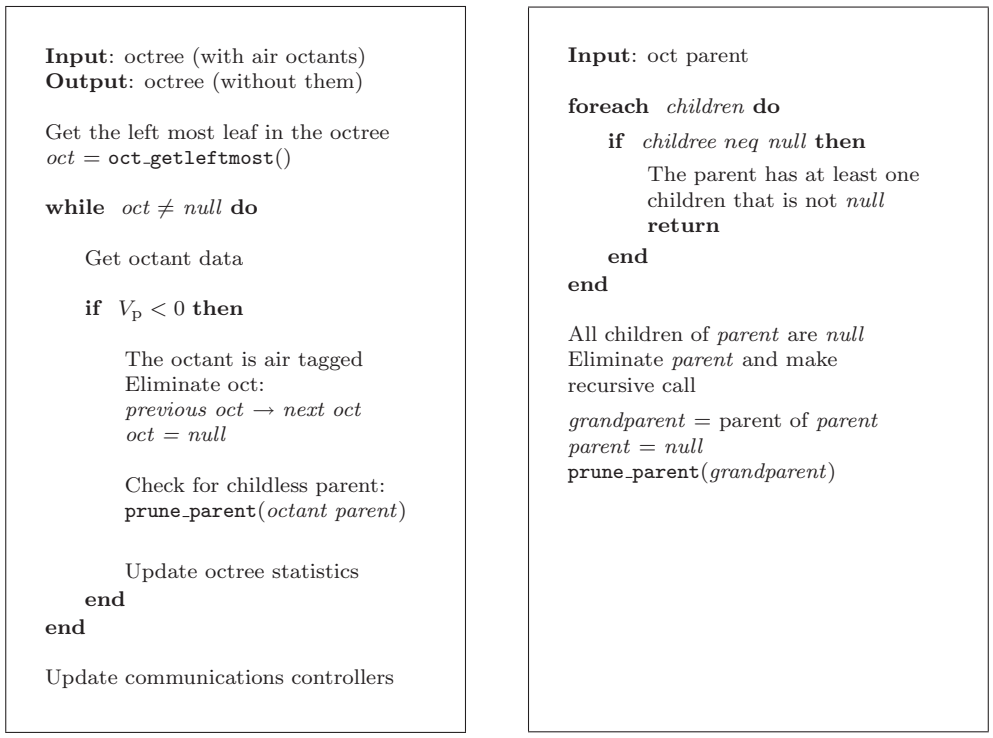

(a) Method `octor_carvebuildings` **(b)** Companion method `prune_parent`

Figure 4.5: Algorithms of the `octor_carvebuildings` and `prune_parent` methods.

elements that share the node, or number of *vertex touches*. Here, we understand by a vertex, any of the eight corners of an element, which coincide with the mesh nodes. Therefore, counting the number of touches for each vertex—that is, the number of elements sharing a particular node—is accomplished by traversing the leaf octants in the mesh octree (as the table of elements is being created) and pouring the nodes into a hash table while checking for duplicates along the way. If the node is new to the hash table, it is stored and the touches count is set to 1. If a duplicate is found, it is not stored, but the touches count is increased by one. Once this operation is done for each local mesh, neighboring processors exchange information and update the number of touches for the nodes they share. Figure 4.6 shows examples of an anchored node touched by four elements and a dangling node touched by two. In this case, both nodes are on the face of one of the domain boundaries.

It follows from Fig. 4.6 that these conditions may change depending on whether the node is in the interior, on a boundary face, or in one of the edges or corners of the domain. Prior to implementing the mesh extrusions representing the buildings, the possible number of touches in any given vertex was 8, 6, 4, 2, or 1. After incorporating the carving process, the possible number of touches changes

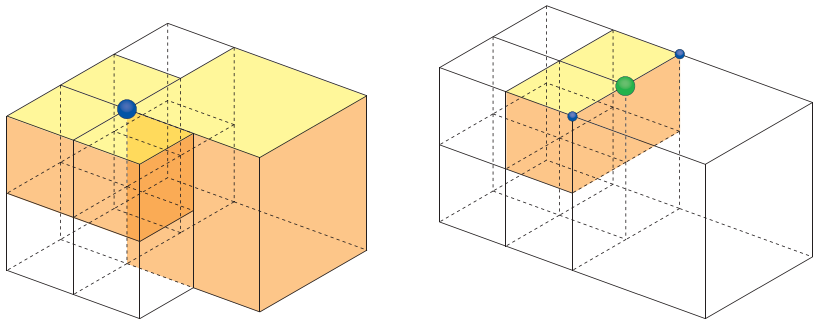

(a) Anchored with 4 touches **(b)** Dangling with 2 touches

Figure 4.6: Examples of an anchored and a dangling node with different number of touches. Blue dots represent anchored nodes, whereas green ones represent dangling ones. Elements touching the particular vertex of interest are colored.

```
Input: vertex touches and coordinates
Output: property:
  0: anchored
  1: dangling from 2
  2: dangling from 4

Determine position of the vertex

switch touches
    case 8
        return 0
    case 6
        if domain interior or
           bldg interior then
            return 1
        else
            return 0
        end
    case 5
        if on the surface and
           at a building-base corner then
        return 0;
    case 4
        if on a domain face or
           on a building face then
            return 0
        end
        if domain interior or
           bldg interior then
            if in an octant edge then
                return 1
            else if on an octant face then
                return 2
            end
        end
```

```
switch (cont.)
    case 3
        if on the surface and
           at the base-corner of a bldg then
            return 1
        end
    case 2
        if in a domain edge or
           in a bldg edge then
            return 0
        else if is interior or
           on a domain edge or
           on a bldg face then
            return 1
        else if at the base of a bldg then
            return 2
        end
    case 1
        if on a domain corner or
           on a bldg-roof corner then
            return 0
        end
        Should be at the base of a bldg
        if dangling on edge then
            return 1
        else if dangling on face then
            return 2
        end
    default:
        return error
end switch
```

Figure 4.7: Pseudocode of the `node_setproperty` method. Sections highlighted in blue font correspond to the new provisions for the cases resulting from the incorporation of the buildings in the mesh.

to 8, 6, 5, 3, 2, or 1. In addition, the conditions for each case changed considerably. For example, before the new implementations the case of 6 touches was invariably that of a dangling node in the interior of the simulation domain. Now, a 6-touches vertex may also be at the base of a building in the edge that a lateral face makes with the surface. In that case the node is anchored. Another example is that of a 1-touch vertex. Before, 1-touch vertices were only possible at the corners of the domain and were always anchored. Now, they may also be at the corners of buildings. When at the roof, they are anchored, but when at the base they may be anchored or dangling.

All former and new possibilities for vertex-touches are summarized and shown in graphical detail in Appendix C. Assigning each vertex as dangling or anchored based on the number of touches is performed by the `node_setproperty` method in the octor library. Figure 4.7 shows the pseudocode of this and other companion methods, highlighting in blue font the new implementations for the different cases and additional considerations. All other operations in `octor_extractmesh`, with the exception of minor interface details, remained the same as described in Tu and O'Hallaron (2004b,c) and Tu et al. (2005).

4.2.4 Modified Meshing Algorithm

The final result of the modified meshing procedure is packaged in the `mesh_generate` method in Hercules' main program. The modified pseudocode of this method is shown in Fig. 4.8. The basic new component is the inclusion of the `octeor_carvebuildings` method highlighted in blue font.

Input:
Domain dimensions
Meshing plug-ins (`setrec`, `toexpand`)
Output:
Distributed, unstructured, balanced mesh

Create a new local octree
myOctree = `octor_newtree`()

Refine the local octree
myOctree = `octor_refinetree`(*myOctree*, `setrec`, `toexpand`)

Balance the local octree
myOctree = `octor_balancetree`(*myOctree*, `setrec`, `toexpand`)

Carve buildings out of the octree
myOctree = `octor_carvebuildings`(*myOctree*)

Partition the octree among processors
myOctree = `octor_partitiontree`(*myOctree*)

Extract the mesh from octree
myMesh = `octor_extractmesh`(*myOctree*)

Figure 4.8: Meshing algorithm after incorporating building models.

5

Case Study and Linear Ground Motion

During the past five years we have been involved in several collaboration projects for earthquake ground motion modeling. Most of our work has focused in the region of Southern California (e.g Taborda et al., 2006a, 2007b, 2009; Bielak et al., 2010) in partnership with other members of the Southern California Earthquake Center and the Community Modeling Environment Group (SCEC/CME). Nonetheless, we have also dedicated some time and effort to apply and test our simulation approach to other regions of high seismic hazard. In Ramírez-Guzmán et al. (2008), for example, we studied the nature of the long-duration ground motion in the valley of Mexico City for a simulation of the M 7 1995 Copala earthquake in the coast of Guerrero. The final results of this work were presented by Ramírez-Guzmán (2008) in his doctoral dissertation.

Another interesting effort has been our participation in the Euroseistest project and its verification and validation exercise. This project studies several problems of interest in seismology and earthquake engineering using information from a well characterized valley in the Mygdonian basin, near Thessaloniki, Greece. We have selected this as our case study for the present work because, although it has some particular challenging characteristics for simulation, its crustal structure is relatively simple. This makes it optimal for contrasting the effects of nonlinear soil behavior and the influence of the urban environment.

This chapter describes the main characteristics of the Mygdonian basin and region of interest, and the employed simulation domain, followed by the results obtained for the linear (anelastic) wave propagation simulation. This first case will be used as reference for later comparisons with the simulations considering nonlinear ground motion and including the presence of a realistic cluster of buildings in the valley, using the new implementations presented in this thesis.

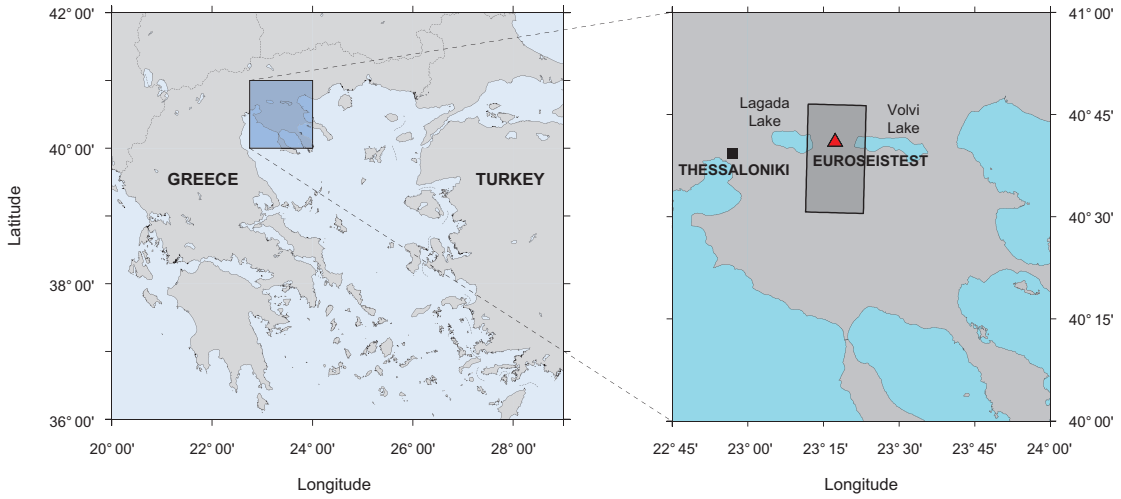

Figure 5.1: Location of the Euroseistest near Thessaloniki in nothern Greece. The map on the right also shows the simulation horizontal projection on the surface of the simulation domain.

5.1 The Euroseistest

The Euroseistest is one of the three research paths (testing, modeling, and risk analysis) of the Euroseis physical laboratory in the Mygdonian basin, near Thessaloniki, in Northern Greece (Fig. 5.1). This multi-purpose test site, whose physical properties and geometry are well characterized, is one of the longest running field laboratories of its type in the world. Other similar efforts are the Turkey Flat and the Ashigara Valley projects in the U.S. and Japan, respectively. The Euroseistest was established in 1993 and is under the operation of the Laboratory of Soil Dynamics and Geotechnical Earthquake Engineering of the Civil Engineering Department of the Aristotle University of Thessaloniki.

Over the past eighteen years a large number of universities and institutes from all over the world have been involved in research activities related to the study of problems in seismology, earthquake engineering, and soil dynamics, using records from past earthquakes in the region and performing large-scale experiments in its testing site. More than 200 scientific papers have been published in journals and proceedings based on data and results from the Euroseistest. Other components of the Euroseis initiative are dedicated to seismic hazard assessment, study of site effects, and soil-structure interaction problems.

Contrasting the results presented ahead with the extensive research on the Euroseistest available from the literature is out of the scope of this thesis. This may be a potential subject for future research. Here, we will use the information about the Euroseistest only as a mean for testing the

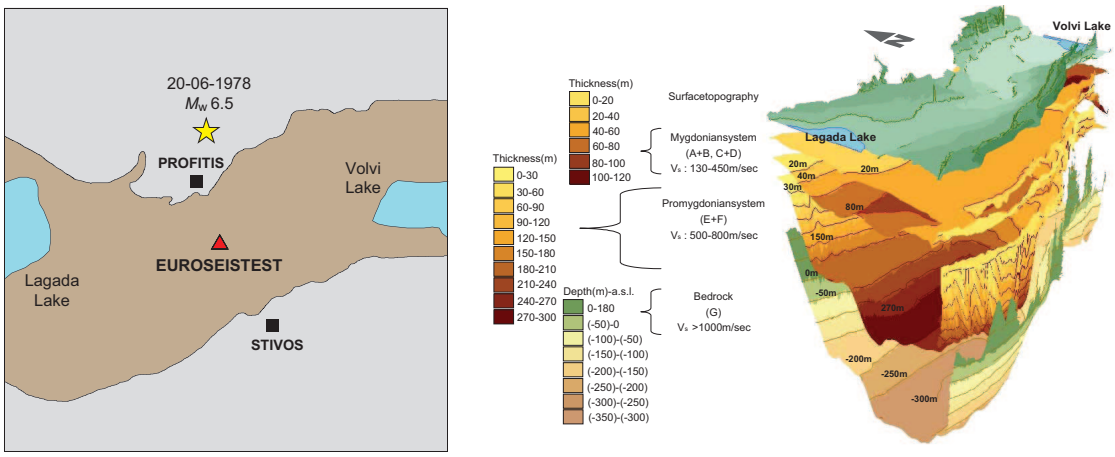

(a) **(b)**

Figure 5.2: Location of the Euroseistest in the Mygdonian basin. **(a)** Detail of the location of the testing site, and **(b)** description of the main geologic units beneath the Valley of Volvi in the Mygdonian basin (after Manakou, 2007).

new implementations made in Hercules and as a valuable example for preliminary analysis of results for drawing general conclusions regarding the nonlinear and site-city interaction effects on the ground response of regions prone to earthquakes.

5.1.1 The Mygdonian Basin and the Valley of Volvi

The testing site of the Euroseis project is located about 30 kilometers northeast from the city of Thessaloniki in the Valley of Volvi between the towns of Profitis and Stivos (Fig. 5.2a). The valley is bordered by two mountains to the North and South, and by the Volvi and Lagada lakes to the East and West, respectively. This is one of the most seismoactive regions in Europe. The epicenter of the M_w 6.5 earthquake of June 20, 1978 occurred just a few kilometers north from the site. This earthquake caused considerable damage in Thessaloniki and other nearby municipalities.

The Mygdonian basin is part of an east-west oriented graben divided by a ridge between the basins of the two lakes. The valley is filled with sediments of two main geologic units, the Pro-Mygdonian and the Mygdonian systems (Fig. 5.2b). The Pro-Mygdonian system is composed of conglomerates, sandstones, silt and sand sediments, and red clay beds; and the Mygdonian system is composed of lacustrine and deltaic sediments with conglomerates, gravel, sand, silt, and a variety of clays. To the East, the deepest portion of the basin is located beneath the Volvi lake, reaching down to the bedrock ($V_s \geq 1000$ m/s) at about 160 m. To the West, beneath the Lagada lake, the bedrock is found at about 370 m in depth. Tectonically, the main fault trend in the area

is oriented NW-SE. Other directions of faulting, E-W and N-S, dominate the eastern part of the basin, in coincidence with the main tectonic lines in Nothern Greece. Historically, besides the 1978 earthquake, this region has seen other moderate to major seismic events, including the M_z6.5 1902 Assiros, M_z7.1 1904 Kresna, M_z6.0 1932 Hierissos, and the M_z6.2 1933 Sohos earthquakes.

The relatively high frequency of events and the well-constrained geometric and mechanical properties make the Valley of Volvi an excellent case study for our purposes. More information about the seismic conditions, geological structure and geomechanical characteristics of the region can be found in Jongmans et al. (1998), Pitilakis et al. (1999), Raptakis et al. (2000, 2005) and Manakou et al. (2010). A description of the experimental site and a set of all data and records may be found in Pitilakis (2008).

5.1.2 The Verification and Validation Project

In 2008 several research groups gathered to define a numerical benchmark to conduct different simulations for the Euroseistest. This initiative was called the Euroseistest Verification and Validation Project, or E2VP. The objective was to thoroughly verify the different numerical methods used by the different participants by performing 2D and 3D ground motion simulations for well-defined test cases in the Valley of Volvi (Bard et al., 2008). The project, finished just recently, consisted of three phases that included more than ten different variations of six real and scenario earthquakes executed by twelve modeling teams from Europe, Japan, and the U.S. Six different numerical methods were used for the simulations: finite elements, finite differences, spectral elements, discrete elements, discontinuous Galerkin, and pseudo-spectral element methods.

Our participation in the E2VP exercise was in the 3D simulations of four minor earthquakes modeled as point-sources for pure elastic and anelastic considerations in a simulation domain of 29 km $\times$ 16 km $\times$ 41 km that included the valley and basin ridge between the lakes, and the epicenters of past prominent earthquakes in the region. A horizontal projection of the simulation domain on the surface is shown in Fig. 5.1 and described in detail in the next section. Comparisons of the synthetics indicated that there was overall good agreement among the different groups. The project also included validation with data recorded from local weak earthquakes. The group found that the simulations matched the overall amplitude, envelope, duration, and response spectra characteristics of the events, though further refinements were needed.

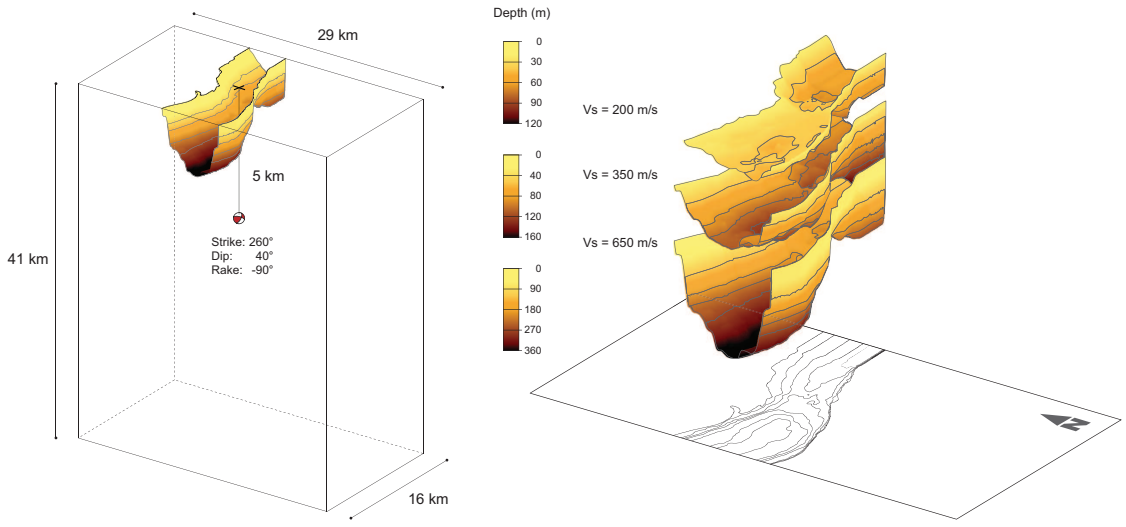

(a) Simulation domain

(b) Strata isosurfaces

Figure 5.3: Simulation volume domain for the case study and isosurfaces of the idealized material model for the upper softer-material layers in the basin.

All 3D simulations in the E2VP project were done for simulation parameters $V_{s_{min}} = 200$ m/s and $f_{max} = 4$ Hz. A preliminary report for both the verification and validation preliminary results may be found in Chaljub et al. (2010) and Moczo et al. (2010), respectively.

5.2 Earthquake Scenario and Material Model

5.2.1 Simulation Domain and Material Model

For our case study, we build upon the verification and validation numerical benchmark. We use the E2VP input data to construct a simulation domain in a volume of 29 km × 16 km × 41 km. Exact dimensions and coordinates of the rectangular projection on the surface, adjusted to comply with the etree version of the domain, are given in Table 5.1. This area encloses the deepest parts of the Lagadia and Volvi basins and the central ridge of the Mygdonian system as shown in Fig. 5.3a.

For the elastic properties of the material model, we adopt the layered structure employed in the E2VP simulations based on the crustal description and nomenclature used by Pitilakis (2008) and Papazachos (1998). This model is composed of three layers of soft material within the basin, which rests on a stiffer bedrock and layered halfspace. The softer layers in the basin have the properties shown in Table 5.2. The properties of the layered halfspace are shown in Table 5.3.

Table 5.1: Simulation domain dimensions and coordinates.

Dimensions	
Length (SN)	29320 m
Width (EW)	16160 m
Depth (UD)	40960 m
Domain coordinates*	
Southwest	23.1910, 40.5116
Northwest	23.1997, 40.7756
Northeast	23.3910, 40.7717
Southeast	23.3816, 40.5078

* The corners of the domains are given in longitude and latitude

Table 5.2: Description of the velocity model used within the basin.

Depth (km)	V_p (m/s)	V_s (m/s)	ρ (kg/m^3)
A+B	1500	200	2100
C+D	1800	350	2100
E+F	2500	650	2200

Table 5.3: Description of the velocity model used outside the basin.

Depth (km)	V_p (m/s)	V_s (m/s)	ρ (kg/m^3)
0–1	4500	2600	2600
1–3	6120	3420	2736
3–5	6130	3430	2744
5–7	6140	3440	2752
7–9	6150	3450	2760
9–11	6190	3480	2784
11–13	6230	3510	2808
13–15	6300	3570	2856
15–17	6420	3630	2904
17–19	6540	3700	2960
19–21	6690	3760	3008
21–23	6830	3820	3056
23–25	6970	3880	3104
25–27	7100	3940	3152
27–29	7240	4000	3200
29–31	7350	4080	3264
31–33	7460	4150	3320
33–35	7580	4240	3392
35–37	7700	4320	3456
37–41	7900	4400	3520

Table 5.4: Location and mechanism of the double-couple source used for the simulations.

Longitude	23°17'32"
Latitude	40°39'52"
Depth	5 km
Strike	260°
Dip	40°
Rake	-90°
Magnitude	M_w 5.2
Moment	7.0×10^{16} N·m

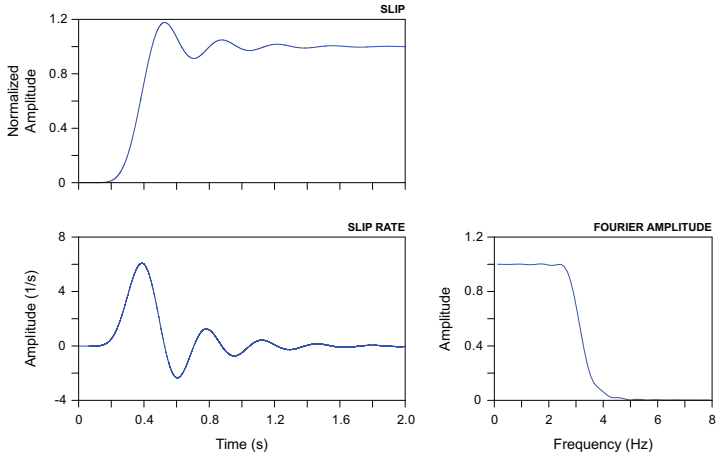

Figure 5.4: Normalized slip function (upper left), slip rate function (bottom left), and Fourier amplitude spectrum of the slip rate (right) for the point-source used for the case-study simulations.

For the material intrinsic attenuation we discarded the material parameters used in the numerical benchmark and kept the built-in implementation in Hercules for Rayeigh damping using the same correlation formula we have typically used in other simulations, i.e., a viscous quality $Q = 50V_s$ where $V_s$is given in km/s.

5.2.2 Source Definition

We consider a single case of excitation with hypocenter at a depth of 5 km right beneath the basin (Fig. 5.3a). The rupture is characterized as a point source modeled with a double-couple. The epicenter surface coordinates and source main characteristics are described in Table 5.4. This source corresponds to the I2c scenario in I2VP scaled up to match an earthquake magnitude $M_w = 5.2$. Figure 5.4 shows the slip function normalized with respect to the final displacement of the point-source dislocation used to calculate the equivalent (kinematic) forces representing the rupture. Also shown in Fig. 5.4 are the slip rate function and its corresponding Fourier amplitude spectrum. The

Table 5.5: Summary of simulation parameters and input data.

	Anelastic	Nonlinear Ground Motion		Site-City Interaction	
	Baseline Case	Linear†	Nonlinear	No Buildings‡	With Buildings
$f_{\max}$	4.0 Hz	4.0 Hz	4.0 Hz	4.0 Hz	4.0 Hz
$V_{s_{\min}}$	200 m/s	200 m/s	200 m/s	200 m/s	100 m/s
Nonlin. $V_{s_{\text{cut}}}$§	–	650 m/s	650 m/s	–	–
Pts/wavelengt	≥ 8	≥ 8	≥ 8	≥ 8	≥ 8
Min. ele. size	5 m	5 m	5 m	5 m	2.5 m
Surface pushed	–	–	–	320 m	320 m
Num. of Bldgs.	–	–	–	0	74
Num. of nodes	78,381,098	78,381,098	78,381,098	78,027,586	79,268,585
Num. of elements	71,024,194	71,024,194	71,024,194	70,697,394	71,798,354
Nonlin. elements	–	28,761,199	28,761,199	–	–
Time step Δt	0.002 s	0.001 s	0.0005 s	0.002 s	0.001 s
Sim. time	20 s	20 s	20 s	20 s	20 s
Total steps	10,000	20,000	40,000	10,000	20,000

† Same as the anelastic baseline case but with smaller Δt for accurate computation of strains.
‡ Same as the anelastic baseline case but with the surface pushed down.
§ All elements with $V_s \leq V_{s_{\text{cut}}}$ enter the nonlinear computational module.

slip function has a corner frequency near 3 Hz and significant energy content up to 4 Hz. The slip rise time is about 0.3 s. This slip function was the same used for all the simulations in the Euroseistest numerical benchmark.

5.2.3 Simulation Parameters

All simulations results presented in the following sections correspond to the same earthquake scenario and volume domain described in the two preceding sections. In all cases the maximum frequency was set to $f_{\max} = 4$ Hz. However, all other parameters were variable depending on particular input data or due to the numerical demands of each particular simulation, depending on whether nonlinear soil or site-city interaction effects were being considered and under what conditions. Table 5.5 shows the different simulation parameters for each type of simulation.

5.3 Linear Ground Motion Response

We first describe the response of the ground for the anelastic baseline case. Figure 5.5 shows snapshots of the magnitude of surface horizontal velocity—calculated as the square root of the sum of squares of the NS and EW components of motion—at different times in the simulation. Results clearly show the effects of the basin on the ground response. Waves travel at a slower velocity

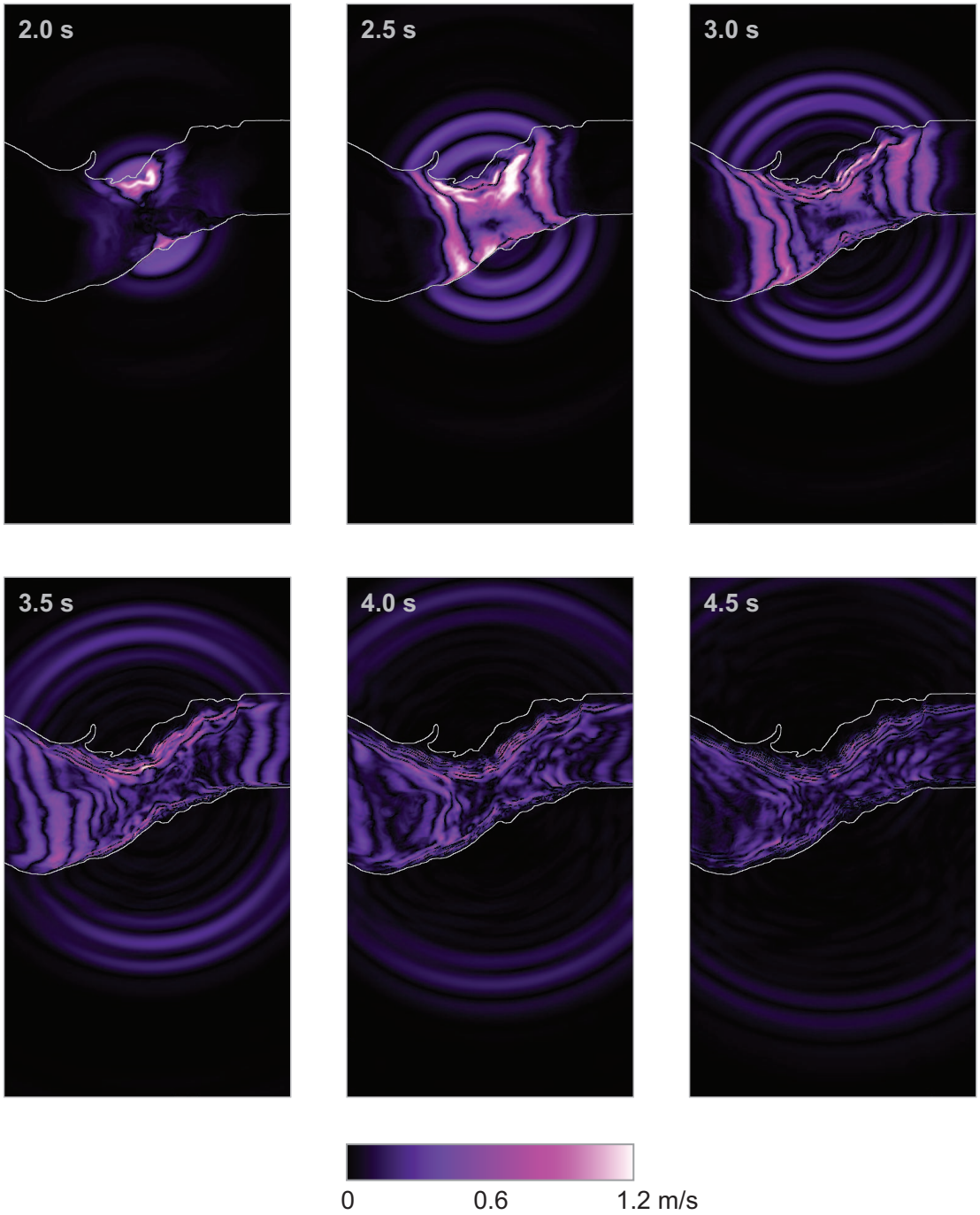

Figure 5.5: Snapshots of the magnitude of surface horizontal velocity at different times during the ground motion simulation of the anelastic baseline case.

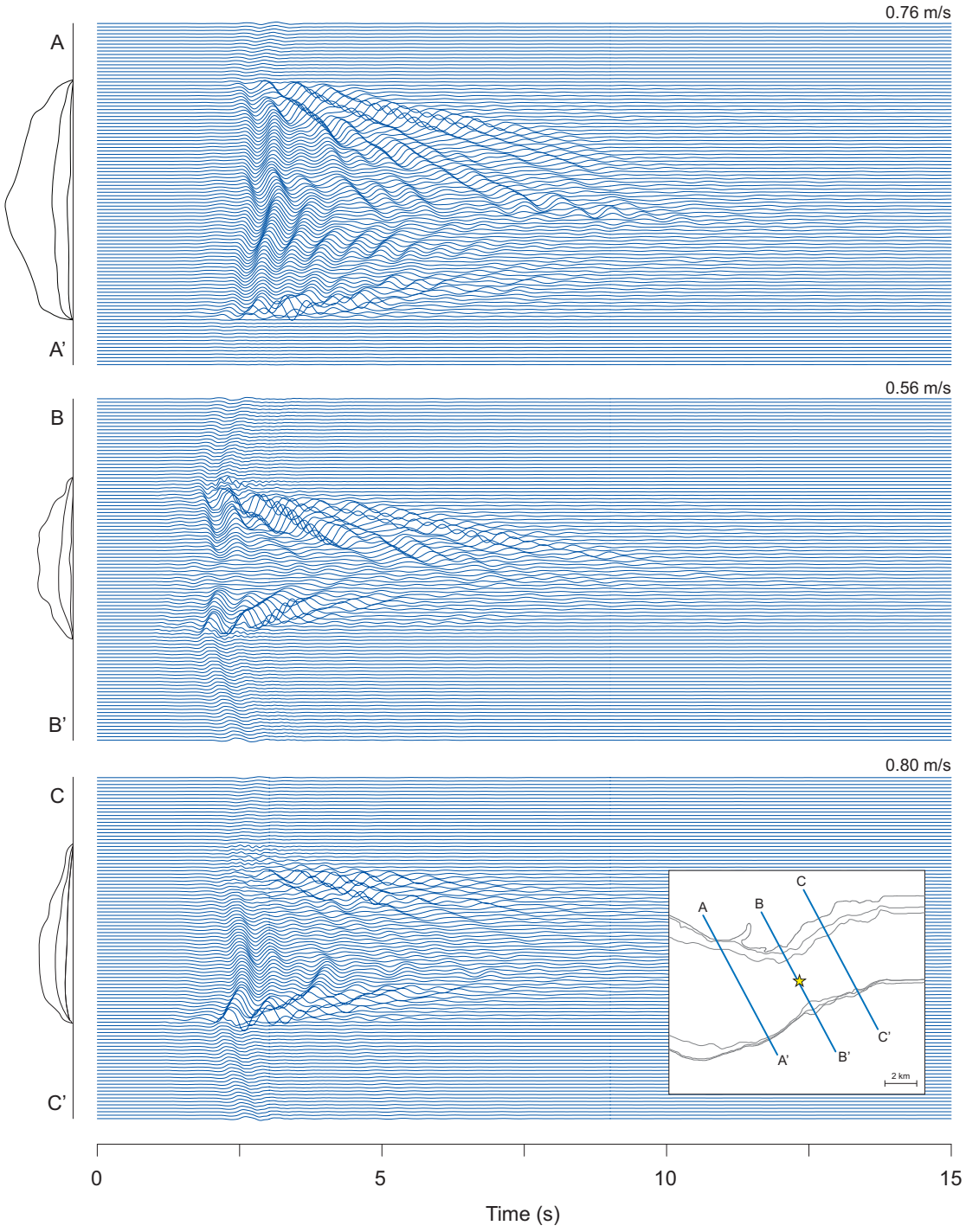

Figure 5.6: Particle velocities in the EW component of motion along three lines AA', BB' and CC' on the surface as shown in the inset at the bottom right corner. The respective soil-profile contours for the strata in the basin are shown to the left of each group of traces. Values at the right on top of each group of synthetics correspond to the maximum peak velocity of each set.

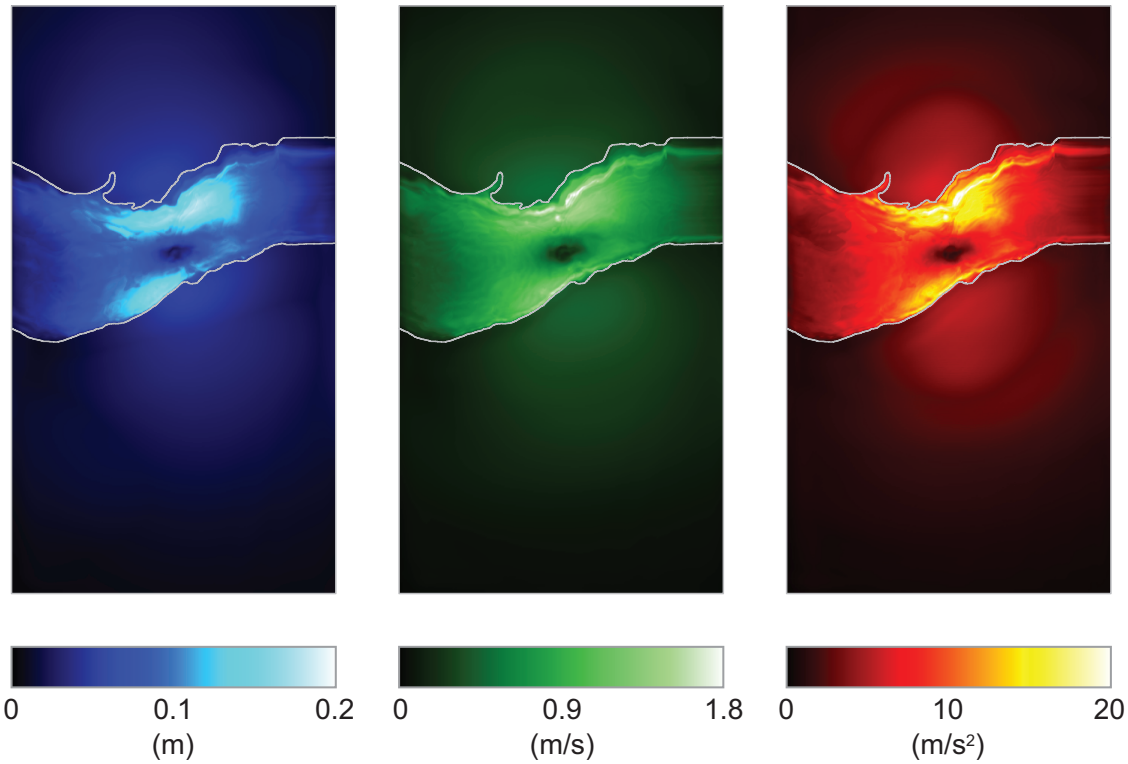

Figure 5.7: Horizontal peak magnitude displacement (left), velocity (middle), and acceleration (right) at the surface of the simulation domain.

through the softer strata in the valley and are trapped within the basin, where they continue to vibrate past the main shock. Also noticeable in these still-frames are the edge effects at the North and South boundaries of the valley with the mountains base. At these points constructive interference between outgoing and reflecting waves amplifies the ground response significantly. This is a complex phenomenon that is easier to observe in Fig. 5.6. This figure shows velocity traces in the EW component of motion along three lines on the surface crossing the basin from the NW to the SE. Note that the first arrival of waves at the deepest portions of the basin, i.e., towards the center of lines AA', BB', and CC', come a few seconds later than at the ends of the same lines. Also notice the amplification of the signals within the basin with respect to those out of it, and the numerous reflections and interferences near the South and North edges.

Figure 5.7 shows the horizontal peak magnitude of the response at the surface of the simulation domain in displacement, velocity, and acceleration. Here one can observe the total cumulative effect of the softer deposits and the geometry of the basin and its correlation with the amplitude of the ground motion. The strongest response occurs near the basin edges. Figures 5.8 and 5.9 show the peak response of displacements, velocities and accelerations for the NS and EW component of

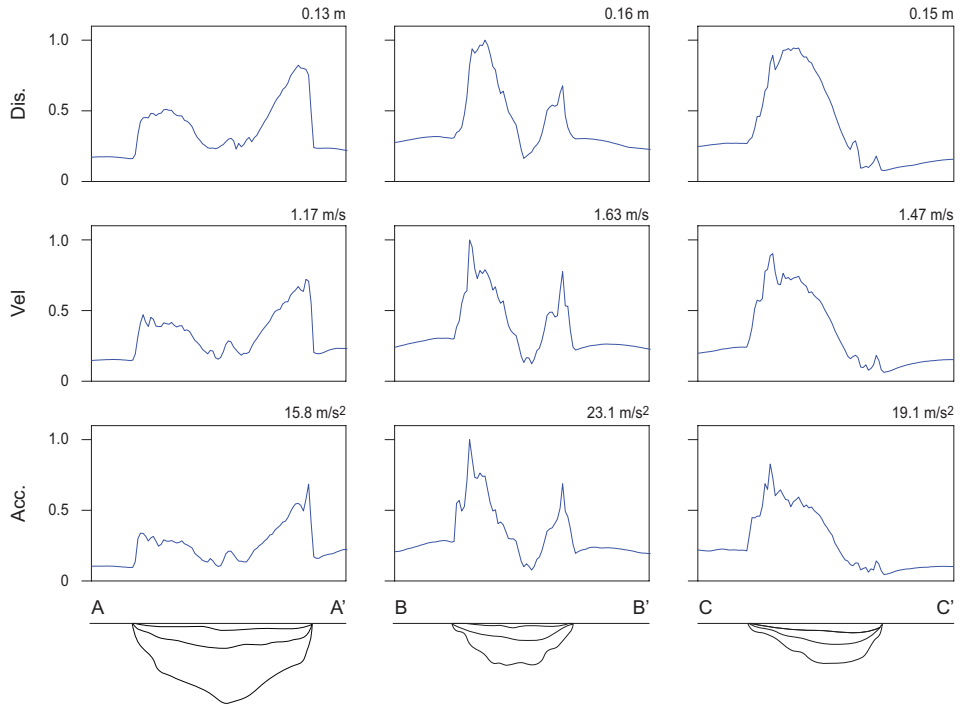

Figure 5.8: Peak displacements (top), velocities (middle), and accelerations (bottom) in the NS component of motion along the lines AA', BB', and CC' across the basin (see Fig. 5.6). Each row is normalized with respect to the maximum value of the set. Peak values for each profile are shown on top of each frame.

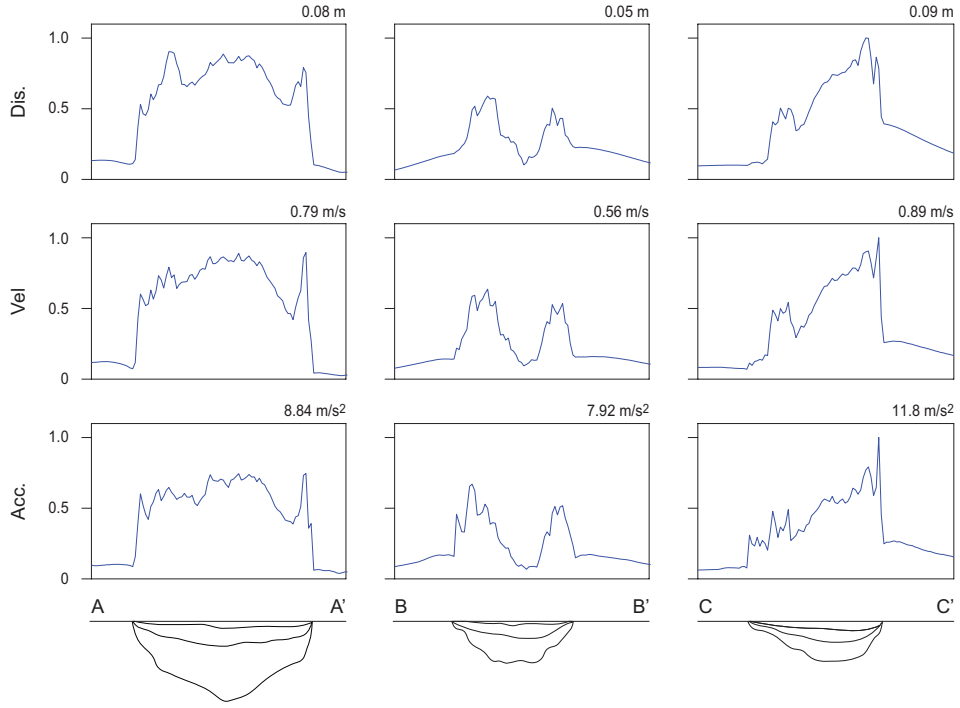

Figure 5.9: Peak displacements (top), velocities (middle), and accelerations (bottom) in the EW component of motion along the lines AA', BB', and CC' across the basin (see Fig. 5.6). Each row is normalized with respect to the maximum value of the set. Peak values for each profile are shown on top of each frame.

motions along lines AA', BB' and CC'. Once again, maximum amplitudes occur within the basin with abrupt changes in amplitude near the edges for all cases. These two figures also evidence the larger variability of the response at the shallower portions of the basin. All these are common manifestation of basin effects.

One last point worth mentioning about the linear response of the valley is the fact that the motion at the epicenter is almost null. This effect comes as a result of modeling the earthquake rupture as a double-couple point-source. It can be observed more clearly in Fig. 5.7 and is also visible near the middle of line BB' in Figs. 5.8 and 5.9.

6

Nonlinear Ground Motion Response

6.1 Simulation Cases

We consider two cases for the elastoplastic ground response of the valley for moderate and severe nonlinearities. These two scenarios were defined upon the response of the valley for the case of anelastic wave propagation. The second and third columns in Table 6.1 show the average and maximum value of the yield function, $F(\sigma, k)$ for each one of the soft layers in the basin. This data was collected for all elements in the mesh and synthetized for decision making. Based on these values we set maximum yield conditions for each stratum for the two nonlinear simulations. These yield limits are values shown in columns four and five in the same table for the moderate and severe cases, respectively.

These quantities do not necessarily correspond to the yield strength of the material. They were arbitrarily set to produce significant nonlinear behavior for illustrative purposes. A more rigorous set of simulations with experimental data regarding the elastoplastic properties of the materials in the deposits of the basin would be required for accurate representation of reality—a matter of

Table 6.1: Yield values measured during the baseline anelastic case and yield limits set for the moderate and severe nonlinear cases for each of the three soft layers in the basin.

Stratum	Anelastic		Moderate	Severe
	Avg.	Max.		
A+B	0.14	5.95	1.00	0.50
C+D	0.25	10.8	3.00	1.00
E+F	0.33	16.0	8.00	5.00

All values are in Pa$\times 10^5$

future work. Therefore, conclusions and analysis drawn from the results of these two simulations are presented in the spirit of illustration about the new modeling implementations; and physical interpretations are bounded by the lack of more realistic material yield properties. As will be seen, despite these limitations, results adjust well to expectations based on the accumulated experience from past earthquakes described in Section 1.2.

The analysis of results is divided in three sections. First we describe the overall regional response of the valley following the similar logic used in the previous section. However, we concentrate only in the central portion of the simulation domain that contains the basin. Then, we analyze the response at nine particular locations from a strong-motion signals perspective, comparing the synthetics at these observation points and its dynamic characteristics. We conclude with a view at the particle level describing the stress-strain relationships as implicit functions of time and other plastic parameters.

6.2 Regional Effects

6.2.1 Wave Propagation

We begin by comparing still-frames of the simulations at different times, as seen in Fig. 6.1. This first parallel of the three cases evidences that the waves traveling outside the basin suffer no change at all. Wavefronts emanating from the source and traveling through the elastic material surrounding the basin continue to do so at the same speed and with the same amplitudes. The large contrast between the material inside the basin ($V_s \leq 650$ m/s) and the material outside ($V_s \geq 2600$ m/s) constitutes a natural barrier that not only traps the waves but also isolates any effect that changes within the basin may suffer due to nonlinearities.

Inside the basin, however, much more is happening. In general, amplitudes diminish because of nonlinearities. The severe case, with the highest degree of nonlinearity, exhibits the smallest amplitudes inside the basin. As a result of these widespread smaller amplitudes, edge effects are attenuated by nonlinear behavior, though they are still present. Waves inside the basin seem to travel at a slightly slower speed. This is visible at two points. First, the waves in the severe case that reach the West boundary at 4 s are a small distance behind the same wavefront in the linear case; and second, also at the last set of frames, while reflections from the North and South basin borders in the linear case are already reaching the center of the basin, the corresponding wavefront in the severe case is clearly behind.

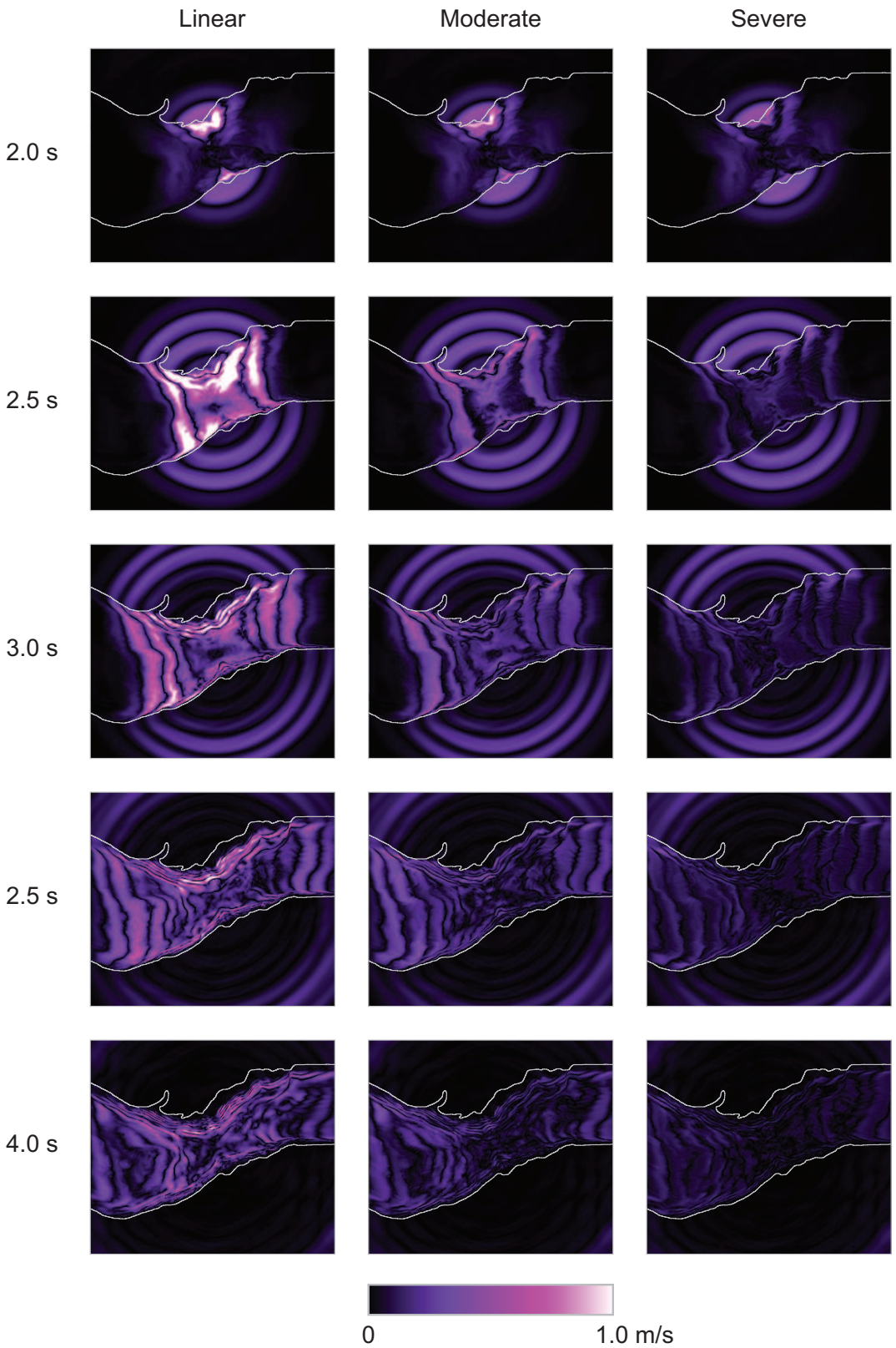

Figure 6.1: Comparison between snapshots of the surface magnitude of horizontal velocity of the linear, moderate nonlinear, and severe nonlinear cases at different times during the simulation.

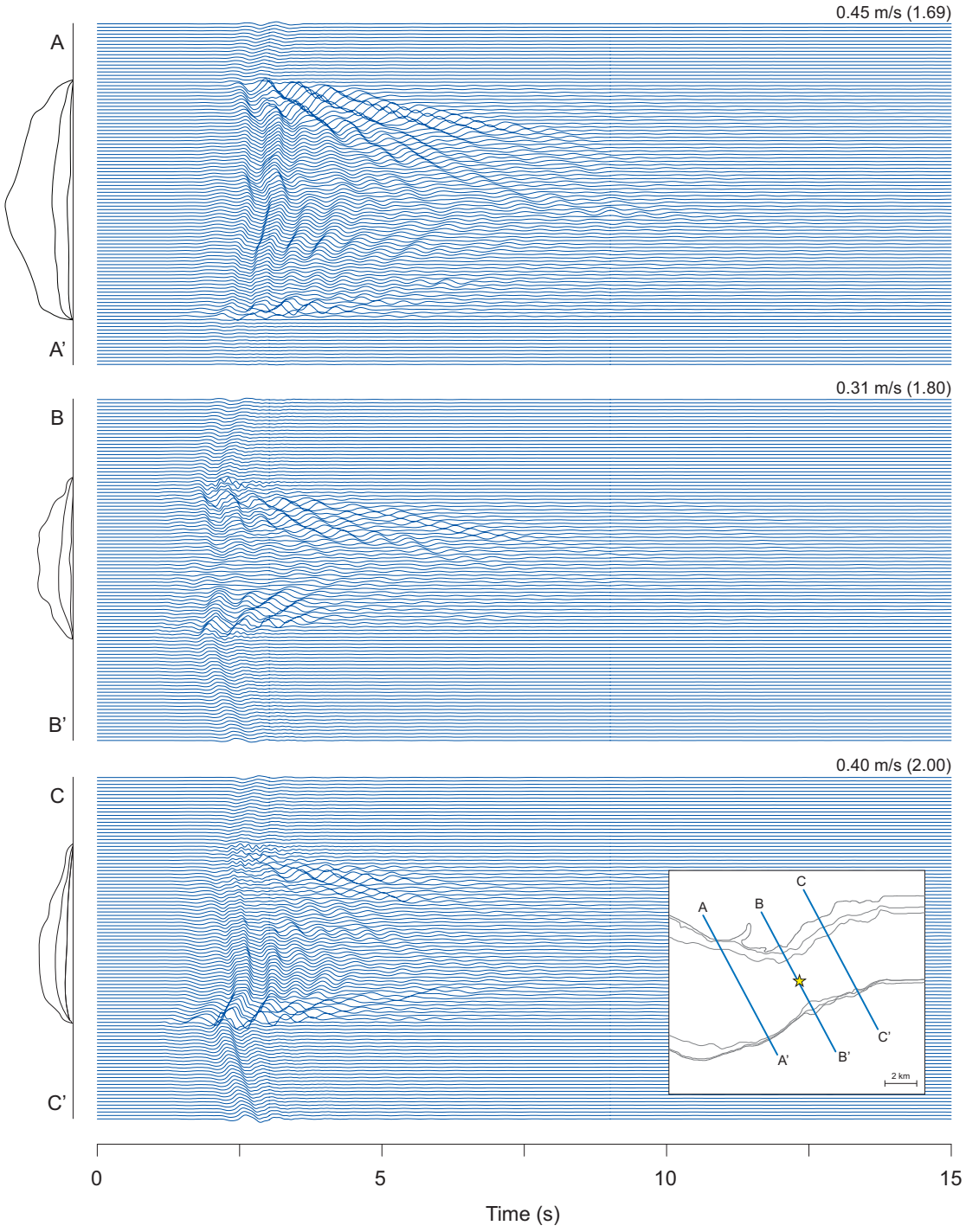

Figure 6.2: Particle velocities in the EW component of motion along three lines AA', BB' and CC' for the moderate nonlinear simulation. Soil-profile contours are shown to the left of each group. The values at the right on top of each group maximum peak velocity of each set and, in parenthesis, the ratio with respect to the linear case, or deamplification factor.

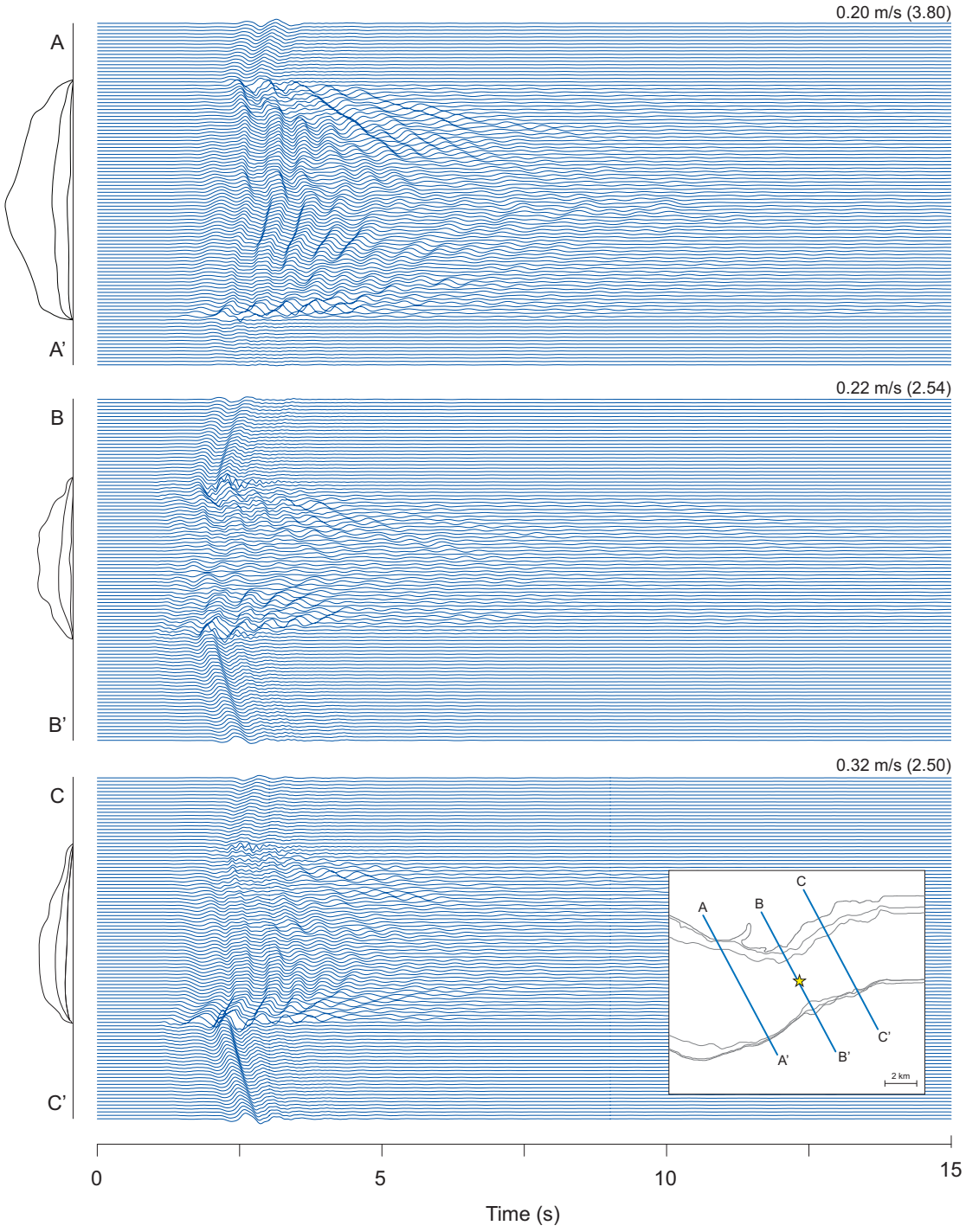

Figure 6.3: Particle velocities in the EW component of motion along three lines AA', BB' and CC' for the severe nonlinear simulation. Soil-profile contours are shown to the left of each group. The values at the right on top of each group maximum peak velocity of each set and, in parenthesis, the ratio with respect to the linear case, or deamplification factor.

Figures 6.2 and 6.3 show velocity traces in the EW component of motion along lines AA', BB' and CC' for the moderate and severe cases as previously done for the elastic case (Fig. 5.6). In general, we observe here the same basin effects as in the linear case. However, it is more evident in these figures that, with increasing level of plasticity, waves within the basin travel more slowly. This is particularly visible in the third front at the south border of the basin in line CC' (Fig. 6.3) in comparison with the corresponding wavefront in the linear case (Fig. 5.6). In addition, constructive interferences near the center of line BB' in the severe case are more significant than in the anelastic case. Also shown in Figs. 6.2 and 6.3 on the top-right corner of each set of synthetics are the peak value of each set and, in parenthesis, the ratio of this value with respect the peak value of the linear case for the same set of traces. These value are a local measure of the deamplification in velocity due to nonlinear effects. For the moderate case, the largest deamplification occurs along CC' where it reaches a value of 2. In the severe case, the largest deamplification occurs in AA' with a factor of 3.8. Notice also that in the two nonlinear cases, synthetics near the edges of the valley oscillate at a higher frequencies than in the linear case. We will review this in greater detail in the next section.

6.2.2 Peak Ground Response

Figure 6.4 shows a comparison between the linear and nonlinear cases for the horizontal peak magnitude of displacements, velocities, and accelerations at the surface of the basin. In velocities and accelerations, the smallest amplitudes occur for the severe nonlinear case, and the largest in the linear simulation. In displacements, however, the amplitudes near and around the center of the valley decrease from the linear to the moderate nonlinear case, but increase again for the severe nonlinear and are in fact, for the central strip of the basin, larger than in the linear case. It seems that, because the level of nonlinearity at the uppermost layer in the basin during the severe case is greater than in the moderate case, they have a more evident effect in terms of permanent deformation (away from the source) somewhere along the simulation and thus the effect on the peak response.

This might also be related to the location of the source. In these cases, the source being just beneath the basin, nonlinearities should be concentrated at the bottom of each deposit as the vertical transition of waves from stiffer to softer material amplifies the response, thus reaching the yield limit. A source located away from the valley and at a smaller depth would produce larger surface waves at the lateral transition into the basin, causing larger displacements near the free surface. In such a case, the vertical and spatial distribution of nonlinearities would change. A scenario like that would certainly help our understanding of nonlinear effects and should be a future case of study.

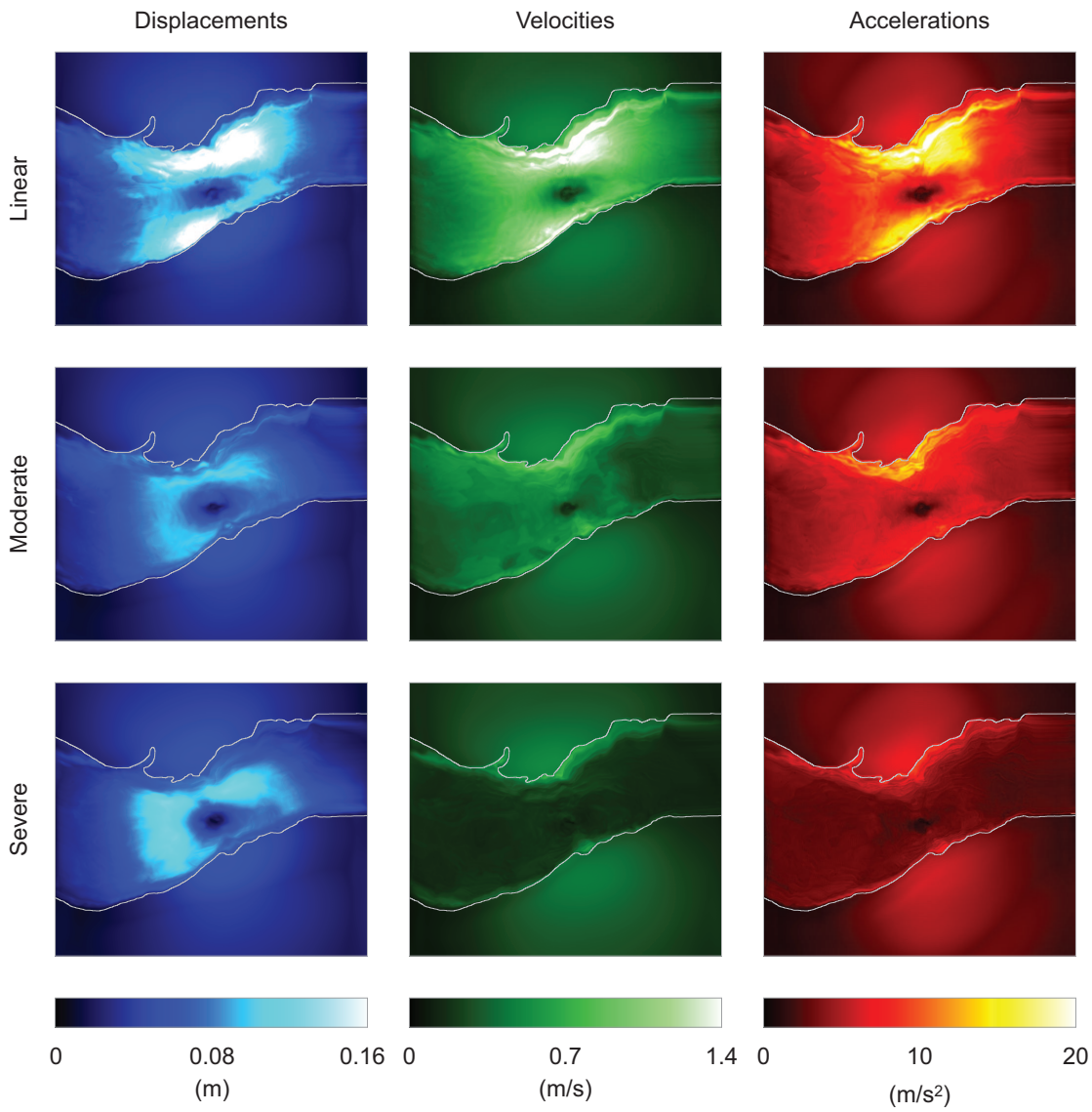

Figure 6.4: Comparison of the horizontal peak magnitude displacement (left), velocity (center), and acceleration (right) at the surface of the simulation domain between the linear (top), moderate nonlinear (middle), and severe nonlinear (right) cases.

6.2.3 Deamplification Effects

Figure 6.5 shows surface maps of deamplification factors of displacement, velocity, and accelerations. By *deamplification* we understand the reduction factor in the amplification expected at soft-soil deposits due to nonlinearities in the soil. Therefore, deamplification values larger than 1, imply a reduction, and inversely, values less than 1, imply an amplification in the response with respect to the linear case. This figure in particular, highlights the differences observed in the peak responses. Notice that in all three frames of the moderate nonlinear case, the factors indicate a reduction in

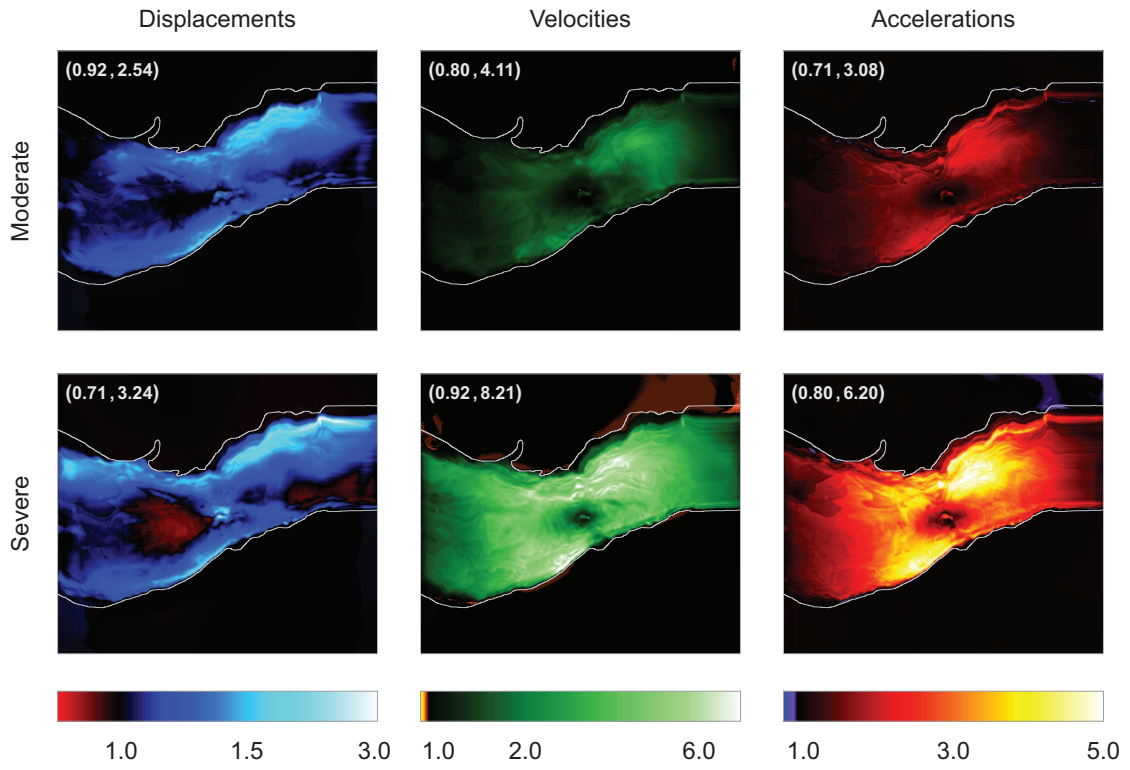

Figure 6.5: Deamplification factors of the moderate (top) and severe (bottom) nonlinear cases with respect to the linear simulation for the horizontal peak magnitude of displacements (left), velocities (center), and accelerations (right) at the free surface. In parenthesis at the left-top corner of each frame are the minimum and maximum value of each case.

the amplitude with respect to the linear case; whereas in the severe one there exist areas of larger peak response than that of the linear simulation. The largest amplifications of motion occur in the case of displacements west from the epicenter. Some other amplification in displacements is visible at the East. Both of these areas correspond to the deepest portions of the basin closer to the lakes (see Figs. 5.2b and 5.3b for reference).

In general, velocities and accelerations present only reductions with respect to the linear case. Only some minor amplifications occur outside and near the edges of the basin. In accelerations, the largest reductions occur NE and SW from the epicentral region and near the near the boundaries of the basin. In Velocities, these two areas are also dominant but there is a larger spatial variability.

The difference between each simulation along surface lines AA', BB', and CC' for the peak displacements, velocities, and accelerations is shown in Figs. 6.6 through 6.8 for the three components of motion. For the two horizontal directions, as before, peak velocities and accelerations in the severe nonlinear case are the lowest. Displacements, on the contrary, alternate between the linear and the two nonlinear cases. In the NS direction, both the nonlinear cases have lower peak values than

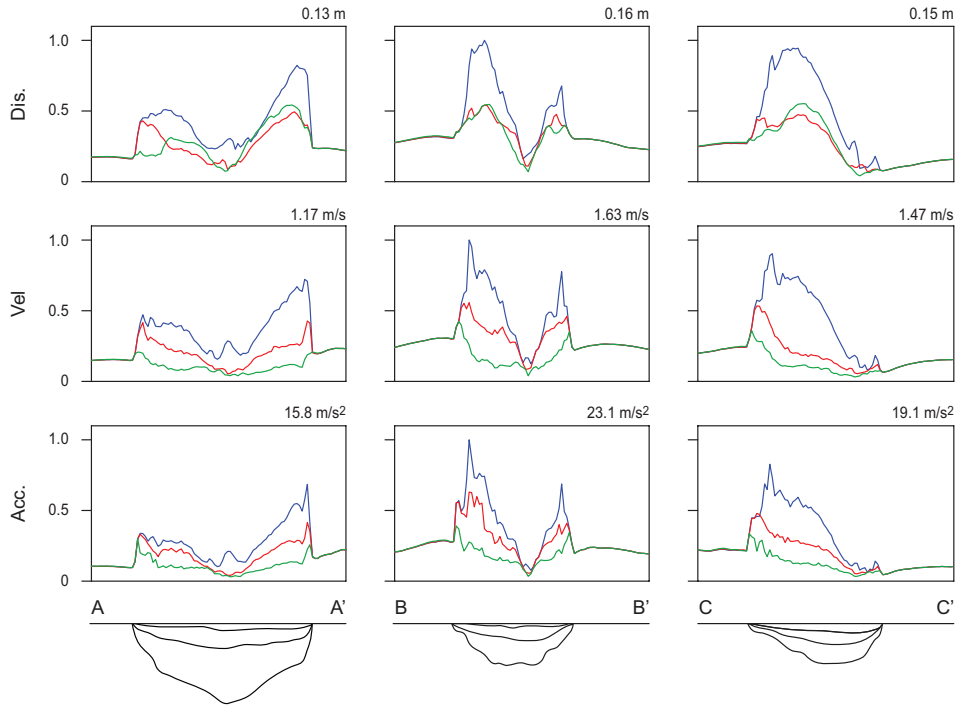

Figure 6.6: Comparison of peak displacements (top), velocities (middle), and accelerations (bottom) in the NS component of motion along lines AA', BB', and CC', between the linear (blue), moderate nonlinear (red), and severe nonlinear (green) cases. Each row is normalized with respect to the maximum value of the set and the largest value of the three curves in each frame is shown at the top. Contour lines of the soil profiles are included at the bottom.

the linear case, but there is no dominance of any of the two nonlinear cases over the other. In the EW direction, the severe nonlinear cases has almost always larger peak displacements than the moderate case, and in some portions (AA' and CC' towards the center) the severe nonlinear-case peak displacements are actually larger than the corresponding linear-case ones.

The effect of nonlinear soil behavior in the vertical response of the valley seems to be almost negligible. Except for the mitigation of edge effects in the North (left) boundary of the basin in line BB' (velocities and accelerations), all UD peak values in the three cases are almost the same. Only in CC' there is some minor amplification in the severe nonlinear case, visible in the displacements and accelerations. This might not be always the case. Sources at different locations or with different mechanisms may reflect larger evidence of nonlinear effects in the vertical motion of the ground.

6.2.4 Permanent Deformations

An important effect of nonlinear soil behavior and one that cannot be reproduced under conditions of pure elasticity is the occurrence of permanent displacements (away from the source, due to plastic

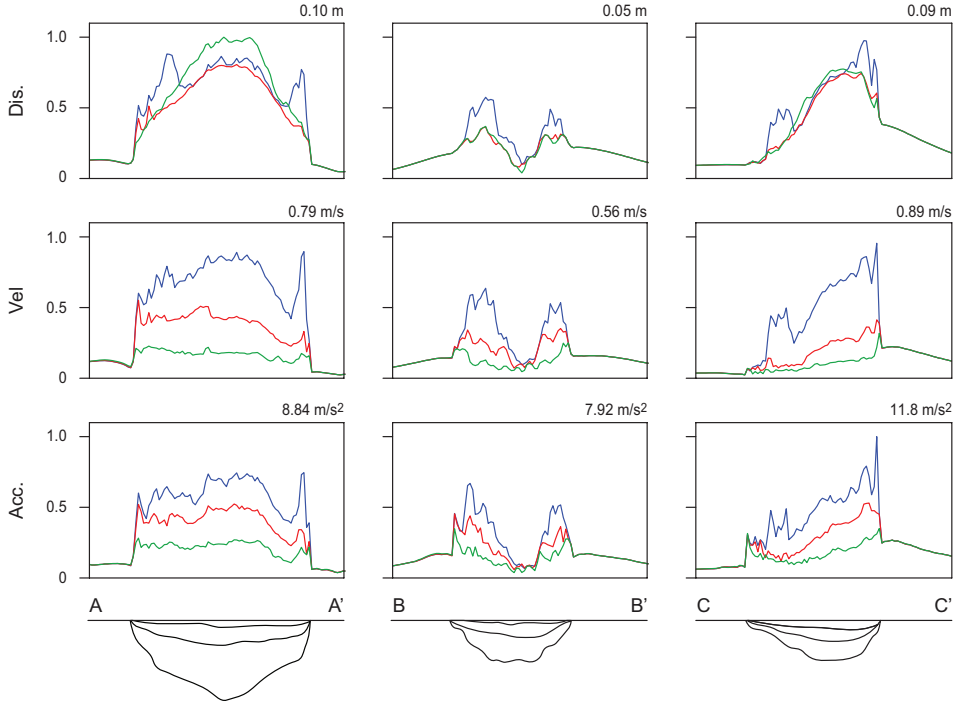

Figure 6.7: Same as Fig. 6.6 but for the EW component of motion.

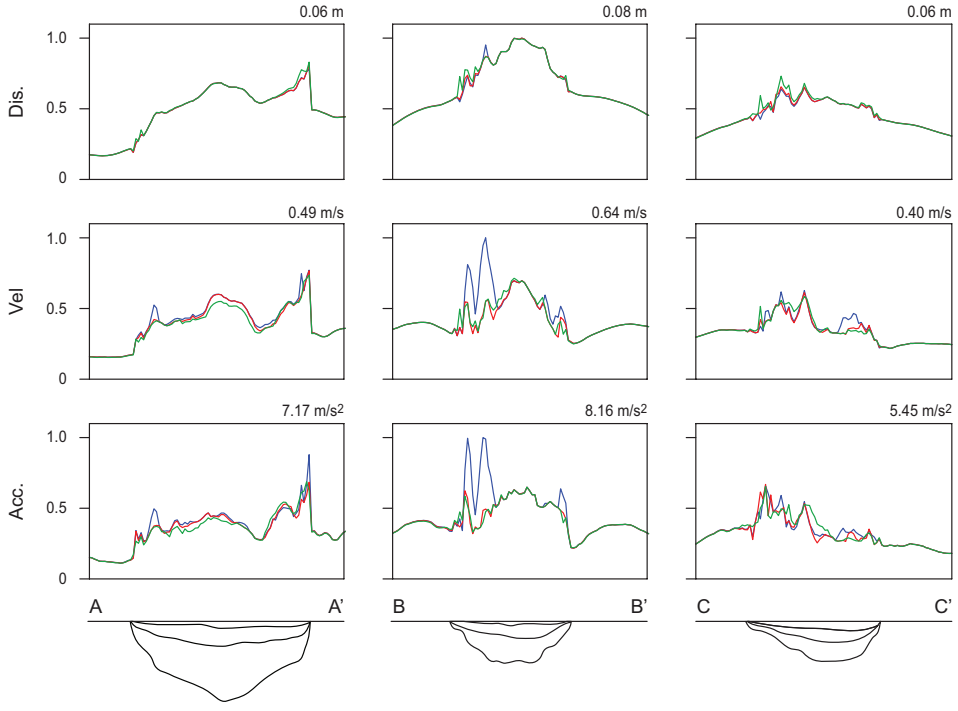

Figure 6.8: Same as Fig. 6.6 but for the UD component of motion.

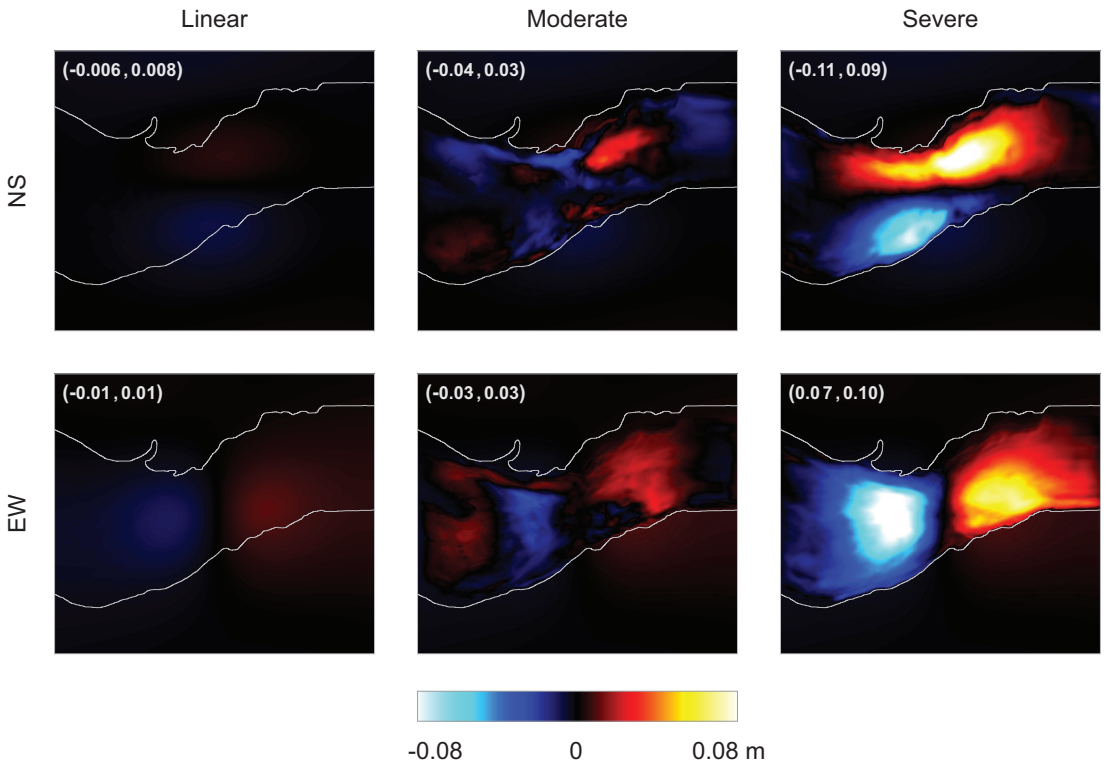

Figure 6.9: Comparison between the linear and nonlinear simulations for the final permanent displacement in the two horizontal components of motion.

deformation). Figure 6.9 shows a comparison between the linear and two nonlinear cases for the final permanent displacement in the two horizontal components of motion at the free surface. In the case of the linear simulation there exist some minor concentration of permanent deformation due to the nature of the source. This follows the typical pattern of radiation from a double couple. The situation is different in the two nonlinear simulations. In the severe case, the radiation patterns are still present but there is an obvious basin effect that concentrates larger permanent deformations toward the deepest portions of the basin and North and South boundaries. The values of these permanent deformations are of more than one order of magnitude larger than those of the linear case.

In the moderate nonlinear simulation, the permanent deformations are not as large but the spatial distribution is more chaotic and has less to no evident association with the radiation pattern of the source. Permanent displacements oscillate from negative to positive at both sides of the epicentral region and are not necessarily associated with the depth of the basin either. This is a clear departure from other studies limited to 2D analysis and are evidence of the importance of conducting 3D simulations considering nonlinear soil behavior.

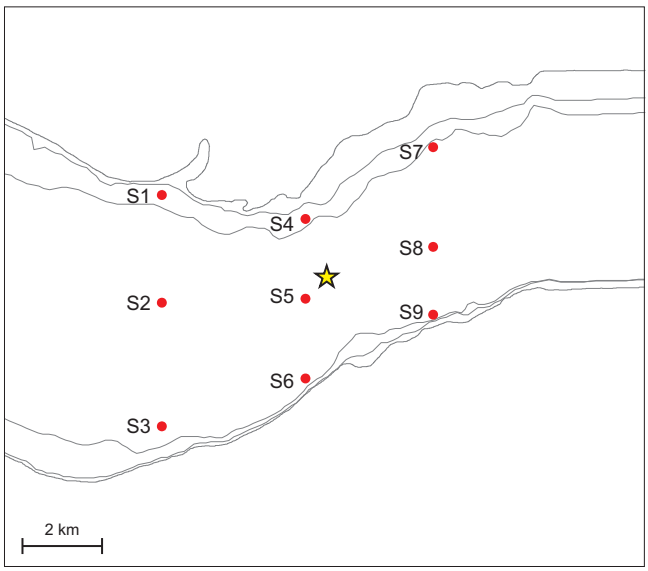

Figure 6.10: Location of the nine observation points (or stations) selected for comparison.

6.3 Local Effects

6.3.1 Observation Points

To evaluate the effects of nonlinear soil behavior at a local scale we analyze the ground motion at selected locations on the surface. Figure 6.10 shows the position of these observation points, or stations, on a horizontal projection of the edges of the basin layers. These points were arbitrarily chosen as representative of the general characteristics of potential basin and edge effects. Three of them are located near the North boundary, three in the middle at the deepest portion of the basin, and the last three near the South border. They are arranged from West to East, with a set in the center above the ridge that divides the two lakes' basins, with one station just about 1 km SW from the epicenter.

6.3.2 Time Synthetics

Figures 6.11 through 6.19 show a comparison of the synthetics of displacement, velocity, and acceleration for the linear, moderate nonlinear, and severe nonlinear simulations in all three components of motion for each station. The following observations can be made based on these comparisons.

In the case of the two horizontal components of motion, attenuation or deamplification of velocities and accelerations seems to be the general trend, with the severe nonlinear case showing the largest reductions in both cases. Displacements, however, are different. For some stations like S2

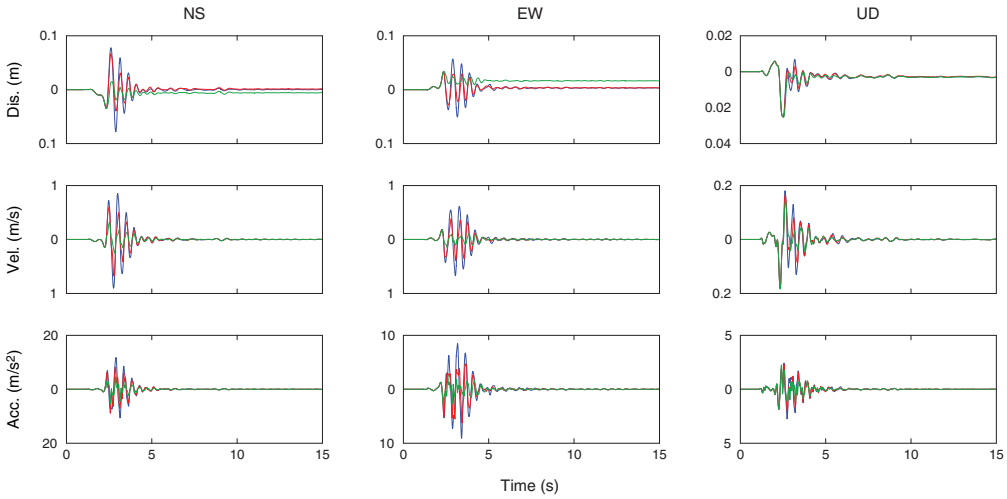

Figure 6.11: Comparison of time synthetics of displacement, velocity and acceleration at station S1 between the linear (blue), moderate nonlinear (red), and severe nonlinear (green) cases.

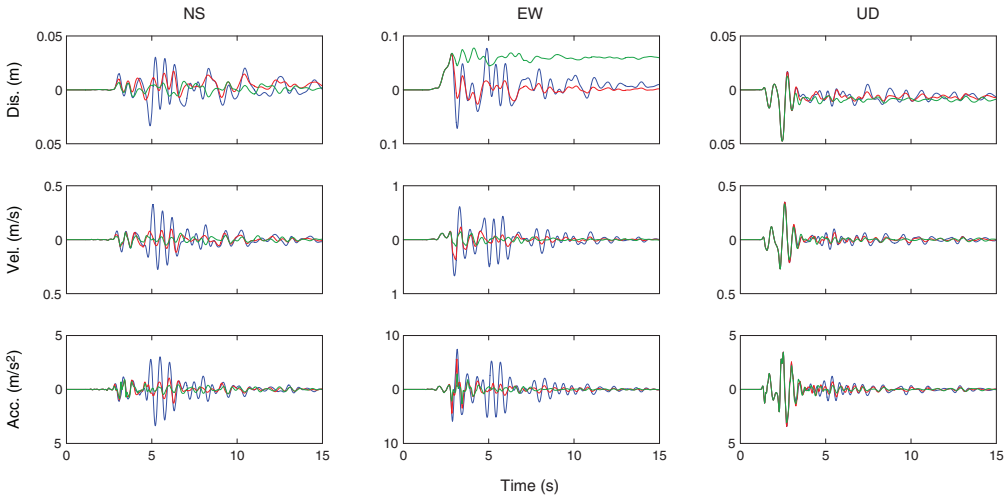

Figure 6.12: Same as Fig. 6.11 but for station S2.

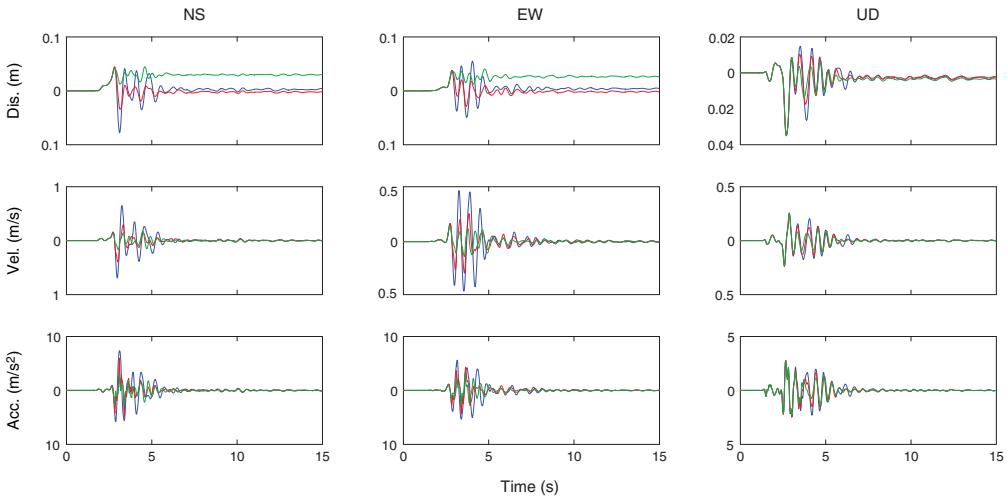

Figure 6.13: Same as Fig. 6.11 but for station S3.

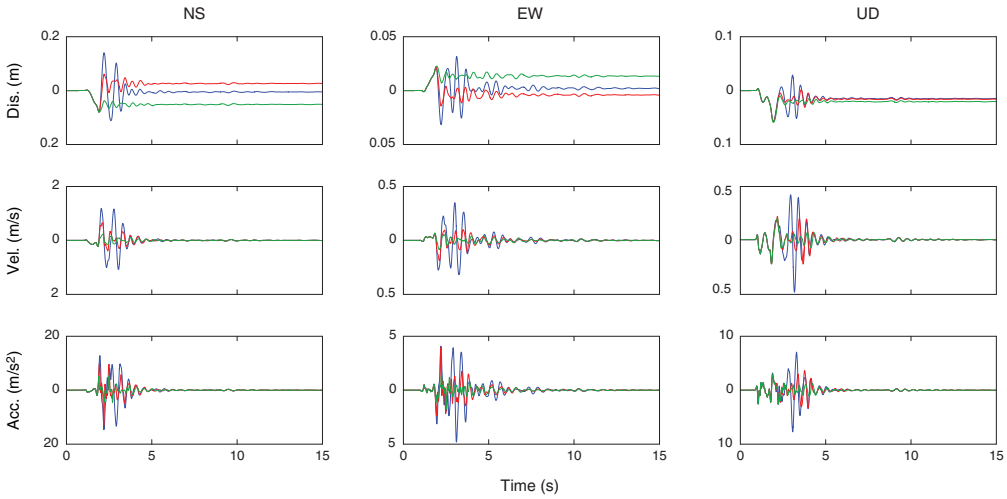

Figure 6.14: Same as Fig. 6.11 but for station S4.

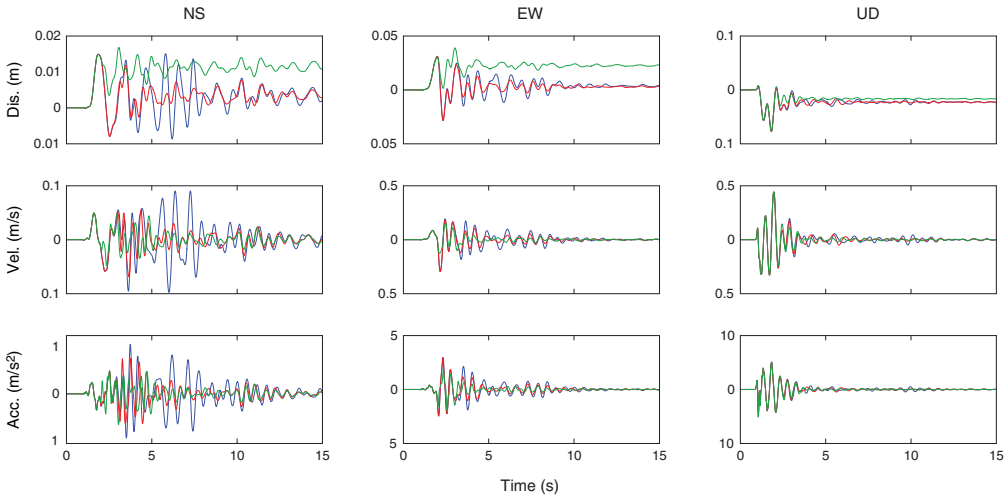

Figure 6.15: Same as Fig. 6.11 but for station S5.

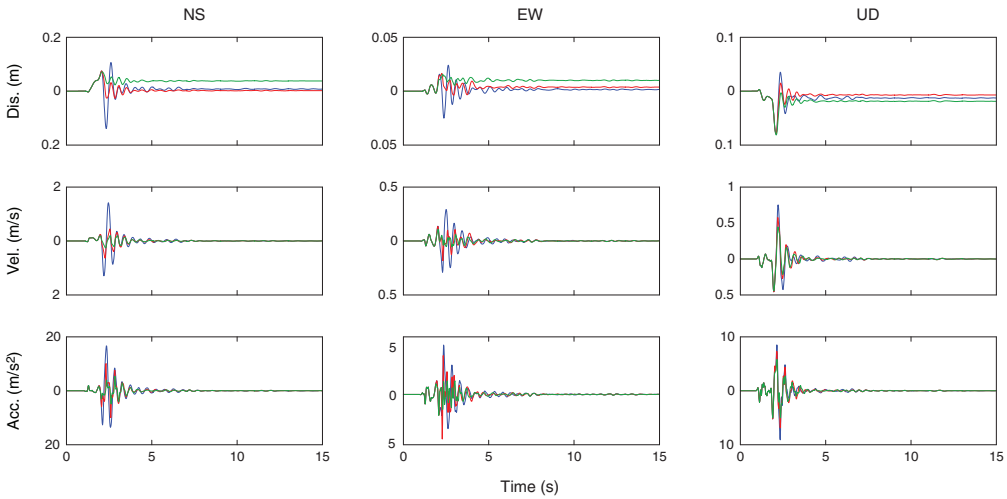

Figure 6.16: Same as Fig. 6.11 but for station S6.

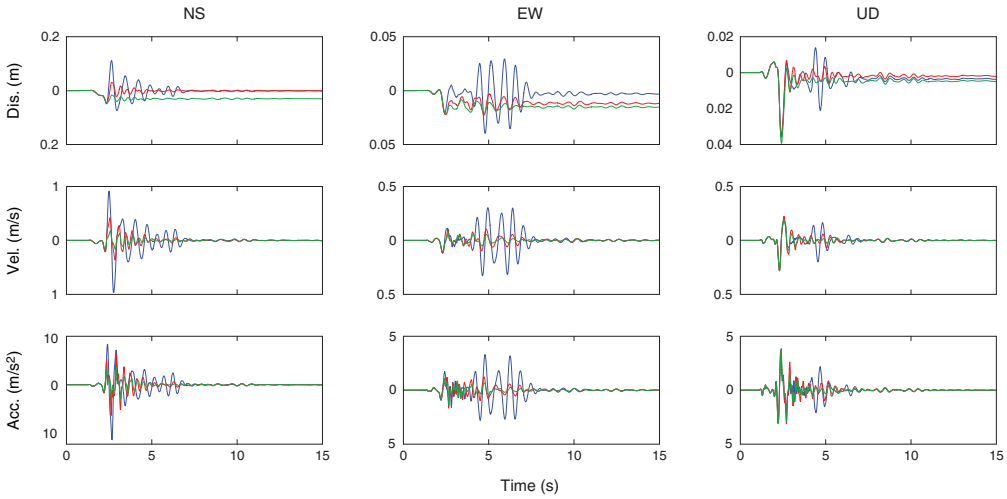

Figure 6.17: Same as Fig. 6.11 but for station S7.

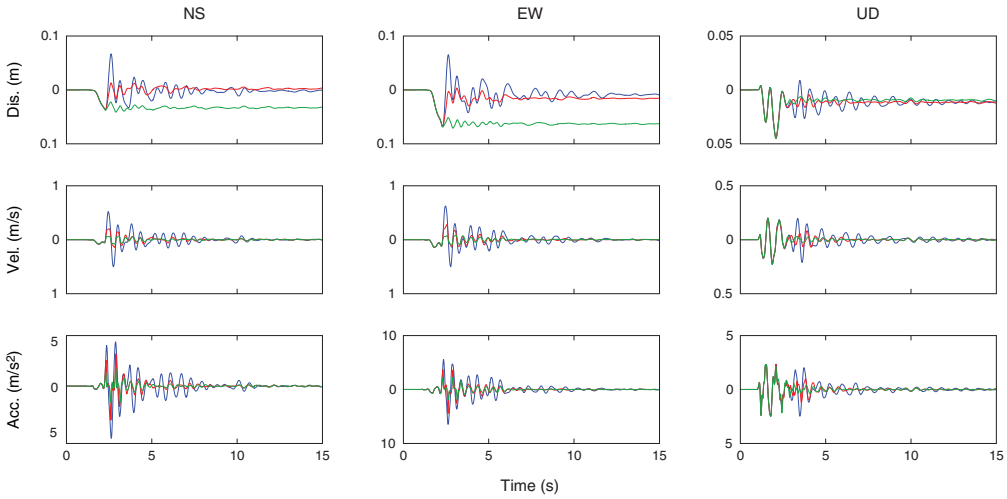

Figure 6.18: Same as Fig. 6.11 but for station S8.

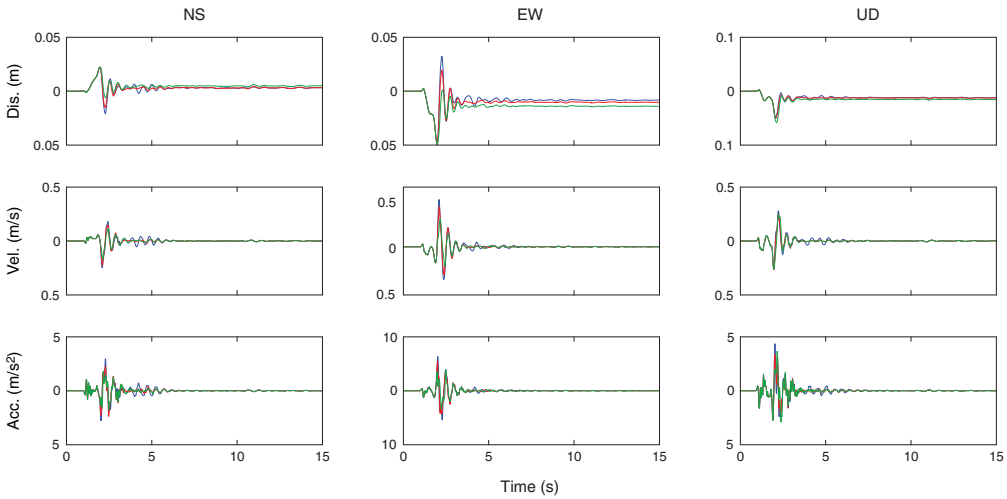

Figure 6.19: Same as Fig. 6.11 but for station S9.

(EW) and S5 (both components), peak displacements are larger in the severe nonlinear case than in the moderate one. In addition, displacements exhibit permanent deformation characteristic of nonlinear behavior, especially for the simulation with severe nonlinearities, but also present in some stations (S3, S4, S7) for the moderate case.

Curiously, permanent deformations do not always occur in the same direction for the two different nonlinear synthetics. In stations S3 and S4, for example, permanent deformations in the horizontal component of motion switch signs from the moderate to the severe nonlinear cases. We believe that this is a phenomenon that can only be modeled with full 3D simulations, but is something that would require further research for a complete understanding.

The case of the vertical component of motion evidences little to no effect from the nonlinear behavior of the soil, except for stations S4, S7, and S8. These stations are located to the North and Northeast of the epicentral area. The changes in their responses seem to be associated with surface waves produced at the edges of the basin. Notice that the first set of fluctuations is almost identical to that of the linear case, and it is only in a second train of waves that differences become more evident, to the point of almost completely attenuating the vertical motion.

In terms of time, most changes due to nonlinearities seem to occur within the first 5 seconds of simulation. Only stations S5 (NS) and S7 (EW) show indications of nonlinearities occurring after this time-window. In the case of station S5, this being in the NS component of motion, it is possible to think that it happens because of the confluence and constructive interference of wavefronts coming back from the North and South edges of the basin. In the case of S7, this should be the effect of surface waves originated at the shallower and more extensive portion of the valley in that area of the basin.

6.3.3 Fourier Analysis

Another relevant aspect of nonlinear effects is the change in the frequency content of the ground motion due to abrupt changes in the stress-strain path, or transitions from the linear range to plastic flow and vice versa. The specific case of stress-strain curves as implicit functions of time will be analyzed in the next section, but the consequences of these transitions can be first observed in the frequency domain for the signals at the stations. Figures 6.20 through 6.28 show the amplitudes of the Fourier transform of velocities in the three components of motion for each selected location and the spectral ratios of the transforms of the two nonlinear cases with respect to the linear simulation.

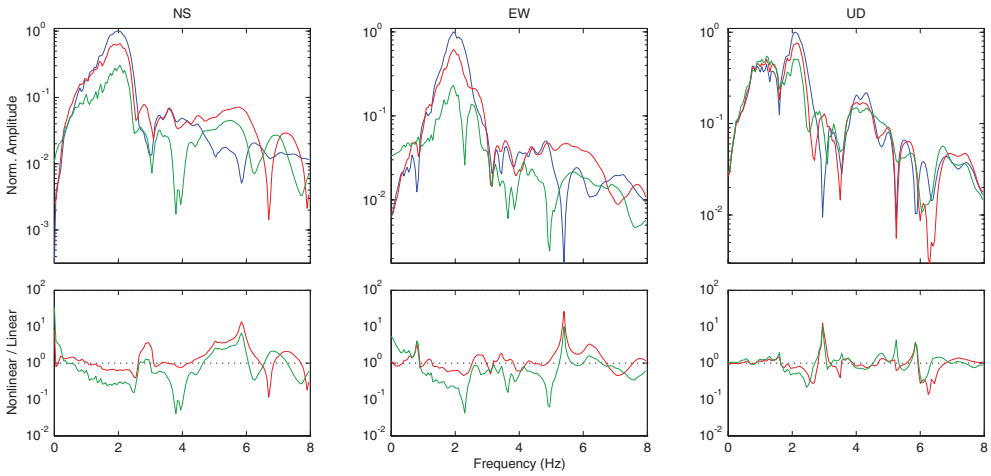

Figure 6.20: Comparison for station S1 between the linear (blue), nonlinear moderate (red), and nonlinear severe (green) cases for the amplitude of the Fourier transform of velocities in each component of motion normalized with respect the linear results (top); and spectral ratios between the nonlinear and the linear spectra (bottom).

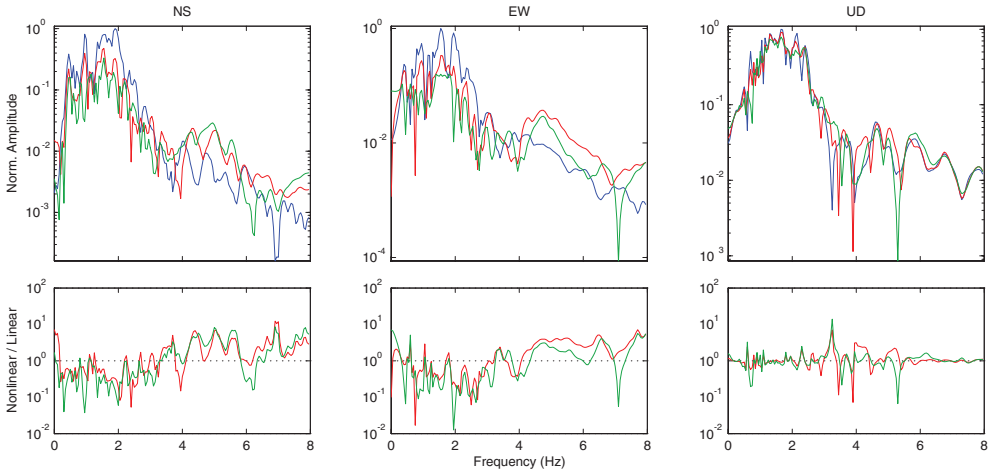

Figure 6.21: Same as Fig. 6.20 but for station S2.

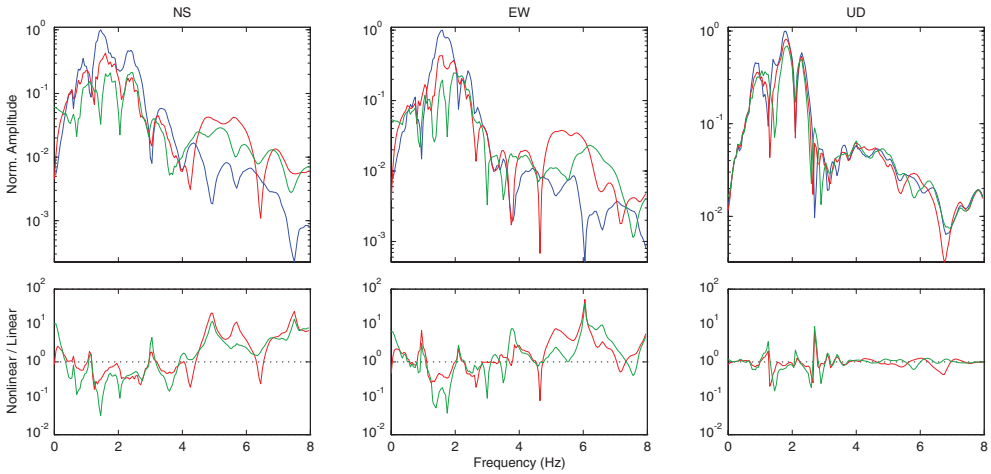

Figure 6.22: Same as Fig. 6.20 but for station S3.

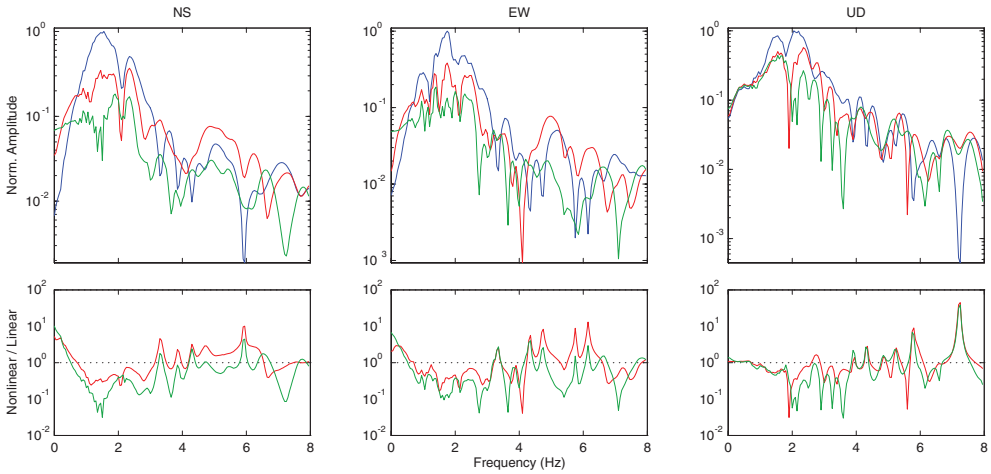

Figure 6.23: Same as Fig. 6.20 but for station S4.

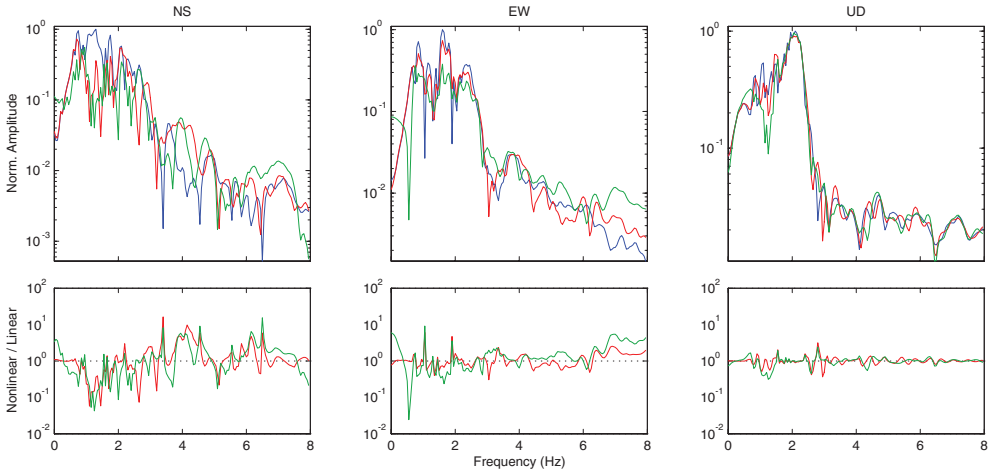

Figure 6.24: Same as Fig. 6.20 but for station S5.

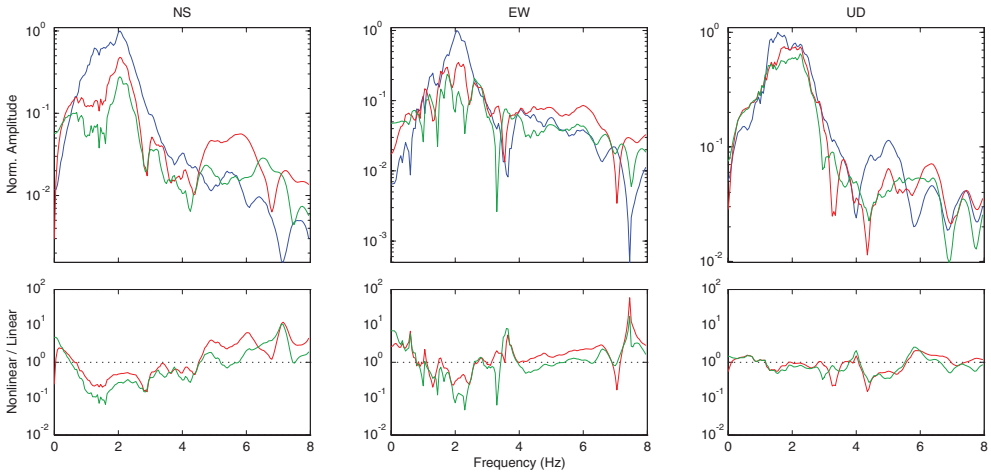

Figure 6.25: Same as Fig. 6.20 but for station S6.

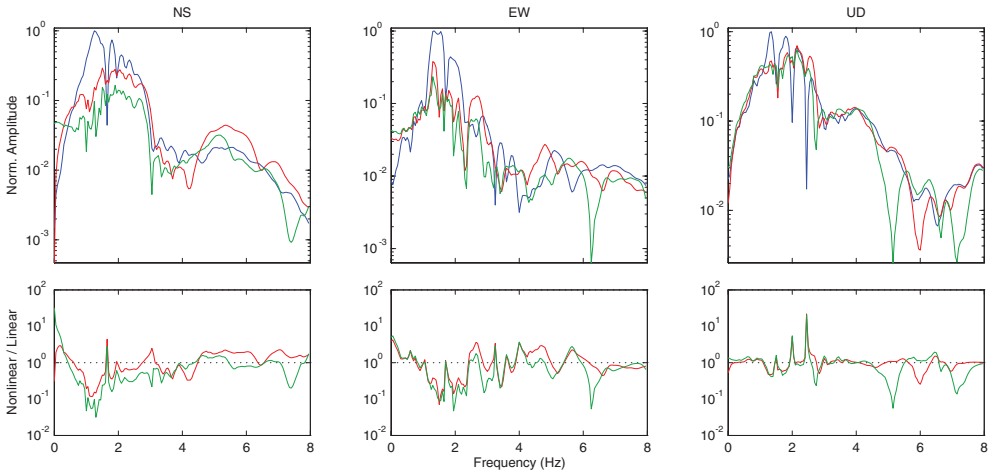

Figure 6.26: Same as Fig. 6.20 but for station S7.

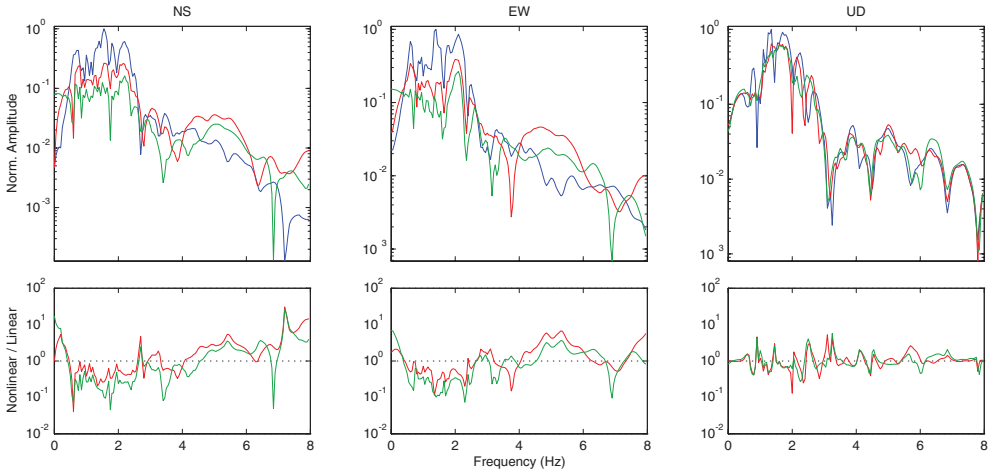

Figure 6.27: Same as Fig. 6.20 but for station S8.

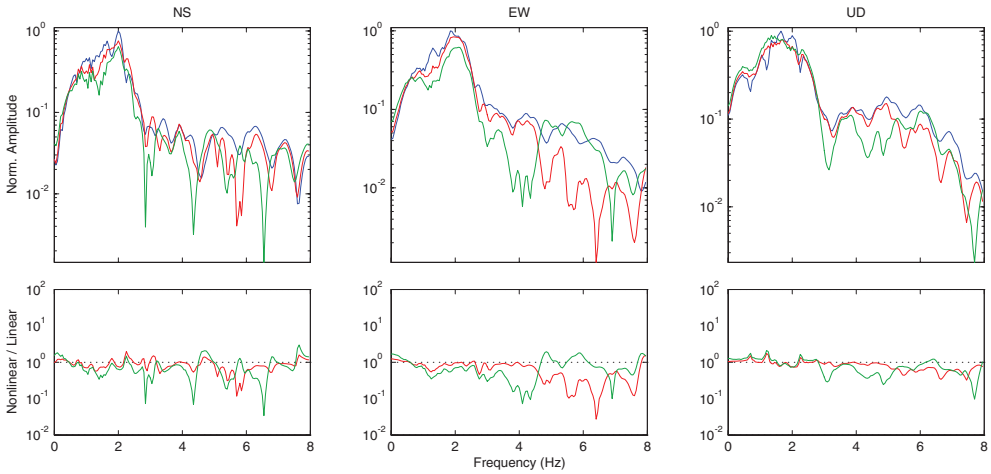

Figure 6.28: Same as Fig. 6.20 but for station S9.

Although the mesh for the simulations is (in principle) valid only up to 4 Hz, in Figs. 6.20 to 6.28 we have set the frequency axis range up to 8 Hz to observe the possible presence of increased higher frequency content. We consider this to be valid given that, because of the 2-to-1 constraint of continuity imposed in the mesh, we know the results are valid beyond the maximum frequency set at the simulation parameters.

Here we observe further evidence of the effect of nonlinearities in forms that are typical in strong-ground motion analysis, namely, deamplification of low-frequency energy and increasing high-frequency content. With the exception of S1 and S9, all other cases in the NS component of motion present a decrease (ratios < 1) in the spectral amplitude between 0.5 and 3 Hz. Of these cases, except for S6, the remaining stations also present an increase in the amplitudes (ratios > 1) for frequencies higher than 4 Hz. The situation is the same for the EW component of motion, for which all but stations S1, S5 and S9, present a decrease in energy content between 1 and 3.5 Hz, approximately, and an increase in higher frequencies for stations S2, S3, S4 and S8. Although no clear distinction can be made between the two nonlinear cases, it is evident that this behavior is present in both and it is noteworthy that in some cases the energy increase in higher frequencies is larger for the moderate nonlinear case than for the severe one (e.g., stations S1, S4, S6).

In the vertical component of motion only station S4 seems to have an increase in frequencies above 5 Hz and a deamplification between 1 and 4 Hz. All other ratios in the UD component remain close to unity, and in station S9 tend to decrease beyond 3 Hz. This is in agreement with observations made on the time synthetics, where little to no effect of nonlinearities was detected.

6.4 Stress-Strain and Yield Histories

6.4.1 Stress-Strain Relationships

We now focus on the stress-strain histories at the same selected locations but at different depths. For that we have stored data every 25 m in downhole-like arrays beneath each station until reaching bedrock ($V_s = 2600$ m/s). The results are shown in Figs. 6.29 through 6.37. In these figures, points for which stress-strain curves have been omitted (marked with empty dots) remained within the elastic range during the entire simulation. On the other hand, solid dots are points of interest either because they did exhibit plastic deformation or because they are at the free surface or at a transition from stiffer to softer material.

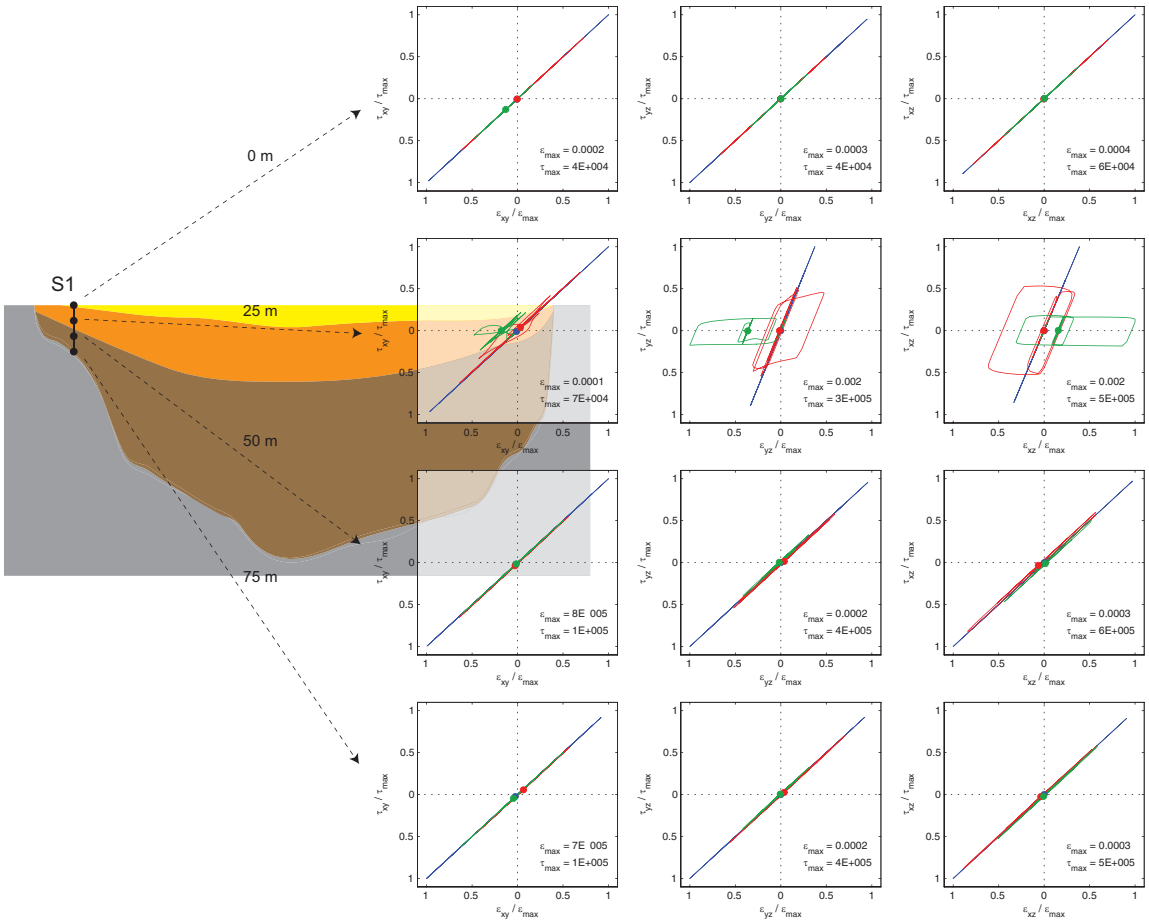

Figure 6.29: Stress-strain relationships as implicit functions of time for the downhole observation points beneath station S1. Blue lines correspond to the linear case, red and green correspond to the moderate and nonlinear cases, respectively. Solid dots indicate the final state of stresses and strains.

As would be expected, in all points where plastic flow occurs for the moderate case, inelastic excursions are also present for the severe nonlinear simulation. In general, these plastic deformations are larger for the severe case. However, at station S8 (25 m depth) strains are larger for the moderate case than for the severe one. It seems that at this particular location, in the first moderate case the lower layers remained elastic and plasticity occurred at a larger scale at the transition from the $V_s = 350$ m/s to the $V_s = 200$ m/s deposits, whereas in the severe case, larger amounts of energy were dissipated first by the deeper deposits.

For the most part loops are well shaped and characteristic of the no-hardening condition of the constitutive model, i.e., flat at yield as in elastic-perfectly-plastic materials. This also indicates that the deformation was well defined in or dominated by a particular component of motion (as in uniaxial or pure shear tests). Nonetheless, some station points such as S1(xy 25 m), S2(xy, xz 25 m), S6(yz 25 m) and S7(yz 50 m) exhibit irregular curves with complicate interactions between

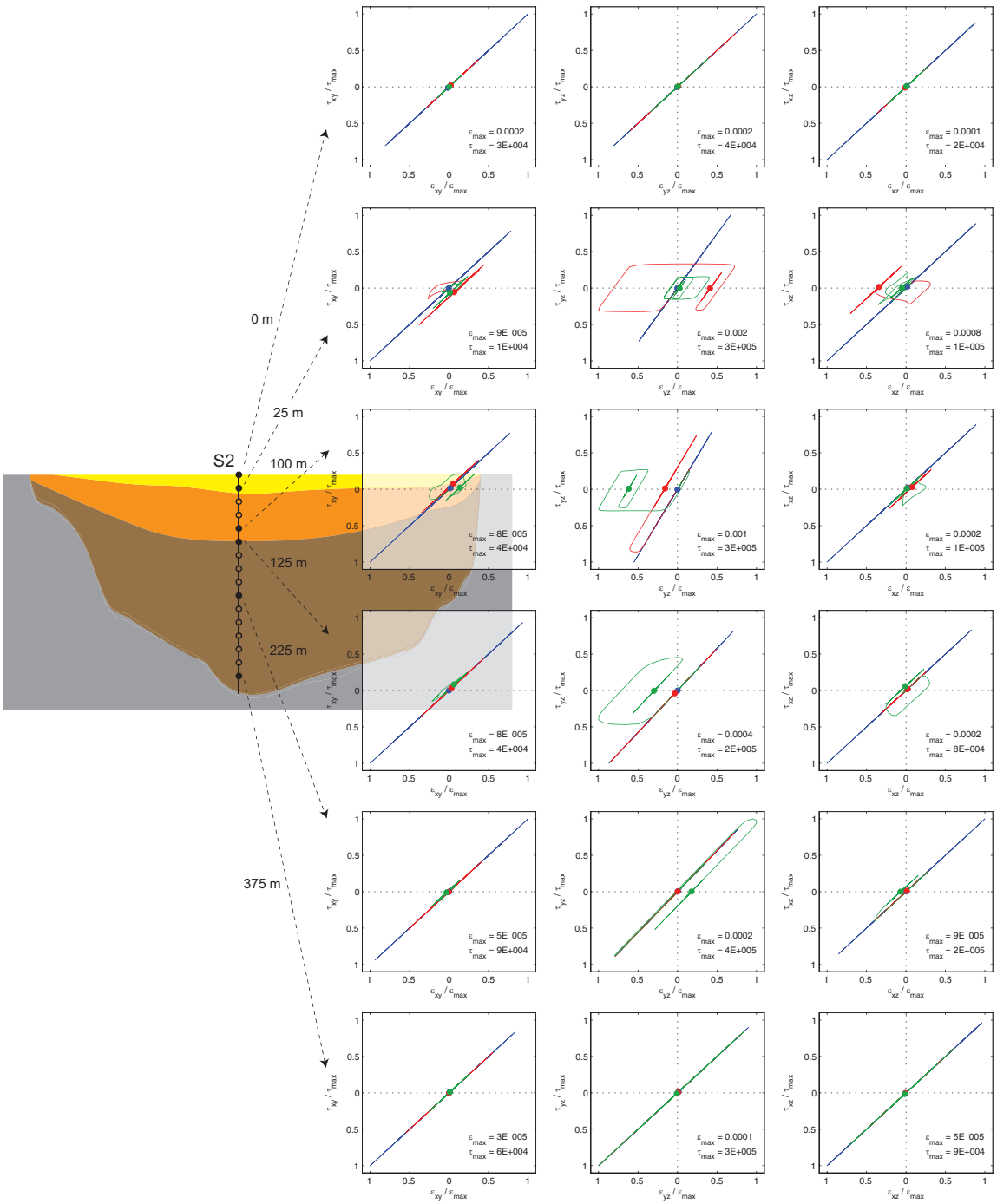

Figure 6.30: Same as Fig. 6.29 but for downhole points at station S2.

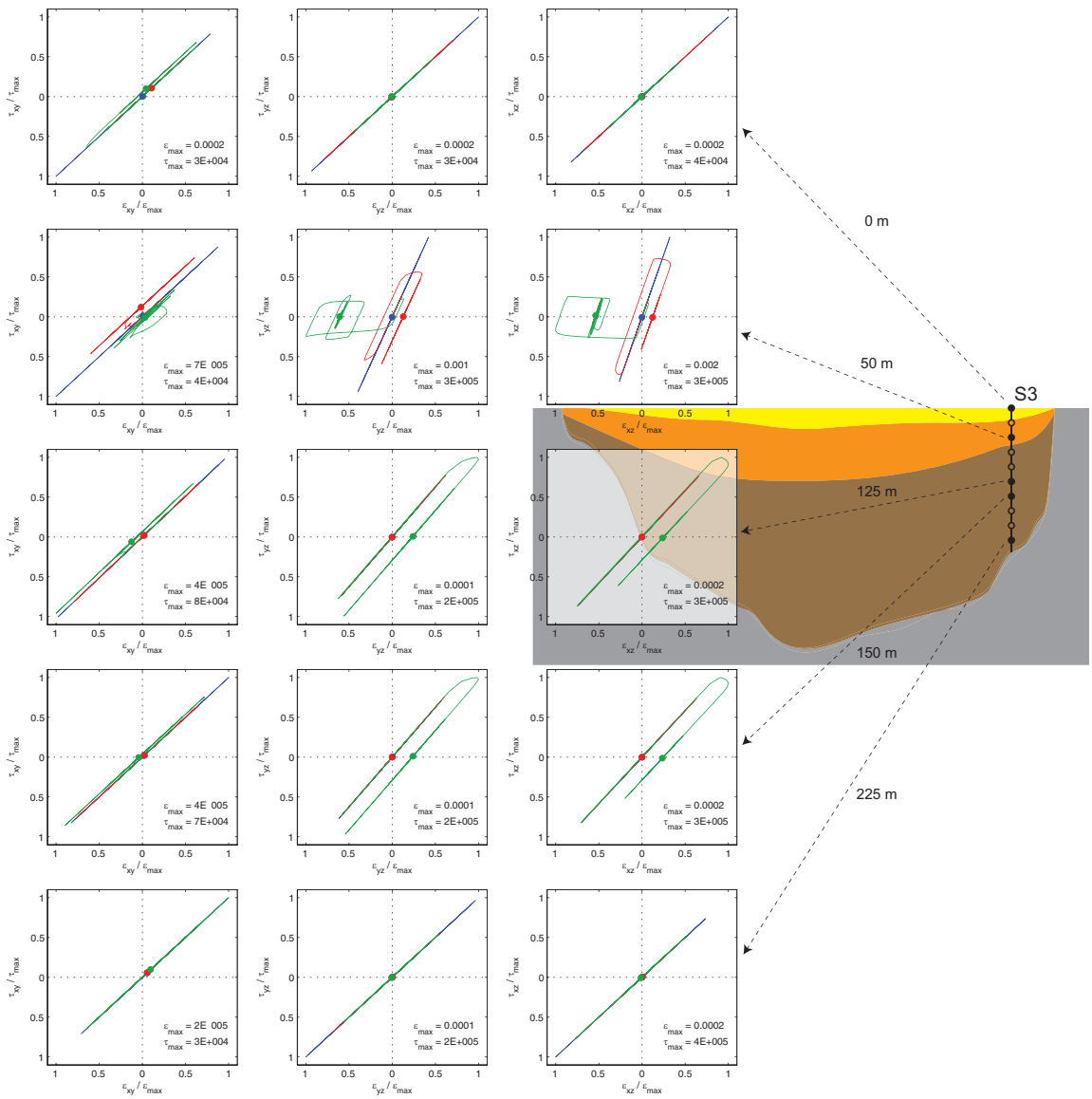

Figure 6.31: Same as Fig. 6.29 but for downhole points at station S3.

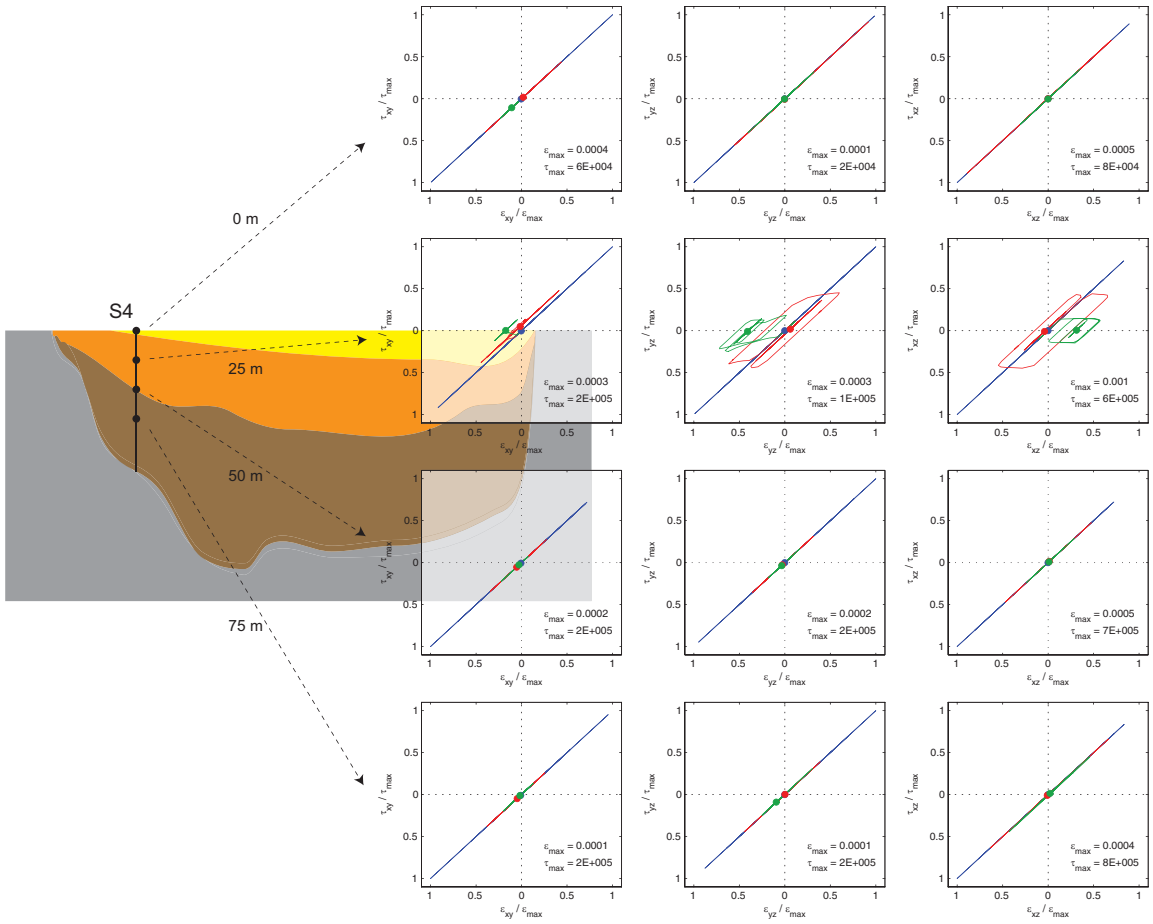

Figure 6.32: Same as Fig. 6.29 but for downhole points at station S4.

the three (xy, yz, xz) components of the shear stress and strain tensors. We believe these more elaborate stress paths corroborate the evidence of more complex 3D effects not usually visible in simplified 2D simulations.

In addition, although most plastic excursions occur at the upper two layers (V_s = 200 and 350 m/s), it is difficult to observe a dominant relationship with depth or with the transitions from stiffer to softer layers, as it is commonly shown in 2D nonlinear simulations under vertically incident waves or with 1D (soil-column) approximations. The only downhole array which exhibits that kind of 'typical' behavior is that of station S8, where all the larger plastic excursions occurred right above each layer's transition. On the opposite side of things, the clearest example of the lack of a clear pattern is the array at station S3. Here, the point at depth 225 m just at the transition from the bedrock to the base of the basin remains elastic and some plastic excursions occur halfway through the V_s = 650 m/s layer. Another 'irregular' behavior is that of station S2, where there is no plastic

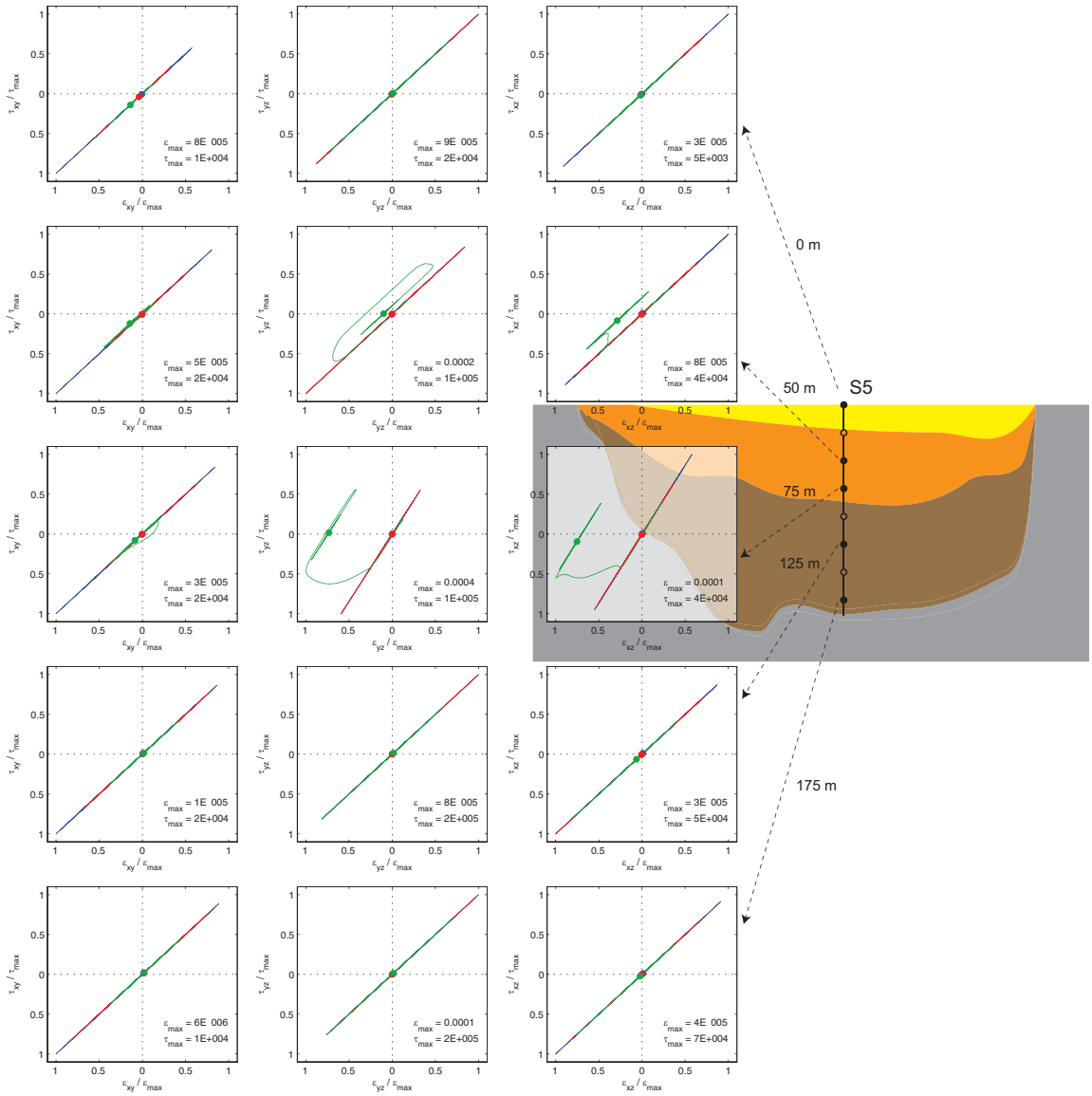

Figure 6.33: Same as Fig. 6.29 but for downhole points at station S5.

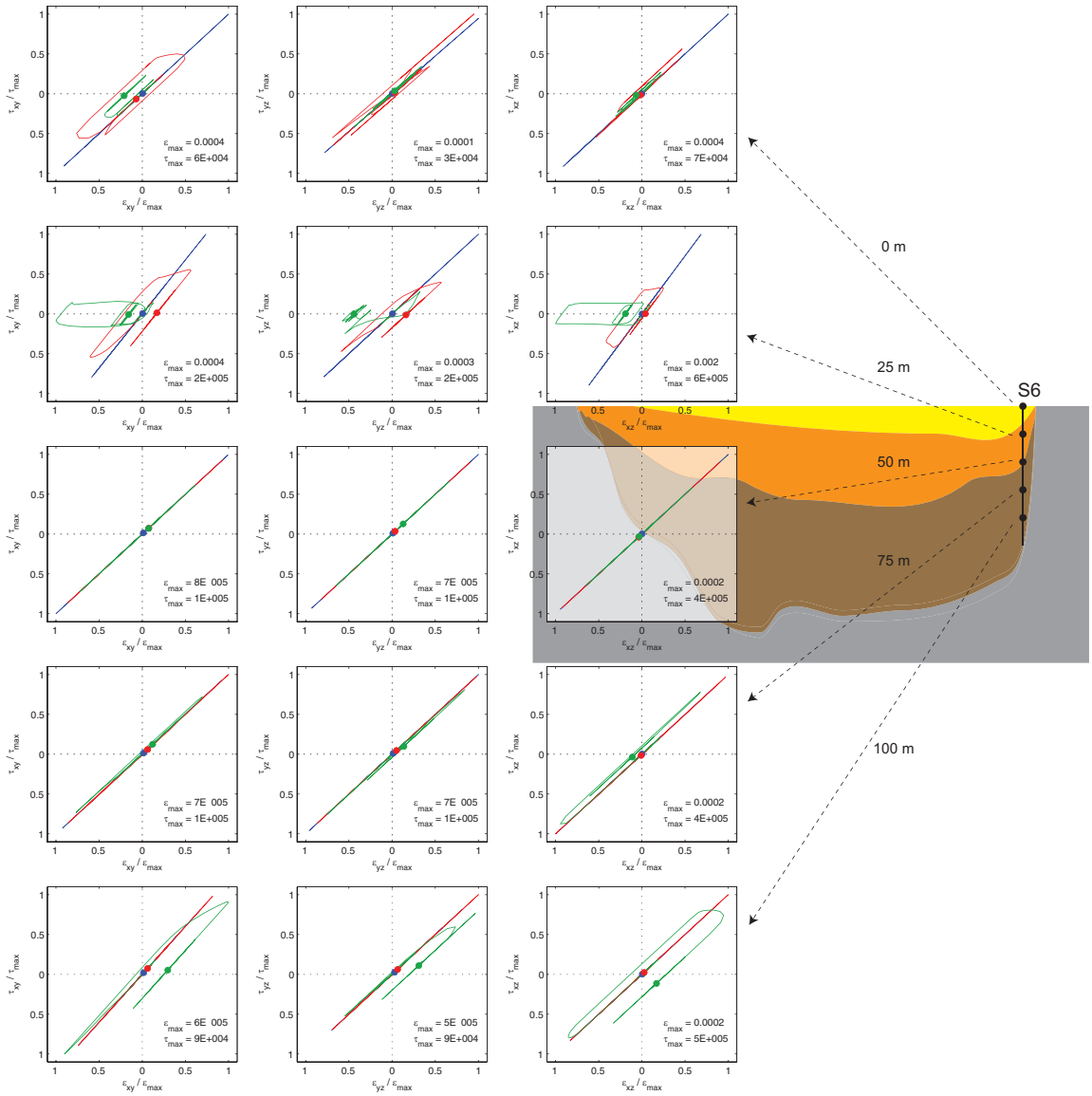

Figure 6.34: Same as Fig. 6.29 but for downhole points at station S6.

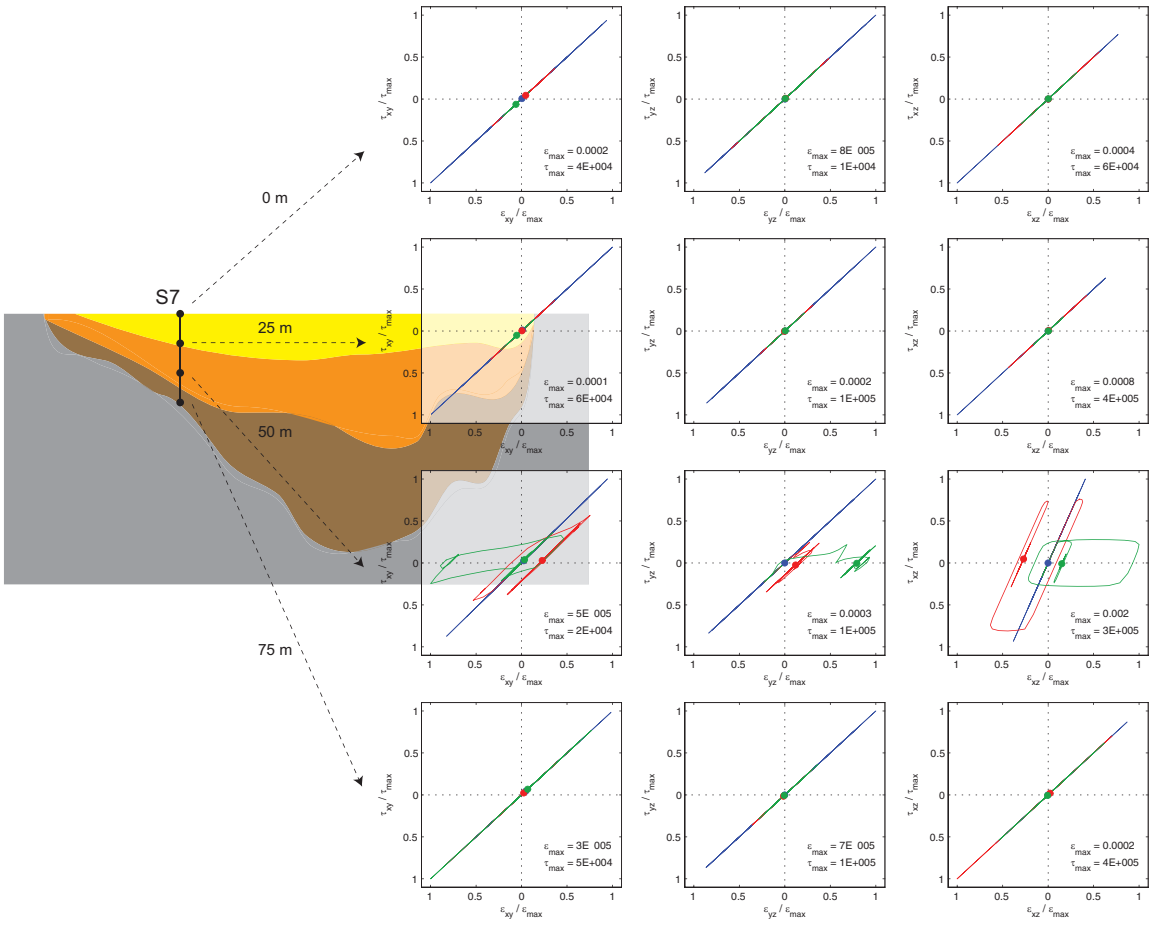

Figure 6.35: Same as Fig. 6.29 but for downhole points at station S7.

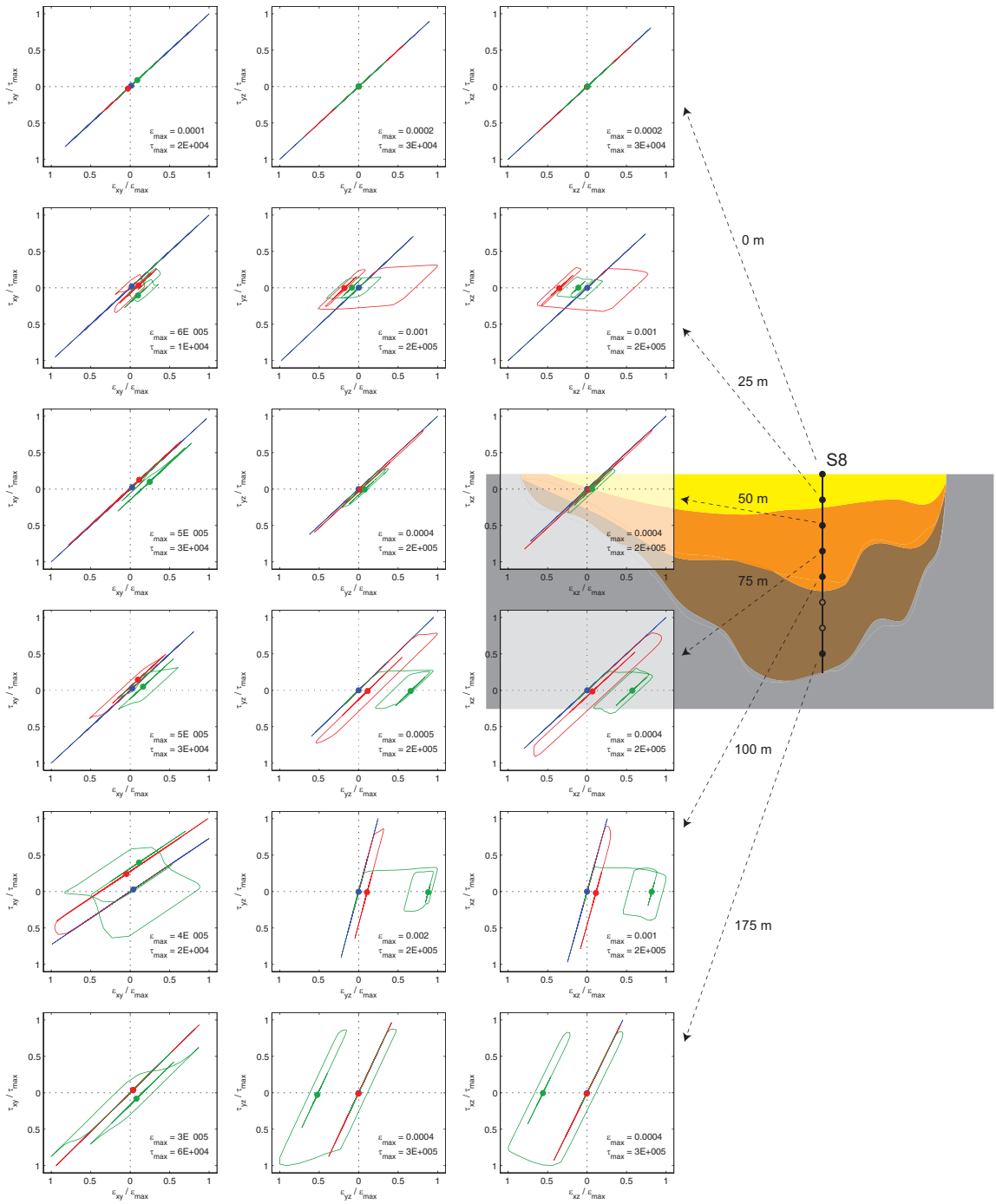

Figure 6.36: Same as Fig. 6.29 but for downhole points at station S8.

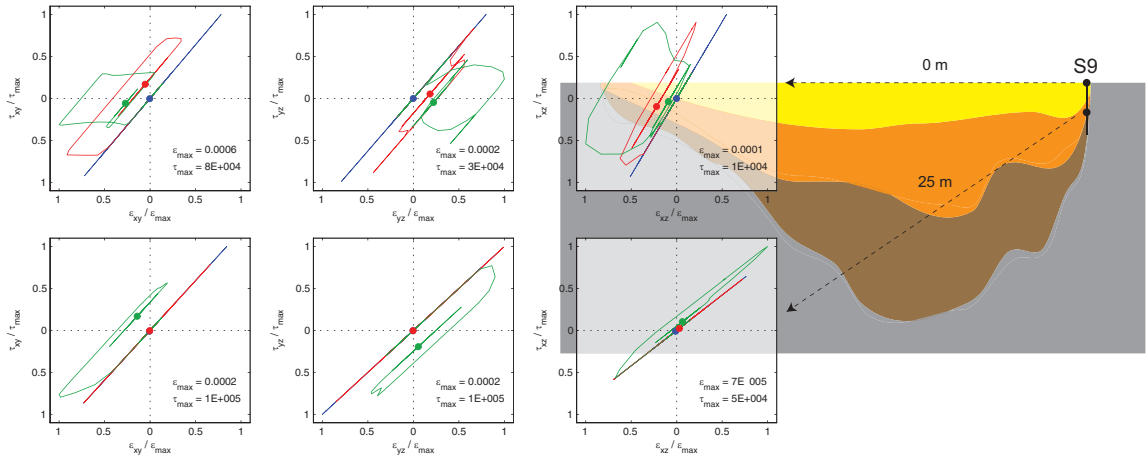

Figure 6.37: Same as Fig. 6.29 but for downhole points at station S9.

deformation at 200 or 250 m, but there is a minor plastic flow just in between, at 225 m. The same happens at points S4(25 m) and S7(50 m).

In terms of their hysteretic behavior and energy dissipation, most of the upper layer stress-strain loops are two-sided with larger enclosed areas than the predominantly one-sided curves at the bottom layer transitions. This may be as a result of the larger number of oscillations near the top because of surface waves, where as at the bottom of the basin, the motion is dominated by the source slip. Most of the curves also seem to indicate that the plastic flow occurred only for a limited period of time, after which the material remained elastic.

6.4.2 Yield Histories

To better understand the timing of the plastic excursions we now study the yield as a function of time. Figs. 6.38 and 6.39 show the history of the yield function $F(\sigma)$ in contrast with the yield limit set for each case (see Table 6.1) for the most representative points—those with the largest plastic deformations—of the downhole arrays of each station. From these figures it follows that the plastic excursions occur within 2 and 4 seconds of simulation, beyond which the system remains elastic, though having suffered permanent deformation. Plastic excursions occur at the instant $F(\sigma)$ reaches or flattens near the yield limit k, shown as a dotted line.

Note that the red and green lines corresponding to the moderate and severe nonlinear cases of $F(\sigma)$ never actually equal k. That is because of our selection of the strain sensitivity factor m in the power law (3.11), as seen in Section 3.1.2. For our simulations we have used $m = 0.05$. Should we have opted for a smaller value (e.g., $m = 0.01$), $F(\sigma)$ would get closer to k as in the rate-independent

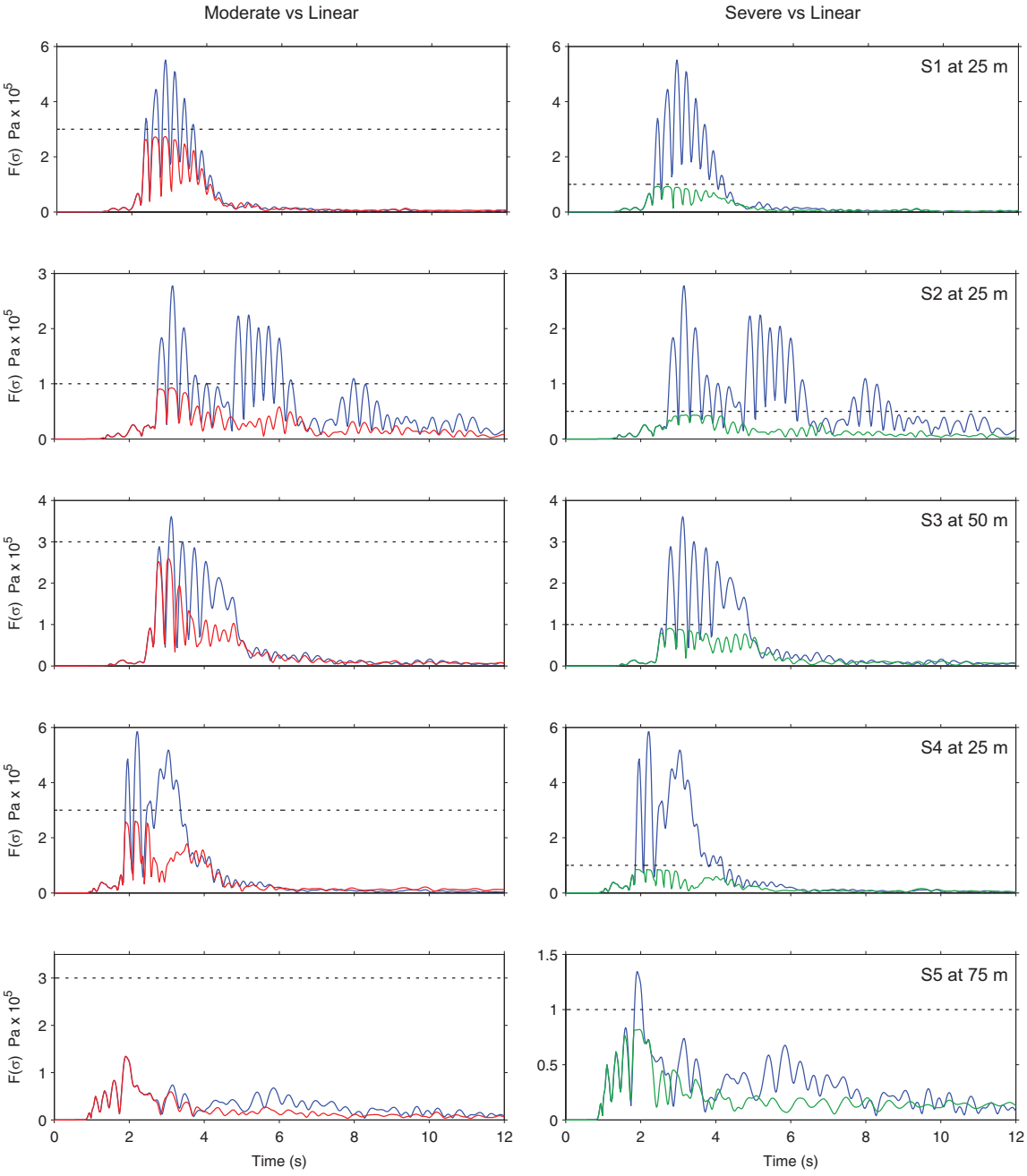

Figure 6.38: Comparison of the time histories of the yield function at selected downhole points in stations S1 through S5 for the linear and moderate nonlinear cases (left), and the linear and severe nonlinear (right). The black dashed-line represents the corresponding yield limit of the material at each point.

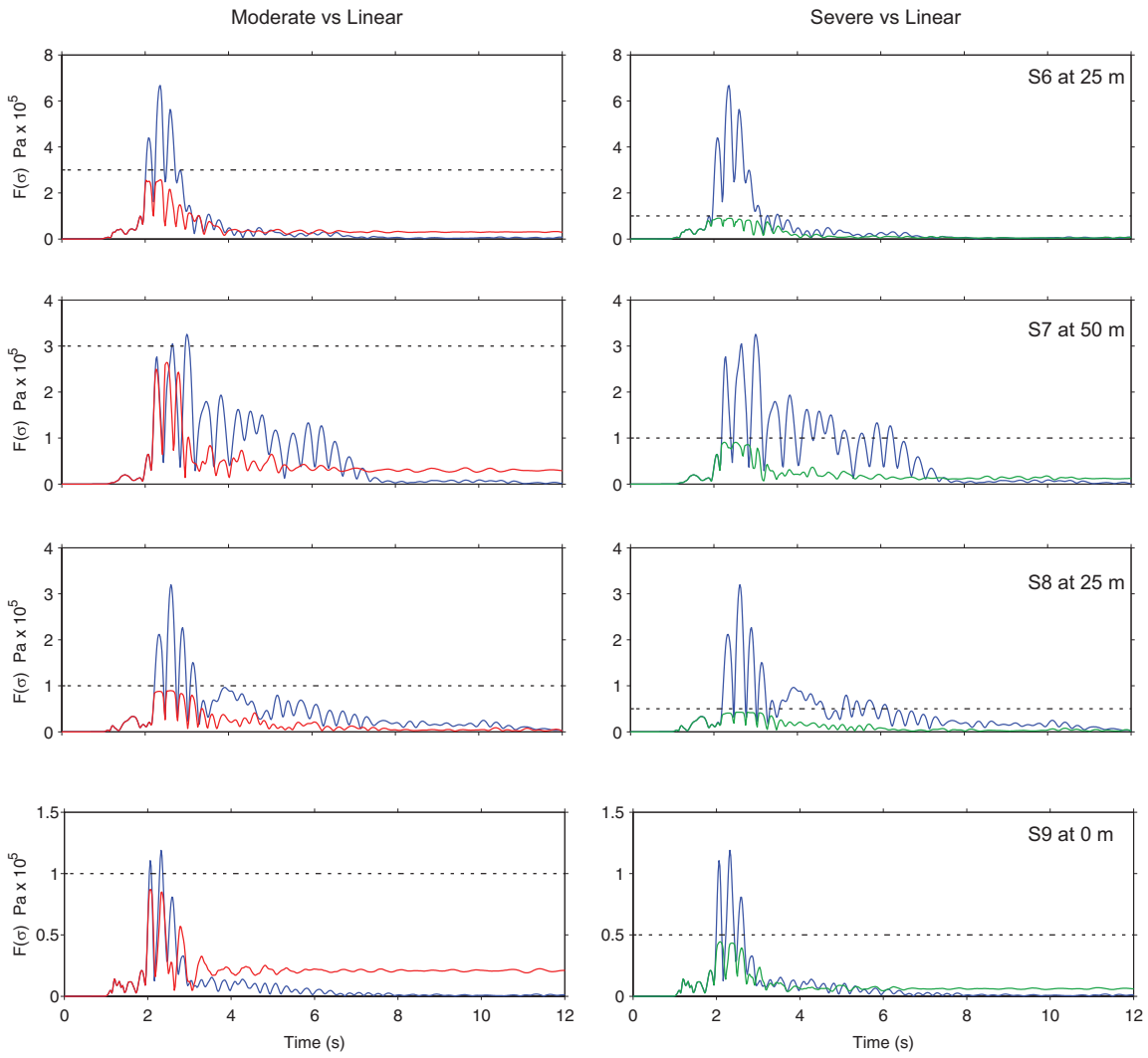

Figure 6.39: Comparison of the time histories of the yield function at selected downhole points in stations S6 through S9 for the linear and moderate nonlinear cases (left), and the linear and severe nonlinear (right). The black dashed-line represents the corresponding yield limit of the material at each point.

case. However, doing so would have demanded a smaller simulation Δt; we have found the final response to vary very little, thus we found the value of $m = 0.05$ to be an appropriate efficiency vs. accuracy compromise. Further research and validation would be necessary to calibrate the use of the rate-dependent methodology in other, more realistic, earthquake simulation applications.

7

Site-City Interaction

7.1 Building Models

7.1.1 Inventory and Distribution

For this part of the research we compiled an inventory of 74 idealized buildings. Table 7.1 lists the plan dimensions, number of stories, total height, inter-story height, and the fundamental period of vibration estimated as 1/10 the number of stories (as suggested in Section 4.1.2). Figure 7.1 shows a horizontal projection of the spatial distribution of the buildings.

This inventory was built based on information collected for the downtown financial district of a major city in the U.S. The location of all the buildings and their dimensions, except for minor adjustments to have them match a basic grid of reference, correspond to those of the actual buildings. The height and number of stories of buildings 1 through 43 also match those of the real structures. The inter-story height was estimated based on the total height and the number of stories. The plan dimensions and spatial distribution of buildings 44 through 74 also correspond to physical buildings located in this area. However, due to lack of information, their heights and corresponding number of stories and inter-story heights were arbitrarily set to match those of a building with fundamental period $T_0 = 1$ s.

7.1.2 Location

Figure 7.2 shows the location selected for the inventory in the simulation domain of the Mygdonian basin. We chose this location because it was one of the areas with the largest response, as seen in preceding sections. In addition, due to the proximity to the basin layers' boundary with the bedrock,

Table 7.1: Inventory of buildings modeled for the simulation considering site-city interaction effects.

No.	Key	Dim. (m)		Height	Stories	Interstory	Period (s)
		NS	EW	(m)	N	Height (m)	$N/10$
1	UBT	85	50	148	40	3.70	4.0
2	JCL	50	30	48	12	4.00	1.2
3	MPL	40	60	84	21	4.00	2.1
4	FW1	70	70	220	53	4.15	5.3
5	WIL	48	68	92	23	4.00	2.3
6	WBB	65	45	32	8	4.00	0.8
7	ACO	60	45	141	33	4.27	3.3
8	EYP	40	70	163	41	3.98	4.1
9	777	35	65	221	52	4.25	5.2
10	801	50	50	116	24	4.83	2.4
11	BVH	90	90	112	35	3.20	3.5
12	CNT	35	65	213	52	4.10	5.2
13	PHT	35	65	213	52	4.10	5.2
14	FW2	30	30	60	15	4.00	1.5
15	B01	30	30	80	20	4.00	2.0
16	B02	40	40	95	23	4.13	2.3
17	TCW	30	55	158	39	4.05	3.9
18	888	50	40	92	23	4.00	2.3
19	BTW	60	70	111	29	3.83	2.9
20	BOA	50	55	224	55	4.07	5.5
21	CIT	40	40	191	48	3.98	4.8
22	AON	50	30	262	62	4.23	6.2
23	7F1	40	20	68	17	4.00	1.7
24	7F2	40	70	48	12	4.00	1.2
25	7F3	20	40	36	9	4.00	0.9
26	MPM	60	35	126	31	4.06	3.1
27	MPS	60	20	100	24	4.17	2.4
28	MPP	90	100	16	4	4.00	0.4
29	WF1	60	40	220	54	4.07	5.4
30	WF2	40	60	171	45	3.80	4.5
31	MPB	50	50	114	26	4.38	2.6
32	USB	40	40	310	73	4.25	7.3
33	LAL	60	150	16	4	4.00	0.4
34	611	50	50	189	42	4.50	4.2
35	SHB	60	40	107	28	3.82	2.8
36	TSL	60	35	91	21	4.33	2.1
37	1CP	55	45	176	42	4.19	4.2
38	2CP	45	55	229	54	4.24	5.4
39	PBT	70	95	56	14	4.00	1.4
40	GCT	30	65	228	52	4.38	5.2
41	MBH	90	100	52	13	4.00	1.3
42	1WS	50	40	120	30	4.00	3.0
43	CNB	50	30	106	24	4.42	2.4
44	B03	30	30	40	10	4.00	1.0
45	B04	30	30	40	10	4.00	1.0
46	B05	40	90	40	10	4.00	1.0
47	B06	40	40	40	10	4.00	1.0
48	B07	40	70	40	10	4.00	1.0
49	B08	30	30	40	10	4.00	1.0
50	B09	80	40	40	10	4.00	1.0
51	B10	40	40	40	10	4.00	1.0
52	B11	40	90	40	10	4.00	1.0
53	B12	30	50	40	10	4.00	1.0
54	B13	50	30	40	10	4.00	1.0
55	B14	30	80	40	10	4.00	1.0
56	B15	25	40	40	10	4.00	1.0
57	B16	25	40	40	10	4.00	1.0
58	B17	25	40	40	10	4.00	1.0
59	B18	40	90	40	10	4.00	1.0
60	B19	40	40	40	10	4.00	1.0
61	B20	40	90	40	10	4.00	1.0
62	B21	30	30	40	10	4.00	1.0
63	B22	30	50	40	10	4.00	1.0
64	B23	30	40	40	10	4.00	1.0
65	B24	40	40	40	10	4.00	1.0
66	B25	40	90	40	10	4.00	1.0
67	B26	40	40	40	10	4.00	1.0
68	B27	40	40	40	10	4.00	1.0
69	B28	45	90	40	10	4.00	1.0
70	B29	40	40	40	10	4.00	1.0
71	B30	40	40	40	10	4.00	1.0
72	B31	70	40	40	10	4.00	1.0
73	B32	40	90	40	10	4.00	1.0
74	B33	40	90	40	10	4.00	1.0

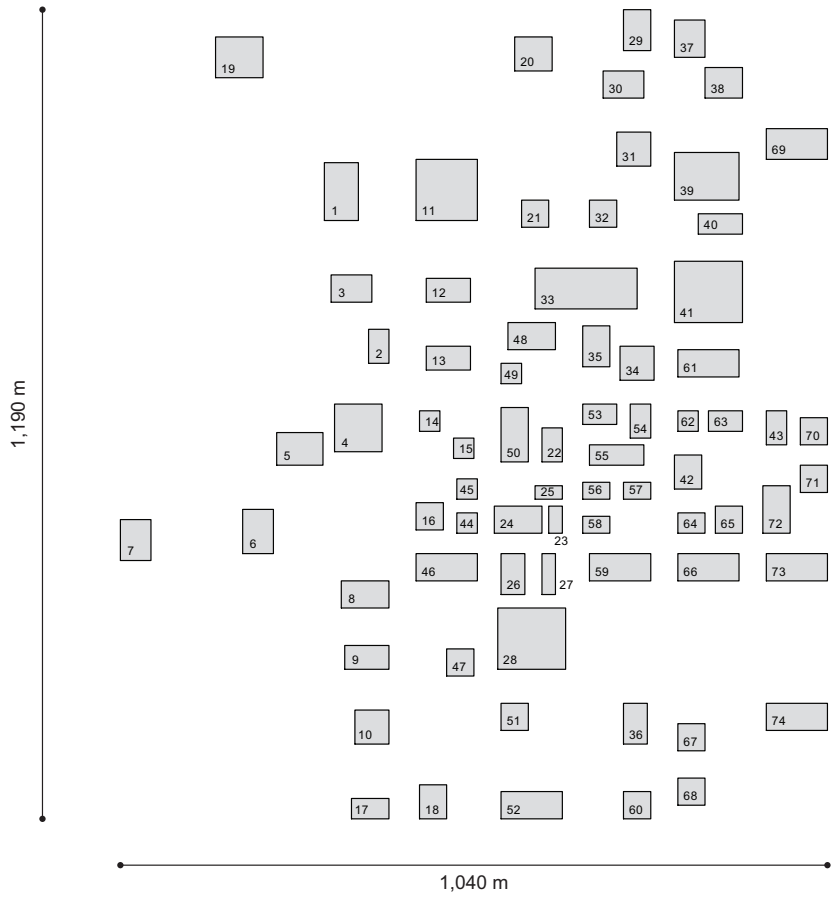

Figure 7.1: Spatial distribution of the buildings inventory.

this area has a larger spatial variability in the response because of basin and edge effects—ground motion characteristics that are known to affect the dynamic response of buildings.

The selection was, however, completely arbitrary. Although there are no such buildings in the Valley of Volvi, we consider this realistic inventory to serve well the objectives of this thesis to gain insights about the relevance of site-city interaction effects in soft-soil deposits such as those of the Mygdonian basin. Future research that reproduce the urban environment of cities in the area, like Profitis or Stivos (see Fig. 5.1), would positively contribute to seismic hazard studies in the region.

7.1.3 Mesh Representation

Using the new implementation in Hercules for modeling urban environments (described in Section 4.2), a modified mesh that included the buildings inventory was generated at run-time for the simulation of site-city interaction effects. Figure 7.3 shows a coarse representation of a subset of a mesh with the building models. The finer mesh with the buildings models used in the simulation

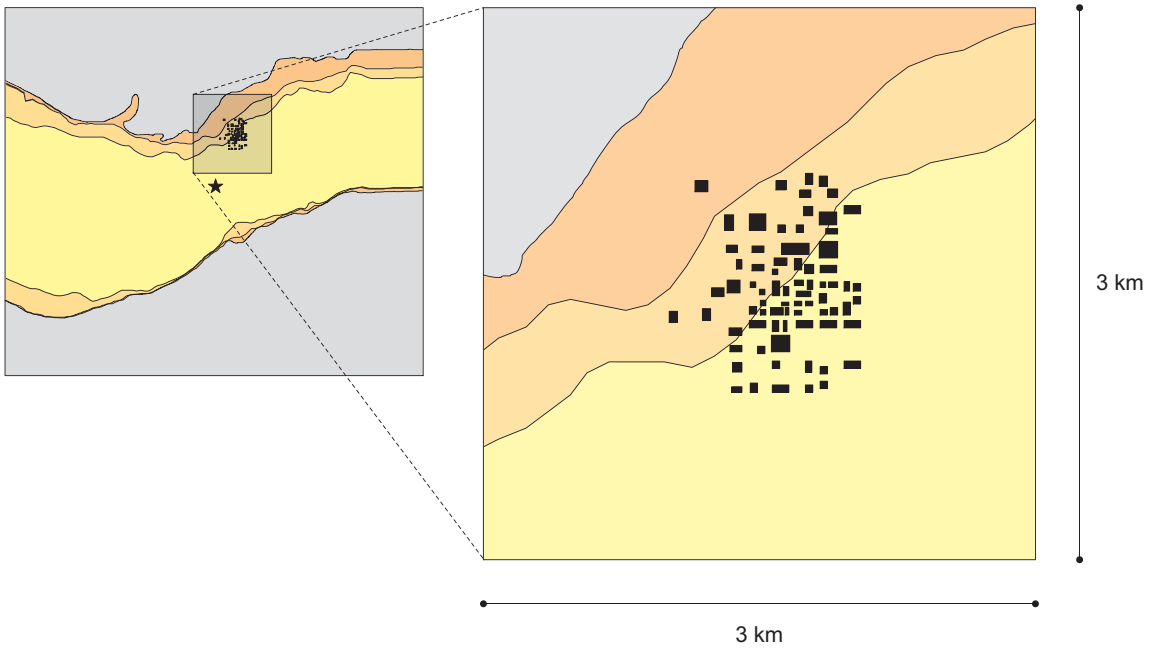

Figure 7.2: Location of the buildings inventory used for the simulation of site-city effects with reference to the central area of the domain containing the basin.

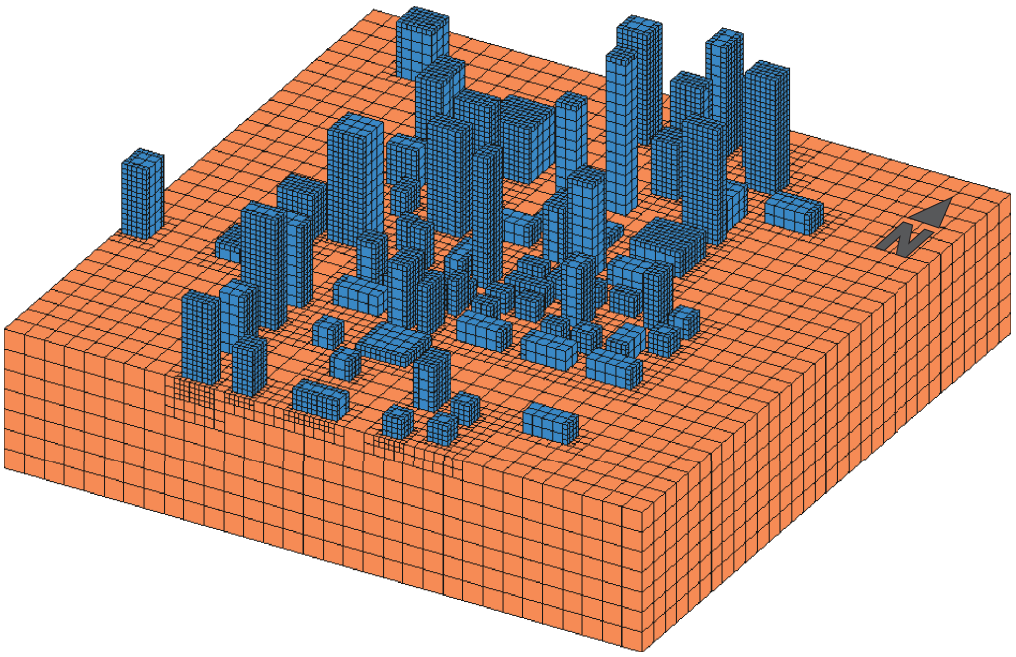

Figure 7.3: Subset of a coarse mesh including the structural models corresponding to the 74 buildings in the inventory used for simulations including site-city interaction effects.

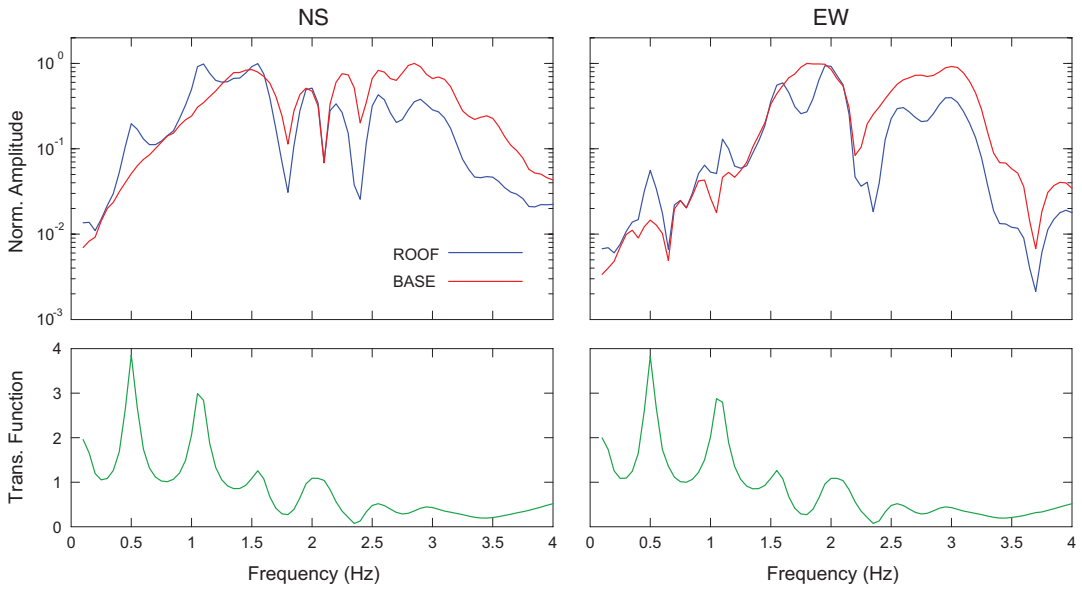

Figure 7.4: Fourier analysis of the fixed-base response of building B01 for determining the fundamental frequency of vibration of the model using the homogeneous-blocks analogy. The top panels show the response of the building at its roof and base and in both components of motion. The bottom panels show the corresponding transfer functions used for the system identification problem.

represented a total of 1,100,960 additional elements and 1,240,999 extra nodes with respect to the case with no buildings.

In addition, in order to comply with the V_s-rule (2.17) and the minimum critical time-step, the smallest octant size was reduced from 5 to 2.5 m, and the simulation Δt was lowered from 0.002 to 0.001 s (see Table 5.5).

7.1.4 Building Properties

As mentioned in Section 4.1.2, we use simple approximations to determine the dynamic properties of the superstructures and set the material constants of the elements conforming to the building models. According to such approximations, a value of $V_s = 100$ m/s was found appropriate to match the fundamental period of typical frame structures with the homogeneous-blocks analogy.

For the foundation we tried three different values of $V_s = 100$, 200, and 400 m/s. Since the buildings were located on soft material deposits ($V_s = 200$ m/s), foundations with $V_s = 100$ and 200 m/s represented a low impedance between the foundations and the soil. Preliminary results using these values resulted in less noticeable interaction effects. Therefore, the final results shown in the following sections correspond to the case of foundations with $V_s = 400$ m/s.

Table 7.2: Comparison of the fundamental frequencies of building models in the two components of motion (NS and EW) with the expected frequency determined based on the number of stories using the expression $T_0 = N/10$. A measure of the error obtained as the average of $|f_{NS,EW} - f_0|/f_0 \times 100$ is shown in the rightmost column.

No.	Frequency f_0 (Hz)			Err.
	$1/T_0$	NS	EW	(%)
1	0.25	0.30	0.25	10
2	0.83	0.85	0.90	5
3	0.48	0.50	0.55	10
4	0.19	0.15	0.15	21
5	0.43	0.50	0.50	15
6	1.25	0.75	0.70	42
7	0.30	0.30	0.25	9
8	0.24	0.20	0.25	10
9	0.19	0.25	0.15	26
10	0.42	0.35	0.35	16
11	0.29	0.15	0.15	48
12	0.19	0.30	0.15	39
13	0.19	0.15	0.30	39
14	0.67	0.70	0.70	5
15	0.50	0.50	0.50	0
16	0.43	0.45	0.45	3
17	0.26	0.40	0.25	29
18	0.43	0.50	0.45	9
19	0.34	0.40	0.40	16
20	0.18	0.15	0.15	18
21	0.21	0.15	0.15	28
22	0.16	0.25	0.20	40
23	0.59	0.65	0.50	13
24	0.83	0.85	0.90	5
25	1.11	1.25	1.30	15
26	0.32	0.35	0.30	8
27	0.42	0.45	0.30	18
28	2.50	1.60	1.60	36
29	0.19	0.15	0.30	41
30	0.22	0.20	0.25	11
31	0.38	0.35	0.35	9
32	0.14	0.15	0.15	10
33	2.50	1.55	1.60	37
34	0.24	0.20	0.20	16
35	0.36	0.40	0.40	12
36	0.48	0.50	0.45	5
37	0.24	0.20	0.20	16
38	0.19	0.30	0.30	62
39	0.71	0.75	0.80	9
40	0.19	0.25	0.15	26
41	0.77	0.45	0.45	42
42	0.33	0.35	0.30	8
43	0.42	0.40	0.35	10
44	1.00	1.15	1.15	15
45	1.00	1.15	1.15	15
46	1.00	1.15	1.15	15
47	1.00	1.15	1.15	15
48	1.00	1.15	1.15	15
49	1.00	1.15	1.15	15
50	1.00	1.15	1.15	15
51	1.00	1.15	1.15	15
52	1.00	1.15	1.15	15
53	1.00	1.15	1.15	15
54	1.00	1.15	1.15	15
55	1.00	1.15	1.15	15
56	1.00	1.15	1.15	15
57	1.00	1.15	1.15	15
58	1.00	1.15	1.15	15
59	1.00	1.15	1.15	15
60	1.00	1.15	1.15	15
61	1.00	1.15	1.15	15
62	1.00	1.15	1.15	15
63	1.00	1.15	1.15	15
64	1.00	1.15	1.15	15
65	1.00	1.15	1.15	15
66	1.00	1.15	1.15	15
67	1.00	1.15	1.15	15
68	1.00	1.15	1.15	15
69	1.00	1.15	1.15	15
70	1.00	1.15	1.15	15
71	1.00	1.15	1.15	15
72	1.00	1.15	1.15	15
73	1.00	1.15	1.15	15
74	1.00	1.15	1.15	15

The mass density for both the superstructures and the foundations was set to 300 km/m^3 and the value of V_p was determined using the rule $V_\mathrm{p} = 2.5V_\mathrm{s}$.

In order to check our choice of material properties for the building elements, we used the mesh created for the simulation to run a problem with the building models fixed at their bases, i.e., without soil-foundation interaction. Using the excitation at the base and the response of the buildings at the roof we obtained Fourier transfer functions as shown in Fig. 7.4 for building B01. In this example, the transfer functions' first peak occurs at frequency $f_0 = 0.5$ Hz in both components of motion. According to Table 7.1, the fundamental period of this building is 2 s, which corresponds to 0.5 Hz in frequency as observed in Fig. 7.4.

We identified the frequencies of all the buildings in the two horizontal components of motion using the transfer functions obtained for the fixed-base simulation and compared the results with the fundamental frequencies expected from using the rule $T_0 = N/10$ for the corresponding first periods of vibration in Table 7.1. The results are shown in Table 7.2, which also includes a measure of the error of the models' frequencies with respect to the one initially estimated for the buildings.

The comparison of the expected frequencies with those obtained from the transfer functions indicate that for a majority of the building models, the observed frequencies are within a range of 20 percent from the corresponding expected value. In general, the approximations used seem to work better for buildings with frequencies between 0.25 and 1.25 Hz, and is not so good for higher and lower frequencies outside this range.

Considering the level of simplification, we believe this is an acceptable margin of error. However, large errors such as those for buildings MPP y LAL are not acceptable. In the future, each building should be calibrated individually to correctly match the expected fundamental period of vibration by varying the properties of its elements accordingly. Meanwhile, for simplicity, we decided to work with these models as acceptable ones, especially because the rule of $T_0 = N/10$ is only approximate.

7.2 Regional Effects

We start the analysis for the case with site-city interaction by looking at the surface response in the simulation domain from a regional perspective. Figure 7.5 shows wave propagation progression in the central portion of the domain that contains the basin in terms of the horizontal magnitude of velocities. Very little, if any, difference is noticeable between the two cases due to the presence of the buildings. Only the still-frame at 2 s shows the influence in the passage of the strongest wavefront,

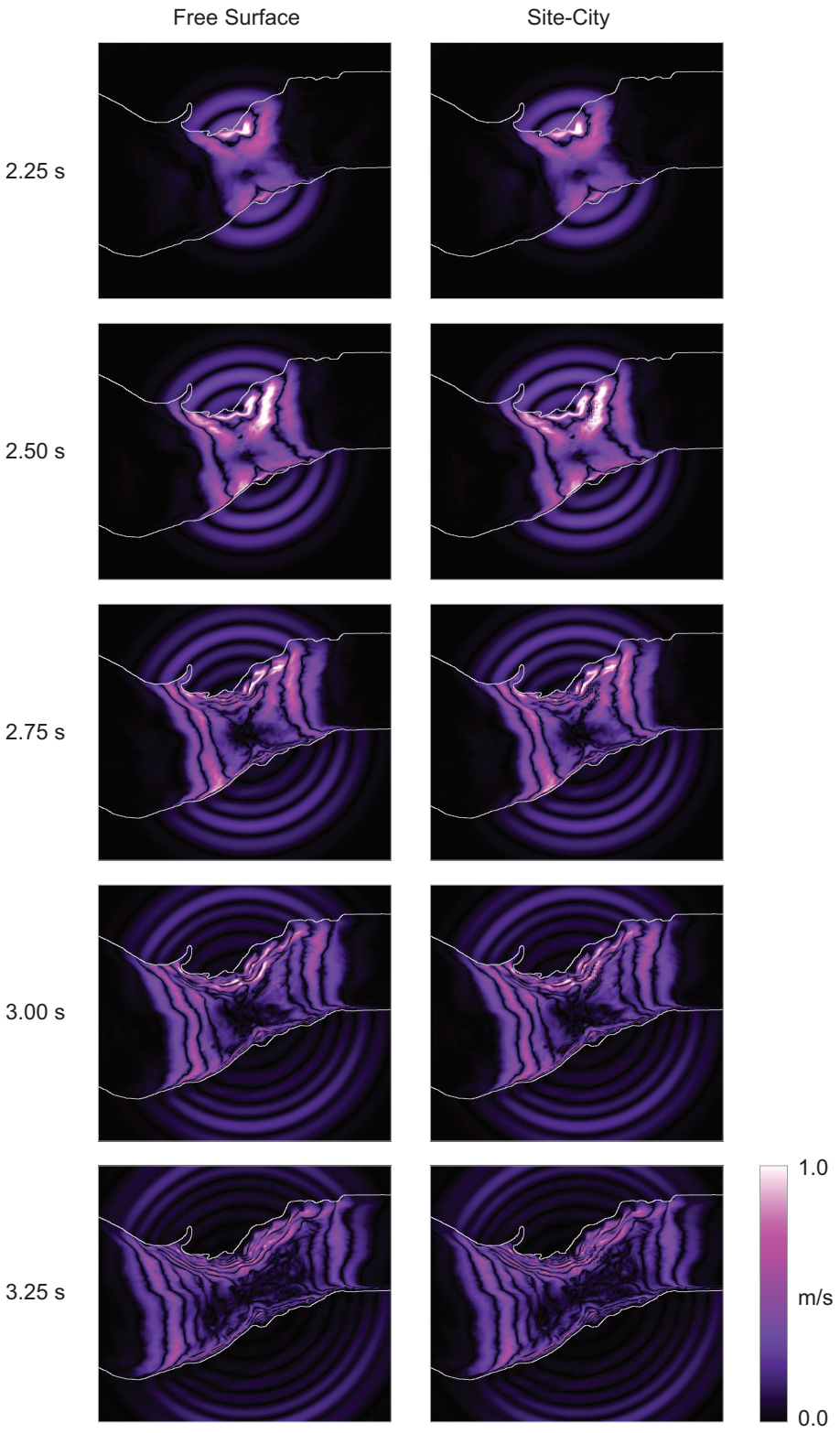

Figure 7.5: Comparison a regional scale between snapshots of the surface magnitude of horizontal velocity of the simulations with (site-city) and without (free-surface) considering the presence of buildings in the model.

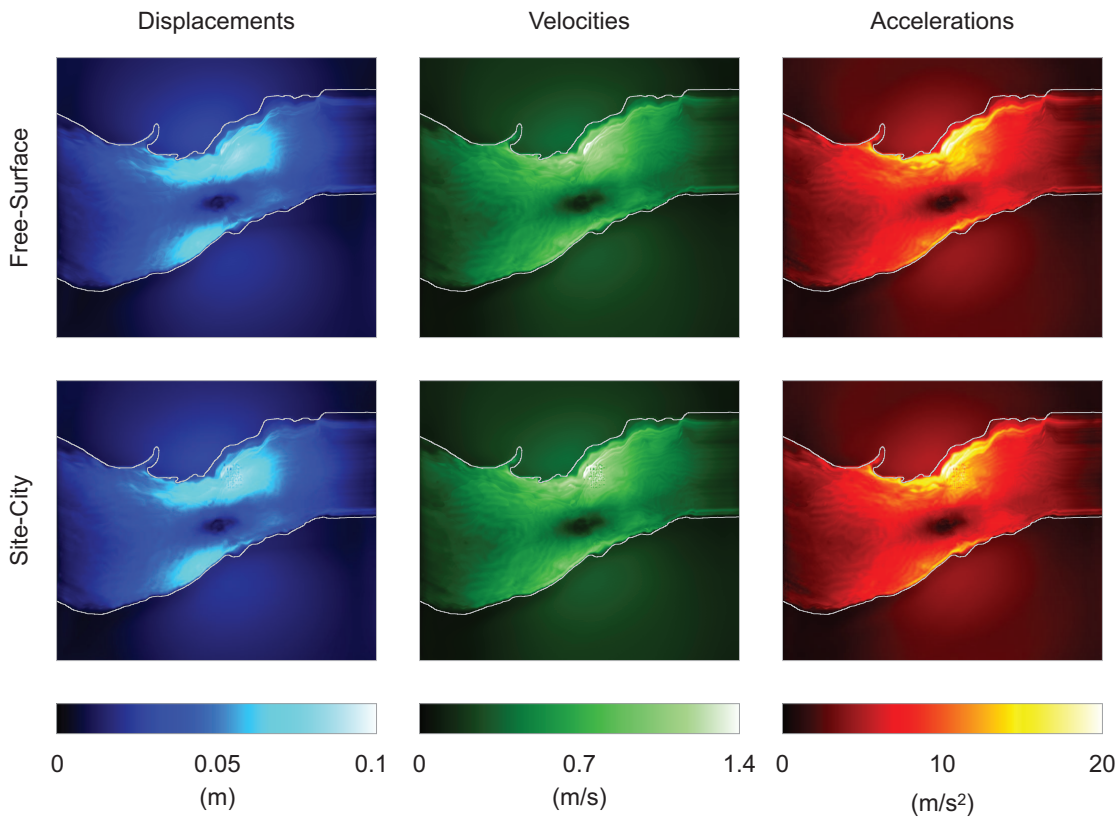

Figure 7.6: Comparison of the horizontal peak magnitude displacement (left), velocity (center), and acceleration (right) at the surface of the simulations with (bottom) and without (top) considering the presence of the buildings in the model.

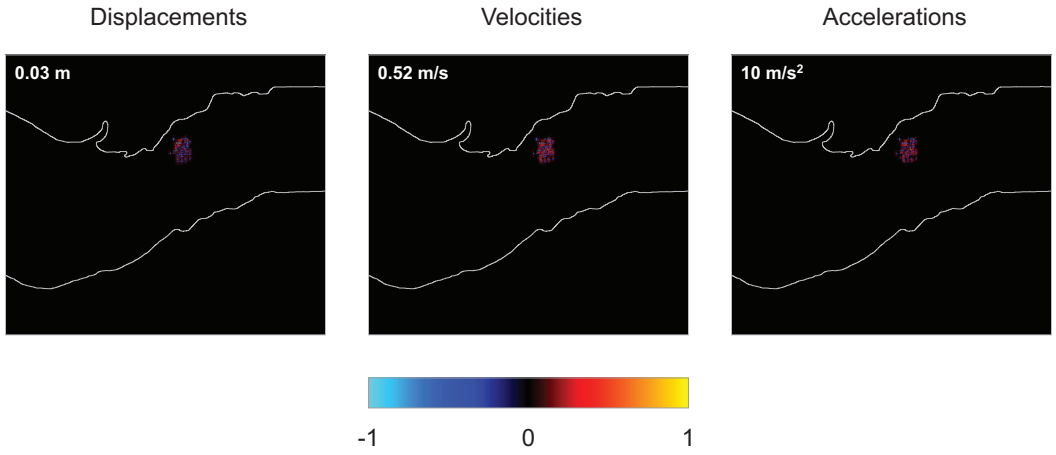

Figure 7.7: Normalized difference between the case with buildings and the free-surface response for the horizontal peak magnitude of displacements (left), velocities (center), and accelerations (right). Warm colors indicate larger response in the site-city case, and cold colors otherwise. The absolute value of the maximum difference used for normalization is shown in the top-left corner of each panel.

revealed by spots of smaller amplitude where the buildings are. Although less evident, these spots are also present at 2.75 s.

The snapshots at 3 and 3.25 s seem to show a small perturbation in the surface waves bouncing from the edge. However, in general, a comparison of these snapshots indicates that the propagation at the regional level is unchanged by the presence of the buildings, which seem to have only a local effect. This is corroborated by Fig. 7.6, which shows the cumulative peak horizontal magnitude of displacements, velocities, and accelerations at the surface of the simulation domain for the two cases with and without the presence of the buildings; and by comparing the two as done in Fig. 7.7, which shows the difference between the peak response in the two simulations, normalized with respect to the maximum values shown in top-left corner of each panel.

In these figures one can easily point at the location of the buildings whose presence is visible in the site-city simulation results because the amplitudes of the response at their base is smaller (Fig. 7.6), and the response of the surface between buildings is larger (Fig. 7.7).

From these comparisons it is clear that the presence of the buildings do affect the response but, in this particular case, they do so only at a local level. We will therefore focus our attention in the smaller area surrounding the buildings. However, it is worth noting that a larger inventory of buildings covering a greater area of the surface, as is the case in real cities, may have a more noticeable effect at the regional level. This is an aspect to be explored in the future now that the implementations presented in this thesis will make it possible.

7.3 Local Site Effects

7.3.1 Wave Propagation

Since the effects of the urban environment concentrate in the local area around the building models, we will focus on the smaller region of 3 km $\times$ 3 km shown on the right hand side of Fig. 7.2.

Figure 7.8 shows the propagation of the horizontal magnitude velocity throughout this subdomain in still-frames every 0.25 s from 2.25 until 5 s of simulation, comparing the results of the site-city case with the wavefield of the free-field simulation, without the building models. We can now more clearly see the effect that the structures and their foundations have on the ground response. From $t = 2.25$ to 2.75 s, the amplitude of the motion under each building seems to be noticeably reduced by the presence of the foundation. This effect is especially visible at $t = 2.5$ s for the main wavefront with the larger period.

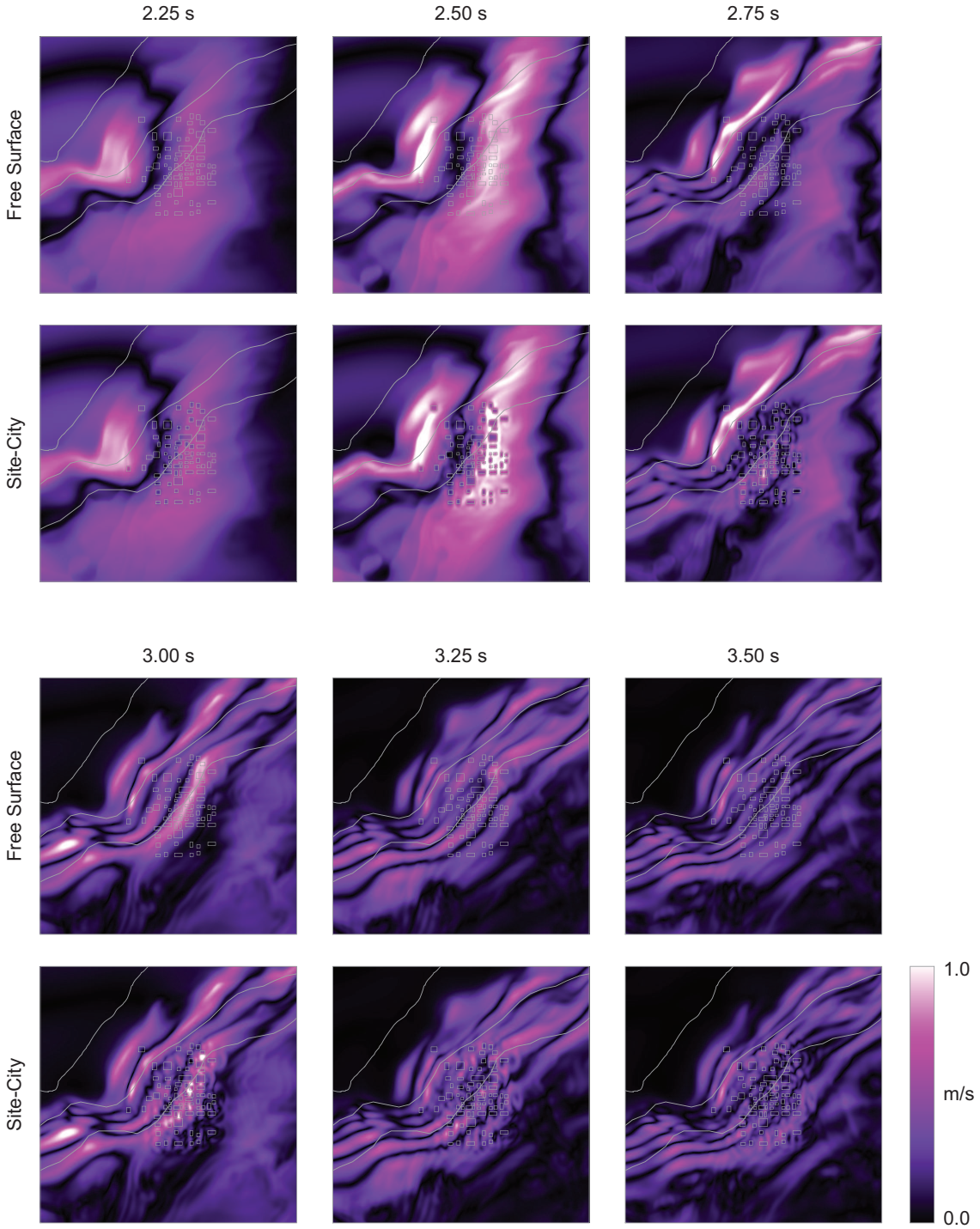

Figure 7.8: Comparison at a local scale between snapshots of the surface magnitude of horizontal velocity of the simulations with (site-city) and without (free-surface) considering the presence of buildings in the model. In the free-surface case the buildings are shown only for reference.

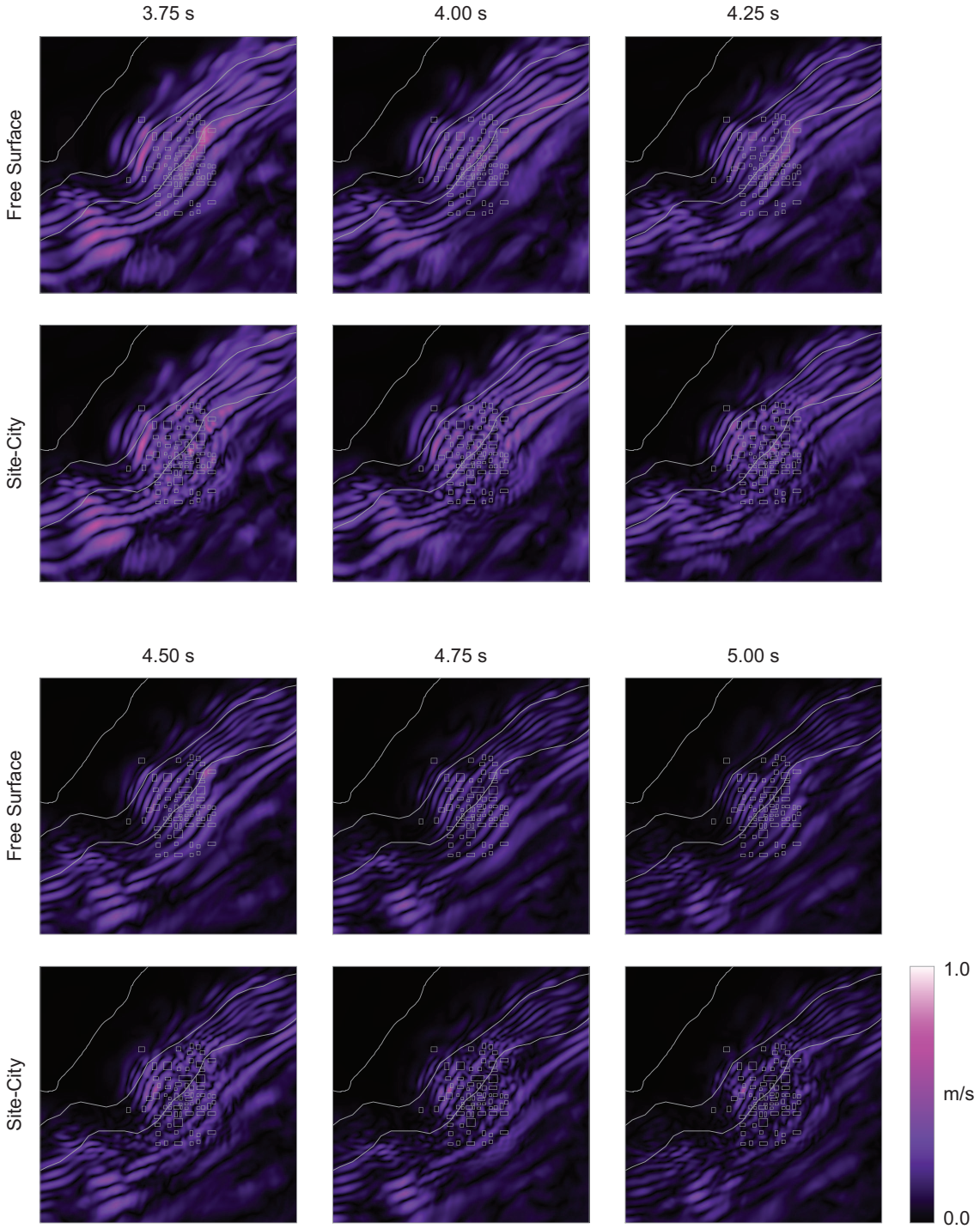

Figure 7.8: (*Continued*) Comparison at a local scale between snapshots of the surface magnitude of horizontal velocity of the simulations with (site-city) and without (free-surface) considering the presence of buildings in the model. In the free-surface case the buildings are shown only for reference.

As the simulation progresses, shorter (surface) waves from the basin boundary start to propagate through the urban setting and more complex interactions occur. At $t = 3$ s, for example, there are bright spots in the spaces between buildings, indicating a larger response at those points than in the free-surface case. Then, after 3.25 s it is possible to see that, in addition to the scattering of waves because of the presence of the structures, there are also small wave fronts coming out of the 'city'. These waves are generated by the continued vibration of the structure-foundation systems, which act as secondary sources.

Between 3.5 and 4.25 s, these outgoing waves are more prominent in the East and South limits of the city. Then, after 4.5 s, they become visible all around the buildings group boundaries, causing both constructive and destructive interferences with the waves passing through and near the city. As far as one can tell from these still-frames, such perturbations do not go farther than a few hundred meters. We will revisit this point in Section 7.3.3.

7.3.2 Peak Ground Response

Following the same format of the results we presented at the regional level, we now examine the peak ground response of the site where the buildings are located. Figure 7.9 shows the magnitude of the peak horizontal displacements, velocities, and accelerations in the smaller subdomain, comparing the results for the free-surface and site-city cases. In addition, Fig. 7.10 shows the difference of these two sets, or perturbation due to the presence of the urban environment. Here, warm colors indicate a larger ground response in the case considering site-city interaction effects, while cold colors indicate a larger response in the free-field simulation.

It is clear from these figures that the presence of the foundations (composed of stiffer material) greatly decreases the ground response. This is a well-known, though seldom quantified effect of soil-structure interaction. Moreover, there are additional characteristics in the response that are not so well understood. First, note that the reduction in the ground response is greater at the buildings to the North and West limits. These are the first structures to receive the wavefront and subsequent surface waves arriving from the basin boundary and traveling SW (see Fig. 7.8).

In general, all buildings present an 'aura' of ground amplification around them and in between. Only the 'isolated' building in the North-West (No. 19 in Fig. 7.1) exhibits a first inner perimeter of deamplification and an outer zone of amplification. The largest increase in inter-building ground response occurs near the center of the city between buildings No. 34, 35, 53, and 54, for all the displacements, velocities and accelerations; and between buildings No. 1 and 11, predominantly in

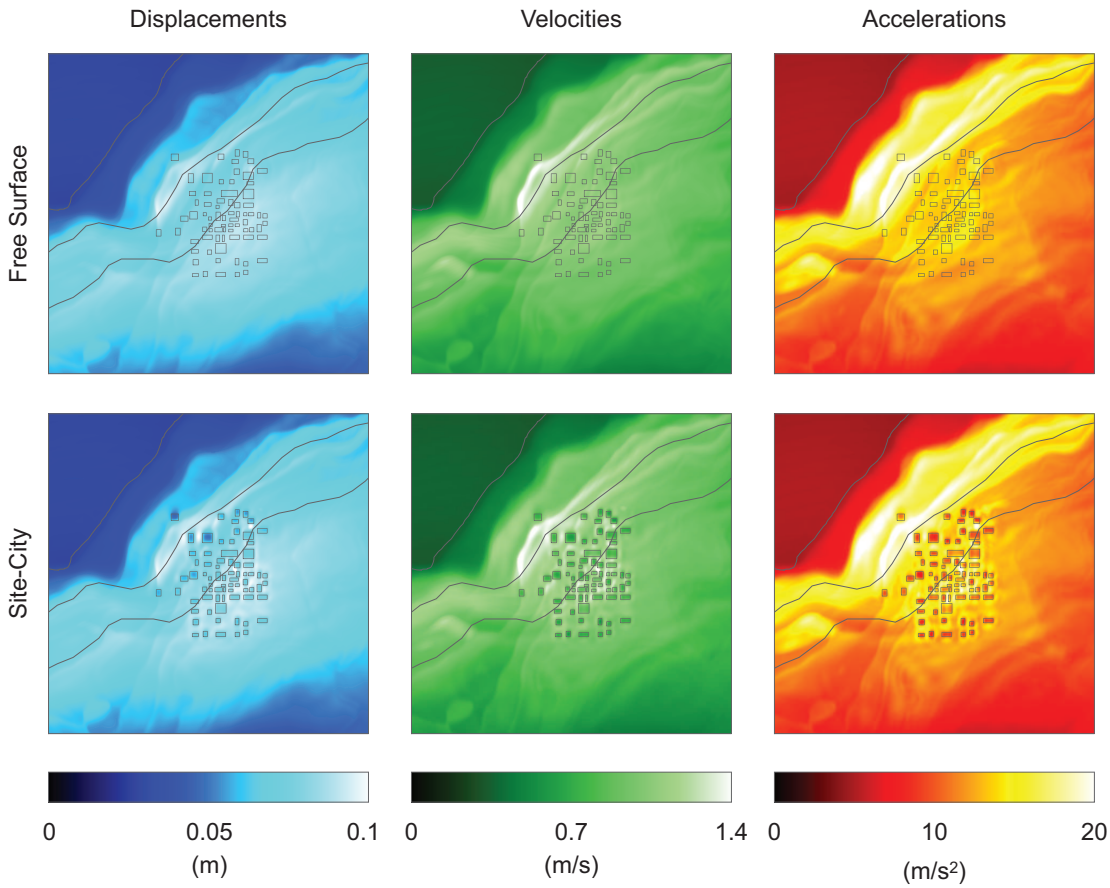

Figure 7.9: Comparison of the horizontal peak magnitude displacement (left), velocity (center), and acceleration (right) at the surface of the simulations with (bottom) and without (top) considering the presence of the buildings at a local scale. In the free-surface case the buildings are shown only for reference.

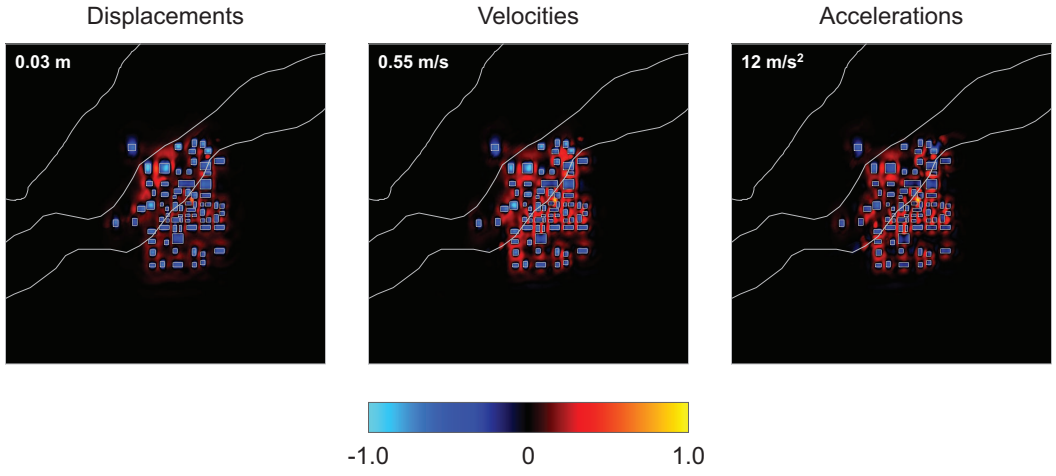

Figure 7.10: Normalized difference at a local scale between the case with buildings and the free-surface response for the horizontal peak magnitude of displacements (left), velocities (center), and accelerations (right). Warm colors indicate larger response in the site-city case, and cold colors otherwise. The absolute value of the maximum difference used for normalization is shown in the top-left corner of each panel.

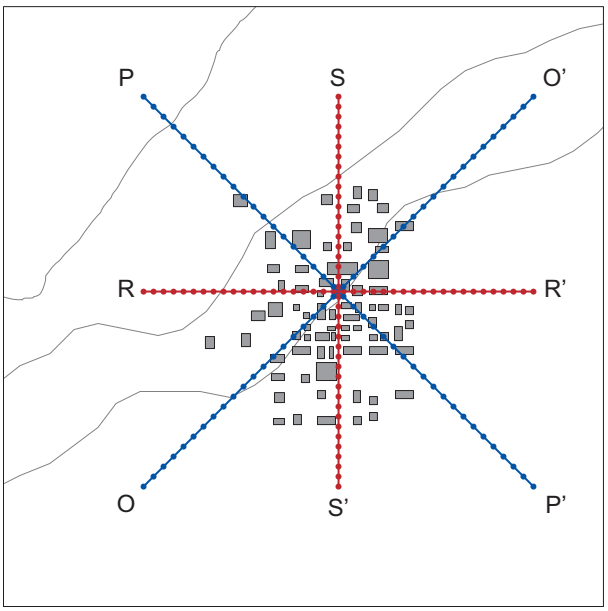

Figure 7.11: Location of the four lines used to study the perturbations across the city and the surrounding area due to the presence of the urban environment.

the. There is also a significant amplification in inter-building velocities between buildings No. 29, 30, 31, 37, 38, and 39.

Perturbations due to the presence of the urban environment extend out of the city limits for about 30 to 50 m. In displacements, these perturbations represent only amplification of the peak response. In velocities and accelerations, both amplifications and reductions are observed in the perturbation field in Fig. 7.10. However, the magnitude of the reductions out of the city area are smaller than the amplifications in and around the urban setting.

7.3.3 Local Perturbations

We examine now how the presence of the structures changes the wavefield in and around the city. For that, we have selected four lines crossing through the urban setting as shown in Fig. 7.11, and recorded the histories of velocity for the two simulation cases, with and without the buildings. In addition, we have computed the difference between the two, or *perturbation field*. The results are shown in Figs. 7.12 through 7.15 for the EW component of motion. The NS and UD components are omitted here for brevity, but in general, they exhibit the same qualitative characteristics observed in these figures and discussed next, although for smaller amplitudes.

We begin by noting that the largest perturbations shown in Figs. 7.12–7.15 concentrate within the city boundaries and towards the center of it. From the peak values shown at the top of each

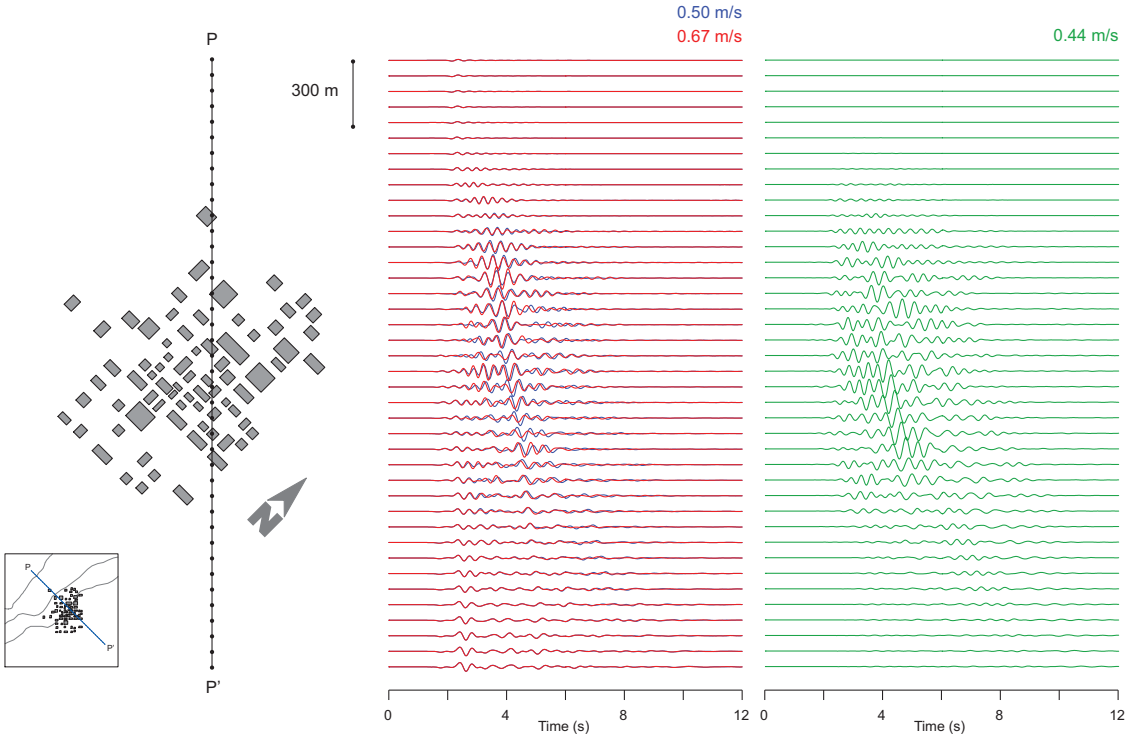

Figure 7.12: Traces of velocity in the EW component of motion along the crossing line PP' for the free-surface (blue) and the site-city (red) simulations on the left hand side and the perturbation field (green) on the right. The leftmost portion of the figure shows the relation of the buildings distribution with respect to the line of interest. Peak values for each group of synthetics are shown at the top.

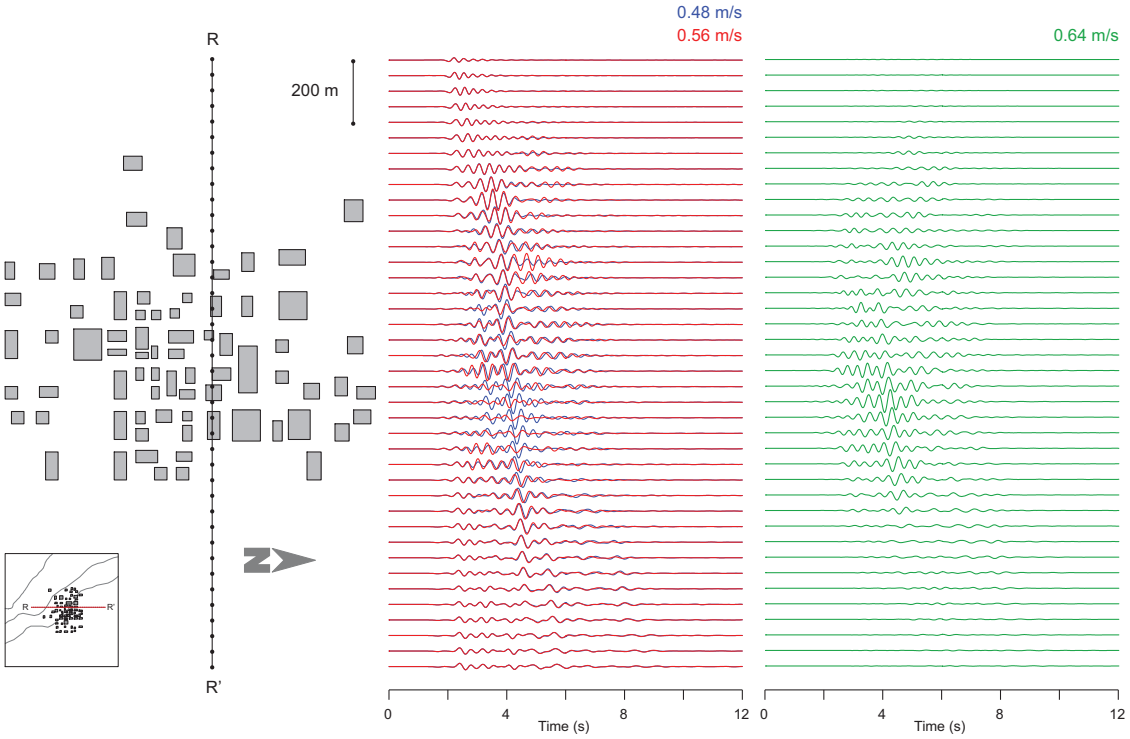

Figure 7.13: Same as Fig. 7.12, but for the crossing line RR'.

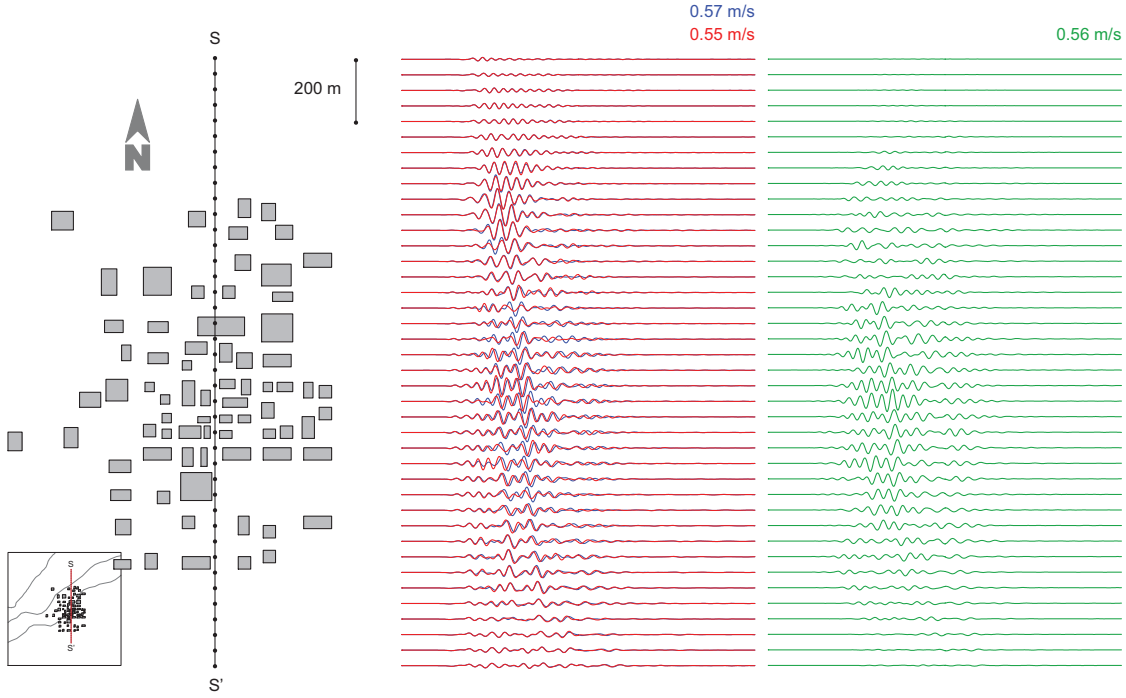

Figure 7.14: Same as Fig. 7.12, but for the crossing line SS'.

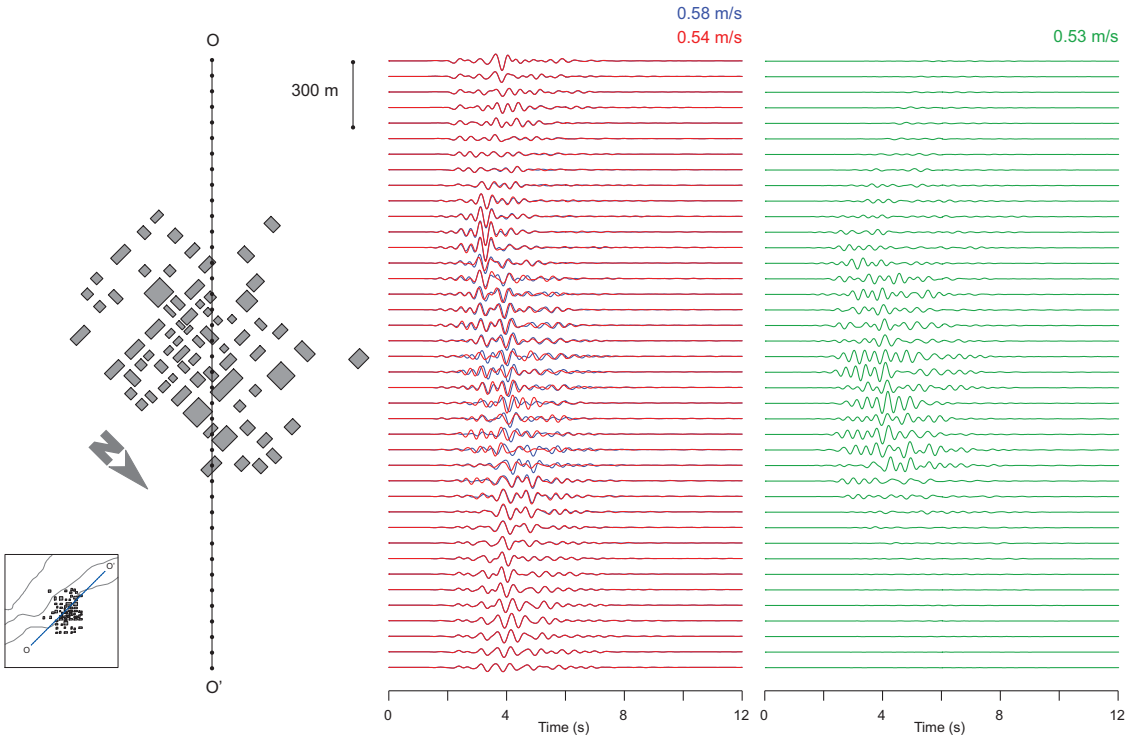

Figure 7.15: Same as Fig. 7.12, but for the crossing line OO'.

figure we gather that the magnitude of the difference between the free-field motion and the site-city cases is of the same order as that of each individual simulation—which are, for the most part, very close to each other. This indicates that the differences, however large, must be a balance combination between shifting in phase and amplitude reduction and amplification.

In general, the presence of the buildings and their foundations seem to delay the passage of the wavefronts, as seen by the slower arrival of waves at the South, East, and South-East ends of lines SS', RR', and PP', respectively. Therefore, the amplitude of the perturbation field in this areas seems to be more the result of the synthetics being shifted in face than a net difference in their amplitudes. Near the center, however, the discrepancies between the simulations are present in both the phase and amplitude of the signals—and they are the largest.

Whenever an observation point falls within a building, the synthetic of the site-city case is filtered out—its amplitude decreases and its period becomes larger. This is a known consequence of the presence of the stiffer medium of the foundation. By contrast, observation points within the city but in between buildings, shorten their period and, in some cases, exhibit larger amplitudes right from the first arrival of incoming waves and after the main wavefront has passed. Similarly, those observation points right next to a building have larger and longer oscillations with semi-monochromatic characteristics; and they extend in time over the free-field. We interpret this as the influence of the continued vibration of the superstructures.

Site-city effects extend for about 200 m in the front-field (where the waves come from, i.e., the North-West; whereas the back-field to the South-East exhibits perturbations beyond 500 m from the city boundaries.

7.3.4 Spatial Variability

We use the synthetics along the same four lines to investigate the effects of the presence of the urban setting in the spatial variability of the ground response by looking at the peak values of displacement, velocity, and acceleration in the three components of motion as shown in Figs. 7.16 through 7.18.

From these figures it is obvious that the presence of the urban setting greatly changes the spatial variability of the response. For this particular scenario, the largest variations occur in the EW component of motion and the smallest in the vertical one. The effect is noticeable and similar in displacements, velocities and accelerations, and changes abruptly from reduction to amplification.

Contrary to the perturbations observed in the previous section, this variability on the peak response seems to be better constrained to the city boundaries. The largest amplifications are of

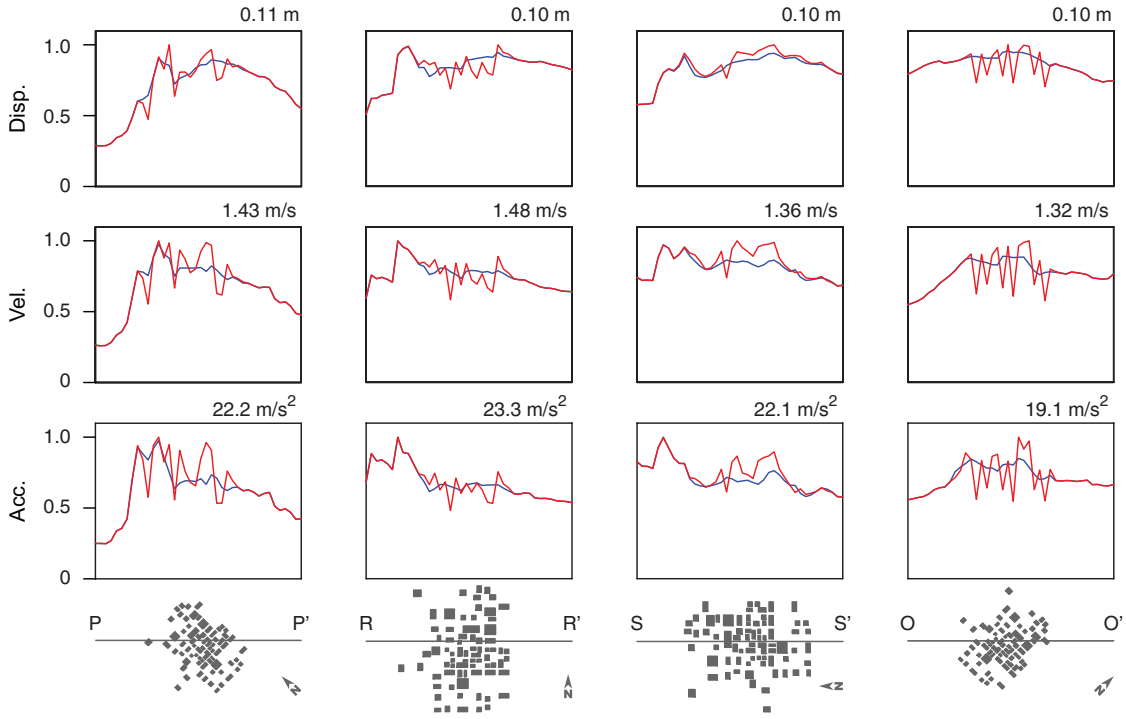

Figure 7.16: Comparison of peak displacements (top), velocities (middle), and accelerations (bottom), between the free-surface (blue) and site-city (red) cases in the NS component of motion along the lines PP', RR', SS', and OO' crossing the city. Each pair is normalized with respect to the largest of the two and the peak value is shown on the top-right corner of each panel. The horizontal projection of the city and the location of each line with respect to it is shown at the bottom.

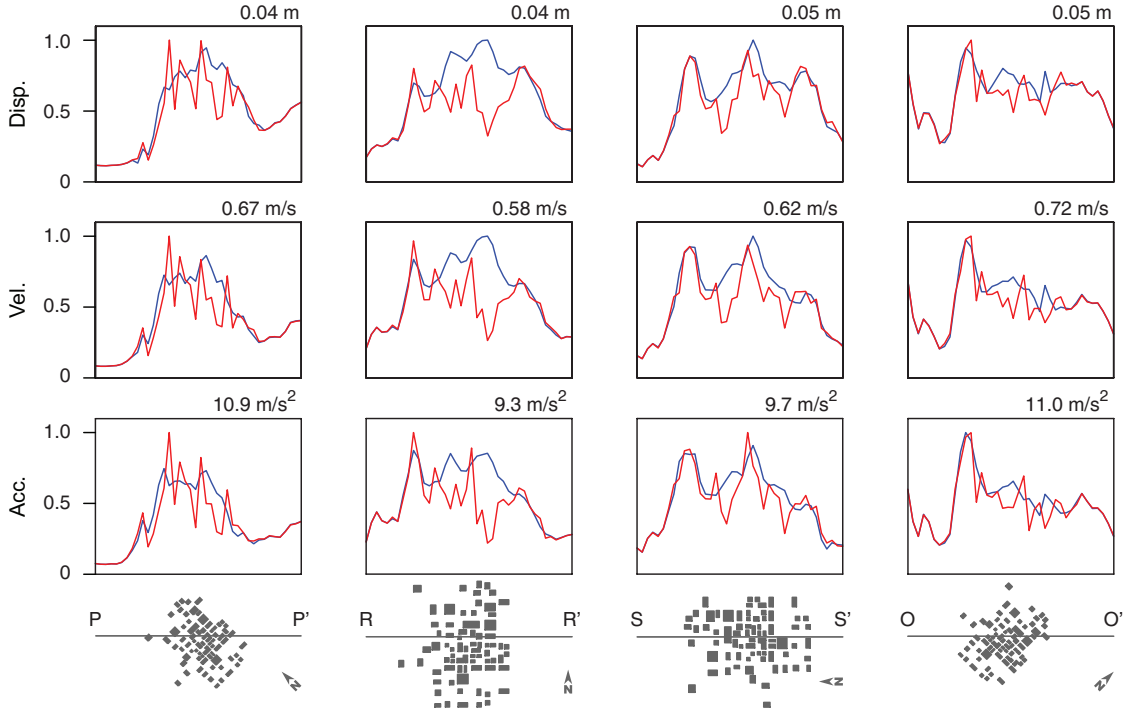

Figure 7.17: Same as Fig. 7.16 but for the EW component of motion.

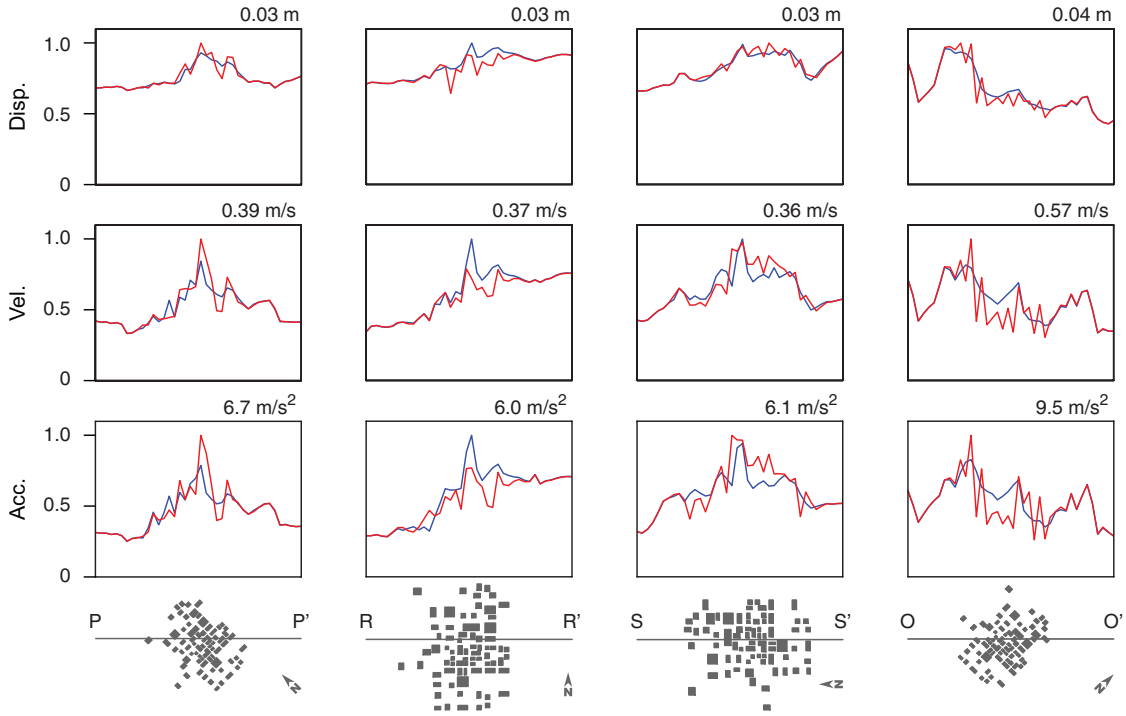

Figure 7.18: Same as Fig. 7.16 but for the UD component of motion.

about 30 percent the amplitude of the free-surface. They occur in the observation points toward the NW end of line PP' in the EW component of motion (Fig. 7.16). The largest reductions (of about 50 percent) also occur in the EW component of motion, in line RR' near the center and to the East boundary of the city.

7.4 Structural Behavior

7.4.1 Excitation at the Base of the Buildings

Time and Frequency Analysis

As mentioned in Sections 1.3 and 4.1, it is a common practice in design to use free-field motion records or synthetics as input excitation for building models. This input is imposed at the base of models, which are usually considered to be fixed to the ground. Since it is well known from SSI studies that this is not always a valid assumption, it is important to study the effect that the multiple soil-structure systems have on the actual motion obtained for the location of each building.

Figure 7.19 shows the velocity time histories and their corresponding Fourier amplitudes at the center of the location of twelve buildings for the two simulations, with and without the presence

of the structure-foundation systems. These points were selected for buildings with fundamental frequencies varying from 0.15 to 1.6 Hz, and are shown in the figure in ascending order.

It is observed from these comparisons that the presence of the buildings reduces the amplitude of the motion at all locations. In the time histories, the velocities in the EW component of motion exhibit a phase shift—waves travel faster in the simulation incorporating the building models.

In the frequency domain, with the exception of the EW spectrum at the location of building No. 6, all other spectra present an overall dissipation of energy (diffraction) in the case with the building models; and for the most part, their shape continues to be dominated by the original free-field ground motion, only that reduced and with a minor frequency shift to the right, possibly as a product of the stiffer material of the foundation elements.

With exception of building No. 6, the amplitude in the EW spectrum between 2.8 and 3.1 Hz for the site-city case is dominantly larger than that of the free-field. It may be that a higher mode of the superstructure resonated for a few seconds. This frequency actually matches that of the larger oscillations observed in the time signal between 5 and 8.2 s. Although further analysis would be required to understand all the small details in the signals at each location, these provide clear evidences of the more complex phenomena of site-city interaction effects.

Peak Response and Reduction Factors

These results can be summarized for all the locations of the buildings by comparing the peak velocities recorded at each point for the two simulations with and without the urban environment, as seen in. Fig. 7.20.

Here we can see that at all the building locations, the motion at their bases is smaller for the site-city case than for the free-field simulation. The difference is most evident in the NS component of motion where, in the case without the building models all peak velocities are greater than ~0.9 m/s, whereas they are all smaller than the same limit value for the site-city simulation. Similar differences occur in the EW direction with a limit value in ~0.4 m/s.

The magnitude of the reductions that result from considering site-city interaction effects at the base of the buildings is summarized in Fig. 7.21. Here we see that the largest reductions occur in the EW component of motion, as we discussed earlier in the analysis of the perturbation field. On average, the peak values of velocities in the NS direction for the simulation with site-city interaction effects are about 1.6 times smaller than the response of the free field at the same locations. In the

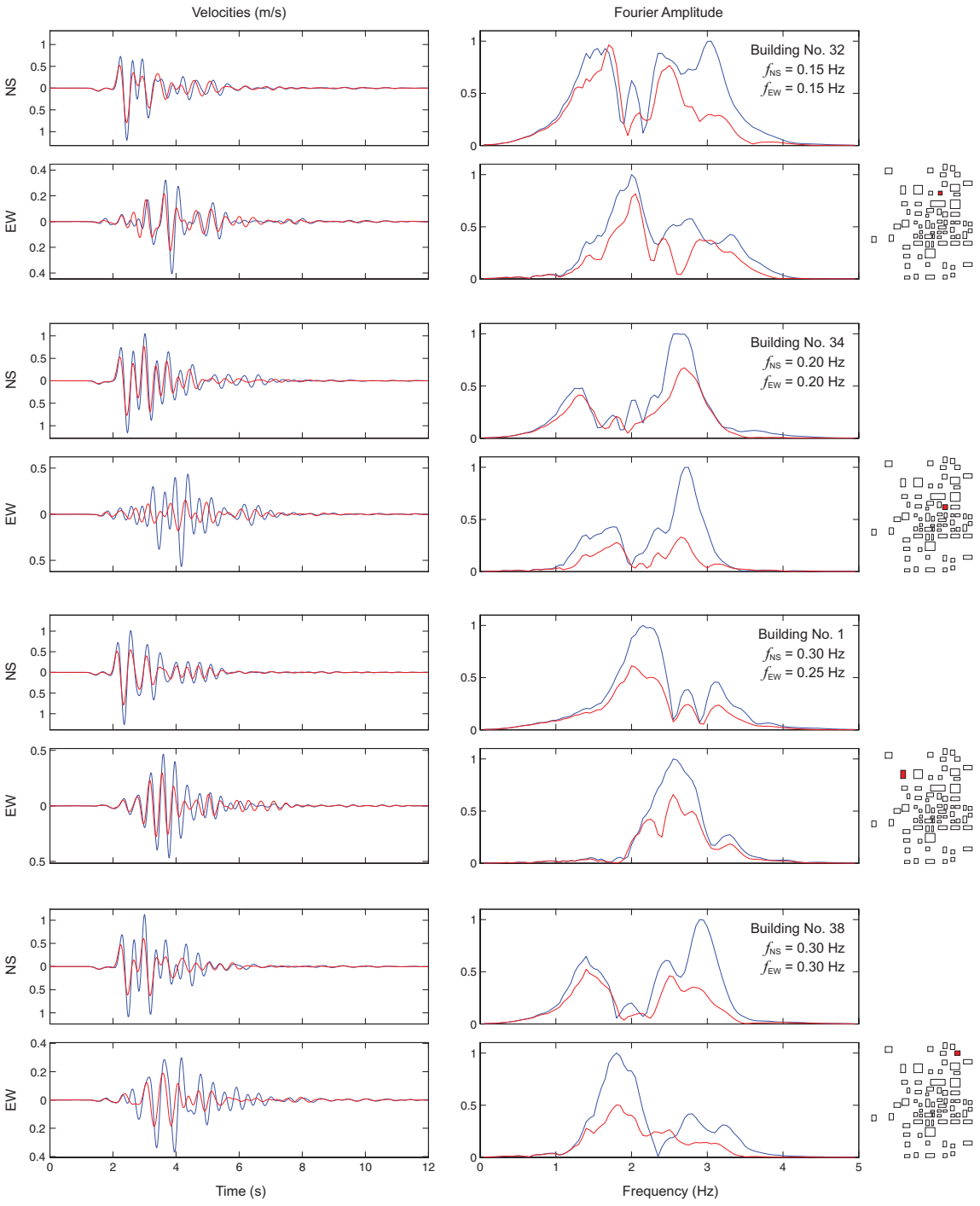

Figure 7.19: Comparison at the center of the base of selected buildings between the case with (red) and without (blue) the building models for the particle velocities in the two components of motion in both the time (left) and the frequency (right) domains.

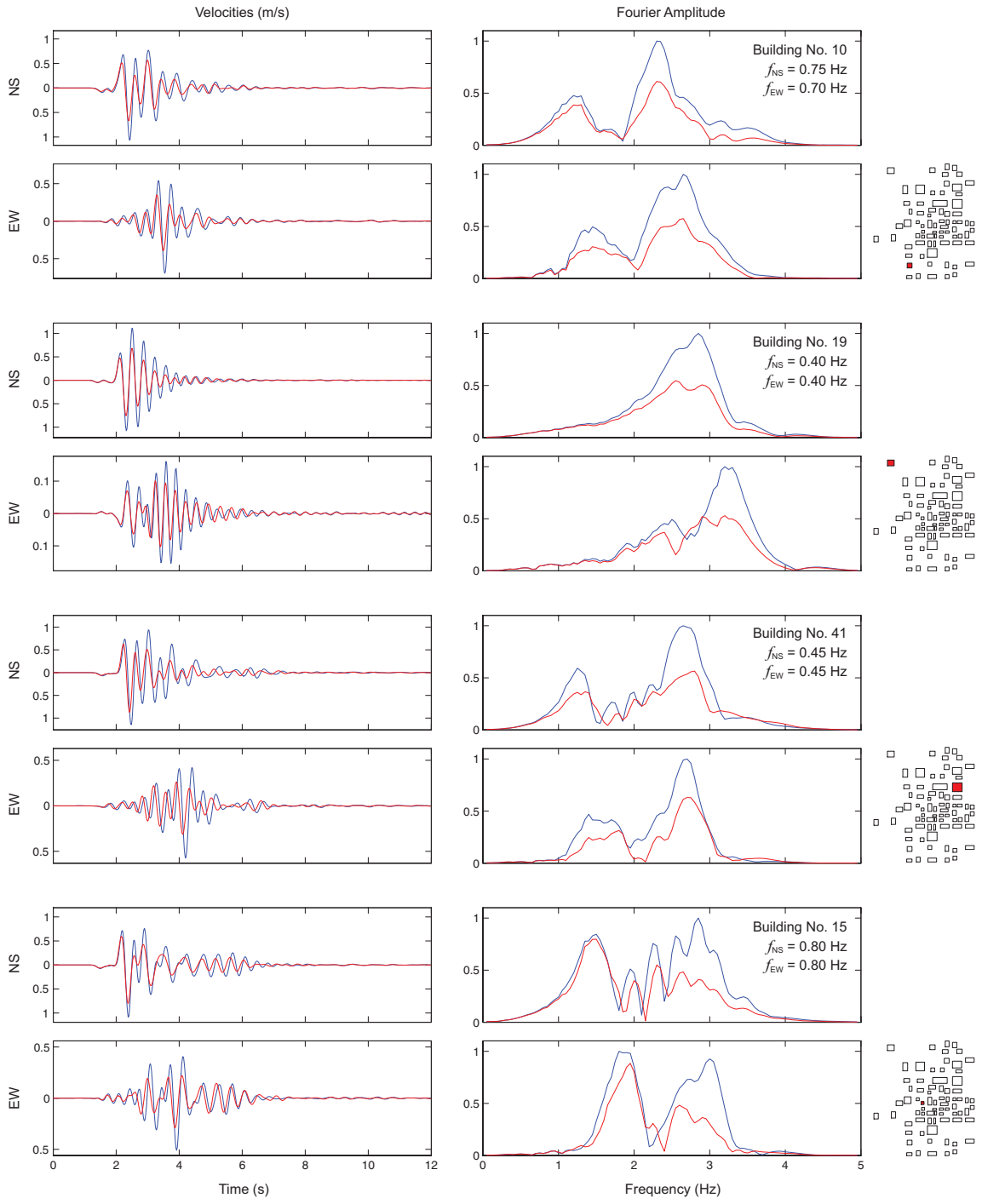

Figure 7.19: (*Continued*) Comparison at the center of the base of selected buildings between the case with (red) and without (blue) the building models for the particle velocities in the two components of motion in both the time (left) and the frequency (right) domains.

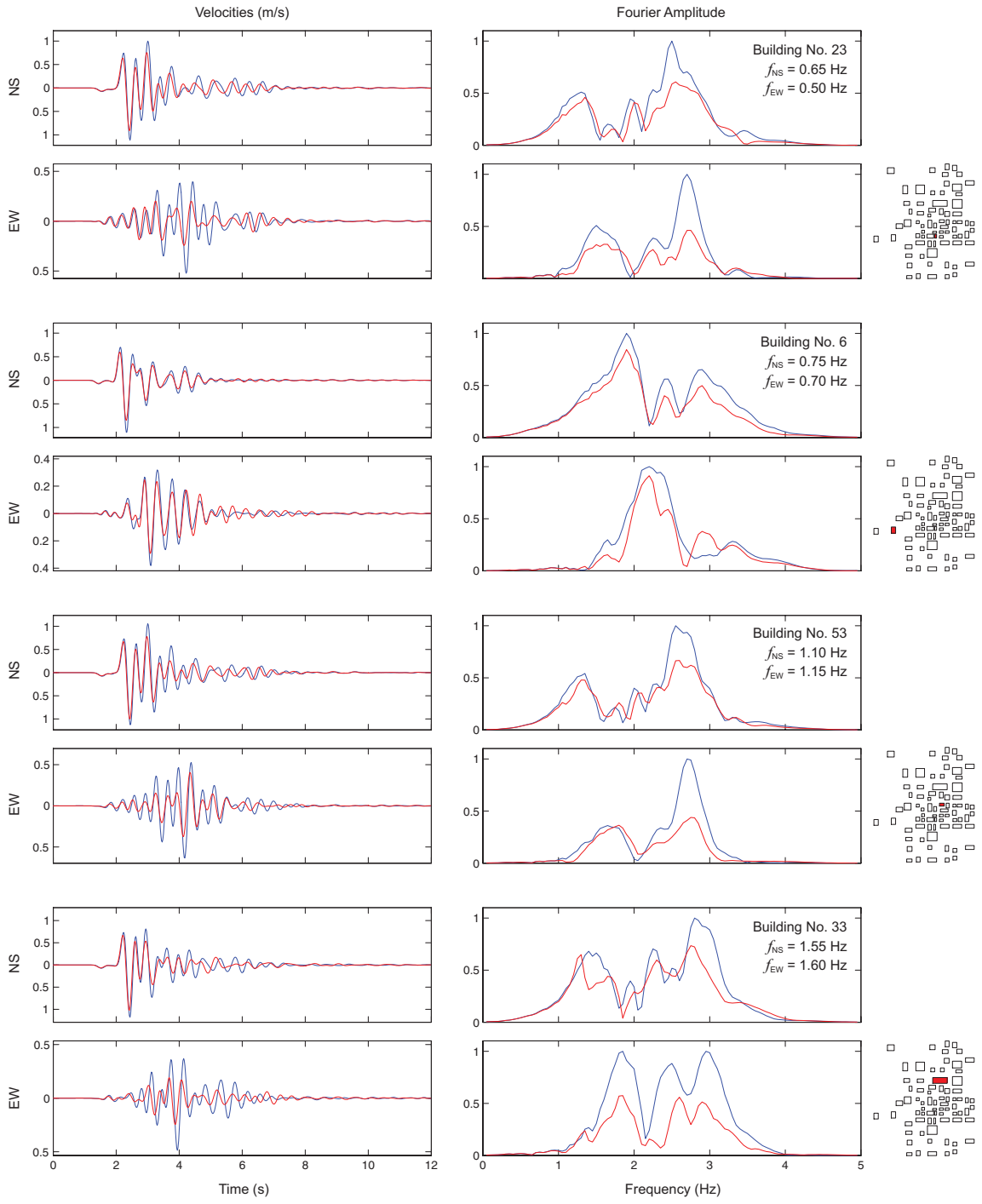

Figure 7.19: (*Continued*) Comparison at the center of the base of selected buildings between the case with (red) and without (blue) the building models for the particle velocities in the two components of motion in both the time (left) and the frequency (right) domains.

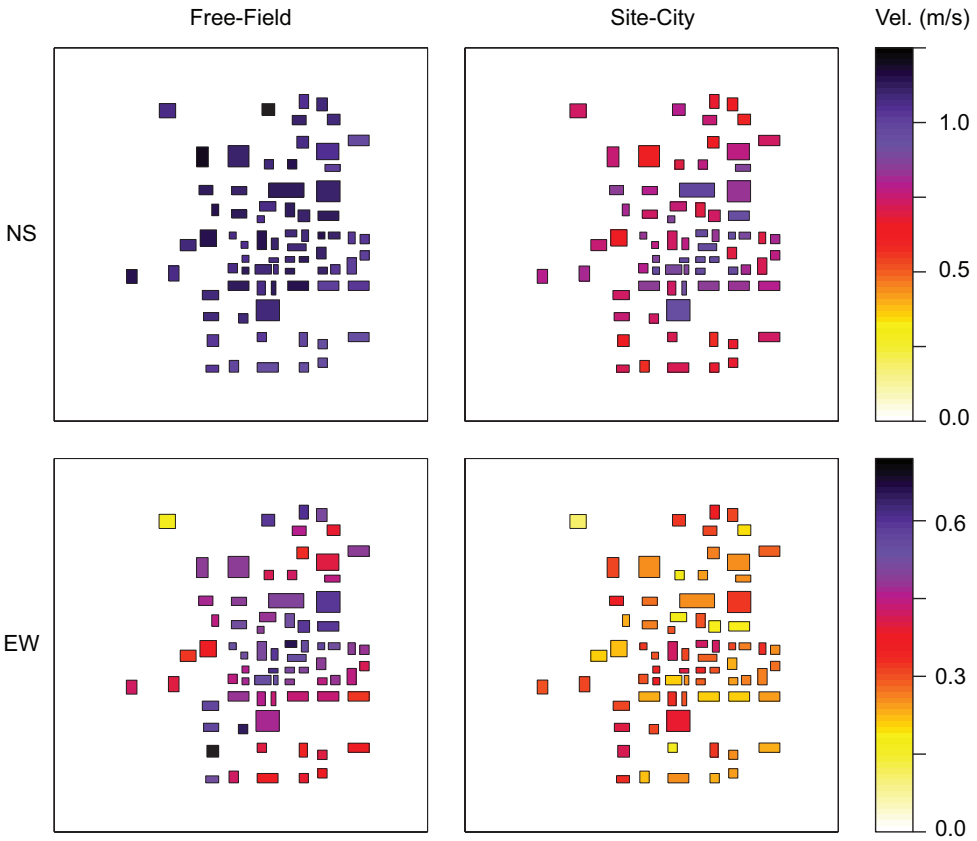

Figure 7.20: Comparison of peak velocities recorded at the center of the base of each building between the simulations with (right) and without (left) the building models, in the two components of motion (top: NS; bottom: EW).

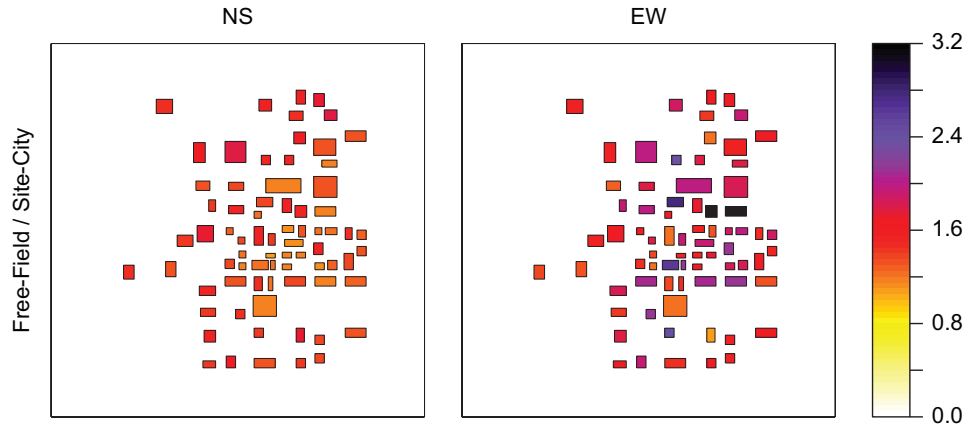

Figure 7.21: Reduction factors in peak velocity at the base of each building for the case of site-city interaction effects with respect to the response of the free-field.

EW component of motion the reduction is in all cases greater than 1.2 and at two locations it reaches a factor of 3.2. The distribution, however, does not seem to obey any particular pattern.

7.4.2 Response at the Roof of the Buildings

Time and Frequency Analysis

We now analyze the response of the buildings under two conditions, with and without considering site-city interaction effects. In the case without soil-structure coupling we use the motion recorded at the free-field to excite the building models with their base fixed to the ground. In this case the base is not allowed to rotate in any direction, NS and EW motion is imposed and we record the response at the center of the roof. On the other hand, the case with interaction effects is that of the site-city simulation that incorporate all the building models at once. The results for the same buildings used in the previous section are shown in Fig. 7.22.

In general, the response of the buildings with interaction is smaller than under the fixed-base condition. Except for the cases of buildings No. 33, 34, and 41, the phases and shape of the oscillations is similar in both cases. The most drastic changes occur in the case of building No. 41 in both components of motion, and in building No. 33 in EW. These are buildings with large plan dimensions and it is to be expected that their foundations will be more effective filtering the input motion and thus experiencing greater soil-structure interaction effects, especially at the larger frequencies, as it is the case with building No. 41 for $f \geq 2$ Hz.

Although in the time domain the responses are, in general, smaller for the site-city case, in frequency that is not always the case. Buildings No. 38 and 19, at 2.5 and 2.8 Hz in EW exhibit larger amplitudes than in the fixed-base simulation. These differences seem to be the result of a shift to the left in the resonance frequencies because of the more flexible soil-structure system—something we will see in greater detail in Section 7.4.3.

Peak Response and Reduction Factors

The overall effect of reduction in the response of the buildings at their roof is presented in Fig. 7.23, which shows the peak response in each direction for the velocities at the top of the structures under the fixed-base and flexible foundation cases. In general, responses for the fixed-base case are larger than those of the site-city interaction one.

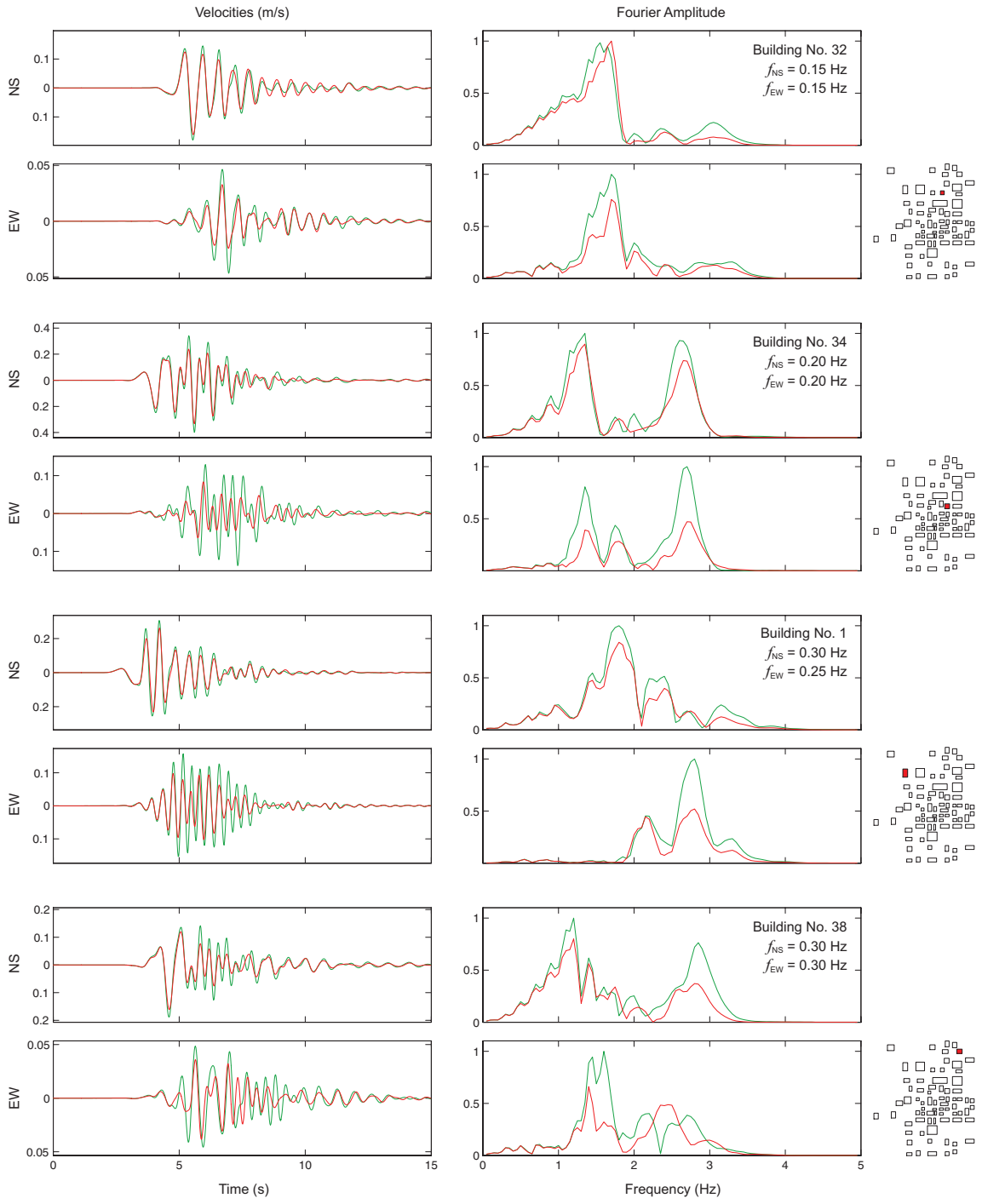

Figure 7.22: Comparison at the center of the roof of selected buildings between the case with (red) and without (green) soil-structure interaction for the particle velocities in the two components of motion in both the time (left) and the frequency (right) domains.

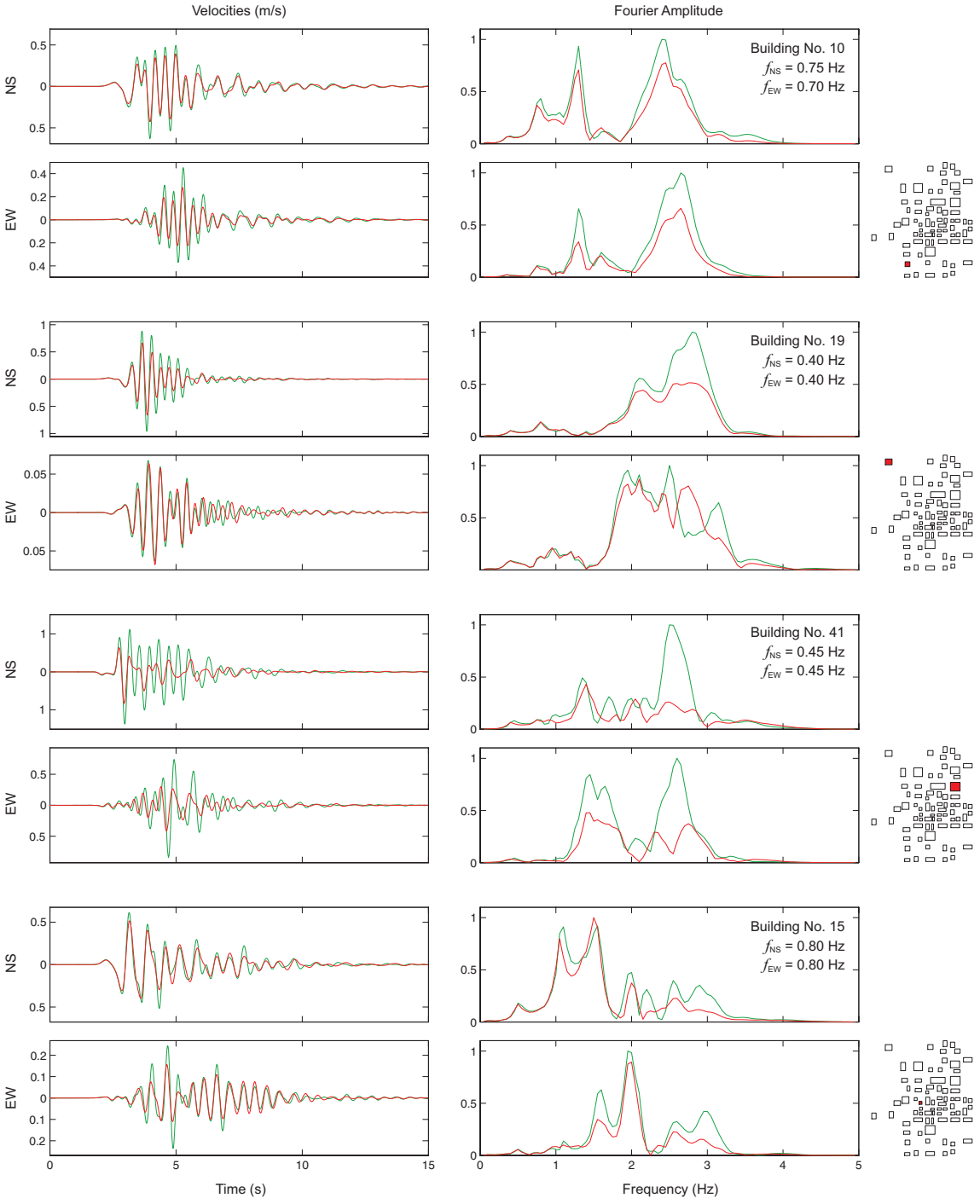

Figure 7.22: (*Continued*) Comparison at the center of the roof of selected buildings between the case with (red) and without (green) soil-structure interaction for the particle velocities in the two components of motion in both the time (left) and the frequency (right) domains.

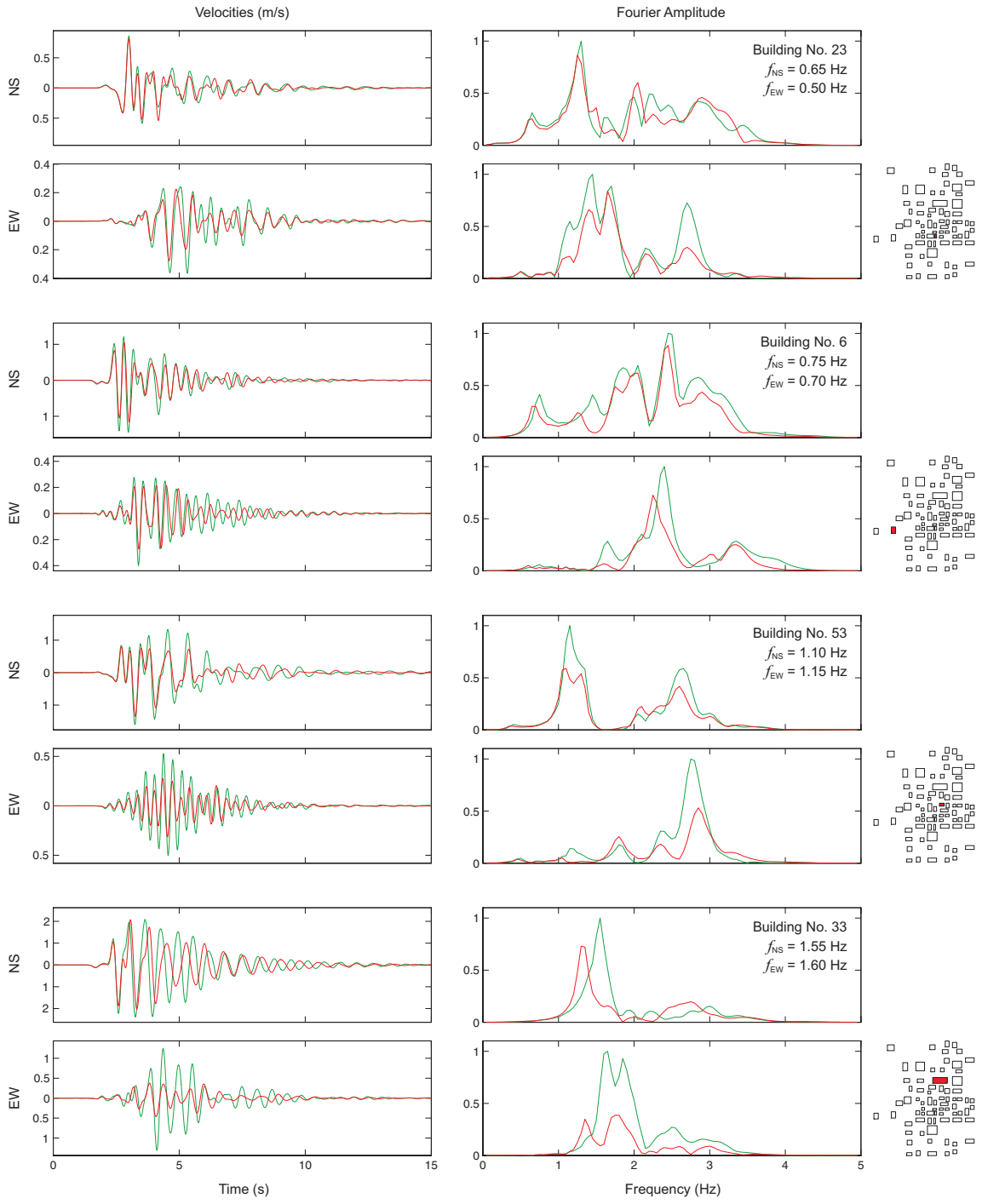

Figure 7.22: (*Continued*) Comparison at the center of the roof of selected buildings between the case with (red) and without (green) soil-structure interaction for the particle velocities in the two components of motion in both the time (left) and the frequency (right) domains.

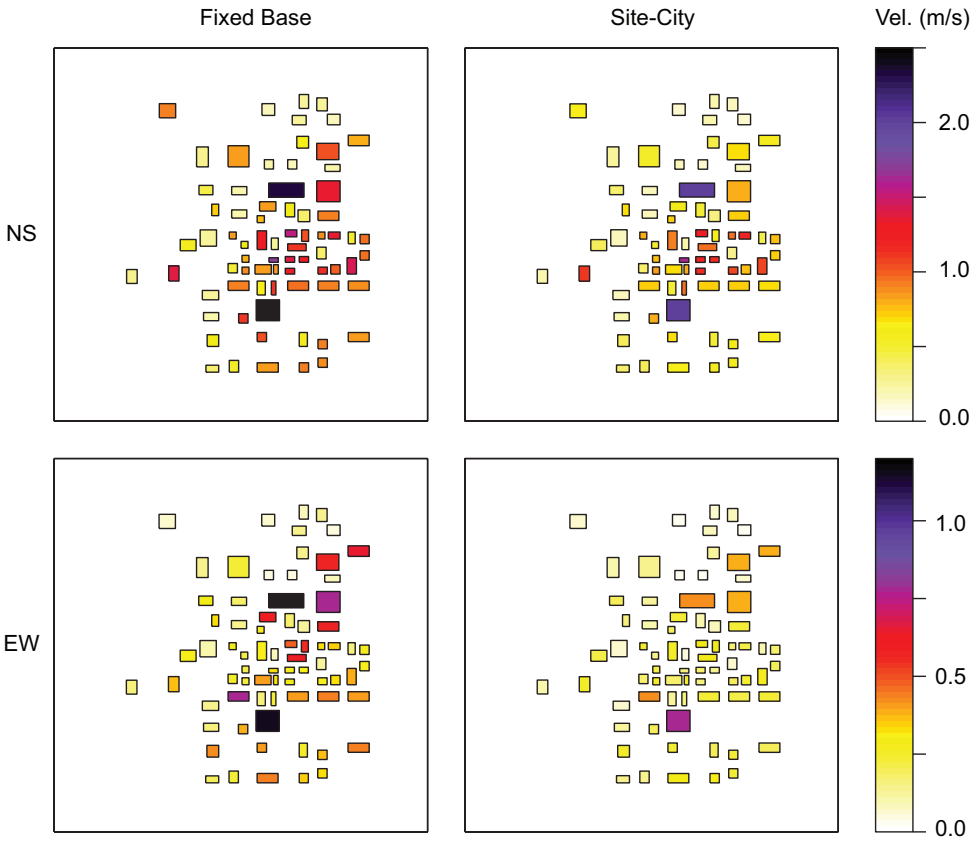

Figure 7.23: Comparison of peak velocities recorded at the center of the roof of each building between the simulations with (right) and without (left) the building models, in the two components of motion (top: NS; bottom: EW).

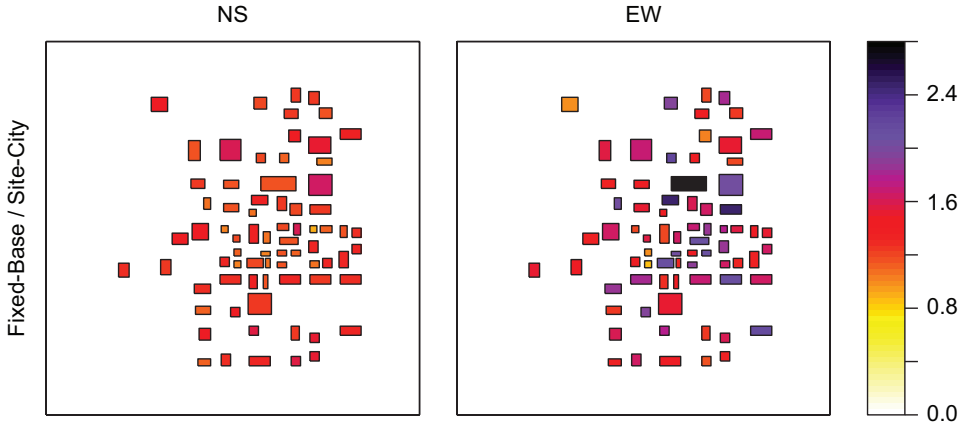

Figure 7.24: Reduction factors in peak velocity at the roof of each building for the case of site-city interaction effects with respect to the response of the free-field.

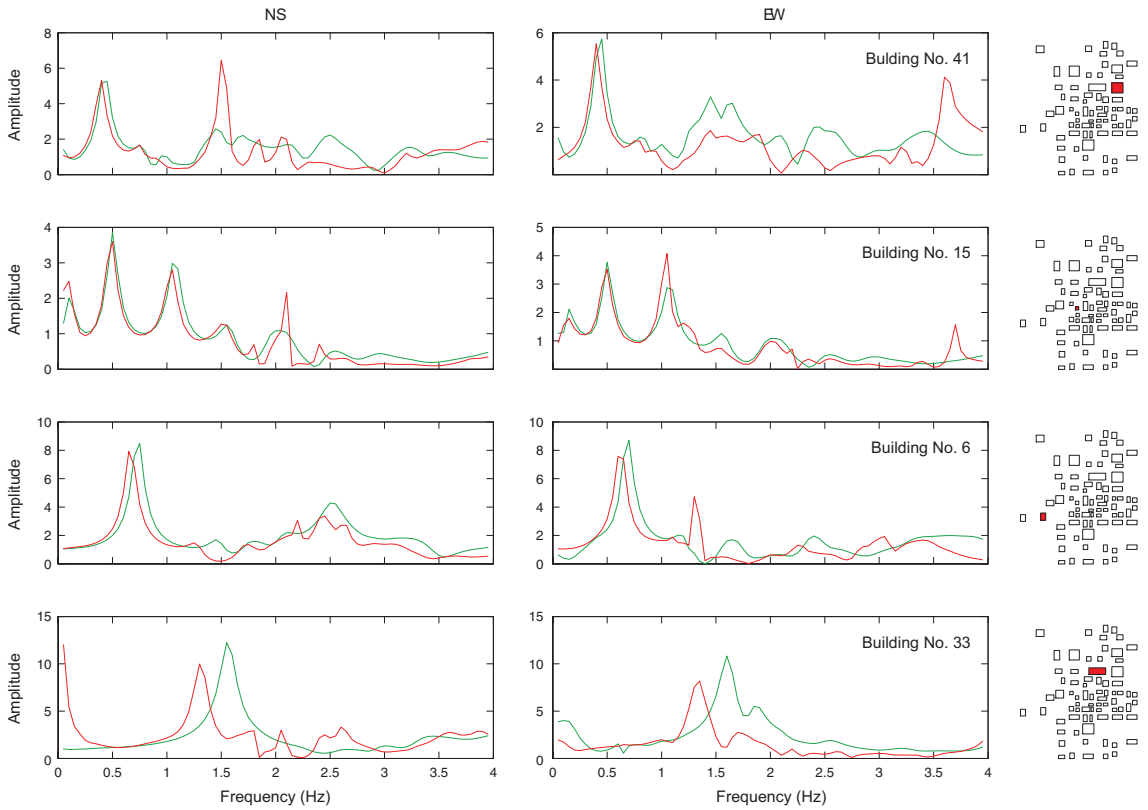

Figure 7.25: Comparison of fixed- (green) and flexible-base (red) transfer functions at selected buildings.

The reduction factors of the site-city case with respect to the fixed-base one are shown in Fig. 7.24. In this figure we see again that the larger reductions occur in the EW component of motion, most being larger than 1.2 and one as high as 2.8. In the NS direction, the reduction factors are more evenly distributed and are, on average, ~1.2–1.4.

7.4.3 Buildings Frequency Shift

We conclude our analysis of site-city and soil-structure interaction effects with a note on the change in the natural frequency of the buildings because of the flexibility introduced through coupling of the structures and their foundations with the soil.

Figure 7.25 shows a comparison of the fixed- and flexible-base transfer functions (roof-to-base) in the two components of motion. These comparisons clearly show how the fundamental frequencies of the buildings in the site-city case, because of their interaction with the underlaying soil, become more flexible, thus shifting the resonance frequencies to the left. The largest change of them all occurs in building No. 33, a reduction in the first mode of vibration of about 30 percent. All other cases exhibit a reduction of less than 10 percent.

8

Concluding Remarks

8.1 Summary and Conclusions

This thesis presents two new implementations in Hercules, the octree-based finite-element earthquake simulator developed by the Quake Group at Carnegie Mellon, that allow us to include nonlinear soil behavior in ground motion simulations and to incorporate the effects of the built environment while preserving the computational advantages that have made Hercules one of the most efficient computer programs in large-scale parallel-supercomputing applications for problems in computational seismology.

Including the effect of material nonlinearities for soft-soil deposits in three-dimensional heterogeneous basins has been achieved by implementing a finite-element procedure derived from the theory of rate-dependent plasticity, applied to reproduce the behavior of soils—typically considered to be rate-independent materials—by predicting the changes in the plastic strain by means of a power law as proposed by (Perzyna, 1963).

Incorporating the effect of the presence of urban settings is achieved by modifying Hercules' finite-element meshing routines so that models of large inventory of buildings can be included in the simulation domain as additional block elements that are adjusted to emulate the general geometric and dynamic characteristics of buildings in city-like arrangements. Each subset of elements representing a building-foundation system is assigned the corresponding material properties so that it reproduces the expected fundamental frequency of the real structure.

These implementations are tested under realistic conditions in the three-dimensional model of a sedimentary basin under the excitation of a scenario earthquake of magnitude M_{w} 5.2. The results of two nonlinear simulations with moderate and severe conditions of plasticity, and an independent

simulation considering the effects of an inventory of 74 buildings, under linear soil material behavior, led us to conclude that:

- There exist three-dimensional, basin, and directivity effects in modeling the response of a basin with soil capable of deforming nonlinearly that are different from those observed under purely elastic conditions. It would not be possible to reproduce this behavior by means of simplified one- and two-dimensional approximations.
- The simulations performed considering the effect of elastoplastic soil materials exhibit the typical characteristics of deamplification of peak velocities and accelerations (by factors ≥ 2), increase in permanent displacements away from the source due to plastic deformation, slower shear wave velocities, dissipation of low-frequency energy, and introduction of higher frequencies in the response. These effects are qualitatively similar to those observed been observed in actual records from past earthquakes, and can be regarded as evidence of nonlinearities in soft deposits.
- The inclusion of a large inventory of buildings has the potential of greatly altering the ground motion at the interior of urban boundaries and within a radius of a few hundred meters (or more, depending on the impedance of the foundations with respect to the underlying soil). These changes manifest themselves through perturbations to the free-field motion and by a drastic increase in the spatial variability of the ground response.
- In general, it was found that the response of buildings (at their base and in the superstructure) is considerably attenuated by the consideration of soil-structure and site-city effects—with reduction factors varying from 1.2 to 3. Individual buildings, however, may experience larger or smaller excitation due to ground shaking depending on their dynamic properties, and on their location with respect to other structures and incoming waves, increasing the level of complexity and the number of factors one must consider in delicate urban seismology studies.

8.2 Future Work

The accomplishments made by this research open a variety of avenues for future research. Among the most relevant ones, we highlight the following.

- To improve and incorporate more elaborate soil constitutive models that include desired physical phenomena such as non-constant hardening conditions, and two-phase continuum formulations for undrained materials including pore-pressure.

- To calibrate the strain rate and strain-rate sensitivity constants used in the rate-dependent plasticity formulation implemented here, so that this approach can effectively and accurately be used in simulations of material models with increased heterogeneity. Alternative approaches to this could be: to compare results with other nonlinear simulation codes (verification), or to reproduce laboratory results of nonlinear soil behavior (validation).
- To conduct parametric studies to understand the inner details of multiple soil-structure interaction effects, so that these can be extrapolated for the interpretation of the more complex phenomena observed in larger site-city interaction problems.
- To perform simulations with building inventories at scale, and study the regional effect that even more realistic urban settings may have beyond the city boundaries.
- To extend the implementations used for meshing the building models in two directions: (1) to incorporate irregular (non-rectangular) prismatic models of buildings; and (2) to emulate the surficial topography.

A

Background Chronology

This appendix contains three figures that follow the chronology of major publications, events, and developments related to the three main subjects of this thesis. All figures roughly follow the narrative of the research background and literature review presented in the Introduction (Sections 1.1–1.3). Additional items that were not covered in the text are included for reference. In the interest of space some relevant publications may have been left out.

Figure A.1 presents the chronology of major events and publications in seismic ground motion simulation; Fig. A.2 does the same for the study and evidence of nonlinear soil behavior in seismology and engineering; and Fig. A.3 shows the transition from classical soil-structure to modern site-city interaction effects. In each case, other relevant events and developments are included, as denoted in the figures. Those comprise items such as research projects initiatives, research centers, and software developments. When related to a particular publication, major earthquakes are also indicated.

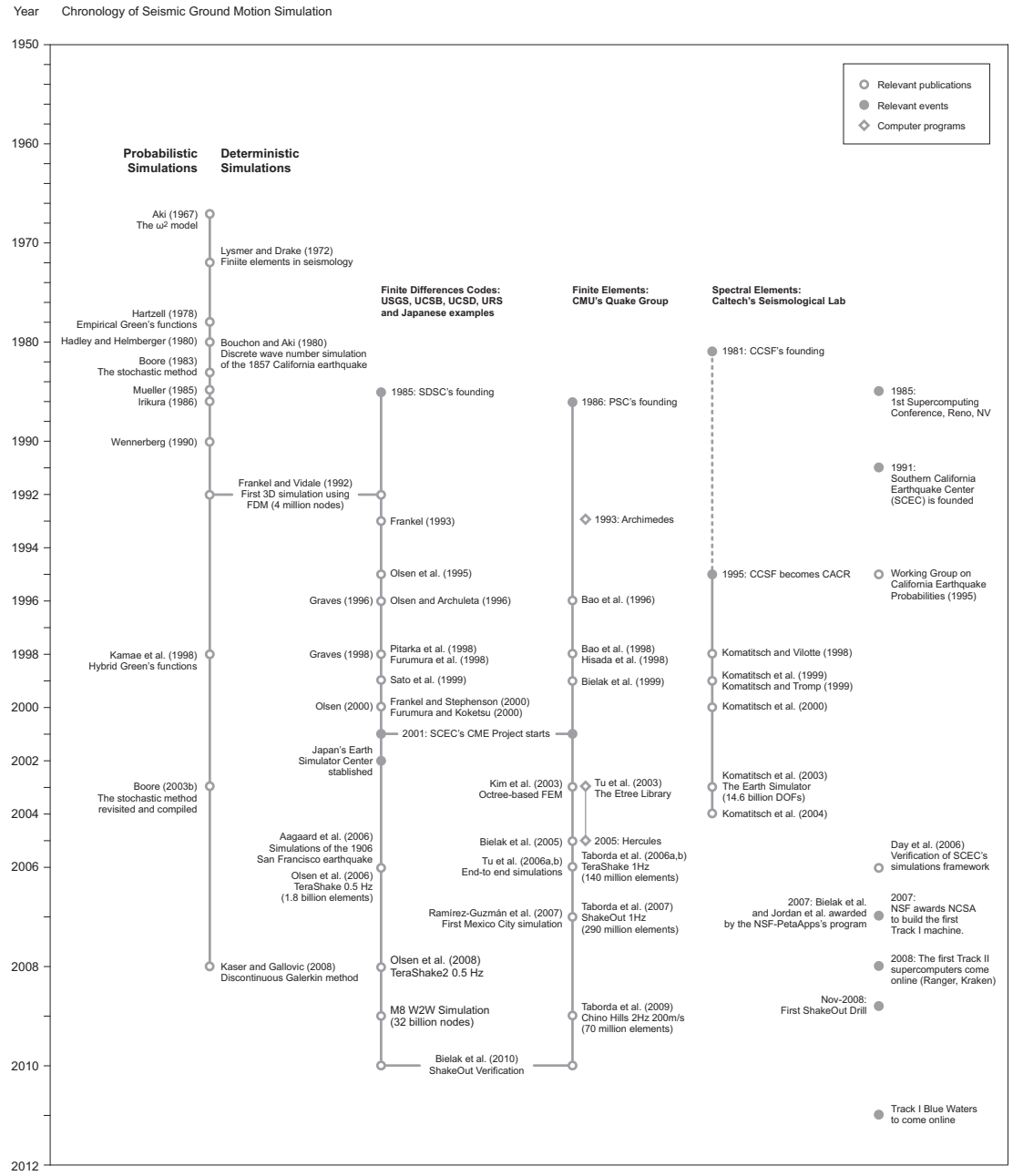

Figure A.1: Chronology of seismic ground motion simulations. The leftmost timeline divides non-deterministic from deterministic approaches. The other lines show three other independent timelines associated with three of the major numerical methods used to conduct earthquake simulations. Each timeline is associated with the establishment of a supercomputing center most commonly accessed by research groups working on each method. Other events related to large-scale simulation projects are included in the rightmost set.

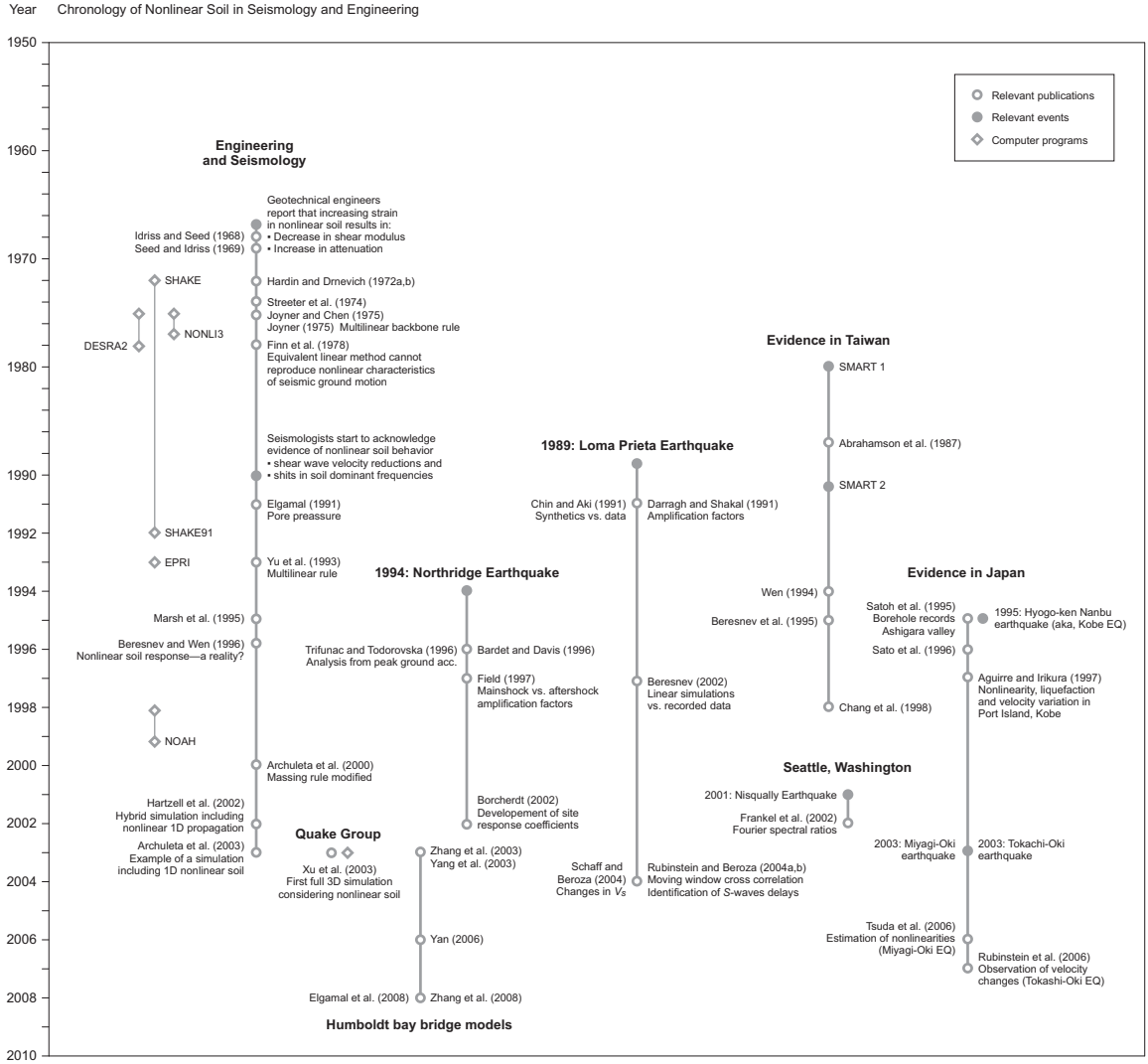

Figure A.2: Chronology of nonlinear soil in seismology and engineering. The left hand timeline presents a sequence of publications that demark mindset changes in the perception of soil nonlinearities from geotechnical engineers to seismologists. The leftmost set shows the progress of commercial software for nonlinear soil analysis. On the right, grouped by major earthquakes or country, the other timelines present relevant publications to each field. There are additional relevant projects and publications scattered throughout.

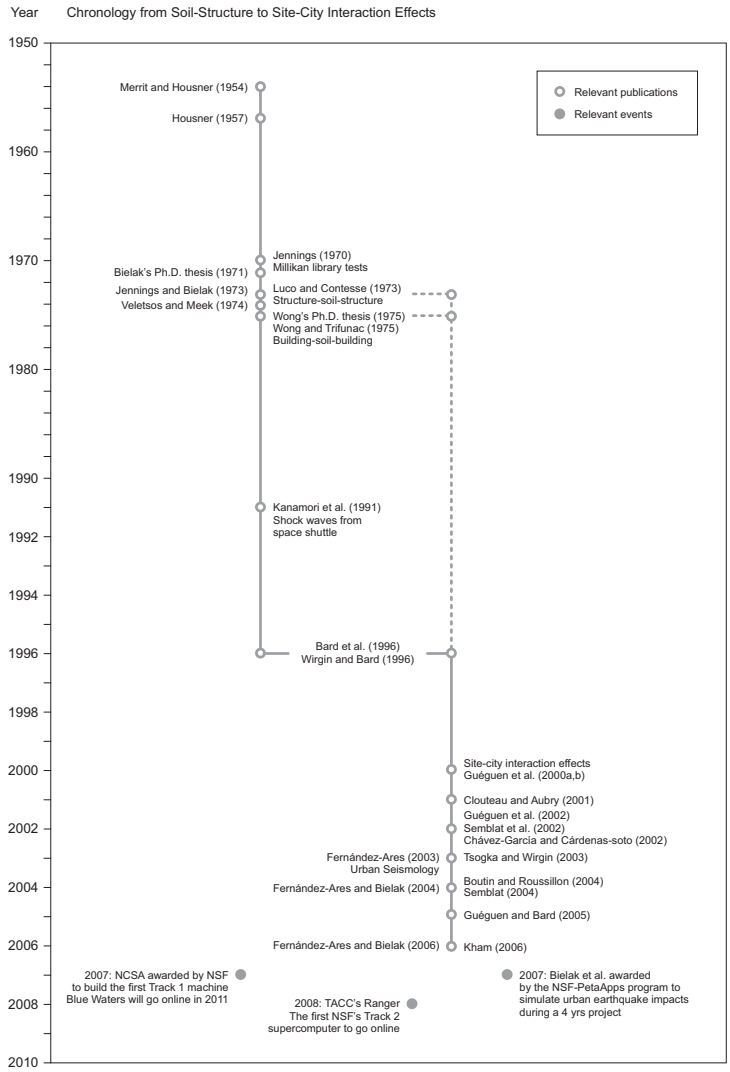

Figure A.3: Chronology of the development from classical soil-structure to modern site-city interaction effects. A major line of transition is placed at 1996, after Bard et al.; but as suggested earlier, a double-bridge is marked after Luco and Contesse (1973), Wong (1975) and Wong and Trifunac (1975). Scattered at the bottom are three major events related to the topic and this proposal.

B

Stiffness Contribution Computation

This appendix presents an illustration on a 1D problem of the differences between the conventional and efficient methods used in Hercules for the computation of the stiffness contribution to the solution of the wave propagation differential equation after numerical discretization (after Taborda et al., 2010).

We evaluate the number of operations required to obtain the product $\mathbf{K^e u^e}$ for a longitudinal wave propagation problem, modeling an elastic bar in free vibration with a 1D second-order element. In this case, the linear momentum equation shown in Section 2.1.1 reduces to (B.1). σ is the normal stress, ρ the mass density, and u the displacement, which is both a function of time and space, i.e., $u = u(x,t)$. Here, spatial derivatives will be denoted with a prime. Dots stand for derivatives with respect to time.

$$\sigma' = \rho\ddot{u} \tag{B.1}$$

The internal virtual work in a given element for a homogeneous material with Young's modulus, E, constant, can be written as seen in (B.2).

$$V = \int_\Omega \upsilon'\sigma d\Omega = E\int_0^h \upsilon' u' dx \tag{B.2}$$

Here, $\sigma = E\epsilon$ and $\epsilon = u'$, therefore $\sigma = Eu'$. With this, (B.1) is the one-dimensional wave equation. In (B.2), υ is a test function that depends only on x, i.e., $\upsilon = \upsilon(x)$; and h is the mesh

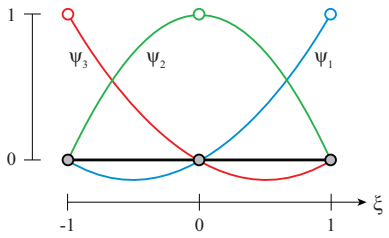

Figure B.1: 1D element with Lagrangian quadratic shape functions $\psi_i(\xi)$.

size, or element's length. Introducing the change of coordinates in (B.3), (B.2) becomes (B.4).

$$x = \frac{h}{2}(\xi + 1) \tag{B.3}$$

$$V = \frac{2E}{h}\int_{-1}^{1} \upsilon'(\xi)u'(\xi,t)dx \tag{B.4}$$

The displacement and test functions are approximated by (B.5), where ψ are the shape functions of the element in local ξ coordinates. Then, the internal virtual work (B.4) becomes (B.6).

$$\begin{aligned} u(\xi,t) &= \psi^T(\xi)\mathbf{u^e}(t) \\ \upsilon(\xi) &= \psi^T(\xi)\mathbf{v} \end{aligned} \tag{B.5}$$

$$\begin{aligned} V &= \mathbf{v}^T \frac{2E}{h}\int_{-1}^{1} \psi'\psi'^T d\xi \ \mathbf{u^e} \\ &= \mathbf{v}^T\mathbf{K^e}\mathbf{u^e} \end{aligned} \tag{B.6}$$

It follows from (B.6) that the element stiffness is given by (B.7). This is a particular case of (2.19), seen in Section 2.2.2, in which $\mathbf{C} = 2E/h$ is constant, thus can be taken out of the integrand.

$$\mathbf{K} = \frac{E}{2h}\int_{-1}^{1} \psi'\psi'^T d\xi \tag{B.7}$$

$$\psi^T(\xi) = \left\{ \frac{1}{2}\xi - \frac{1}{2}\xi^2 \ , \ 1 - \xi^2 \ , \ \frac{1}{2}\xi + \frac{1}{2}\xi^2 \right\} \tag{B.8}$$

Adopting a 1D element with Lagrangian quadratic shape functions as shown in Fig. B.1 and defined by (B.8), one can easily expand (B.7) and solve the stiffness contribution given by the product $\mathbf{Ku}$ for the two conventional and efficient methods as follows.

B.1 Conventional Method

Replacing (B.8) into (B.7) and multiplying with the displacement vector we can expand the product **Ku** as seen in (B.9). Not counting the operations necessary to obtain the outer constant $E/3h$, the matrix-vector product in (B.9) requires 9 multiplications, then 2 additions per row, and finally 3 more multiplications. This yields a total 18 operations: 12 multiplications and 6 additions.

$$\mathbf{Ku} = \frac{E}{3h}\begin{bmatrix} 7 & 8 & -1 \\ 8 & 16 & -8 \\ -1 & -8 & 7 \end{bmatrix}\begin{Bmatrix} u_1 \\ u_2 \\ u_3 \end{Bmatrix} \tag{B.9}$$

B.2 Efficient Method

To apply the efficient method we need to write (2.21) in Section 2.2.2 using (2.20) and (B.7). This yields (B.10) as the new expression for the 1D element stiffness matrix. The auxiliary matrix **A** and vector ϕ that satisfy (2.20) are shown in (B.11).

$$\mathbf{K} = \frac{2E}{h}\mathbf{A}^T \int_{-1}^{1} \phi' \left(\phi'\right)^T d\xi \ \mathbf{A} \tag{B.10}$$

$$\mathbf{A}^T\phi = \begin{bmatrix} 0 & \frac{1}{2} & -\frac{1}{2} \\ 1 & 0 & -1 \\ 0 & \frac{1}{2} & \frac{1}{2} \end{bmatrix}\begin{Bmatrix} 1 \\ \xi \\ \xi^2 \end{Bmatrix} = \begin{Bmatrix} \psi_1 \\ \psi_2 \\ \psi_3 \end{Bmatrix} \tag{B.11}$$

Using **A** and ϕ as in (B.11), the element stiffness matrix (B.10) becomes (B.12), which can be written in compact form as in (B.13).

$$\mathbf{K^e} = \frac{E}{2h}\begin{bmatrix} 0 & 1 & -1 \\ 2 & 0 & -2 \\ 0 & 1 & 1 \end{bmatrix}\begin{bmatrix} 0 & 0 & 0 \\ 0 & 2 & 0 \\ 0 & 0 & \frac{8}{3} \end{bmatrix}\begin{bmatrix} 0 & 2 & 0 \\ 1 & 0 & -1 \\ -1 & -2 & 1 \end{bmatrix} \tag{B.12}$$

$$\mathbf{K^e}\frac{E}{2h}\mathbf{A}^T\mathbf{HA} \tag{B.13}$$

Finally, to compute the stiffness contribution one must compute the product $\mathbf{K^e u^e}$ grouping the terms in (B.13) with $\mathbf{u^e}$ in the order denoted by the parenthesis in (B.14).

$$\mathbf{K^e u^e} = \frac{E}{2h}\left(\mathbf{A}^T\left(\mathbf{H}\left(\mathbf{A u}\right)\right)\right) \tag{B.14}$$

As when comparing (2.19) and (2.21) in Section 2.2.2, (B.12) and (B.14) seem, at first sight, to entail a larger number of operations than the equivalent $\mathbf{Ku}$ product in the conventional method (B.9). However, as previously mentioned, matrix $\mathbf{H}$ is sparse and made up of constants and matrix $\mathbf{A}$ consists only of 1 and -1 terms. Thus, (B.14) can be easily expanded explicitly, resulting in (B.15).

$$\begin{aligned}
\alpha = \mathbf{A u} &= \begin{Bmatrix} 2u_2 \\ u_1 - u_3 \\ -u_1 - 2u_2 \end{Bmatrix} \qquad \beta = \mathbf{H}\alpha = \begin{Bmatrix} 0 \\ 2\alpha_1 \\ \frac{8}{3}\alpha_3 \end{Bmatrix} \\
\gamma = \mathbf{A}^T\beta &= \begin{Bmatrix} \beta_1 - \beta_2 \\ 2(\beta_1 - \beta_3) \\ \beta_2 + \beta_3 \end{Bmatrix} \qquad \mathbf{Ku} = \frac{E}{2h}\begin{Bmatrix} \gamma_1 \\ \gamma_2 \\ \gamma_3 \end{Bmatrix}
\end{aligned} \tag{B.15}$$

It follows from (B.15), that the breakdown of operations in the efficient method to compute the stiffness contribution for a 1D quadratic element is: 8 multiplications and 6 additions; for a total of 14 operations. A net difference of 4 with respect to the conventional method, representing a reduction of 22 percent.

B.3 Computational Implications

Table B.1 shows a comparison of the number of operations required using both methods for three different kind of elements in 1D, 2D, and 3D. It also includes the percentage of reduction in the efficient method with respect to the conventional one for each case broken in multiply, add, and total number of operations. The 2D 4-node square element in the middle of Table B.1 is equivalent to the case presented by the authors who originally proposed the efficient method (Balazovjech and Halada, 2007).

The rightmost column in Table B.1 shows the results for an 8-node trilinear cubic element just as the hexahedra used in Hercules. Note that the reduction in multiply operations is of one order

Table B.1: Number of operations for three different type of elements

		1D Quadratic	 2D Bilinear	 3D Trilinear
Multiply	Conventional	12	64	576
	Efficient	8	26	56
	(Reduction)	(33%)	(59%)	(90%)
Add	Conventional	6	56	552
	Efficient	6	22	317
	(Reduction)	(0%)	(60%)	(42%)
Total Ops.	Conventional	18	120	1128
	Efficient	14	48	373
	(Reduction)	(22%)	(60%)	(67%)

of magnitude. The reduction in the total number of additions is over 40 percent. As a result, the implementation of the efficient method in Hercules meant a reduction of 67 percent in the total number of operations required to obtain the stiffness contribution to the solution of the equation of motion with respect to the previous conventional implementation. Comparisons of the reduction in the share of computation time were presented in Fig. 2.5 in Section 2.2.3.

C

Vertex Touches

As mentioned in Section 4.2.3 of the main body of the thesis, the key ingredients to constructing the nodes table during the mesh extraction process is the identification of the nodes as either anchored or dangling. To do so, knowing the number of vertex touches and their characteristics is essential. This appendix presents all the possible cases of vertex touches and distinguish them as anchored or dangling (Table C.1 and Figs. C.1 to C.7). In the figures, for reference, the elements touching the vertex of interest are colored. Anchored nodes are represented with large blue spheres and dangling nodes are represented with green ones. Small blue spheres are the anchored nodes that control the values at the dangling ones. New cases that did not occur before the implementations presented in this thesis for modeling buildings, are pointed out in the figure caption.

Table C.1: Summary of vertex touches and the different possibilities for dangling and anchored nodes depending on the number of touches.

Number	Node Type		Location		Hanging from	New	Shown
of Touches	Anchored	Dangling	Interior	Exterior	n Nodes	Case	in Fig.
8	•		•				C.1
6	•			•		•	C.2a
6		•	•		2		C.2b
5	•			•		•	C.3
4	•			•			C.4a
4		•	•		2		C.4b
4		•	•		4		C.4c
3		•		•	2	•	C.5
2	•			•			C.6a
2		•	•		2		C.6b
2		•		•	2		C.6c
1	•			•			C.7a
1		•		•	2	•	C.7b
1		•		•	4	•	C.7c

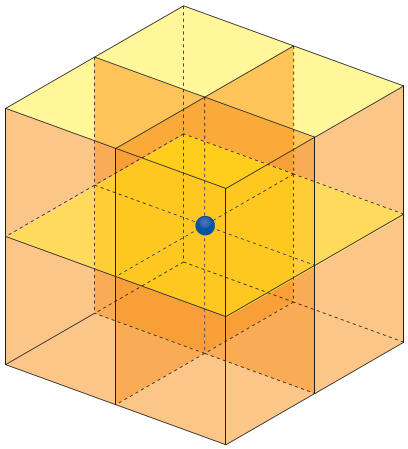

Figure C.1: Eight touches vertex, anchored interior.

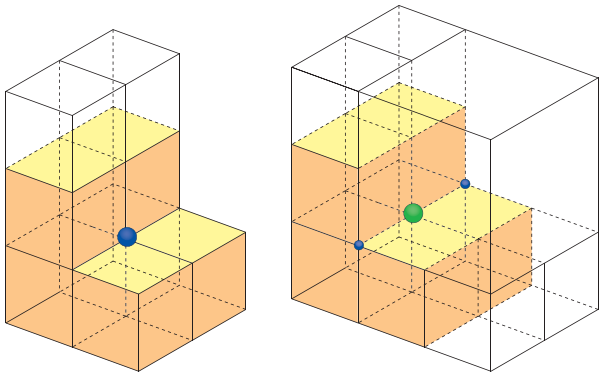

(a) Anchored exterior (**new**)

(b) Dangling interior

Figure C.2: Six touches vertices.

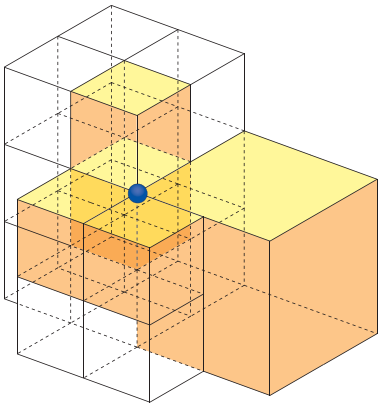

Figure C.3: Five touches vertex, anchored exterior (**new**).

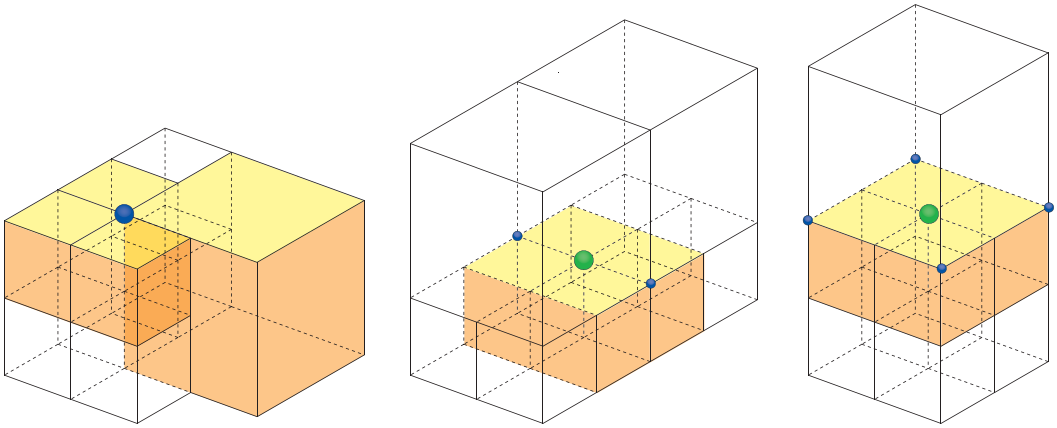

(a) Anchored exterior **(b)** Dangling from 2, interior **(c)** Dangling from 4, interior

Figure C.4: Four touches vertices.

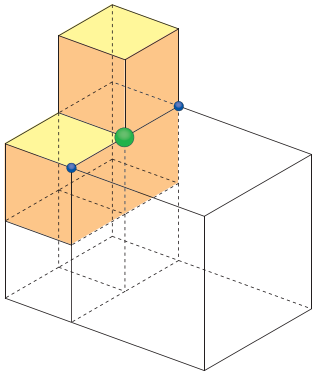

Figure C.5: Three touches vertex, anchored exterior (**new**).

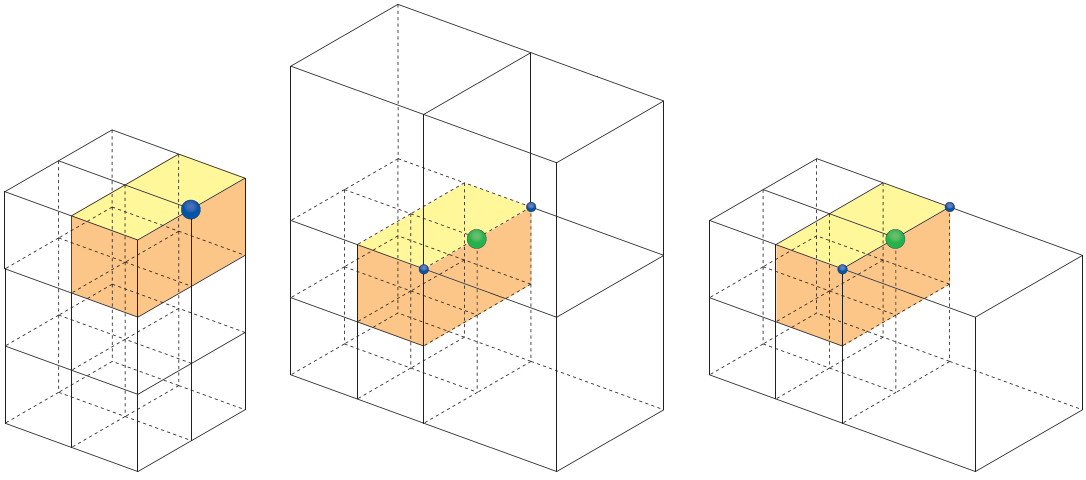

(a) Anchored exterior **(b)** Dangling interior **(c)** Dangling exterior

Figure C.6: Two touches vertices.

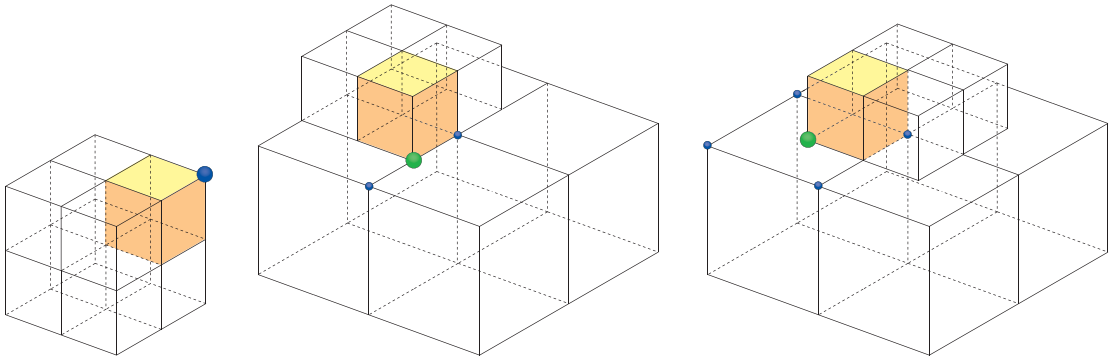

(a) Anchored **(b)** Dangling from 2 (**new**) **(c)** Dangling from 4 (**new**)

Figure C.7: One touch vertices.

References

Aagaard, B. T., Brocher, T. M., Dolenc, D., Dreger, D., Graves, R. W., Harmsen, S., Hartzell, S., Larsen, S., and Zoback, M. L. (2008). Ground-motion modeling of the 1906 San Francisco earthquake, Part I: Validation using the 1989 Loma Prieta earthquake. *Bulletin of the Seismological Society of America*, 98(2):989–1011.

Abrahamson, N. A., Bolt, B. A., Darragh, R. B., Penzien, J., and Tsai, Y. B. (1987). The SMART I accelerograph array (1980-1987): A review. *Earthquake Spectra*, 3(2):263–287.

Adachi, T. and Oka, F. (1982). Constitutive equations for normally consolidated clay based on elasto-viscoplasticity. *Soils and Foundations*, 22(4):57–70.

Adrion, W. R., Branstad, M. A., and Cherniavsky, J. C. (1982). Validation, verification, and testing of computer software. *Computer Surveys*, 14(2):159–192.

Aguirre, J. and Irikura, K. (1997). Nonlinearity, liquefaction, and velocity variation of soft soil layers in Port Island, Kobe, during the Hyogo-ken Nanbu earthquake. *Bulletin of the Seismological Society of America*, 87(5):1244–1258.

Akcelik, V., Bielak, J., Biros, G., Epanomeritakis, I., Fernández, A., Ghattas, O., Kim, E. J., López, J., O'Hallaron, D., Tu, T., and Urbanic, J. (2003). High resolution forward and inverse earthquake modeling on terasacale computers. In *SC '03: Proceedings of the 2003 ACM/IEEE Conference for High Performance Computing and Networking*, page 8, Phoenix, Arizona. IEEE Computer Society.

Aki, K. (1967). Scaling law of seismic spectrum. *Journal of Geophysical Research*, 72(4):1217–1231.

Aki, K. (2003). A perspective on the history of strong motion seismology. *Physics of The Earth and Planetary Interiors*, 137(1-4):5–11.

Alterman, Z. and Karal, F. C. (1968). Propagation of elastic waves in layered media by finite difference methods. *Bulletin of the Seismological Society of America*, 58(1):367–398.

Anderson, J. G. (2004). Quantitative measure of the goodness-of-fit of synthetic seismograms. In Canadian Association for Earthquake Engineering, editor, *Proceedings of the 13th World Conference on Earthquake Engineering*, Vancouver, British Columbia, Canada. International Association for Earthquake Engineering. Paper 243.

Archuleta, R. J. and Day, S. M. (1980). Dynamic rupture in a layered medium: The 1966 Parkfield earthquake. *Bulletin of the Seismological Society of America*, 70(3):671–689.

Archuleta, R. J. and Frazier, G. A. (1978). Three-dimensional numerical simulations of dynamic faulting in a half-space. *Bulletin of the Seismological Society of America*, 68(3):541–572.

Archuleta, R. J., Liu, P., Steidl, J. H., Bonilla, L. F., Lavallée, D., and Heuzé, F. E. (2003). Finite-fault site-specific acceleration time histories that include nonlinear soil response. *Physics of The Earth and Planetary Interiors*, 137(1-4):153–181.

Askan, A., Akcelik, V., Bielak, J., and Ghattas, O. (2007). Full waveform inversion for seismic velocity and anelastic losses in heterogeneous structures. *Bulletin of the Seismological Society of America*, 97(6):1990–2008.

Assimaki, D., Li, W., Steidl, J., and Schmedes, J. (2008). Quantifying nonlinearity susceptibility via site-response modeling uncertainty at three sites in the Los Angeles basin. *Bulletin of the Seismological Society of America*, 98(5):2364–2390.

Balazovjech, M. and Halada, L. (2007). Effective computation of restoring force vector in finite element method. *Kybernetika*, 49(6):767–776.

Balci, O. (1994). Validation, verification, and testing techniques throughout the life cycle of a simulation study. *Annals of Operations Research*, 53(1):121–173.

Bao, H., Bielak, J., Ghattas, O., Kallivokas, L. F., O'Hallaron, D. R., Shewchuk, J. R., and Xu, J. (1996). Earthquake ground motion modeling on parallel computers. In *SC '96: Proceedings of the 1996 ACM/IEEE Conference on High Performance Networking and Computing*, page 13, Pittsburgh, Pennsylvania, United States. IEEE Computer Society.

Bao, H., Bielak, J., Ghattas, O., Kallivokas, L. F., O'Hallaron, D. R., Shewchuk, J. R., and Xu, J. (1998). Large-scale simulation of elastic wave propagation in heterogeneous media on parallel computers. *Computer Methods in Applied Mechanics and Engineering*, 152(1-2):85–102.

Bard, P.-Y., Chaljub, E., Hollender, F., Manakou, M., and Pitilakis, K. (2008). Euroseistest numerical benchmark: Phase I. Technical report, Commissariat à l'énergie atomique (CEC), Report distributed to the participants of the Cashima-Euroseistest Benchmark.

Bard, P.-Y., Guéguen, P., and Wirgin, A. (1996). A note on the seismic wavefield radiated from large building structures into soft soils. In Sociedad Mexicana de Ingeniería Sísmica, editor, *Proceedings of the 11th World Conference on Earthquake Engineering*, Acapulco, Mexico. International Association for Earthquake Engineering, Elsevier Science Ltd. Paper 1838.

Bardet, J. P. and Davis, C. (1996a). Engineering observations on ground motion at the Van Norman Complex after the 1994 Northridge earthquake. *Bulletin of the Seismological Society of America*, 86(1B):S333–349.

Bardet, J. P. and Davis, C. A. (1996b). Performance of San Fernando dams during 1994 Northridge earthquake. *Journal of Geotechnical Engineering, ASCE*, 122(7):554–564.

Bardet, J. P. and Kapuskar, M. (1993). Liquefaction sand boils in san francisco during 1989 loma prieta earthquake. *Journal of Geotechnical Engineering, ASCE*, 119(3):543–562.

Beresnev, I. A. (1995). Seismological evidence for nonlinear elastic ground behavior during large earthquakes. *Soil Dynamics and Earthquake Engineering*, 14(2):103–114.

Beresnev, I. A. (2002). Nonlinearity at California generic soil sites from modeling recent strong-motion data. *Bulletin of the Seismological Society of America*, 92(2):863–870.

Beresnev, I. A. and Atkinson, G. M. (1998). Stochastic finite-fault modeling of ground motions from the 1994 Northridge, California, earthquake. I. Validation on rock sites. *Bulletin of the Seismological Society of America*, 88(6):1392–1401.

Beresnev, I. A. and Wen, K.-L. (1996). Nonlinear soil response—A reality? *Bulletin of the Seismological Society of America*, 86(6):1964–1978.

Beresnev, I. A., Wen, K.-L., and Tein Yeh, Y. (1995). Nonlinear soil amplification: Its corroboration in Taiwan. *Bulletin of the Seismological Society of America*, 85(2):496–515.

Bielak, J. (1971). *Earthquake response of building-foundation systems*. PhD thesis, California Institute of Technology, Pasadena, California.

Bielak, J., Ghattas, O., and Kim, E. J. (2005). Parallel octree-based finite element method for large-scale earthquake ground motion simulation. *Computer Modeling in Engineering and Sciences*, 10(2):99–112.

Bielak, J., Graves, R. W., Olsen, K. B., Taborda, R., Ramírez-Guzmán, L., Day, S. M., Ely, G. P., Roten, D., Jordan, T. H., Maechling, P. J., Urbanic, J., Cui, Y., and Juve, G. (2010). The ShakeOut earthquake scenario: Verification of three simulation sets. *Geophysical Journal International*, 180(1):375–404.

Bielak, J., Loukakis, K., Hisada, Y., and Yoshimura, C. (2003). Domain reduction method for three-dimensional earthquake modeling in localized regions, Part I: theory. *Bulletin of the Seismological Society of America*, 93(2):817–824.

Bielak, J., MacCamy, R. C., McGhee, D. S., and Barry, A. (1991). Unified symmetric BEM-FEM for site effects on ground motion—SH waves. *Journal of Engineering Mechanics, ASCE*, 117(10):2265–2285.

Bielak, J., Xu, J., and Ghattas, O. (1999). Earthquake ground motion and structural response in alluvial valleys. *Journal of Geotechnical and Geoenvironmental Engineering, ASCE*, 125(5):413–423.

Biot, M. A. (1956a). Theory of propagation of elastic waves in a fluid-saturated porous solid. I. Low-frequency range. *Journal of the Acoustical Society of America*, 28(2):168–178.

Biot, M. A. (1956b). Theory of propagation of elastic waves in a fluid-saturated porous solid. II. Higher frequency range. *Journal of the Acoustical Society of America*, 28(2):179–191.

Biot, M. A. (1962). Mechanics of deformation and acoustic propagation in porous media. *Journal of Applied Physics*, 33(4):1482–1498.

Boore, D. M. (1970). Love waves in nonuniform wave guides: Finite difference calculations. *Journal of Geophysical Research*, 75(8):1512–1527.

Boore, D. M. (1972). *Methods in Computational Physics*, volume II, chapter Finite difference methods for seismic wave propagation in heterogeneous materials. ed. Bolt, B. A., Academic Press.

Boore, D. M. (2003a). Phase derivatives and simulation of strong ground motions. *Bulletin of the Seismological Society of America*, 93(3):1132–1143.

Boore, D. M. (2003b). Simulation of ground motion using the stochastic method. *Pure and Applied Geophysics*, 160(3-4):635–676.

Bouchon, M. and Aki, K. (1980). Simulation of long-period, near-field motion for the great California earthquake of 1857. *Bulletin of the Seismological Society of America*, 70(5):1669–1682.

Bouchon, M. and Barker, J. S. (1996). Seismic response of a hill: The example of Tarzana, California. *Bulletin of the Seismological Society of America*, 86(1A):66–72.

Boutin, C. and Roussillon, P. (2004). Assessment of the urbanization effect on seismic response. *Bulletin of the Seismological Society of America*, 94(1):251–268.

Brocher, T. M. (2005). Empirical relations between elastic wavespeeds and density in the Earth's crust. *Bulletin of the Seismological Society of America*, 95(6):2081–2092.

Castro, R. R. and Ruiz-Cruz, E. (2005). Stochastic modeling of the 30 september 1999 M_{w} 7.5 Earthquake, Oaxaca, Mexico. *Bulletin of the Seismological Society of America*, 95(6):2259–2271.

Chaljub, E., Bard, P.-Y., Hollender, F., Theodulidis, N., Moczo, P., Tsuno, S., Kristek, J., Cadet, H., Franek, P., Bielak, J., and Pitilakis, K. (2010). Euroseistest numerical simulation project: Comparison with local earthquake recordings for validation. In *Abstracts of the 2010 SSA Annual Meeting*.

Chang, C. Y., Power, M. S., Tang, Y. K., and Mok, C. M. (1989). Evidence of nonlinear soil response during a moderate earthquake. In *Proceedings of the 12th International Conference on Soil Mechanics and Foundation Engineering*, volume 3, pages 1927–1930, Rio de Janerio, Brazil.

Chávez-García, F. J. and Cárdenas-Soto, M. (2002). The contribution of the built environment to the 'free-field' ground motion in Mexico City. *Soil Dynamics and Earthquake Engineering*, 22(9–12):773–780.

Chin, B.-H. and Aki, K. (1991). Simultaneous study of the source, path, and site effects on strong ground motion during the 1989 loma prieta earthquake: A preliminary result on pervasive nonlinear site effects. *Bulletin of the Seismological Society of America*, 81(5):1859–1884.

Clouteau, D. and Aubry, D. (2001). Modifications of the ground motion in dense urban areas. *Journal of Computational Acoustics*, 9(4):1659–1675.

Cornou, C., Guéguen, P., Bard, P.-Y., and Haghshenas, E. (2004). Ambient noise energy bursts observation and modeling: Trapping of harmonic structure-soil inducedwaves in a topmost sedimentary layer. *Journal of Seismology*, 8(4):507–524.

Cultrera, G., Boore, D. M., Joyner, W. B., and Dietel, C. M. (1999). Nonlinear soil response in the vicinity of the van Norman complex following the 1994 Northridge, California, earthquake. *Bulletin of the Seismological Society of America*, 89(5):1214–1231.

Dafalias, Y. F. (1986). Bounding surface plasticity. I: Mathematical foundation and hypoplasticity. *Journal of Engineering Mechanics, ASCE*, 112(9):966–987.

Dafalias, Y. F. and Popov, E. P. (1975). A model of nonlinearly hardening materials for complex loading. *Acta Mechanica*, 21(3):173–192.

Dafalias, Y. F. and Popov, E. P. (1977). Cyclic loading for materials with a vanishing elastic region. *Nuclear Engineering and Design*, 41(2):293–302.

Darragh, R. B. and Shakal, A. F. (1991). The site response of two rock and soil station pairs to strong and weak ground motion. *Bulletin of the Seismological Society of America*, 81(5):1885–1899.

Davis, C. A. and Bardet, J. P. (1996). Performance of two reservoirs during 1994 Northridge earthquake. *Journal of Geotechnical Engineering, ASCE*, 122(8):613–622.

Drucker, D. C. and Prager, W. (1952). Soil mechanics and plastic analysis or limit design. *Quarterly of Applied Mathematics*, 10:157–164.

Elgamal, A., Yan, L., Yang, Z., and Conte, J. P. (2008). Three-dimensional seismic response of the Humboldt bay bridge-foundation-ground system. *Journal of Structural Engineering, ASCE*. Accepted for publication.

Elgamal, A. W. (1991). Shear hysteretic elasto-plastic earthquake response of soil systems. *Earthquake Engineering and Structural Dynamics*, 20(4):371–387.

Elgamal, A.-W., Zeghal, M., Tang, H. T., and Stepp, J. C. (1995). Lotung downhole array. I: Evaluation of site dynamic properties. *Journal of Geotechnical Engineering, ASCE*, 121(4):350–362.

Erlingsson, S. (1999). Three-dimensional dynamic soil analysis of a live load in Ullevi Stadium. *Soil Dynamics and Earthquake Engineering*, 18(5):373–386.

Erlingsson, S. and Bodare, A. (1996). Live load induced vibrations in Ullevi Stadium—dynamic soil analysis. *Soil Dynamics and Earthquake Engineering*, 15(3):171–188.

Faccioli, E., Maggio, F., Paolucci, R., and Quarteroni, A. (1997). 2D and 3D elastic wave propagation by a pseudo-spectral domain decomposition method. *Journal of Seismology*, 1(3):237–251.

FEMA P-705 (2009). *NEHRP Recommended Seismic Provisions for New Buildings and Other Structures*. Prepared by the Building Seismic Safety Council of the National Institute of Building Sciences for the Federal Emergency Management Agency of the U.S. Department of Homeland Security.

Fernández-Ares, A. (2003). *Urban Seismology: Interaction between earthquake ground motion and response of urban regions*. PhD thesis, Carnegie Mellon University.

Fernández-Ares, A. and Bielak, J. (2004). Interaction between earthquake ground motion and multiple buildings in urban regions. In Celebi, M., Todorovska, M. I., Okawa, I., and Iiba, M., editors, *Proceedings of the 3rd UJNR Workshop on Soil-Structure Interaction*, Menlo Park, California.

Fernández-Ares, A. and Bielak, J. (2006). Urban Seismology: Interaction between earthquake ground motion and multiple buildings in urban regions. In *Proceedings of the 3rd International Symposium on the Effects of Surface Geology on Seismic Motion*, Grenoble, France. IASPEI and IAEE.

Fernández León, J. A. (2007). *Numerical Simulation of Earthquake Ground Motions in the Upper Mississippi Embayment*. PhD thesis, Georgia Institute of Technology.

Field, E. H., Johnson, P. A., Beresnev, I. A., and Zeng, Y. (1997). Nonlinear ground-motion amplification by sediments during the 1994 Northridge earthquake. *Nature*, 390(6660):599–602.

Finn, W. D. L., Martin, G. R., and Lee, M. K. W. (1978). Comparison of dynamic analyses for saturated sands. In *Proceedings of the ASCE Geotechnical Engineering Div. Specialty Conference*, Earthquake Engineering and Soil Dynamics, ASCE, pages 472–491, Pasadena, CA.

Frankel, A. (1993). Three-dimensional simulations of ground motions in the San Bernardino Valley, California, for hypothetical earthquakes on the San Andreas fault. *Bulletin of the Seismological Society of America*, 83(4):1020–1041.

Frankel, A. and Stephenson, W. (2000). Three-dimensional simulations of ground motions in the Seattle region for earthquakes in the Seattle fault zone. *Bulletin of the Seismological Society of America*, 90(5):1251–1267.

Frankel, A. and Vidale, J. (1992). A three-dimensional simulation of seismic waves in the Santa Clara Valley, California, from a Loma Prieta aftershock. *Bulletin of the Seismological Society of America*, 82(5):2045–2074.

Frankel, A. D., Carver, D. L., and Williams, R. A. (2002). Nonlinear and linear site response and basin effects in Seattle for the M 6.8 Nisqually, Washington, earthquake. *Bulletin of the Seismological Society of America*, 92(6):2090–2109.

Furumura, T. and Koketsu, K. (2000). Parallel 3-D simulation of ground motion for the 1995 Kobe earthquake: The component decomposition approach. *Pure and Applied Geophysics*, 157(11-12):2047–2062.

Gorini, A., Marcucci, S., Marsan, P., and Milana, G. (2004). Strong motion records of the 2002 Molise, Italy, earthquake sequence and stochastic simulation of the main shock. *Earthquake Spectra*, 20(S1):S65–S79.

Graves, R. W. (1996). Simulating seismic wave propagation in 3D elastic media using staggered-grid finite differences. *Bulletin of the Seismological Society of America*, 86(4):1091–1106.

Graves, R. W. (1998). Three-dimensional finite-difference modeling of the San Andreas fault: Source parameterization and ground-motion levels. *Bulletin of the Seismological Society of America*, 88(4):881–897.

Graves, R. W. (2008). The seismic response of the San Bernardino basin region during the 2001 Big Bear lake earthquake. *Bulletin of the Seismological Society of America*, 98(1):241–252.

Graves, R. W., Aagaard, B. T., Hudnut, K., Star, L. M., Stewart, J. P., and Jordan, T. H. (2008). Broadband simulations for M_w7.8 southern San Andreas earthquakes: ground motion sensitivity to rupture speed. *Geophysical Research Letters*, 35:L22302.

Graves, R. W. and Pitarka, A. (2004). Broadband time history simulation using a hybrid approach. In Canadian Association for Earthquake Engineering, editor, *Proceedings of the 13th World Conference on Earthquake Engineering*, Vancouver, British Columbia, Canada. International Association for Earthquake Engineering. Paper 1098.

Graves, R. W. and Wald, D. J. (2004). Observed and simulated ground motions in the San Bernardino basin region for the Hector Mine, California earthquake. *Bulletin of the Seismological Society of America*, 94(1):131–146.

Groby, J.-P., Tsogka, C., and Wirgin, A. (2005). Simulation of seismic response in a city-like environment. *Soil Dynamics and Earthquake Engineering*, 25(7–10):487–504.

Groby, J.-P. and Wirgin, A. (2008). Seismic motion in urban sites consisting of blocks in welded contact with a soft layer overlying a hard half-space. *Geophysical Journal International*, 172(2):725–758.

Guéguen, P. and Bard, P.-Y. (2005). Soil-structure and soil-structure-soil interaction: Experimental evidence at the Volvi test site. *Journal of Earthquake Engineering*, 9(5):657–693.

Guéguen, P., Bard, P.-Y., and Chávez-García, F. J. (2002). Site-city seismic interaction in Mexico City-like environments: An analytical study. *Bulletin of the Seismological Society of America*, 92(2):794–811.

Guéguen, P., Bard, P.-Y., and Oliveira, C. S. (2000a). Experimental and numerical analysis of soil motions caused by free vibrations of a building model. *Bulletin of the Seismological Society of America*, 90(6):1464–1479.

Guéguen, P., Bard, P.-Y., and Semblat, J.-F. (2000b). From soil-structure interaction to site-city interaction. In New Zealand Society for Earthquake Engineering, editor, *Proceedings of the 12th World Conference on Earthquake Engineering*, Auckland, New Zealand. International Association for Earthquake Engineering. Paper 0555.

Hadley, D. M. and Helmberger, D. V. (1980). Simulation of strong ground motions. *Bulletin of the Seismological Society of America*, 70(2):617–630.

Hardin, B. O. and Drnevich, V. P. (1972). Shear modulus and damping in soils: Measurement and parameters effects. *Journal of the Soil Mechanics and Foundations Division, ASCE*, 98(SM6):603–624. Paper 8977.

Hartzell, S., Harmsen, S., Frankel, A., and Larsen, S. (1999). Calculation of broadband time histories of ground motion: Comparison of methods and validation using strong-ground motion from the 1994 Northridge earthquake. *Bulletin of the Seismological Society of America*, 89(6):1484–1504.

Hartzell, S., Harmsen, S., Williams, R. A., Carver, D., Frankel, A., Choy, G., Liu, P.-C., Jachens, R. C., Brocher, T. M., and Wentworth, C. M. (2006). Modeling and validation of a 3D velocity structure for the Santa Clara Valley, California, for seismic-wave simulations. *Bulletin of the Seismological Society of America*, 96(5):1851–1881.

Hartzell, S. H. (1978). Earthquake aftershocks as green's functions. *Geophysical Research Letters*, 5(1):1–4.

Hisada, Y., Aki, K., and Teng, T.-L. (1993). 3-D simulations of surface wave propagation in the Kanto sedimentary basin, Japan Part 2: Application of the surface wave BEM. *Bulletin of the Seismological Society of America*, 83(6):1700–1720.

Hisada, Y., Bao, H., Bielak, J., Ghattas, O., and O'Hallaron, D. (1998). Simulations of long-period ground motions during the 1995 Hyogoken-Nanbu (Kobe) earthquake using 3D finite element method. In *Proceedings of the 2nd International Symposium on Effect of Surface Geology on Seismic Motion*, pages 59–66, Yokohama, Japan.

Hisada, Y. and Bielak, J. (2003). A theoretical method for computing near-fault ground motions in layered half-spaces considering static offset due to surface faulting, with a physical interpretation of fling step and rupture directivity. *Bulletin of the Seismological Society of America*, 93(3):1154–1168.

Housner, G. W. (1957). Interaction of building and ground during an earthquake. *Bulletin of the Seismological Society of America*, 47(3):179–186.

Idriss, I. M. and Seed, H. B. (1968a). An analysis of ground motions during the 1957 San Francisco earthquake. *Bulletin of the Seismological Society of America*, 58(6):2013–2032.

Idriss, I. M. and Seed, H. B. (1968b). Seismic response of horizontal soil layers. *Journal of the Soil Mechanics and Foundations Division, ASCE*, 94(SM4):1003–1031.

Idriss, I. M. and Seed, H. B. (1970). Seismic response of soil deposits. *Journal of the Soil Mechanics and Foundations Division, ASCE*, 96(SM2):631–638. Paper 7175.

Idriss, I. M. and Sun, J. I. (1993). *User's manual for SHAKE91: A computer program for conducting equivalent linear seismic response analyses of horizontally layered soil deposits.* Center for Geotechnical Modeling, Dept. of Civil and Environmental Engineering, University of California, Davis Davis, CA.

Irikura, K. (1984). Prediction of strong ground motions using observed seismograms from small events. In *Proceedings of the 8th World Conference on Earthquake Engineering*, volume 2, pages 465–472, San Francisco, California. International Association for Earthquake Engineering, Prentice Hall Professional Technical Reference.

Irikura, K. (1986). Prediction of strong acceleration motion using empirical green's function. In *Proceedings of the 7th Japan Earthquake Engineering Symposium*, pages 151–156, Tokyo, Japan.

Irikura, K. and Kamae, K. (1994). Estimation of strong ground motion in broad-frequency band based on a seismis source scaling model and an empirical Green's function technique. *AG*, 37(6):1721–1743.

Iwan, W. (1967). On a class of models for the yielding behavior of continuous and composite systems. *Journal of Applied Mechanics, ASME*, 34:612–617.

Jennings, P. C. (1970). Distant motions from a building vibration test. *Bulletin of the Seismological Society of America*, 60(6):2037–2043.

Jennings, P. C. and Bielak, J. (1973). Dynamics of building-soil interaction. *Bulletin of the Seismological Society of America*, 63(1):9–48.

Jones, L. M., Bernknopf, R., Cox, D., Goltz, J., Hudnut, K., Mileti, D., Perry, S., Ponti, D., Porter, K., Reichle, M., Seligson, H., Shoaf, K., Treiman, J., and Wein, A. (2008). The ShakeOut scenario. Technical Report USGS-R1150, CGS-P25, U.S. Geological Survey and California Geological Survey.

Jongmans, D., Pitilakis, K., Demanet, D., Raptakis, D., Riepl, J., Horrent, C., Tsokas, G., Lontzetidis, K., and Bard, P.-Y. (1998). EURO-SEISTEST: Determination of the geological structure of the Volvi basin and validation of the basin response. *Bulletin of the Seismological Society of America*, 88(2):473–487.

Joyner, W. B. (1975). A method for calculating nonlinear seismic response in two dimensions. *Bulletin of the Seismological Society of America*, 65(5):1337–1357.

Joyner, W. B. and Chen, A. T. F. (1975). Calculation of nonlinear ground response in earthquakes. *Bulletin of the Seismological Society of America*, 65(5):1315–1336.

Kamae, K. and Irikura, K. (1998). Source model of the 1995 Hyogo-Ken Nanbu earthquake and simulation of near-source ground motion. *Bulletin of the Seismological Society of America*, 88(2):400–412.

Kamae, K., Irikura, K., and Pitarka, A. (1998). A technique for simulating strong ground motion using hybrid Green's function. *Bulletin of the Seismological Society of America*, 88(2):357–367.

Kanamori, H., Mori, J., Anderson, D. L., and Heaton, T. H. (1991). Seismic excitation by the space shuttle Columbia. *Nature*, 349(6312):781–782.

Käser, M. and Dumbser, M. (2006). An arbitrary high-order discontinuous galerkin method for elastic waves on unstructured meshes — I. The two-dimensional isotropic case with external source terms. *Geophysical Journal International*, 166(2):855–877.

Käser, M. and Gallovic, F. (2008). Effects of complicated 3D rupture geometries on earthquake ground motion and their implications: A numerical study. *Geophysical Journal International*, 172(1):276–292.

Katona, M. G. (1984). Evaluation of viscoplastic cap model. *Journal of Geotechnical Engineering, ASCE*, 110(8):1106–1125.

Kawase, H. and Aki, K. (1990). Topography effect at the critical SV-wave incidence: Possible explanation of damage pattern by the Whittier Narrows, California, earthquake of 1 October 1987. *Bulletin of the Seismological Society of America*, 80(1):1–22.

Kelly, K. R., Ward, R. W., Treitel, S., and Alford, R. M. (1976). Synthetic seismograms: A finite-difference approach. *Geophysics*, 41(1):2–27.

Kham, M., Semblat, J.-F., Bard, P.-Y., and Dangla, P. (2006). Seismic site-city interaction: Main governing phenomena through simplified numerical models. *Bulletin of the Seismological Society of America*, 96(5):1934–1951.

Kim, A., Dreger, D. S., and Larsen, S. (2010). Moderate earthquake ground-motion validation in the San Francisco Bay area. *Bulletin of the Seismological Society of America*, 100(2):819–825.

Kim, E. J., Bielak, J., and Ghattas, O. (2003). Large-scale Northridge earthquake simulation using octree-based multiresolution mesh method. In *Proceedings of the 16th ASCE Engineering Mechanics Conference*, Seattle, Washington. University of Washington.

Kim, W. Y., Armitage, J., Armbruster, J., Jacob, K., Lerner-Lam, A., Richards, P., Sykes, L. R., and Xie, J.-K. (2001). Seismic waves generated by aircraft impacts and building collapses at World Trade Center, New York City. Technical report, Lamont-Doherty Earth Observatory, Columbia University, Palisades NY 10964.

Kleindorfer, G. B. and Ganeshan, R. (1993). The philosophy of science and validation in simulation. In *Proceedings of the 1993 Winter Simulation Conference*, pages 50–57.

Kohrs-Sansorny, C., Courboulex, F., Bour, M., and Deschamps, A. (2005). A two-stage method for ground-motion simulation using stochastic summation of small earthquakes. *Bulletin of the Seismological Society of America*, 95(4):1387–1400.

Komatitsch, D., Liu, Q., Tromp, J., Suss, P., Stidham, C., and Shaw, J. H. (2004). Simulations of ground motion in the Los Angeles basin based upon the spectral-element method. *Bulletin of the Seismological Society of America*, 94(1):187–206.

Komatitsch, D. and Vilotte, J.-P. (1998). The spectral element method: An efficient tool to simulate the seismic response of 2D and 3D geological structures. *Bulletin of the Seismological Society of America*, 88(2):368–392.

Kristekova, M., Kristek, J., Moczo, P., and Day, S. M. (2006). Misfit criteria for quantitative comparison of seismograms. *Bulletin of the Seismological Society of America*, 96(5):1836–1850.

Laurenzano, G., Priolo, E., Gallipoli, M. R., Mucciarelli, M., and Ponzo, F. C. (2010). Effect of vibrating buildings on free-field motion and on adjacent structures: The Bonefro (Italy) case history. *Bulletin of the Seismological Society of America*, 100(2):802–818.

Lemaitre, J. and Chaboche, J.-L. (1990). *Mechanics of Solid Materials*. Cambridge University Press, The Pitt Building, Trumpington Street, Cambridge CB2 1RP, UK, English Translation edition.

Lubliner, J. (1990). *Plasticity Theory*. Dover Publications, Mineola, New York, Third edition.

Luco, J. E. and Contesse, L. (1973). Dynamic structure-soil-structure interaction. *Bulletin of the Seismological Society of America*, 63(4):1289–1303.

Lysmer, J. and Drake, L. A. (1972). A finite element method for seismology. In Alder, B., Fernbach, S., and Bolt, B., editors, *Methods in Computational Physics*, volume 11, chapter 6. Academic Press, New York.

Lysmer, J. and Kuhlemeyer, R. L. (1969). Finite dynamic model for infinite media. *Journal of the Engineering Mechanics Division, ASCE*, 95(EM4):859–877.

Manakou, M. V. (2007). *Contribution of the determination of a 3D soil model for the site response study. Application to the sedimentary Mygdonian basin.* PhD thesis, Department of Civil Engineering, Aristotle University of Thessaloniki. In Greek.

Manakou, M. V., Raptakis, D. G., Chávez-García, F. J., Apostolidis, P. I., and Pitilakis, K. D. (2010). 3D soil structure of the Mygdonian basin for site response analysis. *Soil Dynamics and Earthquake Engineering*, 30(11):1198–1211.

Marsh, J., Larkin, T. J., Haines, A. J., and Benites, R. A. (1995). Comparison of linear and nonlinear seismic responses of two-dimensional alluvial basins. *Bulletin of the Seismological Society of America*, 85(3):874–889.

Mavroeidis, G. P., Zhang, B., Dong, G., Papageorgiou, A. S., Dutta, U., and Biswas, N. N. (2008). Estimation of strong ground motion from the great 1964 M_{w} 9.2 Prince William Sound, Alaska earthquake. *Bulletin of the Seismological Society of America*, 98(5):2303–2324.

Mena, B., Durukal, E., and Erdik, M. (2006). Effectiveness of hybrid Green's function method in the simulation of near-field strong motion: An application to the 2004 Parkfield earthquake. *Bulletin of the Seismological Society of America*, 96(4B):S183–S205.

Meremonte, M., Frankel, A., Cranswick, E., Carver, D., and Worley, D. (1996). Urban seismology–Northridge aftershocks recorded by multi-scale arrays of portable digital seismographs. *Bulletin of the Seismological Society of America*, 86(5):1350–1363.

Merritt, R. G. and Housner, G. W. (1954). Effect of foundation compliance on earthquake stresses in multistory buildings. *Bulletin of the Seismological Society of America*, 44(4):551–569.

Miyake, H., Iwata, T., and Irikura, K. (2003). Source characterization for broadband ground-motion simulation: Kinematic heterogeneous source model and strong motion generation area. *Bulletin of the Seismological Society of America*, 93(6):2531–2545.

Moczo, P., Kristek, J., Franek, P., Chaljub, E., Bard, P.-Y., Tsuno, S., Hollender, F., Iwan, W., Iwaki, A., Priolo, E., Klin, P., Aoi, S., Mariotti, C., Bielak, J., Taborda, R., Karaoglu, H., Etienne, V., and Virieux, J. (2010). Numerical modeling of earthquake ground motion in the mygdonian basin, greece: Verification of the 3D numerical methods. In *Abstracts of the 2010 SSA Annual Meeting*.

Moczo, P., Kristek, J., Galis, M., Pazk, P., and Balazovjech, M. (2007). The finite-difference and finite-element modeling of seismic wave propagation and earthquake motion. *Acta Physica Slovaca*, 57(2):177–406.

Mossessian, T. K. and Dravinski, M. (1987). Application of a hybrid method for scattering of P, SV, and Rayleigh waves by near-surface irregularities. *Bulletin of the Seismological Society of America*, 77(5):1784–1803.

Mróz, Z. (1967). On the description of anisotropic workhardening. *Journal of the Mechanics and Physics of Solids*, 15(3):163–175.

Mróz, Z. (1980). On hypoelasticity and plasticity approaches to constitutive modelling of inelastic behaviour of soils. *International Journal for Numerical and Analytical Methods in Geomechanics*, 4(1):45–55.

Mueller, C. S. (1985). Source pulse enhancement by deconvolution of an empirical Green's function. *Geophysical Research Letters*, 12(1):33–36.

Munguia, L. and Brune, J. N. (1984). Simulations of strong ground motion for earthquakes in the Mexicali-Imperial Valley region. *Geophysical Journal International*, 79(3):747–771.

Olsen, K. B. and Archuleta, R. J. (1996). Three-dimensional simulation of earthquakes on the Los Angeles fault system. *Bulletin of the Seismological Society of America*, 86(3):575–596.

Olsen, K. B., Archuleta, R. J., and Matarese, J. R. (1995a). Three-dimensional simulation of a magnitude 7.75 earthquake on the San Andreas fault. *Science*, 270(5242):1628–1632.

Olsen, K. B., Day, S. M., Dalaguer, L. A., Mayhew, J., Cui, Y., Zhu, J., Cruz-Atienza, V. M., Roten, D., Maechling, P., Jordan, T. H., Okaya, D., and Chourasia, A. (2009). ShakeOut-D: Ground motion estimates using an ensemble of large earthquakes on the southern San Andreas fault with spontaneous rupture propagation. *Geophysical Research Letters*, 36:L04303.

Olsen, K. B., Day, S. M., Minster, J. B., Cui, Y., Chourasia, A., Faerman, M., Moore, R., Maechling, P., and Jordan, T. (2006). Strong shaking in Los Angeles expected from southern San Andreas earthquake. *Geophysical Research Letters*, 33(L07305):1–4.

Olsen, K. B., Day, S. M., Minster, J. B., Cui, Y., Chourasia, A., Okaya, D., Maechling, P., and Jordan, T. (2008). TeraShake2: Spontaneous rupture simulations of M_{W} 7.7 earthquakes on the southern San Andreas fault. *Bulletin of the Seismological Society of America*, 98(3):1162–1185.

Olsen, K. B., Pechmann, J. C., and Schuster, G. T. (1995b). Simulation of 3D elastic wave propagation in the Salt Lake basin. *Bulletin of the Seismological Society of America*, 85(6):1688–1710.

Orenstein, J. A. (1986). Spatial query processing in an object-oriented database system. In *SIGMOD '86: Proceedings of the 1986 ACM SIGMOD international conference on Management of data, Washington, D.C., United States*, pages 326–336, New York, NY, USA. ACM.

Orenstein, J. A. and Merrett, T. H. (1984). A class of data structures for associative searching. In *PODS '84: Proceedings of the 3rd ACM SIGACT-SIGMOD symposium on Principles of database systems, Waterloo, Ontario, Canada*, pages 181–190, New York, NY, USA. ACM.

Oreskes, N., Shrader-Frechette, K., and Belitz, K. (1994). Verification, validation, and confirmation of numerical models in the earth sciences. *Science*, 263(5147):641–646.

Papazachos, C. B. (1998). Crustal p- and s-velocity structure of the Serbomacedonian Massif (Northern Greece) obtained by non-linear inversion of traveltimes. *Geophysical Journal International*, 134(1):25–39.

Perzyna, P. (1963). The constitutive equations for rate sensitive plastic materials. *Quarterly of Applied Mathematics*, 20:321–332.

Perzyna, P. (1966). Fundamental problems in viscoplasticity. In Chernyi, G., Dryden, H., Germain, P., Howarth, L., Olszak, W., Prager, W., Probstein, R., and Ziegler, H., editors, *Advances in Applied Mechanics*, volume 9, pages 243–377. Elsevier.

Pitarka, A., Irikura, K., Iwata, T., and Sekiguchi, H. (1998). Three-dimensional simulation of the near-fault ground motion for the 1995 Hyogo-Ken Nanbu (Kobe), Japan, earthquake. *Bulletin of the Seismological Society of America*, 88(2):428–440.

Pitarka, A., Somerville, P., Fukushima, Y., Uetake, T., and Irikura, K. (2000). Simulation of near-fault strong-ground motion using hybrid Green's functions. *Bulletin of the Seismological Society of America*, 90(3):566–586.

Pitarka, A., Somerville, P. G., Fukushima, Y., and Uetake, T. (2002). Ground-motion attenuation from the 1995 kobe earthquake based on simulations using the hybrid green's function method. *Bulletin of the Seismological Society of America*, 92(3):1025–1031.

Pitilakis, K. (2008). EUROSEISTEST: A European test site for engineering seismology, earthquake engineering and seismology. Technical report, Department of Civil Engineering, Aristotle University of Thessaloniki, Greece.

Pitilakis, K., Raptakis, D., Lontzetidis, K., and Tika-Vassilikou, T. H. (1999). Geotechnical and geophysical description of euro-seistest, using field, laboratory tests and moderate strong motion records. *Journal of Earthquake Engineering*, 3(3):381–409.

Potluri, S., Lai, P., Tomko, K., Sur, S., Cui, Y., Tatineni, M., Schulz, K. W., Barth, W. L., Majumdar, A., and Panda, D. K. (2010). Quantifying performance benefits of overlap using mpi-2 in a seismic modeling application. In *ICS '10: Proceedings of the 24th ACM International Conference on Supercomputing*, pages 17–25, Tsukuba, Ibaraki, Japan. ACM, ACM.

Pousse, G., Bonilla, L. F., Cotton, F., and Margerin, L. (2006). Nonstationary stochastic simulation of strong ground motion time histories including natural variability: Application to the K-Net Japanese database. *Bulletin of the Seismological Society of America*, 96(6):2103–2117.

Prevost, J.-H. (1977). Mathematical modelling of monotonic and cyclic undrained clay behaviour. *International Journal for Numerical and Analytical Methods in Geomechanics*, 1(2):195–216.

Prevost, J.-H. (1978). Plasticity theory for soil stress-strain behavior. *Journal of the Engineering Mechanics Division, ASCE*, 104(5):1177–1194.

Prevost, J.-H. (1980). Mechanics of continuous porous media. *International Journal of Engineering Science*, 18(6):787–800.

Prevost, J.-H. (1985). A simple plasticity theory for frictional cohesionless soils. *Soil Dynamics and Earthquake Engineering*, 4(1):9–17.

Prevost, J.-H. and Popescu, R. (1996). Constitutive relations for soil materials. *Electronic Journal of Geotechnical Engineering*, 1:1–45.

Ramírez-Guzmán, L. (2008). *Earthquake source mechanics and wave propagation in sedimentary basins using the finite element method*. PhD thesis, Carnegie Mellon University, Pittsburgh, PA.

Ramírez-Guzmán, L., Contreras, M., Taborda, R., and Bielak, J. (2008). Ground motion in the valley of Mexico: Basin effects. In *Abstracts of the 2008 SSA Annual Meeting*, Santa Fe, NM, April 16–18.

Raptakis, D., Chávez-García, F. J., Makra, K., and Pitilakis, K. (2000). Site effects at Euroseistest–I. Determination of the valley structure and confrontation of observations with 1D analysis. *Soil Dynamics and Earthquake Engineering*, 19(1):1–2.

Raptakis, D. G., Manakou, M. V., Chávez-García, F. J., Makra, K. A., and Pitilakis, K. D. (2005). 3D configuration of Mygdonian basin and preliminary estimate of its site response. *Soil Dynamics and Earthquake Engineering*, 25(11):871–887.

Roumelioti, Z., Kiratzi, A., and Theodulidis, N. (2004). Stochastic strong ground-motion simulation of the 7 September 1999 Athens (Greece) earthquake. *Bulletin of the Seismological Society of America*, 94(3):1036–1052.

Rubinstein, J. L. and Beroza, G. C. (2004a). Evidence for widespread nonlinear strong ground motion in the M_{W} 6.9 Loma Prieta earthquake. *Bulletin of the Seismological Society of America*, 94(5):1595–1608.

Rubinstein, J. L. and Beroza, G. C. (2004b). Nonlinear strong ground motion in the M_{L} 5.4 Chittenden earthquake: Evidence that preexisting damage increases susceptibility to further damage. *Geophysical Research Letters*, 31(23):L23614.1–4.

Rubinstein, J. L., Uchida, N., and Beroza, G. C. (2007). Seismic velocity reductions caused by the 2003 Tokachi-Oki earthquake. *Journal of Geophysical Research*, 112(B11):B05315.

Sánchez-Sesma, F. J. and Luzón, F. (1995). Seismic response of three-dimensional alluvial valleys for incident P, S, and Rayleigh waves. *Bulletin of the Seismological Society of America*, 85(1):269–284.

Sargent, R. G. (2005). Verification and validation of simulation models. In Kuhl, M. E., Steiger, N. M., Armstrong, F. B., and Joines, J. A., editors, *Proceedings of the 2005 Winter Simulation Conference*, pages 130–143.

Sato, K., Kokusho, T., Matsumoto, M., and Yamada, E. (1996). Nonlinear seismic response and soil property during strong motion. *Soils and Foundations*, January(Special issue):41–52.

Sato, T., Graves, R. W., and Somerville, P. G. (1999). Three-dimensional finite-difference simulations of long-period strong motions in the Tokyo metropolitan area during the 1990 Odawara earthquake (M_{J} 5.1) and the great 1923 Kanto earthquake (M_{S} 8.2) in Japan. *Bulletin of the Seismological Society of America*, 89(3):579–607.

Satoh, T., Sato, T., and Kawase, H. (1995). Nonlinear behavior of soil sediments identified by using borehole records observed at the Ashigra Valley, Japan. *Bulletin of the Seismological Society of America*, 85(6):1821–1834.

Schaff, D. P. and Beroza, G. C. (2004). Coseismic and postseismic velocity changes measured by repeating earthquakes. *Journal of Geophysical Research*, 109(B10):B10302.

Schlesinger, S., Crosbie, R. E., Gagné, R. E., Innis, G. S., Lalwani, C. S., Loch, J., Sylvester, R. J., Wright, R. D., Kheir, N., and Bartos, D. (1979). Terminology for model credibility. *Simulation*, 32(3):103–104.

Schnabel, P., Seed, H. B., and Lysmer, J. (1972a). Modification of seismograph records for effects of local soil conditions. *Bulletin of the Seismological Society of America*, 62(6):1649–1664.

Schnabel, P. B., Lysmer, J., , and Seed, H. B. (1972b). SHAKE: A computer program for earthquake response analysis of horizontally-layered sites. Technical Report EERC-72/12, Earthquake Engineering Research Center, University of California, Berkeley, CA.

Scott, R. F. (1985). Plasticity and constitutive relations in soil mechanics. *Journal of Geotechnical Engineering, ASCE*, 111(5):559–605.

Seed, H. B. and Idriss, I. M. (1969). Influence of soil condition on ground motions during earthquakes. *Journal of the Soil Mechanics and Foundations Division, ASCE*, 95(SM1):99–137. Paper 6347.

Semblat, J.-F., Guéguen, P., Kham, M., Bard, P.-Y., and Duval, A.-M. (2002). Site-city interaction at local and global scales. In *Proceedings of the 12th European Conference on Earthquake Engineering*. Elsevier Science Ltd. Paper 807.

Semblat, J.-F., Kham, M., Bard, P.-Y., and Guéguen, P. (2004). Could "site-city interaction" modify site effects in urban areas? In Canadian Association for Earthquake Engineering, editor, *Proceedings of the 13th World Conference on Earthquake Engineering*, Vancouver, British Columbia, Canada. International Association for Earthquake Engineering. Paper 1978.

Seriani, G. (1998). 3-D large-scale wave propagation modeling by spectral element method on Cray T3E multiprocessor. *Computer Methods in Applied Mechanics and Engineering*, 64(1–2):235–247.

Seriani, G. and Priolo, E. (1994). Spectral element method for acoustic wave simulation in heterogeneous media. *Finite Elements in Analysis and Design*, 16(3–4):337–348.

Silva, W., Wong, I., Siegel, T., Gregor, N., Darragh, R., and Lee, R. (2003). Ground motion and liquefaction simulation of the 1886 Charleston, South Carolina, earthquake. *Bulletin of the Seismological Society of America*, 93(6):2717–2736.

Somerville, P., Sen, M., and Cohee, B. (1991). Simulation of strong ground motions recorded during the 1985 Michoacan, Mexico and Valparaiso, Chile earthquakes. *Bulletin of the Seismological Society of America*, 81(1):1–27.

Sørensen, M. B., Atakan, K., and Pulido, N. (2007). Simulated strong ground motions for the great m 9.3 Sumatra-Andaman earthquake of 26 December 2004. *Bulletin of the Seismological Society of America*, 97(1A):S139–S151.

Streeter, V. L., Wylie, E. B., and Richart, F. E. (1974). Soil motion computations by characteristics method. *Journal of the Geotechnical Engineering Division, ASCE*, 100(3):247–263.

Taborda, R., Karaoglu, H., Bielak, J., Urbanic, J., López, J., and Ramírez-Guzmán, L. (2009). Chino Hills — A highly computationally efficient 2 Hz validation exercise. *Eos Transcripts of the American Geophysical Union*, 88(52): Fall Meeting Supplement, Abstract S43A–1977.

Taborda, R., López, J., Karaoglu, H., Urbanic, J., and Bielak, J. (2010). Speeding up finite element wave propagation for large-scale earthquake simulations. Technical Report CMU-PDL-10-109, Carnegie Mellon University, Parallel Data Lab.

Taborda, R., López, J., O'Hallaron, D., Tu, T., and Bielak, J. (2007a). A review of the current approach to CVM-Etrees. In *Proceedings and Abstracts of the 2007 SCEC Annual Meeting*, Palm Springs, CA, September 8-12.

Taborda, R., Ramírez-Guzmán, L., López, J., Urbanic, J., Bielak, J., and O'Hallaron, D. (2007b). ShakeOut and its effects in Los Angeles and Oxnard areas. *Eos Transcripts of the American Geophysical Union*, 88(52): Fall Meeting Supplement, Abstract IN21B–0477.

Taborda, R., Ramírez-Guzmán, L., Tu, T., Kim, E. J., López, J., Bielak, J., Ghattas, O., and O'Hallaron, D. (2006a). Scaling up TeraShake: A 1-Hz case study. *Eos Transcripts of the American Geophysical Union*, 87(52): Fall Meeting Supplement, Abstract S51E–07.

Taborda, R., Ramírez-Guzmán, L., Tu, T., López, J., Bielak, J., and O'Hallaron, D. (2006b). TeraShake simulations using Hercules: Analysis and comparison. In *Proceedings and Abstracts of the 2006 SCEC Annual Meeting*, Palm Springs, CA, September 10-13.

Trifunac, M. D. and Todorovska, M. I. (1996). Nonlinear soil response—1994 Northrdge, California, Earthquake. *Journal of Geotechnical Engineering, ASCE*, 122(9):725–735.

Tsogka, C. and Wirgin, A. (2003a). Seismic response of a set of blocks partially imbedded in soft soil. *Comptes Rendus Mecanique*, 331(3):217–224.

Tsogka, C. and Wirgin, A. (2003b). Simulation of seismic response in an idealized city. *Soil Dynamics and Earthquake Engineering*, 23(5):391–402.

Tsuda, K., Steidl, J., Archuleta, R., and Assimaki, D. (2006). Site-response estimation for the 2003 Miyagi-Oki earthquake sequence considering nonlinear site response. *Bulletin of the Seismological Society of America*, 96(4A):1474–1482.

Tu, T. and O'Hallaron, D. R. (2004a). Balanced refinement of massive linear octrees.

Tu, T. and O'Hallaron, D. R. (2004b). A computational database system for generatinn unstructured hexahedral meshes with billions of elements. In *SC '04: Proceedings of the 2004 ACM/IEEE International Conference for High Performance Computing, Networking, Storage and Analysis*, Pittsburgh, PA, November 6–12.

Tu, T. and O'Hallaron, D. R. (2004c). Extracting hexahedral mesh structures from balanced linear octrees. In *Proceedings of the Thirteenth International Meshing Roundtable*, Williamsburgh, VA, November.

Tu, T., O'Hallaron, D. R., and Ghattas, O. (2005). Scalable parallel octree meshing for terascale applications. In *SC '05: Proceedings of the 2005 ACM/IEEE International Conference for High Performance Computing, Networking, Storage and Analysis*, Seattle, Washington, November 12–18.

Tu, T., Yu, H., Ramírez-Guzmán, L., Bielak, J., Ghattas, O., Ma, K.-L., and O'Hallaron, D. R. (2006). From mesh generation to scientific visualization: An end-to-end approach to parallel supercomputing. In *SC '06: Proceedings of the 2006 ACM/IEEE International Conference for High Performance Computing, Networking, Storage and Analysis*, page 15, Tampa, Florida. IEEE Computer Society.

U.S. Coast and Geodetic Survey (1936). Earthquake investigations in California, 1934–1935. Special Publication 201, U.S. Department of Commerce, Washington, D.C.

Veletsos, A. S. and Meek, J. W. (1974). Dynamic behaviour of building-foundation systems. *Earthquake Engineering and Structural Dynamics*, 3(2):121–138.

Wen, K.-L. (1994). Non-linear soil response in ground motions. *Earthquake Engineering and Structural Dynamics*, 23(6):599–608.

Wennerberg, L. (1990). Stochastic summation of empirical Green's functions. *Bulletin of the Seismological Society of America*, 80(6A):1418–1432.

Wirgin, A. (2002). Seismic response at urbanized sites. In *Proceedings of the 12th European Conference on Earthquake Engineering*. Elsevier Science Ltd. Paper 803.

Wirgin, A. and Bard, P.-Y. (1996). Effects of buildings on the duration and amplitude of ground motion in Mexico City. *Bulletin of the Seismological Society of America*, 86(3):914–920.

Wong, H. L. (1975). *Dynamic Soil-Structure Interaction*. PhD thesis, California Institute of Technology, Pasadena, California.

Wong, H. L. and Trifunac, M. D. (1975). Two-dimensional, antiplane, building-soil-building interaction for two or more buildings and for incident plane SH waves. *Bulletin of the Seismological Society of America*, 65(6):1863–1885.

Xu, J. (1998). *Three dimensional simulation of wave propagation in inelastic media on parallel computers*. PhD thesis, Carnegie Mellon University.

Xu, J., Bielak, J., Ghattas, O., and Wang, J. (2003). Three-dimensional nonlinear seismic ground motion modeling in basins. *Physics of The Earth and Planetary Interiors*, 137(1-4):81–95.

Yan, L. (2006). *Sensor data analysis and information extraction for structural health monitoring, Appendices A and B: Three-dimensional bridge-foundation-ground system, computational model and seismic response*. PhD thesis, University of California, San Diego.

Yang, Z., He, L., Bielak, J., Zhang, Y., Elgamal, A., and Conte, J. P. (2003). Nonlinear seismic response of a bridge site subjected to spatially varying ground motion. In *Proceedings of the 16th ASCE Engineering Mechanics Conference*, Seattle, Washington. University of Washington.

Yu, G., Anderson, J. G., and Siddharthan, R. (1993). On the characteristics of nonlinear soil response. *Bulletin of the Seismological Society of America*, 83(1):218–244.

Zeghal, M., Elgamal, A.-W., Tang, H. T., and Stepp, J. C. (1995). Lotung downhole array. II: Evaluation of soil nonlinear properties. *Journal of Geotechnical Engineering, ASCE*, 121(4):363–378.

Zhang, B. and Papageorgiou, A. S. (1996). Simulation of the response of the Marina District Basin, San Francisco, California, to the 1989 Loma Prieta earthquake. *Bulletin of the Seismological Society of America*, 86(5):1382–1400.

Zhang, Y., Acero, G., Conte, J. P., Yang, Z., and Elgamal, A. (2004). Seismic reliability assesment of a bridge ground system. In Canadian Association for Earthquake Engineering, editor, *Proceedings of the 13th World Conference on Earthquake Engineering*, Vancouver, British Columbia, Canada. International Association for Earthquake Engineering. Paper 2978.

Zhang, Y., Conte, J. P., Yang, Z., Elgamal, A., Bielak, J., and Acero, G. (2008). Two-dimensional nonlinear earthquake response analysis of a bridge-foundation-ground system. *Earthquake Spectra*, 24(2):343–386.

Zhang, Y., Yang, Z., Bielak, J., Conte, J. P., and Elgamal, A. (2003). Treatment of seismic input and boundary conditions in nonlinear seismic analysis of a bridge ground system. In *Proceedings of the 16th ASCE Engineering Mechanics Conference*, Seattle, Washington. University of Washington.

Zienkiewicz, O. C. and Cormeau, I. C. (1974). Visco-plasticity—Plasticity and creep in elastic solids—A unified numerical solution approach. *International Journal for Numerical Methods in Engineering*, 8(4):821–845.